Dissertation

submitted to the

Combined Faculty of Mathematics, Engineering and Natural Sciences of Heidelberg University, Germany

for the degree of

Doctor of Natural Sciences

Put forward by
Dhruv Aalok Muley
Born in: Mountain View, California, United States of America
Oral examination: 25 June 2025

THREE-TEMPERATURE RADIATION HYDRODYNAMICS: A POWERFUL TOOL TO INVESTIGATE PROTOPLANETARY DISKS

DHRUV AALOK MULEY

Referees: apl. Prof. dr. H. Hubertus Klahr
Prof. dr. Jochen Heidt

Dhruv Aalok Muley: *Three-temperature radiation hydrodynamics: A powerful tool to investigate protoplanetary disks,* Dissertation submitted to the Combined Faculty of Mathematics, Engineering and Natural Sciences of Heidelberg University (Germany) for the degree of Doctor of Natural Sciences © May 2025

This work is licensed under Creative Commons Attribution-ShareAlike 4.0 International. This license requires that reusers give credit to the creator. It allows reusers to distribute, remix, adapt, and build upon the material in any medium or format, even for commercial purposes. If others remix, adapt, or build upon the material, they must license the modified material under identical terms. To view a copy of this license, visit

https://creativecommons.org/licenses/by-sa/4.0/

ABSTRACT

High-resolution observations of protoplanetary disks over a range of wavelengths have uncovered a wealth of large-scale substructures—including gaps, rings, and spirals—often attributed to the gravitational influence of nascent planets. This problem has long been studied using numerical hydrodynamics, with recent works demonstrating that the thermodynamic properties of the disk play a defining role in substructure morphology. To better model these properties within simulations, we have developed a "three-temperature" (3T; gas, dust, radiation) scheme for the PLUTO hydrodynamics code, including absorption/emission of radiation (principally by the dust, which supplies most of the opacity) and collisional thermal relaxation between dust gains and gas (which contains most of the mass/heat capacity). Although dust and gas are thermally well-coupled in the dense midplane of a typical disk, thermal relaxation times in the more rarefied disk atmosphere reach order-unity of the dynamical time, allowing perturbations driven by an orbiting planet to decouple the dust and gas temperatures. We apply 3T to open questions inspired by disk observations, finding that planet-driven gas-kinematic and temperaure spirals (such as that seen in TW Hya) are strengthened by planetary accretion luminosity, and that large-scale, double-armed spirals in the near-infrared (such as those in SAO 206462 and V1247 Ori) may be induced not by a planet's gravity directly, but by the effect of planet-carved gaps on shadowing and illumination of the outer disk.

ZUSAMMENFASSUNG

Hochauflösende Beobachtungen protoplanetarer Scheiben, die in verschiedenen Wellenlängenbereichen gemacht wurden, haben eine große Vielfalt an Substrukturen entdeckt, darunter Lücken, Ringe und Spiralwellen. Diese werden oft auf den gravitativen Einfluss entstehender Planeten zurückgeführt. Das Problem wird seit Jahrzehnten durch numerische Hydrodynamik untersucht, und in jüngster Zeit haben viele Studien gezeigt, dass die Thermodynamik der protoplanetaren Scheibe eine entscheidende Rolle für die Morphologie der durch Planeten angetriebenen Substrukturen spielt. Um dieser Prozess besser zu modellieren, haben wir ein “Drei-Temperatur-Modell"(3T) für den PLUTO-Hydrodynamik-Code entwickelt, das die Absorption und Emission von Strahlung (hauptsächlich vom Staubteilchen, die den größten Teil der Opazität des Systems umfassen) sowie Kollisionen zwischen Staubteilchen und Gasmolekülen (die die meiste Wärmekapazität und Masse des Systems besitzen) berücksichtigt. Obwohl der Staub und das Gas in der dichten Midplane der Scheibe thermisch stark gekoppelt sind, wird diese Kopplung in der höheren Atmosphäre der Scheibe schwächer, und die thermische Relaxationszeit länger. Daher können Temperaturstörungen im Gas, die durch einen umlaufenden Planeten verursacht werden, in diesen oberen Schichten der Scheibe weniger stark gekoppelt mit der Temperatur des Staubes sein. Wir wenden das 3T-Modell auf offene, beobachtungsinspirierte Fragestellungen an. Dabei stellen wir fest, dass die durch Planeten angetriebene Spiralwellen in der Gasgeschwindigkeit und Temperatur (wie in TW Hya beobachtet) durch die Akkretionshelligkeit verstärkt werden. Außerdem zeigen unsere Ergebnisse, dass die großen, zweiarmigen Spiralwellen im nahen Infrarot (wie in den Scheiben von SAO 206462 und V1247 Ori zu sehen) möglicherweise nicht direkt durch die Gravitation eines Planeten entstehen, sondern vielmehr durch die Auswirkungen der vom Planeten gemeißelten Lücke auf die Beleuchtung und Schattenbildung in der äußeren Scheibe.

Chapters of this work are derived from the following publications:

Muley, Dhruv, Julio David Melon Fuksman, and Hubert Klahr (Oct. 2023). "Three-temperature radiation hydrodynamics with PLUTO. Tests and applications in the context of protoplanetary disks." In: *A&A* 678, A162, A162. DOI: 10.1051/0004-6361/202347101. arXiv: 2308.03504 [astro-ph.IM].

— (Oct. 2024a). "Spiral excitation in protoplanetary disks through gap-edge illumination: Three-temperature radiation hydrodynamics and NIR image modeling." In: *A&A* 690, A355, A355. DOI: 10.1051/0004-6361/202451554. arXiv: 2408.16461 [astro-ph.EP].

— (July 2024b). "Three-temperature radiation hydrodynamics with PLUTO: Thermal and kinematic signatures of accreting protoplanets." In: *A&A* 687, A213, A213. DOI: 10.1051/0004-6361/202449739. arXiv: 2405.03375 [astro-ph.EP].

Other publications by the author, which are not part of the thesis:

Fung, Jeffrey and Dhruv Muley (Oct. 2019). "A Staggered Semi-analytic Method for Simulating Dust Grains Subject to Gas Drag." In: *ApJS* 244.2, 42, p. 42. DOI: 10.3847/1538-4365/ab45f3. arXiv: 1909.02006 [astro-ph.EP].

Melon Fuksman, Julio David, Mario Flock, Giancarlo Mattia, Hubert Klahr, and Dhruv Muley (2025 submitted). "Multidimensional half-moment multigroup radiative transfer: Improving moment-based thermal models of circumstellar disks." In: *A&A*.

Muley, Dhruv A., Coral R. Wheeler, Philip F. Hopkins, Andrew Wetzel, Andrew Emerick, and Dušan Kereš (Nov. 2021). "Progenitor-mass-dependent yields amplify intrinsic scatter in dwarf-galaxy elemental abundance ratios." In: *MNRAS* 508.1, pp. 508–515. DOI: 10.1093/mnras/stab2572. arXiv: 2008.04901 [astro-ph.GA].

Muley, Dhruv and Ruobing Dong (Nov. 2021). "CI Tau: A Controlled Experiment in Disk-Planet Interaction." In: *ApJ* 921.2, L34, p. L34. DOI: 10.3847/2041-8213/ac32df. arXiv: 2110.13182 [astro-ph.EP].

Muley, Dhruv, Ruobing Dong, and Jeffrey Fung (Oct. 2021). "Observational Signatures of Planets in Protoplanetary Disks: Temperature Structures in Spiral Arms." In: *AJ* 162.4, 129, p. 129. DOI: 10.3847/1538-3881/ac141f. arXiv: 2107.06323 [astro-ph.EP].

Muley, Dhruv, Jeffrey Fung, and Nienke van der Marel (July 2019). "PDS 70: A Transition Disk Sculpted by a Single Planet." In: *ApJ* 879.1, L2, p. L2. DOI: 10.3847/2041-8213/ab24d0. arXiv: 1902.07191 [astro-ph.EP].

van der Marel, Nienke, Til Birnstiel, Antonio Garufi, Enrico Ragusa, Valentin Christiaens, Daniel J. Price, Steph Sallum, Dhruv Muley, Logan Francis, and Ruobing Dong (Jan. 2021). "On the Diversity of Asymmetries in Gapped Protoplanetary Disks." In: *AJ* 161.1, 33, p. 33. DOI: 10.3847/1538-3881/abc3ba. arXiv: 2010.10568 [astro-ph.EP].

ACKNOWLEDGMENTS

It takes a village to raise a child, and it takes a community to educate a scientist—and in the final analysis, it is the people one is surrounded by who are more important than the research topic. To name just a few of the many people who helped me along my journey:

I would like to thank my supervisor, Hubert Klahr, for offering me the opportunity to pursue my PhD at the Max Planck Institute for Astronomy. With every group meeting and discussion, I appreciate more and more the importance of revisiting common simplifying assumptions underpinning our understanding of protoplanetary disks. I offer my gratitude to David Melon Fuksman, who introduced me to numerical radiation hydrodynamics—knowledge that was crucial to developing the three-temperature scheem that is foundational to this work. With Giancarlo Mattia, Mario Flock, and Alexandros Ziampras, I have had many enlightening and stimulating discussions on numerical methods and disk physics alike. Kees Dullemond and Myriam Benisty, the other members of my committee, have helped me better relate my work to radiative transfer and disk observations, and have always been sources of encouragement.

The work I did during my PhD would not have been possible without the research experience I gained as an undergraduate at UC Berkeley. Under the encouraging and patient guidance of Jeffrey Fung, I learned about disk-planet interactions, ran numerical hydrodynamics simulations, and wrote a scientific paper for the first time. Ruobing Dong's offer of a year-long research assistantship at the University of Victoria helped me broaden my professional network and develop a solid profile for PhD applications. All the while, my collaborator Nienke van der Marel has been a valuable source of observational insight, and always generous with her professional and moral support.

Moving from the United States to Germany, and adapting to a new language and culture, forced me to grow not only as a professional, but as a person. To my childhood friends, I appreciate our many conversations about science and current events, the humor we shared, the willingness to lend a comforting ear whenever I had difficulty dealing with the stress of daily life. To the new friends I made here, including those from the Klahr and Flock research groups, Student Coffee office, and the Institute as a whole: thanks for the memories we shared at cooking events, dance socials, and house parties, for helping bring me out of my shell to become a more social person, and for enriching with your daily interactions my nearly four years at MPIA.

Lastly, I would like to convey my thanks to my family. My parents, Aalok and Sheela Muley, instilled in me from an early age the value of education, while my sister Anusha has always been a source of kindness and encouragement in my endeavors. I also owe a debt of gratitude to my paternal grandparents, who helped raise me and lightened the load on my two working parents: the books, magazines, and newspapers that my grandfather Ashok subscribed to were the source of my intellectual curiosity, while my grandmother Alka—who has taken up painting in her 80s!—has shown that learning can truly be a lifelong process. Your love, support, and understanding have been key to helping me achieve this major academic milestone.

CONTENTS

0 INTRODUCTION AND MOTIVATION 1

I PHYSICAL BACKGROUND 5

1 DISK STRUCTURE AND THERMODYNAMICS 7
- 1.1 Structure equations 7
  - 1.1.1 Hydrostatic equilibrium 8
  - 1.1.2 Viscosity 10
- 1.2 Radiative processes 11
  - 1.2.1 Stellar irradiation 11
  - 1.2.2 Two-layer disk models 12
  - 1.2.3 Radiative heating and cooling 14
  - 1.2.4 Viscous heating 16
- 1.3 Dust and gas 17
  - 1.3.1 Grain size distributions 17
  - 1.3.2 Opacity 17
  - 1.3.3 Collisional heating and cooling 19
  - 1.3.4 Dust-gas dynamics 20

2 DISK PERTURBATIONS AND SUBSTRUCTURE 25
- 2.1 Disk-planet interaction 25
  - 2.1.1 Lindblad spirals 27
  - 2.1.2 Gap opening 29
- 2.2 Thermally-driven substructure 31

3 NUMERICAL METHODS FOR PROTOPLANETARY DISK STUDIES 35
- 3.1 Finite-volume schemes 35
- 3.2 Reconstruction and Riemann solvers 36
- 3.3 Implementation of radiation hydrodynamics 39
  - 3.3.1 M1 scheme for thermal infrared 39
  - 3.3.2 Stellar irradiation 40

II THREE-TEMPERATURE RADIATION HYDRODYNAMICS WITH PLUTO 41

4 TESTS AND APPLICATIONS TO PROTOPLANETARY DISKS 43
- 4.1 Introduction 43
- 4.2 Method 45
  - 4.2.1 Basic equations 45
  - 4.2.2 Conservation laws 47
  - 4.2.3 Operator splitting and timestepping 47
  - 4.2.4 Momentum source terms 49
  - 4.2.5 Energy source terms 49
- 4.3 Tests 50
  - 4.3.1 0D test: radiation-matter coupling 50
  - 4.3.2 1D test: Subcritical dusty radiative shock 53
  - 4.3.3 2D test: self-shadowing instability 56
  - 4.3.4 3D test: planet-driven spirals 61

4.4 Conclusion 66
5 THERMAL AND KINEMATIC SIGNATURES OF ACCRETING PROTOPLANETS 69
5.1 Introduction 69
5.2 Methods 71
5.2.1 Basic equations 71
5.2.2 Implementation of accretion luminosity 74
5.2.3 Setup and initial conditions 76
5.3 Disk physics 77
5.3.1 Thermodynamic prescriptions 77
5.3.2 Lindblad and buoyancy resonances 79
5.3.3 Flow analysis 80
5.3.4 Equilibrium temperature 83
5.4 Parameter study 84
5.4.1 Planet mass 85
5.4.2 Accretion luminosity 92
5.5 Observational implications 93
5.6 Conclusion 94
6 CAN GAP-EDGE ILLUMINATION EXCITE SPIRALS IN PROTOPLANETARY DISKS? 97
6.1 Introduction 97
6.2 Methods 98
6.2.1 PLUTO radiation hydrodynamics 98
6.2.2 RADMC3D Monte Carlo radiative transfer 102
6.3 Results 103
6.3.1 Temperature structure and thermal spirals 103
6.3.2 Radiative transfer post-processing 109
6.4 Conclusions 109

III CONCLUSION AND OUTLOOK 111
7 MORE REALISTIC SIMULATIONS OF PROTOPLANETARY DISKS 113
7.1 Summary of thesis work 113
7.2 Future outlook 114
7.2.1 Multispecies dust dynamics and thermodynamics 114
7.2.2 Applications 115

IV APPENDIX 117
A TESTS AND APPLICATIONS TO PROTOPLANETARY DISKS 119
A.1 Newton-Raphson iterations 119
A.2 Self-shadowing instability with long coupling times 120
B THERMAL AND KINEMATIC SIGNATURES OF ACCRETING PROTOPLANETS 125
B.1 Sky-projected figures 125
B.2 Advective terms in spherical coordinates 131
C CAN GAP-EDGE ILLUMINATION EXCITE SPIRALS IN PROTOPLANETARY DISKS? 133

C.1 Vorticity of the flow field 133
C.2 β-cooling tests 135
C.3 Boundary conditions 136

BIBLIOGRAPHY 139

Figure 1 Thermal *(left)* and kinematic *(right)* observations of ^{12}CO by ALMA (Teague et al., 2019). 2

Figure 2 VLT/SPHERE near-infrared scattered light observations of SAO 206462, tracing small dust grains entrained within the gas. 2

Figure 3 Obligatory sub-millimeter images from the Disk Substructures at High Angular Resolution Project (DSHARP) survey with ALMA, tracing larger dust grains which tend to concentrate at pressure maxima. 3

Figure 4 Pictorial representation of the phases of protostellar evolution, from molecular cloud to fully-formed planetary system. The simulations presented in this work principally concern thin, rotationally-supported Class II disks. Figure by Persson (2014). 8

Figure 5 The two-layer disk model of Chiang and Goldreich (1997), reproduced from that work. Stellar radiation strikes the disk at the radial $\tau_r = 1$ surface (τ_ν in their notation), where it gets absorbed and re-emitted vertically at much longer, thermal-infrared wavelengths (τ_{IR} in their notation), of which approximately half reaches the midplane while half is radiated into space. 13

Figure 6 Temperature values obtained at given radial and vertical positions from the MAPS program (points), together with best-fit temperature structures obtained from chemical and radiative transfer modeling (background contour plot). The curvature of the isotherms reflects the transition between the cool, indirectly-heated disk midplane and the hotter, directly-illuminated disk atmosphere. 14

Figure 7 A drawing showing the conceptual differences between optically thin *(left)* and thin *(right)* cooling. In the optically thin case, a layer of material with $\tau \lesssim 1$ partially absorbs incident radiation *(shown in blue)*, heats up, and emits thermalized radiation *(black)*, while allowing some of the incident light to transmit through. In the optically thick case, however, there are many effective layers, each with $\tau \approx 1$. The incident radiation is absorbed within a few optical depths, and transport of radiative energy beyond that depends on absorption and re-emission of thermalized radiation between the successive layers. The net heating rate of any given layer depends on the radiative balance with both the preceding and succeeding layers, which in the continuous limit creates a dependence on the second spatial derivative and thus a diffusion approximation for the radiation. 15

Figure 8 Plots of the opacities used for the Disk Substructures at High Angular Resolution Project (DSHARP) (Birnstiel et al., 2018), reproduced from Zhang et al. (2021). *Above* are grain-size distributions with minimum grain radius $a_{min} = 0.1$ —m and a_{max} as indicated, while *below* are a grain size distribution from [0.1 —m, 1cm] in blue, and another from [0.1 mm, 1cm] in brown. It is clear that opacity at short wavelengths is dominated by smaller grains. 18

Figure 9 Gas cooling times including only radiative cooling *(left)*, and additionally incorporating the effects of gas-grain collisions *(right)*, reproduced from Bae, Teague, and Zhu (2021a). These are evaluated using a detailed prescription for grain settling (see Section 1.3.4) and take $k^{-1} = H$ as the characteristic length scale for radiative diffusion. 20

Figure 10 Different modes of the spiral density wave launched in a disk by a planetary perturber. Reproduced from Bae and Zhu, 2018a. 29

Figure 11 Plots of gap depletion fractions for planet-driven gaps, reproduced from Fung and Chiang (2016). For both of the planet masses tested, there is good agreement between 2D and 3D simulations. 31

Figure 12 Evolution and taxonomy of disk features presented in (Su and Bai, 2024), showing the transition between the linear spiral-launching phase and nonlinear ring phase as a function of increasing thermal forcing. For a sufficiently strong azimuthal temperature variation and fast thermal relaxation, the velocity of a fluid parcel can change susbtantially as it crosses through a shadow, giving rise to vortices. 33

Figure 13 An example of piecewise-linear reconstruction based on the MUSCL scheme (Núñez, 2015). 37

Figure 14 Graphical representation of the Riemann problem, showing the three characteristic lines dividing the left and right states from the intermediate star states (Zingale, 2022). Note that in this case the flux was solved in terms of the primitive, rather than conservative variables. 38

Figure 15 A 0D test of our three-temperature scheme, for which we set the dust-gas stopping time $t_s = 10^{-9} t_0 = 8 \times 10^{-9}$ d and the opacity $\kappa_d = 3.9$ cm^2 g^{-1}. Pluses indicate numerical results, while solid lines indicate analytical solutions taken from equations 100 *(red, black)* and 103 *(purple)*. Because the system is dominated by radiation energy, the radiation temperature *(blue)* is nearly constant throughout the system's evolution. 51

Figure 16 Temperature profiles in the dusty radiative shock test at $t = 0.054 t_0 = 3.75 \times 10^4$ sec, for a variety of stopping times. For $t_s = 10^{-1}$, the gas temperature is that of a standard hydrodynamic shock, with only weak losses to dust and radiation; for $t_s = 10^{-7}$, T_d and T_g have come into equilibrium, and they (along with w_x and T_r) match the results of the two-temperature radiative shock tests in section 4.1 of Melon Fuksman et al., 2021 (note that the signed "reduced flux" $w_x \equiv F_x/E_r$ is denoted as f in their work). 55

Figure 17 *Above*, initial $T_d = T_g$ for our 2D self-shadowing test (4.3.3), based on `dg3t100` from (Melon Fuksman and Klahr, 2022); *below*, the same for our 3D planet-driven spiral test (4.3.4), based on `dg3t0.1`. We overplot contours for radial optical depth τ_r *(red)* (computed using opacities Planck-averaged over the stellar spectrum) and cooling parameter $\beta \equiv t_c \Omega$. Our calculations of these quantities assume an MRN distribution of small silicon-graphite grains, and a $1 M_\oplus$ classical T Tauri star as the source of light and gravity. In the lower plot, a white dot indicates the position of the embedded $1 M_J$ planet, while grey shading covers the region outside the $r = [8, 100]$ au boundaries of our 3D simulation. 57

Figure 18 Two-dimensional temperature profiles from our SSI tests. The T_g *(left)* and T_d *(middle)* columns come from our simulations with realistic t_s, whereas T_{ref} *(right)* is from our reference simulations with $t_s = (2\pi)^{-1} \times 10^{-10}$ y. For ease of interpretation, we overplot $\beta = 1$ *(white)* and $\tau = 1$ *(red)* surfaces. The reference disk relaxes rapidly to a smooth hydrostatic configuration; the bulk of the realistic disk does so as well, although differences persist in the slowly-cooling disk atmosphere. 58

Figure 19 Time evolution of T_d *(top)*, T_g *(center)*, and T_{ref} *(bottom)* in a disk column at the fiducial $r = 2$ au, as compared to the final, relaxed state of T_{ref}. As in Figure 18, we plot the $\tau_r = 1$ optical surface in red and the $\beta = 1$ cooling surface in white. T_{ref}, as well as T_d and T_g, rapidly relax to a smooth equilibrium disk inside the $\beta = 1$ surface. Sound waves in the upper atmosphere—excited by the initial relaxation of the disk—are visible in T_g due to the slow cooling rate at high altitude. 62

Figure 20 Density values for our three-temperature realistic (ρ_{gas}) and reference (ρ_{ref}) simulations, taken at the indicated θ values at a fixed $r = 30$ au. Densities largely agree to within a few percent between both models, but the discrepancy rises to $\sim 20\%$ at the $\tau_r = 1$ surface, causing a mild impact on the temperature structure below. 64

Figure 21 Temperatures in our three-temperature realistic (T_{gas}, T_{dust}) and reference (T_{ref}) simulations, taken at the same cuts as in Figure 20. In the midplane, where coupling times are short, $T_{gas} = T_{dust}$, but in the disk atmosphere, where coupling is weaker, there is a noticeable ($\sim 10\%$) discrepancy between the two: T_{dust} reflects the stellar irradiation field, while T_{gas} is driven by the PdV work done by the planetary spiral. 65

Figure 22 Relative difference between the temperature at $t_{cut} = 500$ y and the initial profile, in polar cuts at $\theta = 0.0$ and $\theta = 0.2$. The morphology of T_d and T_g agree in the midplane, but diverge at higher altitude, while the morphology of T_d and T_{ref} agree everywhere. In each panel, we indicate the Hill sphere of the planet with a small *solid grey* circle, and our cuts in figures 20 and 21 with a large *dotted grey* circle. 67

Figure 23 A plot of initial conditions for density (above) and temperature (below), obtained using the iterative procedure described in Section 5.2.3. White lines indicate the corresponding cooling-time contours, computed using Equation 119. Due to our constant dust-to-gas ratio and assumption of small dust grains throughout the disk, we obtain shorter radiative-diffusion and gas-grain coupling times than in Bae, Teague, and Zhu (2021b). 75

Figure 24 Relative differences in disk density, dust temperature, gas temperature, and radial velocity at $t = 2500$yr ≈ 10 orbits, with respect to initial conditions for different physical prescriptions. We take azimuthal cuts over the whole 2π at fixed $r = 1.5r_p$ and $\theta = 0$ (left) and 0.2 (right) above the midplane. Dust temperatures largely agree between the two- and three-temperature cases, whereas gas temperatures largely agree between the three-temperature and β-cooling cases. 75

Figure 25 Plots of the density (left), indicating the planetary spirals, and meridional velocity (right), for various altitudes in the disk; phase predictions for the primary Lindblad arm (Equation 124, thick line) and $m = 3$ buoyancy arm (Equation 126, thin line) are overplotted. In all panels, cylindrical radius $R \equiv r\sin\theta$ is plotted on the x-axis and azimuthal angle θ on the y-axis. Due to the relatively rapid thermal relaxation in this simulation, buoyancy spirals are markedly weaker than Lindblad spirals in all cases. 78

Figure 26 Midplane flow pattern in our disk, in the co-rotating frame of the planet. Streamlines proceed from bottom to top inside the planet radius $r_p = 40$au, and from top to bottom outside the planet radius. 80

Figure 27 Flow pattern at $r = 1.5r_p = 60$au, in an azimuthal cut of the disk. Streamlines flow right to left; unlike in Figure 26, vector arrows represent velocity differences from the local initial (quasi-)Keplerian value, rather than from the planet's Keplerian speed. 81

Figure 28 Flow pattern at $r = 0.66r_p = 26.6$au, in an azimuthal cut of the disk. Streamlines flow left to right; as Figure 27, vector arrows represent velocity differences from the local initial (quasi-)Keplerian value. 81

Figure 29 Source (red) and advective (blue) terms at a fixed $r = 1.5r_p$ and $\theta = 0.2$, plotted over azimuthal angle ϕ. From top to bottom, we plot these terms for ρ (in units of $\Omega_p \rho_{0,p}$), T_g ($\Omega_p T_{g,0,p}$), v_r, v_θ, and v_ϕ ($\Omega_p c_{s,iso,p}$), where the p subscript indicates quantities taken at the planet location in the initial condition. A thin, grey, dashed line passes through the azimuthal peak of the density spiral, showing the significant offset between terms driving spiral perturbations in each quantity. 83

Figure 30 Plots of background equilibrium, gas, and dust temperatures in our 3T, Saturn-mass simulations, at selected altitudes above the midplane for a fixed $r = 1.5r_p$. Background temperatures deviate by only a few percent from the initial condition, most strongly in the region of the planetary shadow ($\phi \approx \pi/4$) and somewhat more weakly near the Lindblad spiral. T_d agrees well with T_g at $\theta = 0.0$ and 0.1 (and is covered by the line for T_g), and with T_{eq} at $\theta = 0.2$ (covering the line for T_{eq}). 85

Figure 31 Measurement of the azimuthal perturbation in each normalized quantity x, averaged over an azimuthal range of $\phi_{peak} \pm 2h_p$ according to Equation 130. Densities and temperatures are plotted in the left panel while velocities are in the right. Open circles indicate non-accreting planets while closed circles indicate those with accretion luminosity (see Section 5.4.2 for discussion). At $z/r \approx \theta = 0.2$, where dust and gas are not well-coupled, the plotted T_{dust} amplitude reflects the radial "pseudo-arm" (see discussion in Section 5.3.4) rather than the Lindblad spiral. 86

Figure 32 Radial velocities v_r from 3T, zero-accretion-luminosity simulations with Neptune-mass (top row), Saturn-mass (middle row), and Jupiter-mass (bottom row) planets, at various altitudes in the disk (left, middle, right columns). Grey circles indicate the planetary Hill radius. All v_r values are expressed as a function of initial isothermal sound speed at the location of the planet, $c_{iso,p} = \sqrt{p_{p,0}/\rho_{p,0}}$. 87

Figure 33 Gas temperature perturbation for Neptune-mass (top row), Saturn-mass (middle row), and Jupiter-mass (bottom row) planets, at various altitudes in the disk (left, middle, right columns). Grey circles indicate the planetary Hill radius. All temperature values are expressed with respect to the initial condition $T_{g,o}$. 88

Figure 34 Difference from the initial condition in v_r (above) and T_g (below), for three-temperature simulations of Saturn-mass planets without and with accretion luminosity. The strongly luminous planet alters the vertical and azimuthal structure of the circumplanetary region, causing strong shadows behind the planet and greatly enhancing the kinematic signatures of accretion in the outer disk. 90

Figure 35 Plot of density perturbation in a cut through $\phi_p = \pi/4$, as a function of cylindrical radius R and vertical position z, for 3T simulations of Saturn-mass planets without (above) and with (below) accretion luminosity. Grey arrows indicate the velocity field, while the grey circle encloses the planetary Hill radius. When accretion luminosity is included, the circumplanetary envelope becomes larger and the flow around it is altered. 91

Figure 36 Initial conditions for gas density ρ (above), as well as dust and gas temperatures T_d and T_g (below), which are initially equal. Contours for normalized cooling timescales from gas-grain collision (β_{dg}) are plotted above, and from radiation (β_{rad}) below, with white lines. Figure reproduced exactly from Muley, Melon Fuksman, and Klahr (2024b). 102

Figure 37 Azimuthal profiles of various quantities at a fiducial radius of $r = 60\,\text{au} = 1.5r_p$, and at an altitude of $\theta = 0.2$ rad above the midplane in our $M_p = 3 \times 10^{-4} M_\odot$ simulations. In the 3T case, azimuthal asymmetries of even a few percent in disk illumination—potentially induced by the RWI, and visible in the T_d profile—lead to strong non-axisymmetry in ρ, T_g, and the velocity components. 104

Figure 38 Gas density ρ at $t = 1010$ orbits (1000 orbits at the fiducial resolution, 10 at the doubled resolution used in Muley, Melon Fuksman, and Klahr (2024b)), with respect to the initial condition ρ_0, for our simulations with a Saturn-mass planet. The green ellipse indicates the planet's Hill radius. With the 3T scheme, the disk atmosphere shows clear development of $m = 2$ spiral arms, which are absent in the β-cooling simulations. White bands at the interior and exterior of the radiative simulation result from wave-damping to the initial condition. 105

Figure 39 Mock H-band ($\lambda_H = 1.62\mu m$) total intensity for the disks we simulate, including an inverse-square correction factor. We assume the disk is located at a line-of-sight distance $d_r = 100$ pc with a face-on orientation ($i_d = 0°$), and convolve the raw image with a Gaussian of FWHM = 0.06 arcsec to mimic the effects of finite telescope resolution. The differences between the radiative and non-radiative cases are clearly visible. 107

Figure 40 H-band intensity in all of our simulations, taken at fiducial radii $r_{inner,cut} = 30$ au and $r_{outer,cut} = 60$ au, and normalized to the azimuthal average. The 3T simulations show a clear $m = 2$ spiral with a peak-to-trough intensity ratio ~4 in the outer disk and $\sim 1.2 - 1.5$ in the inner disk. By contrast, the β-cooling simulations show negligible asymmetry in the outer disk, alongside asymmetries of $\sim 1.1 - 1.5$ in the inner disk caused by inner Lindblad spirals. 108

Figure 41 A plot similar to our Figure 19, but with T_d and T_g taken from our simulation with cooling times artificially raised by a factor of 100. There are clear vertical patterns in the dust and gas temperature profiles, corresponding to inward-traveling perturbations at the $\tau_r = 1$ surface characteristic of the SSI. 121

Figure 42 Quantitative time evolution of T_d and T_g from the 100×-realistic simulation, and T_{ref} in the reference simulation, at $r = 2$ au, both in the midplane ($\theta = 0$, *above*) and 3 scale heights above it ($\theta \approx 0.088$, *below*). As qualitatively shown in Figure 41, T_{ref} reaches a smooth equilibrium, whereas T_d and T_g exhibit damped oscillations due to the passage of self-shadowing waves. See text for more details. 122

Figure 43 Evolution of the SSI with a dust-gas coupling time 100× longer than in the self-consistent setup presented in 4.3.3. An inward-propagating SSI bump is clearly visible. At $t = 250$ y, the disk has largely relaxed to the same configuration as in the reference simulation. Differences do persist, however, outside the $\beta = 1$ surface and near the inner boundary. 123

Figure 44 Sky-projected velocity perturbation $v'_\perp$ for our fiducial Saturn-mass planet, in a cut at $\theta = 0.3$ radians above the midplane. 125

Figure 45 Sky-projected velocity perturbation $v'_\perp$ for a Saturn-mass planet with an accretion luminosity $L_{acc,p} = 10^{-3} L_\odot$. Compared to the fiducial case, the outer spiral becomes significantly stronger and extends through a larger radial range of the disk. 126

Figure 46 Sky-projected velocity perturbation $v'_\perp$ for a Jupiter-mass planet, with no accretion luminosity. Relative to the fiducial case, circumplanetary and in-gap flow patterns are significantly stronger. 127

Figure 47 Perturbation in gas temperature $T_g - T_{g,0}$ at $\theta = 0.3$ above the midplane, for our fiducial setup with a Saturn-mass, non-accreting planet. The double-armed structure of the Lindblad spiral in the upper atmosphere is clearly visible here. 128

Figure 48 Gas temperature perturbation for an accreting, Saturn-mass planet. As with the kinematic spiral, the thermal spiral extends over a larger radial range and is more prominent than in the non-accreting case. 129
Figure 49 Gas temperature perturbation for a Jupiter-mass planet. As with kinematics, the circumplanetary region and gap make a much larger contribution to the thermal signature than in the fiducial Saturn-mass, non-accreting case. 130
Figure 50 θ-component of vorticity at $\theta = 0.2$, with respect to the initial condition, in units of the planet's orbital frequency Ω_p. Between 200 and 250 orbits, the vorticity profile is largely unchanged in the β-cooling simulations, but deviates strongly in the 3T case as radiation couples to the asymmetries generated by disk-planet interaction. 133
Figure 51 Density perturbation in special β-cooling simulations where the planet is removed, and for which the temperature profile in Fig. 23 is multiplied by the azimuthal perturbation factor $\mathcal{W}_T(\phi, t)$ (Eq. 154). The corotation radius of the temperature profile, equal to the planet radius in the main text, is plotted as a dotted vertical line. Note that the density scale has a much smaller range than in Fig. 38 in the main text. 135
Figure 52 Mock H-band images for different wave-damping prescriptions at the boundary. 136
Figure 53 H-band contrast ratios from post-processed simulations with the standard fixed boundary condition, as well as the strong-damping condition. 137

LIST OF TABLES

Table 1 Table of key simulation parameters. More information can be found in Section 6.2.1.3 of this work, and in Section 2 of Muley, Melon Fuksman, and Klahr (2024b). 101

0 INTRODUCTION AND MOTIVATION

Giant molecular clouds (GMCs) in interstellar space consist overwhelmingly (~99%) of hydrogen and helium gas, along with a dust component (1%). As these clouds collapse due to the Jeans instability, most of their mass is concentrated in a central protostar, while most of their angular momentum is distributed throughout the residual material. Because this material is supported against further collapse primarily by rotation rather than gas pressure, it forms a thin *circumstellar disk*. Over the millions of years of the disk's lifetime, a range of dynamical processes, including concentration of dust via turbulence or the streaming instability, as well as pebble, planetesimal, and gas accretion, lead to the formation of a planetary system; hence the name *protoplanetary disk*. These planets, in turn, gravitationally influence the disk according to the classical theory of disk-planet interaction (Goldreich and Tremaine, 1978, 1979, 1980), generating substructures that serve as telltale signs of their existence.

In recent years, protoplanetary disks have been investigated with increasing resolution and sensitivity in a variety of frequency bands. These include the near- (VLT/-SPHERE, Gemini/GPI) and mid-infrared (JWST), which principally trace micron-sized small dust grains; sub-millimeter continuum (ALMA), which traces larger grains that tend to concentrate around pressure maxima; and molecular lines from species such as ^{12}CO, ^{13}CO, and C^{18}O (ALMA), which trace the gas component. Such observations have uncovered a wealth of large-scale substructure within the disk, including gaps, rings, and spirals, often attributed to gravitational driving by nascent companions in accordance with the classical theory. Concurrent advances in high-contrast imaging, including angular (ADI) and reference (RDI) differential imaging, as well as observations of accretion tracers such as Hα (VLT/MUSE, MagAO), allow this hypothesis to be put to the test directly. Among a number of putative detections (e.g., Sallum et al., 2015), the landmark discoveries in the PDS 70 system—in which two resonant, multi-Jupiter-mass planets have been discovered carving a wide, deep "transition cavity" in the disk—represent a triumph for this view of disk-planet interaction (Bae et al., 2019).

Elsewhere, however—in the two-armed near-infrared spiral in SAO 206462 (Cugno et al., 2024; Muto et al., 2012), the many dust-continuum rings in HL Tau, and the annular ^{12}CO kinematic signatures in MWC 480 (Teague et al., 2021), to name but a few examples—the connection between disk substructure and embedded planet (or indeed, whether a planet is involved at all) is less clear. These expose the key limitations of the classical theory, which was derived under the assumption of a locally isothermal equation of state, and used vertically-integrated hydrodynamical equations to reduce a 3D problem to a more tractable 2D form. In search of an explanation for these and other systems, a growing body of simulation work has sought to move beyond this simplified picture and incorporate additional physics. Including a realistic disk temperature profile, with a warm, directly-illuminated disk atmosphere and a cooler, indirectly-heated disk midplane (Juhász and Rosotti, 2018) alters the morphology of planet-driven spirals. Physically-informed prescriptions for thermal relaxation and the

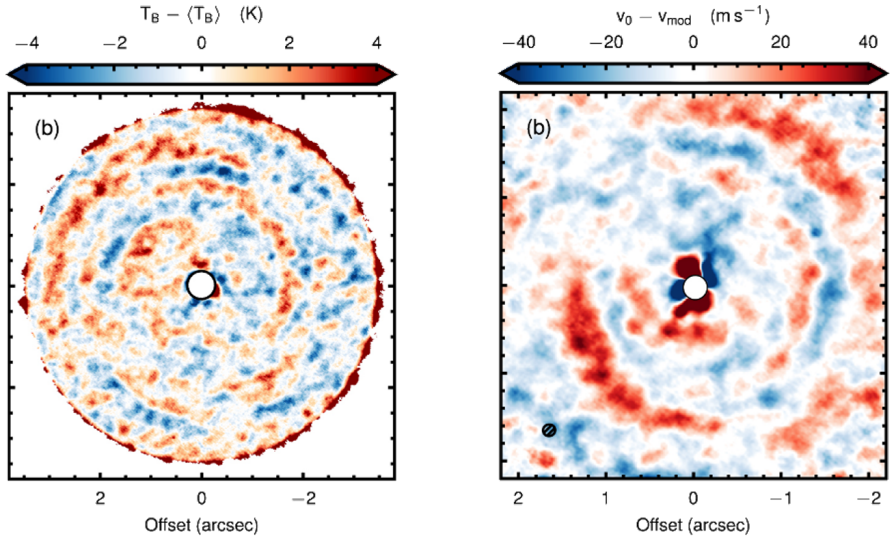

Figure 1: Thermal *(left)* and kinematic *(right)* observations of ^{12}CO by ALMA (Teague et al., 2019).

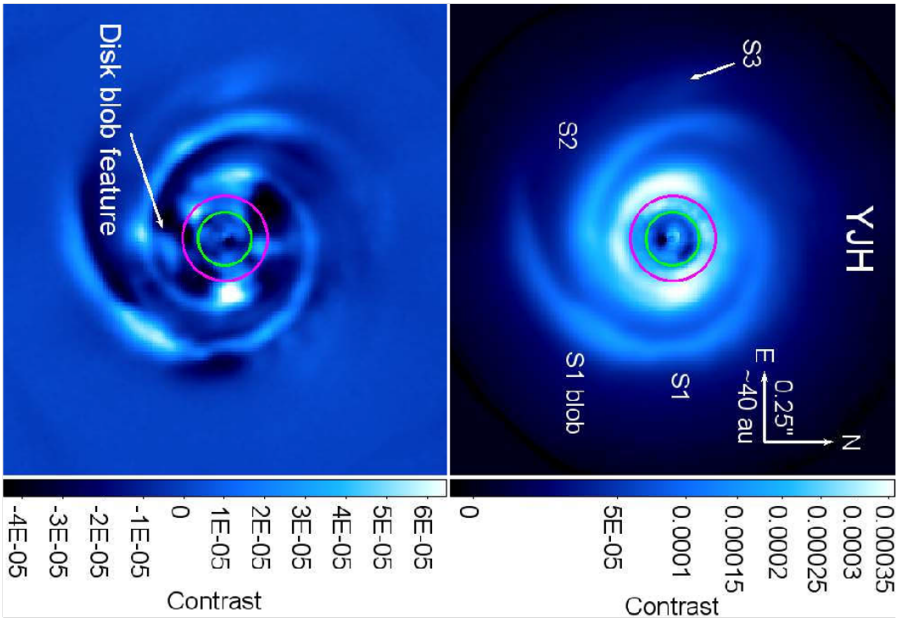

Figure 2: VLT/SPHERE near-infrared scattered light observations of SAO 206462, tracing small dust grains entrained within the gas.

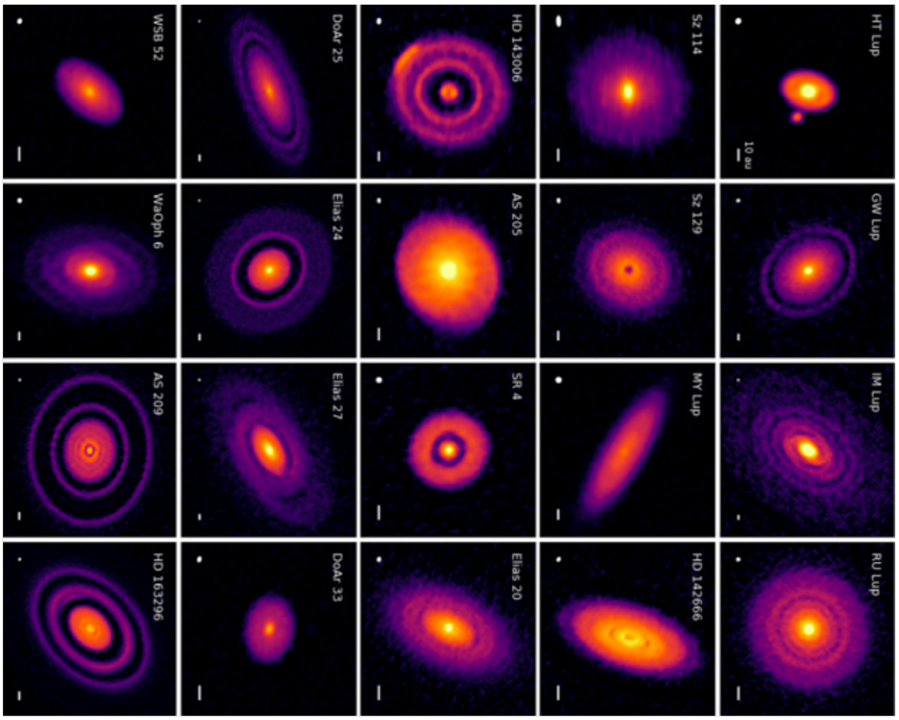

Figure 3: Obligatory sub-millimeter images from the Disk Substructures at High Angular Resolution Project (DSHARP) survey with ALMA, tracing larger dust grains which tend to concentrate at pressure maxima.

use of a 3D grid (e.g., Bae, Teague, and Zhu, 2021a, and references therein) cause the disk to develop an additional, tightly-wound set of "buoyancy spirals", the temperature and kinematic perturbations of which are potentially observable in the brightness temperatures and Doppler-shifting of molecular gas tracers. With a self-consistent treatment of dust dynamics, planets are shown to drive vertical stirring (Bi, Lin, and Dong, 2021) and outward drift (Bi, Lin, and Dong, 2023) of large dust grains. Radiation hydrodynamics (RHD) strongly influences both planetary (Ziampras, Nelson, and Rafikov, 2023) and non-planetary (Melon Fuksman, Flock, and Klahr, 2024a,b; Zhang and Zhu, 2024; Ziampras et al., 2024) mechanisms of generating disk substructure.

In RHD simulations of protoplanetary disks, it is common to make the simplifying assumption that the dust and gas are in thermal equilibrium with one another. In reality, however, most of the opacity within the disk—and thus, most of its interaction with the radiation field—is mediated by the dust component. The gas can only obtain information from the dust about the background radiation field, and convey information about its own heating and cooling due to compression and expansion, via collisions between dust grains and gas molecules. In the midplane of an unperturbed disk, where most of the mass resides, this is a distinction without a difference; collisional coupling is sufficiently strong that the dust and gas temperatures are held essentially equal. In lower-density regions, such as a planet-carved gap or within the atmosphere of a disk, collisional thermal coupling takes place on a longer timescale, and the dust and gas temperatures are able to diverge. Through its influence on the effective equation of state of the gas (that is to say, how it responds to compression and expansion on the continuum from effectively isothermal to effectively adiabatic), the gas-grain thermal

relaxation rate has a significant influence on the formation mechanism, morphology, and observational appearance of disk substructures. **As advancements in instrumentation and data reduction continue, it is essential that radiation-hydrodynamic simulations of protoplanetary disks incorporate gas-grain collisions, in order to remain useful tools for interpreting the increasingly detailed observations.**

Motivated by this purpose, this thesis presents the development, testing, and application of a "three-temperature" (3T; gas, dust, radiation) radiation-hydrodynamics scheme, which we have implemented within the `PLUTO` radiation-hydrodynamics code. We separate this work into three broad segments, each in turn divided into chapters on specific topics. Part I lays the physical foundations for the topic, covering, chapter by chapter, the structural and thermal properties of protoplanetary disks, including both the gas and dust; the generation of substructures in disks by both planetary and non-planetary mechanisms; and a primer on the numerical-hydrodynamics techniques deployed. Part II, based on previously published work, presents the thesis research itself: an exposition of the numerical method and test problems for the 3T scheme; its application in the context of spiral substructures generated by planets (including luminous, accreting planets); and a follow-up study showing that radiation itself may be capable of driving large-scale disk substructure, such as observed in systems such as SAO 206462 and V1247 Ori. Finally, in Part III, we recapitulate our purpose and findings and present proposals for future work.

Part I

PHYSICAL BACKGROUND

1

DISK STRUCTURE AND THERMODYNAMICS

The evolution of protoplanetary disks can be divided into several stages (Adams, Lada, and Shu, 1988), based on their observational characteristics. In the *Class 0* phase, the initial molecular cloud is actively collapsing and has not yet become rotationally supported, with little luminosity visible from the central protostar. In *Class I* disks, the protostar has become luminous and grows rapidly due to accretion from the disk, although its emission is subject to substantial extinction from the surrounding material. At this phase, the disk is also massive and dynamic, being subject to gravitational instabilities (Kratter and Lodato, 2016), internal viscous heating, and infall from the surrounding gas, among other processes. In the *Class II* phase, the star reaches the classical T Tauri phase; the disk, having fallen below the threshold mass to trigger gravitational instability, becomes quiescent and dominated by the azimuthal, quasi-Keplerian flow. Over time, factors like protoplanetary disk disperses due to photoevaporation (Owen, Clarke, and Ercolano, 2012), planet-driven flows (Goodman and Rafikov, 2001), and ongoing accretion via turbulent process and magnetohydrodynamic disk winds (Pascucci et al., 2023), leading to the *Class III* phase.

Owing to its duration (Schwarz et al., 2023; Williams and Cieza, 2011), and the fact that many observed multiplanet systems—including our own Solar System—tend to lie roughly in the same plane (Zhu and Dong, 2021), the multimillion-year, thin-disk Class II phase is of greatest interest for planet formation. Terrestrial planets are born from the aggregation of the dust component into rocky cores via planetesimal (Weidenschilling, 2000) and pebble (Lambrechts and Johansen, 2012; Ormel and Klahr, 2010) accretion, whereas gas and ice giants are created when these cores accrete gas from the surrounding disk (Mordasini et al., 2008). Moreover, the symmetries typical of such a system make it tractable to study and understand, using both numerical and analytical tools. In this Chapter, we present foundational concepts relevant to understanding the structure, thermal processes, and gas-dust interactions within Class II, T-Tauri disks, which are key to motivating and placing in context the results presented in this thesis.

1.1 STRUCTURE EQUATIONS

What gives rise to the characteristic structure of a classical Class II protoplanetary disk? To approach this question, we start from the Navier-Stokes equations of fluid dynamics (continuity, momentum, and energy, in that order):

$$\frac{\partial \rho}{\partial t} + \nabla \cdot (\rho \vec{v}) = 0 \tag{1a}$$

$$\frac{\partial (\rho \vec{v})}{\partial t} + \nabla \cdot (\rho \vec{v} \vec{v}) = -\nabla P - \rho \nabla \Phi + \vec{S}_m \tag{1b}$$

$$\frac{\partial \mathscr{E}_g}{\partial t} + \nabla \cdot ((\mathscr{E}_g + P + \rho\Phi)\vec{v}) = Q_m + \vec{S_m} \cdot \vec{v} \tag{1c}$$

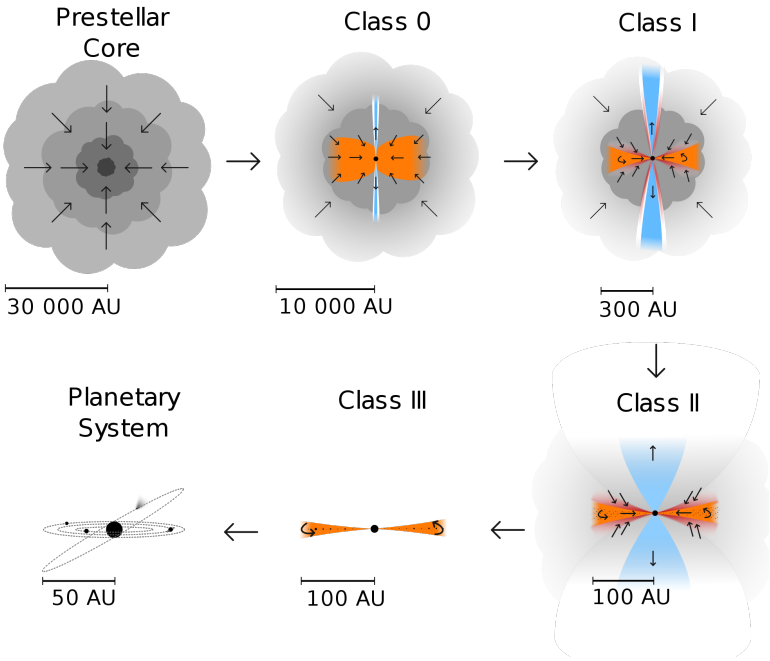

Figure 4: Pictorial representation of the phases of protostellar evolution, from molecular cloud to fully-formed planetary system. The simulations presented in this work principally concern thin, rotationally-supported Class II disks. Figure by Persson (2014).

Where ρ is the density, $\vec{v}$ the velocity, P the gas pressure, Φ the gravitational potential, and $\vec{S}_m$ and S_m additional energy and momentum source terms. We close this system with an ideal equation of state $P = (\mathscr{E}_g - \rho\vec{v}^2/2)(\gamma - 1) = \rho k_B T/\mu = c_s^2\rho/\gamma = c_{s,iso}^2\rho$, where c_s represents the local sound speed, γ the ideal gas constant, μ the mean molecular weight. $c_{s,iso} \equiv c_s/\gamma^{1/2} = \sqrt{k_B T/\mu}$ is the so-called "isothermal sound speed", defined for notational convenience. Nominally, for the mixture of gases contained within a typical protoplanetary disk, $\gamma = 1.43$, but this figure in general can vary as a function of temperature.

1.1.1 *Hydrostatic equilibrium*

As mentioned at the start of this chapter, unperturbed Class II disks are in a form modified of hydrostatic equilibrium in which they are symmetric around the z-axis, and where their velocity is primarily azimuthal. It is also useful, in understanding this equilibrium structure, to assume that the for the moment that the additional source terms ($\vec{S}_m$, S_m, and Q_m) are equal to zero. Taking these approximations, and subtracting equation 1a from 1b, we can reduce the left-hand side of the equation to the centrifugal term

$$\rho(v_\phi\hat{\phi}\cdot\nabla)(v_\phi\hat{\phi}) = -\frac{\rho v_\phi^2}{R}\hat{R} \tag{2}$$

Given that Φ is set by the potential of the star, with mass M_*, the term in 1b involving its gradient is given by

$$-\rho\nabla\Phi = -\frac{GM_*\rho}{(R^2+z^2)^{3/2}}\left(R\hat{R}+z\hat{z}\right) \tag{3}$$

where G is the gravitational constant. Putting together the terms component-wise and making the appropriate simplifications, we obtain that

$$0 = \frac{\rho v_\phi^2}{R} - \frac{GM_*\rho}{(R^2+z^2)^{3/2}}R - P\partial_R \ln P \tag{4a}$$

$$0 = -\frac{GM_*}{c_{s,iso}^2}\frac{z}{(R^2+z^2)^{3/2}} - \partial_z \ln c_{s,iso}^2 - \partial_z \ln \rho \tag{4b}$$

Equation 4a straightforwardly yields an expression for the azimuthal velocity, taking into account both pressure balance and the standard Keplerian velocity in the problem:

$$v_\phi = \left[\frac{v_K^2}{(1+z^2/R^2)^{3/2}} + c_{s,iso}^2\frac{\partial \ln P}{\partial \ln R}\right]^{1/2} \tag{5}$$

Where v_K is the Keplerian velocity within the midplane at cylindrical radius R. We can see immediately that there is a *vertical shear* in the velocity, due to the weakening of the stellar potential as one goes above the midplane, as well as a *modification of the velocity* due to pressure support. In regions where the pressure decreases with radius, the equilibrium flow is sub-Keplerian; conversely, where the pressure increases with radius, the flow is super-Keplerian.

Because the material in a disk is concentrated toward the midplane, it is helpful to make a *thin-disk approximation* in which $z < R$. Using this, we can Taylor-expand Equation 5 as

$$\boxed{v_\phi \approx v_K\left[1 - \frac{3}{4}\frac{z^2}{R^2} + \frac{h^2}{2}\frac{\partial \ln P}{\partial \ln R}\right]} \tag{6}$$

and solve Equation 4b as

$$\ln\left(\frac{\rho}{\rho_0}\right) \approx -\frac{z^2}{2h^2R^2} - \ln\left(\frac{h^2}{h_0^2}\right) + \int_0^z \frac{z'^2}{2R^2}\frac{\partial}{\partial z'}\left(\frac{1}{h^2}\right)dz' \tag{7}$$

where we define $h = c_{s,iso}/v_K$ as the ratio between the local isothermal sound speed and midplane Keplerian velocity. When the temperature is purely a function of R and independent of z (the so-called "vertically isothermal" assumption), the latter two terms drop out and the vertical structure of the disk can be shown to be Gaussian:

$$\boxed{\rho(R,z) \approx \frac{\Sigma(R)}{\sqrt{2\pi H(R)^2}}\exp\left(-\frac{z^2}{2H(R)^2}\right)} \tag{8}$$

in which we have defined the scale height $H = hR$. The midplane density $\rho(R, z = 0)$ is written in terms of the vertically-integrated *surface* density Σ, divided by the Gaussian integral as a normalization factor.

The vertically-constant temperature assumption is a useful approximation within a few H of the midplane, where heating and cooling are dominated by indirect radiation, absorbed and re-emitted (at longer wavelengths than the stellar spectrum, thermal-equilibrium wavelength) at the disk's radial $\tau_r = 1$ surface. At and above this transition, the disk temperature depends more on direct stellar illumination, and the approximation breaks down—a scenario which is relevant in numerical hydrodynamics simulations. We discuss the factors governing disk temperature structure in the following section.

1.1.2 *Viscosity*

The accretion of disk material onto the central star, and thus the depletion of Class II disks over their multi-Myr lifetimes, is thought to result principally from internal shear stresses (e.g., Rafikov, 2017, and references therein). In the Navier-Stokes equation, these can be encapsulated with a viscous momentum source term $\vec{S}_m \equiv \nabla \cdot \mathbf{T}$, where we define $\mathbf{T}$ to be the standard Newtonian stress tensor:

$$\mathbf{T} = \rho\nu \left[(\nabla\vec{v}) + (\nabla\vec{v})^T \right] \tag{9}$$

Under the assumption that $v_z, v_R \ll v_\phi$, one can compute the $R\phi$ and ϕR components of this tensor:

$$T_{R\phi} = T_{\phi R} \approx \rho\nu \left(\frac{\partial v_\phi}{\partial R} - \frac{v_\phi}{R} \right) = \rho\nu \left(R \frac{\partial (v_\phi / R)}{\partial R} \right) \tag{10}$$

with all other components approximately zero. integrating in z to work with surface densities Σ rather than volume densities ρ, and assuming axisymmetry one can write the $\hat{\phi}$-component of the momentum equation as:

$$\frac{\partial}{\partial t} \left(\Sigma v_\phi \right) + \frac{1}{R} \frac{\partial}{\partial R} \left(R \Sigma v_R v_\phi \right) = \frac{1}{R} \frac{\partial}{\partial R} \left[\Sigma \nu R^2 \frac{\partial (v_\phi / R)}{\partial R} \right] \tag{11}$$

Assuming a steady-state in which the time partial derivative term is zero, the radial viscous flow velocity becomes

$$\boxed{v_R = \frac{\nu R}{v_\phi} \frac{\partial (v_\phi / R)}{\partial R} \approx -\frac{3}{2} \frac{\nu}{R}} \tag{12}$$

where the last expression arises from assuming that $v_\phi / R \approx \Omega_K$. A more thorough analysis would also demonstrate that viscosity acts against pressure gradients in a disk, given that the pressure gradient modifies the angular velocity profile.

Angular momentum transport in disks is often held to be mediated by turbulent eddies, with a typical turnover time Ω_K^{-1}. Fluid instabilities, such as the magnetorotational instability (MRI; Balbus and Hawley, 1991) or vertical shear instability (VSI; e.g., Barker and Latter, 2015; Urpin and Brandenburg, 1998). These eddies can, at most,

have a size of $\sim H$ (if they are to fit within the disk) and a speed of $\sim c_s \approx H\Omega_K$, leading us to parametrize the kinematic viscosity ν as:

$$\nu = (\alpha H^2 \Omega_K) \tag{13}$$

where α is a parameter capturing both the size ($l_{eddy} = \sqrt{\alpha}H$) and speed ($v_{eddy} = \sqrt{\alpha}c_{s,iso} \approx \sqrt{\alpha}H\Omega_K$) required to enforce the turnover time (Shakura and Sunyaev, 1973). Certain other forms of disk transport, such as disk winds (Pascucci et al., 2023) and planetary spiral shocks (Goodman and Rafikov, 2001), are not mediated by turbulence, but are nevertheless still often parametrized in terms of an α.

1.2 RADIATIVE PROCESSES

The temperature structure of a protoplanetary disk is determined by the interplay between stellar illumination coming in, and reprocessed stellar radiation emerging. Add another few sentences of physical description to give some context as to how this works. To better understand it, we can start from the radiative transfer equation (inspired by David Melon Fuksman, private communication):

$$\frac{1}{c}\frac{\partial I_\nu}{\partial t} + \nabla_{\vec{x}} \cdot [\hat{s} I_\nu(\vec{x}, \hat{s})] = -\chi_\nu \rho I_\nu + \epsilon_\nu \tag{14}$$

where I_ν represents the specific intensity of radiation, at a given spatial location $\vec{x}$ and oriented in direction $\hat{s}$. $\chi_\nu = \kappa_\nu + \sigma_\nu$ represents the sum of absorption and isotropic scattering, while ϵ_ν represents emissivity. $\nabla_{\vec{x}}$ specifies that the gradient is taken purely in space, not in direction. This equation shows that the illumination of the disk, and thus its temperature profile, depend on the density structure; in turn, hydrostatic-equilibrium considerations (section 5.2.1) mean that the density structure depends on the temperature profile.

1.2.1 *Stellar irradiation*

We break up I_ν into stellar I^*_ν and thermalized I'_ν components:

$$\frac{1}{c}\frac{\partial I^*_\nu}{\partial t} + \nabla_{\vec{x}} \cdot [\hat{s} I^*_\nu(\vec{x}, \hat{s})] = -\chi_\nu \rho I^*_\nu \tag{15a}$$

$$\frac{1}{c}\frac{\partial I'_\nu}{\partial t} + \nabla_{\vec{x}} \cdot \left[\hat{s} I'_\nu(\vec{x}, \hat{s})\right] = -\chi_\nu \rho I'_\nu + \epsilon'_\nu \tag{15b}$$

In principle, every point on the star emits in all directions, but as one goes to a radius much larger than the stellar radius $r \gg R_*$, all stellar rays intercepted become more and more closely aligned with the *spherical* radial direction $\hat{r}$, to within an angle $\arctan R_s/r$. Assuming equilibrium so that the time-dependent term drops out, and integrating over all incident directions, we obtain an equation for irradiation flux:

$$\nabla_{\vec{x}} \cdot [F^*_\nu \hat{r}] = r^{-2}\partial_r(r^2 F^*_\nu) \approx -\chi_\nu \rho F^*_\nu \tag{16}$$

which can be solved as

$$F_\nu \approx F_{\nu,0}(R_*/r)^2 \exp(-\tau_\nu) \tag{17}$$

where $\tau_\nu = \chi_\nu \int_{R_*}^{r} dr' \rho$ is the optical depth between the star and the radial location under consideration. Although strictly speaking our equation is only valid in the far field, the lack of opacity in the innermost disk means that flux is conserved between the stellar surface and far-field limit.

Along each radial ray and in each frequency band, the value of r for which $\tau_\nu = 1$ represents the typical location where radiation is absorbed in the disk. Integrating over frequency and considering all radial rays, one can determine an effective $\tau_r = 1$ surface

$$r(\tau_r = 1) = L_*^{-1} \int_0^\infty d\nu \, L_\nu \int_{R_*}^\infty dr \, r \exp(-\tau_\nu) = L_*^{-1} \int_0^\infty d\nu \, L_\nu r_\nu(\tau_r = 1) \tag{18}$$

where L_* represents the frequency-integrated stellar luminosity and L_ν represents the luminosity in a particular waveband. For an axisymmetric disk, $r(\tau_r = 1)$ is a function only of the polar coordinate θ. Provided that this is a one-to-one mapping, one can recast each $(r(\theta, \tau_r = 1), \theta)$ point as an $(R, z(R, \tau_r = 1))$ in the cylindrical coordinates used in the previous section. The *disk flaring angle* β_F can then be defined as (Chiang and Goldreich, 1997)

$$\beta_F \approx \arctan\left[R \frac{dz(R, \tau_r = 1)}{dR}\right] \tag{19}$$

The larger the flaring angle of the disk at a given radial location, the more direct the incidence of starlight at a given location. This is especially relevant in the innermost regions of disks (Dong, 2015) or at the outer edges of planet-carved gaps (Chrenko and Nesvorný, 2020), where strongly flaring material gets directly exposed to starlight and thus heats up.

1.2.2 *Two-layer disk models*

So far, we have only considered direct stellar illumination, without connecting it to the thermalized radiation re-emitted by the disk. To do so, it is useful to make the simplifying assumption that all absorption of the stellar radiation occurs at the flaring surface defined in Equation 19 (Chiang and Goldreich, 1997; Dullemond, Dominik, and Natta, 2001). Following those works, and assuming further that the stellar spectrum is a blackbody, the frequency-integrated incident radiation flux can be written as

$$F^* \approx \psi^* \beta_F (R_*/R)^2 \sigma_{SB} (T^*)^4 \tag{20}$$

in which ψ^* is a correction factor that varies between 0.5 and 1, corresponding to the cases where the disk extends to the stellar surface (and thus, half of it is obscured by the bottom half of the disk) or cases with an inner hole much larger than the stellar radius (where the entire star would be visible). Assuming that the emission of thermalized radiation also has a blackbody spectrum, one can write the total emitting flux

$$F' = 2\psi' \sigma_{SB} (T')^4 \tag{21}$$

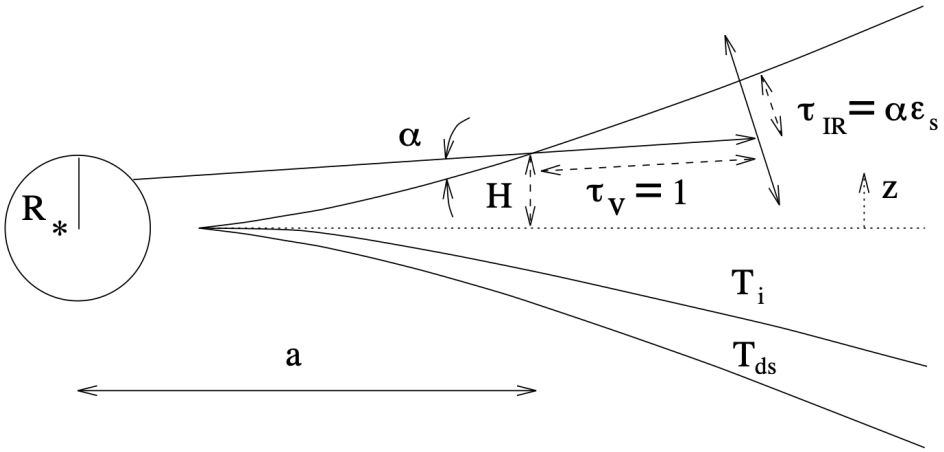

Figure 5: The two-layer disk model of Chiang and Goldreich (1997), reproduced from that work. Stellar radiation strikes the disk at the radial $\tau_r = 1$ surface (τ_ν in their notation), where it gets absorbed and re-emitted vertically at much longer, thermal-infrared wavelengths (τ_{IR} in their notation), of which approximately half reaches the midplane while half is radiated into space.

where the factor of 2 accounts for the fact that emission is bidirectional (down towards the disk midplane, and up towards the disk atmosphere), while the ψ' factor incorporates the fact that the layer may not be optically thick to its own emission. Equating these two fluxes yields the midplane temperature:

$$\boxed{T'_{mid} = T^* \left(\frac{\psi^*}{2\psi'}\right)^{1/4} \beta_F^{1/4} \left(\frac{R_*}{R}\right)^{1/2}} \tag{22}$$

In the optically thin disk atmosphere, we instead consider the balance between absorption and emission:

$$\boxed{a_r (T^*)^4 c\rho\kappa(T^*) \left(\frac{R_*}{R}\right)^2 = a_r (T'_{atm})^4 c\rho\kappa(T'_{atm})} \tag{23}$$

where $a_r = (4\sigma_{SB}/c)$, and κ evaluated at a temperature represents the frequency-dependent absorption opacity κ_ν averaged against a blackbody. Because the opacities are, in general, temperature-dependent (which we explain in Section 1.3.2), this equation does not admit an analytical solution and must be approached numerically.

The value of these two-layer disk models is not in their numerical accuracy, but rather in the physical interpretation: that a disk is divided into a warm disk atmosphere illuminated directly by the star, and a cooler disk midplane region heated by indirect, thermalized radiation. In reality, there is a smooth transition between these regimes, which was modeled parametrically by Dartois, Dutrey, and Guilloteau (2003) for comparison with unresolved observations, and with greater resolution and sophistication as part of the Molecules with ALMA at Planet-forming Scales (MAPS) program (Law et al., 2023).

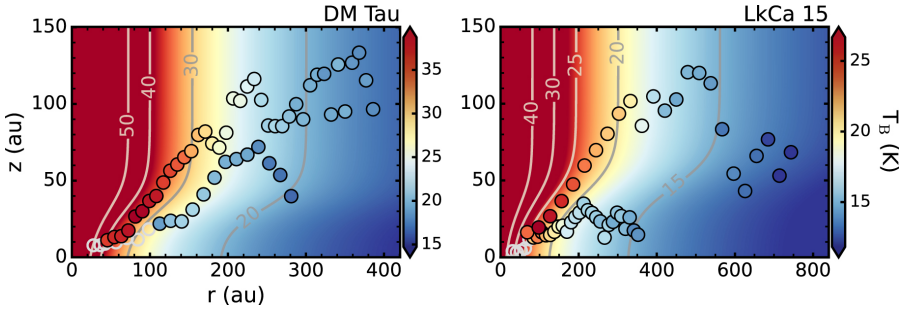

Figure 6: Temperature values obtained at given radial and vertical positions from the MAPS program (points), together with best-fit temperature structures obtained from chemical and radiative transfer modeling (background contour plot). The curvature of the isotherms reflects the transition between the cool, indirectly-heated disk midplane and the hotter, directly-illuminated disk atmosphere.

1.2.3 *Radiative heating and cooling*

Radiation does not act instantaneously on matter, but rather takes time to bring the temperature of a substance into equilibrium with that of the radiation field. In an optically thin medium, radiation can penetrate freely, and the heating and cooling of matter is limited only by the rate of absorption and emission of radiation energy. In an optically thick medium, however, photons cannot directly traverse from one side to the other. In this case, radiation transport is accomplished by photons heating individual, marginally optically thick ($\tau \approx 1$) layers of the medium, which in turn emit photons of their own. Because these re-emitted photons can heat both previous and succeeding layers, it is the gradient of temperature, rather than temperature itself, which sets the net flux—hence the name *radiative diffusion*.

To better understand the timescales involved in radiative heating and cooling, we follow the approach of of Melon Fuksman, Flock, and Klahr (2024a) and take the energy equation (Equation 1c) in the special case of zero velocity, assuming that the right-hand source term consists entirely of radiative heating:

$$\frac{\partial \mathscr{E}}{\partial t} = \rho c_v \frac{\partial T}{\partial t} = c\kappa\rho(E_r - a_r T^4) \tag{24a}$$

where E_r is the radiation energy density, integrated over all solid angles and frequencies. We augment this with the evolution equations for the zeroth and first moments of the radiation intensity:

$$\frac{1}{c}\frac{\partial E_r}{\partial t} + \nabla \cdot \vec{F} = -\kappa\rho(E_r - a_r T^4) \tag{24b}$$

$$\frac{1}{c}\frac{\partial \vec{F}_r}{\partial t} + \nabla \cdot \mathbf{P}_r = -\chi\rho\vec{F}_r \tag{24c}$$

in which $\vec{F}_r$ is the radiation flux and $\mathbf{P}_r$ is the radiation pressure tensor. To close these equations, we restrict ourselves to one dimension and assume that $\mathbf{P}_r = f(E_r, \vec{F})E_r$,

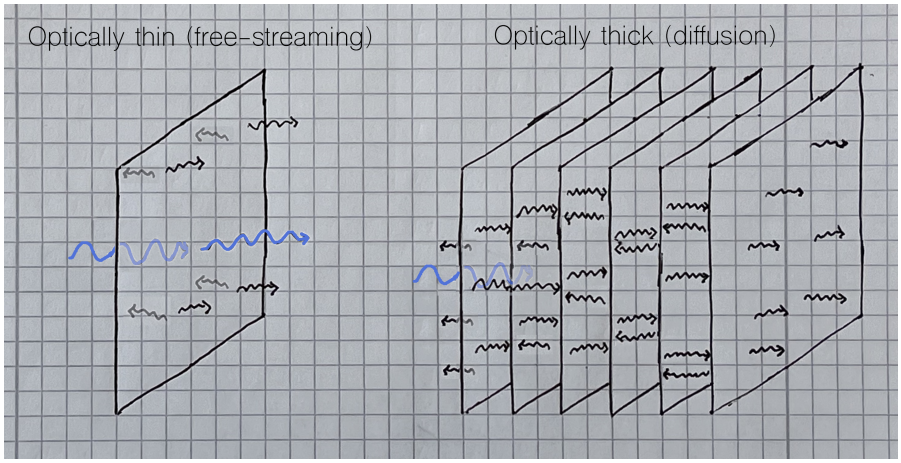

Figure 7: A drawing showing the conceptual differences between optically thin *(left)* and thin *(right)* cooling. In the optically thin case, a layer of material with $\tau \lesssim 1$ partially absorbs incident radiation *(shown in blue)*, heats up, and emits thermalized radiation *(black)*, while allowing some of the incident light to transmit through. In the optically thick case, however, there are many effective layers, each with $\tau \approx 1$. The incident radiation is absorbed within a few optical depths, and transport of radiative energy beyond that depends on absorption and re-emission of thermalized radiation between the successive layers. The net heating rate of any given layer depends on the radiative balance with both the preceding and succeeding layers, which in the continuous limit creates a dependence on the second spatial derivative and thus a diffusion approximation for the radiation.

where $f(E_r, \vec{F})$ is a function varying between $\pm 1/3$ (corresponding to the diffusion limit of radiation hydrodynamics) and ± 1 (corresponding to the free-streaming limit.

Linearizing these equations against a background steady-state $(E_{r,0}, \vec{F}_0, T_0, \mathbf{P}_{r,0})$, we obtain

$$\rho c_v \frac{\partial \delta T}{\partial t} = c\kappa\rho(\delta E_r - 4a_r T_0^3 \delta T) \tag{25a}$$

$$\frac{1}{c}\frac{\partial(\delta E_r)}{\partial t} + \nabla \cdot (\delta \vec{F}) = -\kappa\rho(\delta E_r - 4a_r T_0^3 \delta T) \tag{25b}$$

$$\frac{1}{c}\frac{\partial(\delta \vec{F}_r)}{\partial t} + \nabla \cdot (\delta \mathbf{P}_r) = -\chi\rho\delta\vec{F}_r \tag{25c}$$

For simplicity, we drop terms relating to the derivatives of $f(E_r, \vec{F})$, and so write $\delta\mathbf{P}_{r,0} = f_0 \delta E_r$, where $f_0 = f(E_{r,0}, \vec{F}_{r,0})$. Assuming that perturbations are proportional to $\exp(i(kx - \omega t))$, and making the appropriate substitutions, we can obtain a single dispersion relation:

$$\left[(-i\omega + c\kappa\rho) + \frac{k^2 f_0 c^2}{-i\omega + c\chi\rho}\right] \delta E_r = c\kappa\rho \frac{c\kappa\rho(4a_r T_0^3)/\rho c_v}{(-i\omega + c\kappa\rho 4a_r T_0^3/\rho c_v)} \delta E_r \tag{26}$$

In principle, one could solve the cubic equation for the three characteristic timescales of the system, corresponding roughly to the time evolution of F_r, E_r, and T. However, it is

more expedient and physically insightful to take the limit $\omega \approx \omega_{\rm thin} = c\kappa\rho(4a_r T_0^3/\rho c_v)$. In protoplanetary-disk contexts, the local radiation energy density is typically far outweighed by the gas energy density, implying that $(4a_r T_0^3/\rho c_v) \ll 1$ and $|\omega| \ll c\kappa\rho$. In this case, the ω terms on the left-hand side of the equation drop out, and we obtain

$$t_{\rm gas} = \frac{c_v}{4c\kappa a_r T_0^3}\left[\frac{1}{f_0}\kappa\chi\rho^2 k^{-2} + 1\right] \tag{27}$$

where $t_{\rm gas} \equiv \omega^{-1}$. Physically, this equation implies that when the length scale over which the radiation field changes (k^{-1}) is much longer than the mean free path of photons through the material ($(\rho\sqrt{\kappa\chi})^{-1}$), radiation tends to diffuse through the material; in the opposite limit, $k^{-1} \ll (\rho\sqrt{\kappa\chi})^{-1}$, cooling tends to follow the optically thin expectation.

In the context of protoplanetary disks, it is often assumed that the gas scale height H is the typical length scale over which temperature varies, at least in the vertical direction (e.g., Bae, Teague, and Zhu, 2021a; Muley, Melon Fuksman, and Klahr, 2024b). Approximating the surface density as $\Sigma \approx \rho H$, we can obtain the following rough expression for the cooling time of a vertically-integrated patch of disk:

$$t_{\rm gas} \approx \frac{c_v \Sigma}{16\sigma_{\rm SB} T_0^3}\left[\frac{1}{f_0}\tau_{z,\rm tot} + (\tau_{z,\rm abs})^{-1}\right] \tag{28}$$

Thus, disks that are marginally optically thick to their own infrared emission in the vertical direction ($\tau \approx 1$) respond most rapidly to changes in temperature or external irradiation. Those with $\tau_z \ll 1$ are inefficient absorbers and require more time to absorb/emit the same total quantity of radiation energy, whereas those with $\tau_z \gg 1$ are in the diffusion regime, in which external photons have to heat up many $\tau \approx 1$ layers in succession before they can heat the midplane (or, equivalently, before internally generated photons can escape to the surface).

1.2.4 *Viscous heating*

The previous section described so-called *passive disks*, heated by their interaction with the stellar radiation field. These can be contrasted with *active disks*, in which diffusive processes within the disk contribute to heating (see Chambers, 2009, and references therein) Assuming that $v_\phi \approx \Omega_K R \gg v_r$, we obtain that

$$\boxed{Q_{m,+} = \mathbf{T}\cdot\nabla\vec{v} \approx \rho\nu\left[R\frac{\partial}{\partial R}\left(\frac{v_\phi}{R}\right)\right]^2 \approx \frac{9}{4}\rho\alpha c_{s,\rm iso}^2\Omega_K} \tag{29}$$

As with the passive-heating prescription, we can equate $Q_{m,+}$ to the energy lost from the upper and lower disk surfaces:

$$Q_{m,-} \approx -2\psi'\sigma_{\rm SB}T_{\rm visc}^4\rho(R,z)/\Sigma(R) \tag{30}$$

from which we obtain

$$T_{\rm visc} = \left(\frac{9}{8}\frac{\Sigma\alpha c_{s,\rm iso}^2\Omega_K}{\psi'\sigma_{\rm SB}}\right)^{1/4} = \left(\frac{3}{8\pi}\frac{\dot{M}\Omega_K^2}{\psi'\sigma_{\rm SB}}\right)^{1/4} \tag{31}$$

where $\dot{M} = 2\pi R v_R = 3\pi\nu\Sigma$, and is constant throughout the disk assuming that it is in steady state. In this case, the viscous temperature $T_{visc} \propto R^{-3/4}$, making it the dominant contribution in the innermost disk, but unimportant compared to passive heating (which scales as $T'_{mid} \propto R^{-1/2}$) at greater radii.

1.3 DUST AND GAS

In a protoplanetary disk, the overwhelming majority of the mass and heat capacity are held within the gas. However, most of the opacity is supplied by the dust component, typically held to constitute ~1% of the disk's mass. Consequently, most of the disk's interaction with radiation—through absorption, emission, or scattering—is mediated by dust grains. Collisions between these dust grains and gas molecules act to bring their temperatures into equilibrium, allowing the gas structure of the disk to be influenced by the background radiation field.

1.3.1 *Grain size distributions*

In a real protoplanetary disk, grains are not all of a single size, but tend to follow a distribution $g(a)$, where a is the grain radius. In general, the value of any quantity averaged over the grain-size distribution is given by

$$\langle f(a, ...)\rangle = \int_{a_{min}}^{a_{max}} f(a, ...)g(a)da \tag{32}$$

The distribution is commonly approximated as a power law $g(a) \propto a^{-p}$ between some minimal and maximal grain radii a_{min} and a_{max}, and zero elsewhere. This yields the following useful formula:

$$\langle a^q\rangle = \left[\int_{a_{min}}^{a_{max}} a^{-p}da\right]^{-1}\left[\int_{a_{min}}^{a_{max}} a^{-p+q}da\right] = \frac{(-p+1)\left(a_{max}^{-p+q+1} - a_{min}^{-p+q+1}\right)}{(-p+q+1)\left(a_{max}^{-p+1} - a_{min}^{-p+1}\right)} \tag{33}$$

which holds as long as $-p \neq -1$ and $-p+q \neq -1$—in which case the correct expression would involve natural logarithms. Following the Mathis, Rumpl, and Nordsieck (1977) (MRN) prescription for interstellar dust grains, it is typical to set $p = 3.5$.

1.3.2 *Opacity*

The standard Planck spectrum is derived under the assumption that the blackbody surface is a perfect absorber and emitter at all wavelengths. In practice, however, dust grains have physical dimensions, and are most efficient at absorption, emission, and scattering when their radius a is much larger than the wavelength in question λ. Following works like Bohren and Huffman (1983), we define the dimensionless parameter $x \equiv 2\pi a/\lambda = 2\pi a\nu/c$, and delineate three regimes:

1. $x \ll 1$—the *Rayleigh regime*, in which absorption efficiencies $Q_\kappa \propto x$ and scattering efficiencies $Q_\sigma \propto x^4$, with the scaling factor depending on the (in general, frequency- and material-dependent) complex refractive index of the dust.

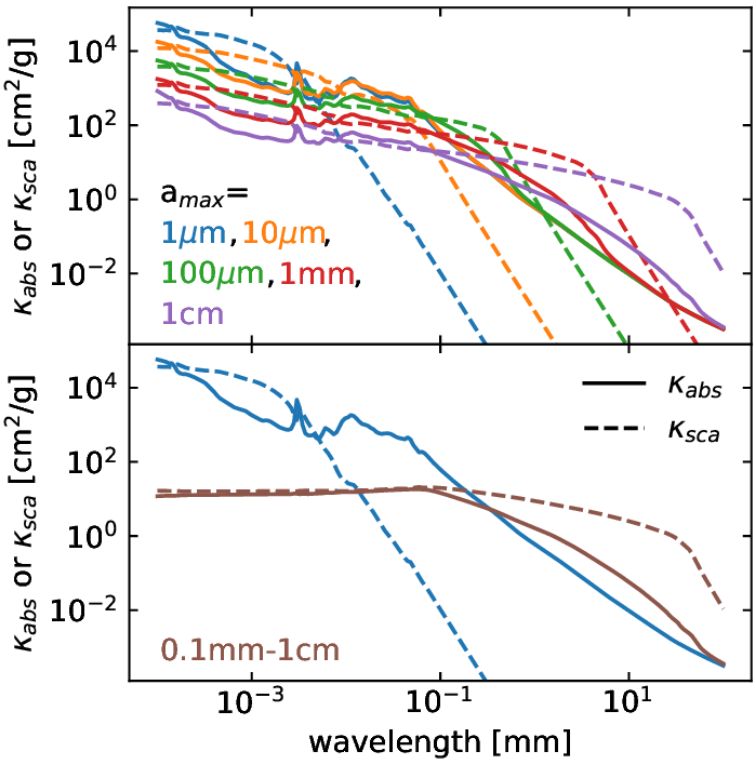

Figure 8: Plots of the opacities used for the Disk Substructures at High Angular Resolution Project (DSHARP) (Birnstiel et al., 2018), reproduced from Zhang et al. (2021). *Above* are grain-size distributions with minimum grain radius $a_{min} = 0.1$ —m and a_{max} as indicated, while *below* are a grain size distribution from [0.1 —m, 1cm] in blue, and another from [0.1 mm, 1cm] in brown. It is clear that opacity at short wavelengths is dominated by smaller grains.

2. $x \approx 1$—the *intermediate regime*, where one must use the full series solution for the interaction of an electromagnetic plane wave with a solid sphere (Mie theory)

3. $x \gg 1$—the *geometric optics regime*, in which $Q_\kappa \approx 1 - Q_\sigma$ depend on the albedo of the dust material.[1]

where the efficiencies are defined such that $\kappa(a, \nu) = \pi a^2 Q_\kappa$ and that the scattering opacity $\sigma(a, \nu) = \pi a^2 Q_\sigma$.

Following Equation 32, we can integrate over the grain-size distribution to obtain purely frequency-dependent opacities, $\kappa(\nu) \equiv \langle \kappa(\nu, a) \rangle$ and $\sigma(\nu) \equiv \langle \sigma(\nu, a) \rangle$. Such a band-by-band treatment is typical in Monte Carlo radiative transfer (MCRT) codes such as `RADMC3D`, but is prohibitively expensive in the context of on-the-fly radiative transfer during hydrodynamical simulations. In this case, it is common to make some

1 Strictly speaking, in the geometric-optics regime, the sum of absorption and scattering efficiencies is 2, due to Fraunhofer diffraction at the edges of the grain's cross-section. It can be shown, however, that the overwhelming majority of this edge scattering occurs within an angle $\theta_{geo} \approx J_{1,0}/x$ of the incident beam (where $J_{1,0} \approx 3.83170597...$ is the first zero of the Bessel J_1 function). Because $x \gg 1$ in the geometric-optics limit, $\theta_{geo} \ll 1$, and this edge scattering can typically be ignored.

assumption about the frequency content of the radiation (the so-called *grey approximation*) and integrate the frequency-dependent opacity against it:

$$\kappa_P(T) = \left[\int_0^\infty B_\nu(\nu, T)d\nu\right]^{-1} \int_0^\infty \kappa(a, \nu)B_\nu(\nu, T)d\nu \tag{34}$$

$$\frac{1}{\kappa_R(T)} = \left[\int_0^\infty \frac{\partial B_\nu(\nu, T)}{\partial T}d\nu\right]^{-1} \int_0^\infty \frac{1}{\kappa(a, \nu)}\frac{\partial B_\nu(\nu, T)}{\partial T}d\nu \tag{35}$$

where κ_P is the *Planck mean opacity*, most relevant in the context of optically thin problems, whereas κ_R is the *Rosseland mean opacity*, which emerges in the optically thick limit of radiative diffusion. A similar exercise can be performed with scattering opacities, although in practice, it is typical to simply assume that $\sigma(T) = \max(\kappa_R(T) - \kappa_P(T), 0)$—if not outright ignore scattering opacity—in radiation-hydrodynamics simulations of protoplanetary disks (e.g., Melon Fuksman et al., 2021). In any case, the above formulation is a simplification that ignores *explicit* temperature dependency in opacities, which arises from change in material properties (up to and including sublimation) as a function of local temperature and pressure.

For gas temperatures typical of the resolved regions of protoplanetary disks ($T_g < 1000$ K), frequency-integrated gas opacities are typically negligible compared to dust opacities, and so do not play a significant role in defining the overall temperature profile [2]. However, there are specific molecular lines—such as ^{12}CO, ^{13}CO, and C^{18}O—which are prominent at specific frequencies, and serve as useful tracers of gas density (if optically thin) and temperature (if optically thick) in observed protoplanetary disks.

1.3.3 *Collisional heating and cooling*

In a protoplanetary disk, the inherent thermal motions of gas molecules cause them to collide with the dust grains (Burke and Hollenbach, 1983a; Speedie, Booth, and Dong, 2022). The rate at which a gas molecule experiences collisions

$$t_{coll}^{-1} = \langle n_{gr}\sigma_{gr}\rangle \bar{v}_{th} \tag{36}$$

where n_{gr} is the number density of dust grains, and σ_{gr} the collisional cross-section of a dust grain. $\bar{v}_{th}$ is the typical thermal velocity of gas particles, which in the limit of zero relative velocity between the gas and dust, equals the collisional velocity. Assuming a standard MRN distribution, $n_{gr} \propto a^{-3.5}$, and that grains are spherical, $\sigma_{gr} = \pi a^2$, one can show that

$$\langle n_{gr}\sigma_{gr}\rangle = \bar{n}_{gr}\langle\sigma_{gr}\rangle = \frac{\rho_d}{4\rho_{gr}/3}\bar{a}_{gr}^{-1} = \frac{\rho_d}{4\rho_{gr}/3}\frac{1}{\sqrt{a_{max}a_{min}}} \tag{37}$$

The volume density of collisions is then given by

$$\dot{n}_{coll} = n_g t_{coll}^{-1} = \mu^{-1}\left[\frac{\rho_g \bar{v}_{th}}{\bar{a}_{gr}\rho_{gr}}\right]\frac{\rho_d}{4/3} = \mu^{-1}t_s^{-1}\frac{\rho_d}{4/3} \tag{38}$$

2 But see Melon Fuksman, Flock, and Klahr (2024a,b) for a more detailed discussion of gas-opacity prescriptions in numerical hydrodynamics simulations.

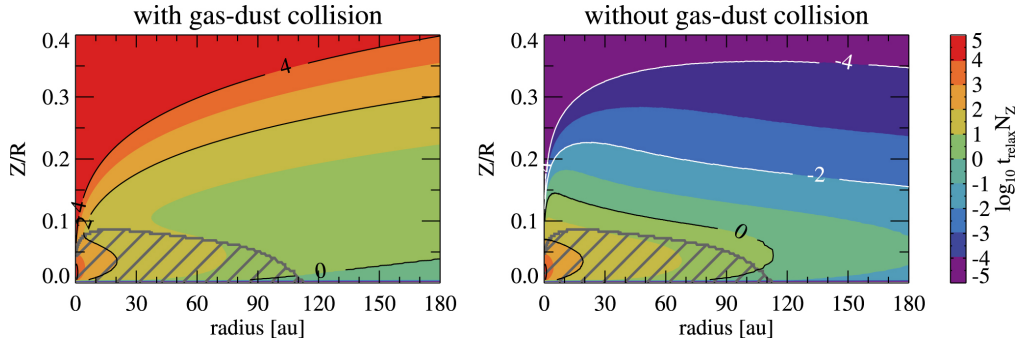

Figure 9: Gas cooling times including only radiative cooling *(left)*, and additionally incorporating the effects of gas-grain collisions *(right)*, reproduced from Bae, Teague, and Zhu (2021a). These are evaluated using a detailed prescription for grain settling (see Section 1.3.4) and take $k^{-1} = H$ as the characteristic length scale for radiative diffusion.

where we equate $n_g = \rho_g/\mu$ (with μ the mean molecular weight), and identify the terms in brackets with the inverse *stopping time*, $t_s = \bar{a}_{gr}\rho_{gr}/\rho_g\bar{v}_{th}$. Following Burke and Hollenbach (1983a), we assume that energy exchange takes place through a process of *thermal accommodation*, which acts to bring the temperatures of the dust and gas into equilibrium:

$$X_{gd} = -\eta_{gd}\left(2k_B T_g - 2k_B T_d\right)\dot{n}_{coll} = -\frac{3}{2}\eta_{gd}\mu^{-1}t_s^{-1}\rho_d\left(k_B T_g - k_B T_d\right) \tag{39}$$

where η_{gd} is an order-unity accommodation coefficient encapsulating the efficiency of the process. Assuming an ideal equation of state, this expression can be written in terms of the internal energies and heat capacities of gas and dust, to obtain a gas cooling time

$$\boxed{t_{cool} = \frac{3/2}{\gamma - 1}\left(\frac{\rho_d}{\rho_g}\right)^{-1} t_s} \tag{40}$$

As visible in Equation 39, the dust stopping time is inversely proportional to the local gas density. The quasi-Gaussian vertical structure of protoplanetary disks means that the local gas density can decrease—and the coupling time can increase—by many orders of magnitude between the disk midplane and atmosphere. Thus, in the disk atmosphere, the gas-grain collision time, rather than the radiative heating and cooling time (Section 1.2.3), become dominant in setting the disk thermodynamics. It can be shown (Melon Fuksman, Flock, and Klahr, 2024b) that the overall cooling time is the sum of the radiative and collisional times.

1.3.4 *Dust-gas dynamics*

By analogy to the thermal coupling between gas and dust, the momentum coupling between them can be written, in the linear Epstein regime, as (Armitage and Kley, 2019)

$$\vec{M}_{gd} = -\rho_d t_s^{-1}\left(\vec{v}_d - \vec{v}_g\right) \tag{41}$$

where $\vec{v}_g$ and $\vec{v}_d$ represent the separate bulk velocities of gas and dust. In the presence of viscosity, the dust also undergoes diffusion across concentration gradients, of which one common functional form is

$$\vec{j}_d = \nu\rho_g \nabla(\rho_d/\rho_g) = \nu\rho_d \nabla \log(\rho_d/\rho_g) = \rho_d \vec{v}_{diff,d} \tag{42}$$

These processes have several important consequences, the most immediately visible of which is the vertical settling of dust grains to the midplane. This can be derived, starting from the continuity and momentum equations for a pressureless fluid:

$$\frac{\partial \rho_d}{\partial t} + \nabla \cdot (\rho_d \vec{v_d}) = -\nabla \cdot \vec{j}_d \tag{43a}$$

$$\frac{\partial (\rho_d \vec{v}_d)}{\partial t} + \nabla \cdot (\rho_d \vec{v_d} \vec{v_d}) = -\nabla \cdot (\vec{j}_d \vec{v_d}) - \rho_d \nabla \Phi + \vec{M}_{gd} \tag{43b}$$

Assuming that the dust profile is in axisymmetric steady-state with no net vertical velocity, one can obtain from the continuity equation that

$$\nabla \cdot \left(\rho_d (\vec{v}_d + \vec{v}_{d,diff})\right) \rightarrow \vec{v}_d \cdot \hat{z} = -\vec{v}_{d,diff} \cdot \hat{z} = -\nu \nabla \log(\rho_d/\rho_g) \cdot \hat{z} \tag{44}$$

and the z-component of the momentum equation as

$$0 = -\frac{GM_* z}{(R^2+z^2)^{3/2}} - t_s^{-1} v_{d,z} \rightarrow v_{d,z} = -\frac{GM_* z t_s}{(R^2+z^2)^{3/2}} \tag{45}$$

To solve for the dust structure, we substitute Equation 44 into Equation 45 For notational convenience, we define the Stokes number $St \equiv t_s \Omega_K$ and write the kinematic viscosity $\nu = \alpha c_{s,iso} H$. Under the thin-disk and vertically-isothermal assumptions, we can substitute Equation 8 for the gas density, yielding that

$$\boxed{\rho_d = \rho_{d,mid} \exp\left(-\frac{GM_*}{R^3 c_{s,iso}^2}\left(\frac{St}{\alpha}+1\right)\frac{z^2}{2}\right) \approx \frac{\Sigma_d(R)}{\sqrt{2\pi H_d^2(R)}} \exp\left(-\frac{z^2}{2H_d^2(R)}\right)} \tag{46}$$

where $\Sigma_d(R)$ is the vertically-integrated dust surface density, and $H_d = H\sqrt{\alpha/(\alpha+St)}$ is the *dust scale height* of the disk. High turbulent diffusivity parameters will tend to increase the thickness of the dust layers, while large Stokes numbers/stopping times (and thus, larger grain sizes) will tend to decrease it (e.g., Youdin and Lithwick, 2007).

In a sub-Keplerian, partially pressure-supported protoplanetary disk, orbiting dust grains will experience a headwind from the gas (Armitage and Kley, 2019). Over time, this will act to reduce the angular momentum of the grains and induce an inward *radial drift*. This can be derived by studying the R and ϕ-components of the momentum equation (Equation 43b), working in the midplane and ignoring the comparatively weak concentration-diffusion term, radial velocity-gradient, and time-derivative terms:

$$-\frac{v_{d,\phi}^2}{R} \approx -\frac{v_K^2}{R} - t_s^{-1}\left(v_{d,R} - v_{g,R}\right) \tag{47a}$$

$$\frac{v_{d,\phi} v_{d,R}}{2R} \approx -t_s^{-1} \left(v_{d,\phi} - v_{g,\phi} \right) \tag{47b}$$

Taylor expanding the azimuthal velocities as the Keplerian velocity plus a deviation, $v_\phi = v_k + \delta v_\phi$, and assuming that the radial velocities are on the order of these perturbations, yields that

$$\boxed{v_{d,R} = \frac{2\delta v_{g,\phi} + v_{g,R} St^{-1}}{St + St^{-1}}} \tag{48}$$

$$\boxed{\delta v_{d,\phi} = \frac{1}{2St} \frac{2\delta v_{g,\phi} - v_{g,R} St}{St + St^{-1}}} \tag{49}$$

This has several important consequences:

- Radial drift due to angular momentum exchange between gas and dust is maximized when $St = 1$, for which the stopping time equals the disk dynamical time. Larger grains are only weakly coupled to the gas, while smaller grains become entrained within it, both of which weaken radial drift.
- Grains in a region of sub-Keplerian gas flow will tend to drift inward, while those in a super-Keplerian region will drift outward. Given the dependency of the azimuthal flow on the pressure gradient (Equation 6), this implies that $St \sim 1$ dust grains tend to rapidly concentrate at pressure maxima.
- Coupling to the background gas radial flow, driven by viscosity, is most efficient for the smallest grains ($St \to 0$).

In a disk with the properties of the protosolar nebula, an $St = 1$ corresponds to an $a \approx 1$ m (Weidenschilling, 1977); at $R = 1$ au, the inward drift timescale $t_{drift} \approx h^{-2}\Omega^{-1} \approx 60$ y. This timescale is far too short for the meter-sized boulders to coagulate into $a \approx 1$ km planetesimals that can grow under their own gravity (Nakagawa, Sekiya, and Hayashi, 1986), a situation known as the *meter-sized barrier* or *radial drift problem* (Laibe, Gonzalez, and Maddison, 2012). Various mechanisms have been proposed to mitigate this issue and retain dust within the disk, including the streaming instability (Youdin and Goodman, 2005), trapping in turbulent eddies (Klahr and Henning, 1997), or at the pressure maxima (Whipple, 1972) in planet-generated substructures such as rings at the outer edges of gaps, or within vortices (Meheut et al., 2012) generated by the Rossby wave instability (RWI). The latter scenarios have acquired increased interest years, as recent high-resolution ALMA continuum observations have indeed uncovered evidence of millimeter/submillimeter grain trapping in rings (Huang et al., 2018; Keppler et al., 2018) and in vortices (van der Marel et al., 2021).

In the works presented here, we focus on the disk's interaction with the radiation field, and on collisional thermal relaxation between dust and gas. This process is mediated principally by the smallest dust grains ($St \ll 1$), which move with the gas and experience negligible settling and radial drift. As such, we opt for a simple, globally-constant dust-to-gas ratio, implying that dust and gas dynamics are essentially identical. In the future, we intend to generalize this scheme to include multiple grain species,

with the intent of modeling the full spectrum of ALMA continuum observations; to do so, a self-consistent treatment of dust dynamics alongside thermodynamics (section 7.2.1) is necessary.

2

DISK PERTURBATIONS AND SUBSTRUCTURE

In the previous section, we derived various properties of Class II protoplanetary disks under simplifying assumptions of axisymmetry and quasi-hydrostatic equilibrium, and explained the microphysics that underlies their thermodynamics. While they do provide useful initial conditions, such models do not capture the reality that Class II disks host rich dynamics of their own, influenced by perturbations from embedded companions, shadow-casting inner disks, infalling material, disk fluid instabilities, and even their own gravity. These, in turn, generate substructures—such as gaps, rings, spirals, and vortices—whose morphologies provide insight as to their origins.

In what follows, we cover three different types of substructure: planet-driven spiral density waves, planet-carved gaps, and thermally-driven substructure. This short list is by no means exhaustive; we choose to focus on these three because they share common mathematical foundations, are the subject of substantial historical and/or current interest in the literature, and are most relevant to interpreting the results presented in Part II of this thesis.

2.1 DISK-PLANET INTERACTION

Planets drive substructure in disk through the excitation of torques at *Lindblad resonances* within protoplanetary disks. This problem has been long studied using analytical (e.g., Artymowicz, 1993; Goldreich and Tremaine, 1978, 1979, 1980; Kley and Nelson, 2012; Miranda and Rafikov, 2020a, and references therein) and numerical (e.g., D'Angelo, Lubow, and Bate, 2006; Dong et al., 2015; Fung, Shi, and Chiang, 2014a; Kley and Dirksen, 2006; Zhu et al., 2015) approaches. For ease of understanding, we assume that the planet is on a circular orbit, and assume that the disk is 2D; moreover, we neglect the indirect potential term associated with the star's orbital motion around the system's common center of mass. Under these assumptions, we decompose the planetary potential into azimuthal Fourier modes:

$$\Phi_p(\vec{r}) = -\frac{GM_p}{|\vec{r}-\vec{r}_p|} = \sum_0^\infty \tilde{\Phi}_{p,m}(R)\exp\left(-im(\phi-\Omega_p t)\right) \tag{50}$$

where the individual modes are given by

$$\tilde{\Phi}_{p,m}(R) = -\frac{GM_p}{r_p} b_{1/2,m}(R/r_p) \tag{51}$$

In the above equation, the $b_{1/2,m}$ terms correspond to the Laplace coefficients of celestial mechanics:

$$b_{a,m}(x) \equiv \frac{1}{\pi}\int_0^{2\pi} \frac{e^{im\phi'}d\phi'}{(1-2x\cos\phi'+x^2)^a} \tag{52}$$

To proceed, we consider a background disk in Keplerian steady-state, $\vec{v}_0 = \vec{v}_k\hat{\phi} = r\Omega_K\hat{\phi}$. Following Goldreich and Tremaine (1979), we expand the continuity and momentum equations to linear order, allowing all perturbations to be written in the form $\delta l \propto F(R)\exp(-im(\phi - \Omega_p t))$. We furthermore assume an isothermal equation of state, $P \propto \rho$, with $c_{s,iso}$ constant irrespective of the local density:

$$\frac{\partial \delta\Sigma}{\partial t} + \nabla\cdot(\Sigma_0\delta\vec{v} + \vec{v}_0\delta\Sigma) = 0 \tag{53a}$$

$$\frac{\partial \delta\vec{v}}{\partial t} + \vec{v}_0\cdot\nabla\delta\vec{v} + \delta\vec{v}\cdot\nabla\vec{v}_0 = -\nabla\left(\Phi_p + c^2_{s,iso,0}\delta\Sigma/\Sigma_0\right) \tag{53b}$$

Solving Equation 53b for the velocity perturbation reveals that it is maximized when the resonant distance, $D_m \equiv \kappa^2 - \omega_m^2$, tends to zero. In this expression, the squared *epicyclic frequency*, $\kappa^2 \equiv 4\Omega^2 + 2R\Omega\partial_R\Omega$, is the frequency at which the perturbed fluid parcel undertakes small radial oscillations around its guiding center; for a Keplerian rotation profile, $\Omega_K \propto R^{-3/2}$, it can be readily shown that $\kappa = \Omega_K$. The squared *Doppler-shifted forcing frequency*, $\omega_m^2 = m^2(\Omega - \Omega_p)^2$, represents the frequency at which the fluid parcel interacts with the mth component of the planetary potential, each on their respective orbits. From the velocity perturbation, it is possible to derive an expression for the surface density perturbation as well—the so-called *spiral density wave*.

In a Keplerian disk, the frequencies at which Lindblad resonances occur are given by

$$\Omega_{m\pm} = (1 \mp 1/m)^{-1}\,\Omega_p \tag{54a}$$

with corresponding locations

$$R_{L,m\pm} = (1 \mp 1/m)^{2/3}\,r_P \tag{54b}$$

where the plus and minus signs correspond to families of *outer* and *inner Lindblad resonances*, respectively. In principle, as $m \to \infty$, the resonant location comes closer and closer to the planetary orbit. However, in a disk with gas pressure, wave excitation becomes inefficient when the relative velocities of the fluid parcel and planetary perturber are subsonic. This occurs when $|R_{l,m} - r_p| < 2H/3$, leading to a "torque cutoff" at $m \approx h^{-1}$. More rigorous analyses demonstrate (Artymowicz, 1993; Kley and Nelson, 2012) that sound modifies the resonant distance expression to $D = \kappa^2(1+\xi^2) - \omega^2$, where $\xi = mh$. Accordingly, one can replace m in Equation 54b with $m/\sqrt{1+\xi^2}$; with this substitution, resonances can be shown to cluster at $R_{l,m} \approx r_P(1 \mp 2h/3)$ as $m \to \infty$.

The torque exerted by the planet on a given ring of the disk is given by integrating the torque exerted on each disk parcel:

$$\frac{d\Gamma(R)}{dR} = \int_0^{2\pi}(\vec{r}\times\nabla\Phi_p)\Sigma(r,\phi)\,d\phi \tag{55}$$

For each azimuthal Fourier mode of the planetary potential, this can be shown to equal (Goldreich and Tremaine, 1979):

$$\Gamma^L_{m,\pm} = \pm\frac{\pi^2 m\Sigma_0}{\mathscr{D}_m}|\Psi|^2 = \frac{\pi^2 m\Sigma_0}{|R(\partial|D_m|/\partial R)|}\left[R\frac{\partial\Phi_{p,m}}{\partial R} + \frac{2\Omega}{\Omega-\Omega_p}\Phi_{p,m}\right]^2_{R_{L,m\pm}} \tag{56}$$

where $\mathscr{D} \equiv |R(\partial|D_m|/\partial R)| = 3m\Omega_{m,\pm}\Omega_p = 3m\Omega_p^2(1 \mp 1/m)^{-1}$ when evaluated at the Lindblad resonances of a Keplerian disk. Summing all Lindblad torques of the same sign leads to an expression for the *one-sided torque* (e.g., Zhang and Zhu, 2020):

$$\Gamma_\pm^L = C_\pm \Gamma_0^L = C_\pm(\Sigma_0 q^2 r_p^4 \Omega_p^2 h^{-3}) \tag{57}$$

in which $q \equiv M_p/M_*$ is the planet-to-star mass ratio, and $C_\pm$ represents a constant scaling factor obtained from the torque calculation. Intuitively, this can be understood in terms of the so-called "impulse approximation" of fluid parcels flying past the planet and being deflected by its gravity; in this picture, the radial torque density can be approximated as (e.g., Ginzburg and Sari, 2018, and references therein)

$$\frac{d\Gamma(R)}{dR} \approx P\Sigma_0 q^2 r_p^4 \Omega_p^2 x_r^{-4} \tag{58}$$

where P is another constant, and $x \equiv R/r_p$ is a dimensionless distance. Integrating in R with a lower cutoff $x_{r,min} \approx h$ yields the expected h^{-3} scaling.

A more sophisticated comparison shows that the net torque on the disk, $\Gamma^L \equiv (C_+ - C_-)\Gamma_0^L$, scales as $h\Gamma_0^L$, and thus with h^{-2} overall (Kley and Nelson, 2012). Via Newton's third law, this net torque causes an equal and opposite reaction on the planet, reducing its angular momentum and causing inward migration. As we do not include migration in any of the simulations presented here, we do not discuss it further, and refer readers to e.g. Baruteau and Masset (2013) and references therein for a more thorough overview of the subject.

2.1.1 *Lindblad spirals*

What consequences do planetary torques have for the morphology of a protoplanetary disk? The one-sided Lindblad torques deposited at $|R - r_p| \approx H$ in the disk lead to the generation of spiral density waves, which propagate as sound waves in a shearing Keplerian medium (Bae and Zhu, 2018a) with dispersion relation $m(\Omega - \Omega_p) = \Omega^2 + k_r^2 c_s^2$, where k_r is the radial and m the azimuthal wavenumber. Using the relation that $d\phi_s/dr = -k_r/m$, one can integrate to find the azimuthal location of the spiral wavecrest, $\phi_s(R)$, corresponding to wavenumber m in the linear regime:

$$\phi_s(R) - \phi_s(r_p) = \int_{r_p}^{R} H(R)^{-1} \left[(1 - \Omega_p/\Omega(R))^2 - m^{-2}\right]^{1/2} dR' \tag{59}$$

For so-called "sub-thermal planets"—those such that $q/h^3 < 1$, (Bae and Zhu, 2018a,b) show that spiral waves interfere to create a single spiral density wave. For "super-thermal planets" with $q/h^3 > 1$, or in the inner disk where wave steepening has otherwise brought wave propagation out of the linear regime, the propagation of spirals differs from the predictions of Equation 59 and there are multiple locations for constructive interference, leading to the creation of a secondary spiral. Spirals excited at Lindblad resonances have been implicated as the cause for various spirals observed in scattered light (as in MWC 758 (Grady et al., 2013) and SAO 206462 (Muto et al., 2012)) as well as in gas tracers like ^{12}CO (as in TW Hya (Teague et al., 2019) and CQ Tau (Wölfer et al., 2021)).

Early numerical studies of Lindblad-spiral launching, such as those by Dong et al. (2015) and Dong and Fung (2017), tended to use a locally isothermal equation of state with a vertically constant temperature profile. While numerically efficient and relatively easy to implement, isothermality tends to overstate the amplitude of density and velocity perturbations by eliminating temperature perturbations, making the gas easier to compress. In addition, a vertically constant temperature structure eliminates the refraction of spiral waves that occurs at the vertical transition between the cool, indirectly-heated disk midplane (in which the perturber is situated) and the warm disk atmosphere exposed to direct starlight (see Section 1.2.2), artificially strengthening spirals in the upper atmosphere. Taken together, these factors cause such simulations to overestimate the observability of spirals in the near-infrared—scattereed by small grains at high altitude within the disk—and obviate the temperature spirals visible in gas molecular tracers.

To rectify these issues, other works have relaxed these assumptions by using vertically varying temperature profiles (Juhász and Rosotti, 2018) and by using β-*cooling* schemes (as in, e.g., Muley, Dong, and Fung, 2021; Zhu et al., 2015)—in which the temperature in a grid cell is relaxed down to an initial condition on a timescale $\beta\Omega^{-1}$, rather than held fixed to the initial condition for all time. These studies have found that spiral wave propagation is strongest for a cooling time $\beta \ll 1$ (the effectively isothermal limit in which the cooling time is much longer than the compression/expansion time for spirals) as well as $\beta \ll 1$ (the effectively adiabatic limit), but significantly weaker for $\beta \approx 1$.

These results find an explanation in the analytical work of Miranda and Rafikov (2020a), who show the damping rate of temperature perturbations within a spiral density wave to be

$$\mathrm{Im}(k_r) = \frac{1}{2}\frac{(\gamma-1)m(\Omega-\Omega_p)\Omega\beta}{\Omega^2+\gamma m^2(\Omega-\Omega_p)^2\beta^2}\mathrm{Re}(k_r) \tag{60}$$

Intuitively, this function can be thought of as the rate at which the temperature component of the spiral's compression/expansion (hence the $\gamma-1$) is radiated away, leading to losses of total energy with each successive wave cycle. It tends to zero for $\beta = 0$ or $\beta \to \infty$, but reaches a maximum of $\mathrm{Im}(k_r) = \left[(\gamma-1)\gamma^{-1/2}/4\right]\mathrm{Re}(k_r)$ in the intermediate regime where $\beta = \gamma^{-1/2}\Omega/m(\Omega-\Omega_p)$. Inserting the formula for the location of the Lindblad resonances (Equation 54a), it can be seen that spiral modes of all wavenumbers m are maximally suppressed at their launching points for a $\boxed{\beta_{max} = \gamma^{-1/2} \approx 1}$, inhibiting their propagation.

More recent studies have sought to better link simulations to observations of spirals by more accurately modeling the underlying thermal physics. Bae, Teague, and Zhu (2021a) performed detailed calculations of dust vertical settling, gas-grain collisional thermal coupling, and optically thick/thin radiative cooling rates, and used these to construct a spatially-varying effective β for their 3D hydrodynamical simulations. Ziampras, Nelson, and Rafikov (2023) made use of 2D simulations with a flux-limited diffusion (FLD; Levermore and Pomraning, 1981) approximation for radiation hydrodynamics, finding that the transport of thermal energy ahead and behind the spiral via radiation affected the spiral morphology, in ways that a purely local β-cooling simulation could not capture.

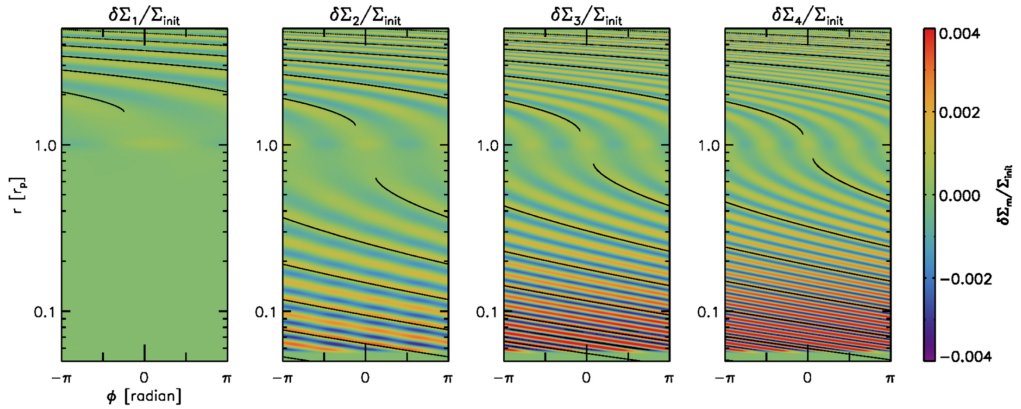

Figure 10: Different modes of the spiral density wave launched in a disk by a planetary perturber. Reproduced from Bae and Zhu, 2018a.

Muley, Melon Fuksman, and Klahr (2024b), from which Chapter 5 of this thesis is adapted, used 3D simulations and tested four different thermodynamic prescriptions (local isothermality, physically-motivated β-cooling, two-temperature radiation hydrodynamics, three-temperature radiation hydrodynamics) with otherwise identical initial conditions. Because these simulations were 3D, and because the disk was marginally optically thin to its own thermal radiation, the disk could cool efficiently by emitting in the vertical direction; this meant that physically-motivated β-cooling could provide a reasonable approximation to 3T in the disk midplane. Proper radiation transport was nevertheless essential in situations were the disk structure (and thus, the stellar illumination which set the background temperature) was substantially altered from the initial condition of the planet, or when the planet itself served as a source of luminosity. Inclusion of gas-grain collisions (either as part of the β-parameter, or with the full 3T scheme) was found to be essential in reproducing temperature spirals in the gas, as found in e.g., TW Hya (Teague et al., 2019).

2.1.2 *Gap opening*

Over time, angular momentum deposition at a planet's Lindblad resonances clears away disk material and excavates a gap in the disk. In steady-state, the planetary torques exerted on the disk material are balanced by the viscous torques inherent to the disk, meaning that the gap depth can be approximately computed by equating the rate of angular momentum deposition by the planet into the gap (the one-sided torque) with the viscous radial transport of angular momentum:

$$-2\pi R\Sigma_{gap}\nu_r R^2\Omega + K(\Sigma_{gap} q^2 r_p^4 \Omega_p^2 h^{-3}) + 2\pi R\Sigma_o \nu_r R^2\Omega \approx 0 \tag{61}$$

where K is an arbitrary constant incorporating the one-sided torque scaling $C_\pm$ times a "fudge factor", and we assume that most of the torque is deposited within the gap. We substitute in that $\nu_r = -(3/2)\nu/R = -(3/2)\alpha h^2 R\Omega$, and estimate that $R \approx r_p$ and

$\Omega \approx \Omega_p$, in order to obtain the following gap-depth scaling (Duffell, 2015; Fung, Shi, and Chiang, 2014a; Kanagawa et al., 2016):

$$\boxed{\frac{\Sigma_{gap}}{\Sigma_0} = \frac{1}{1 + (K/3\pi)\alpha^{-1} q^2 h^{-5}}} \tag{62}$$

The larger the planet-to-star mass ratio is relative to the disk scale height, and the less viscous the disk is, the deeper the gap becomes.

Early numerical studies of planet-carved gaps (e.g., Crida and Morbidelli, 2007; Kley and Dirksen, 2006) typically used 2D, locally-isothermal setups, and aimed principally at understanding disk accretion and planetary migration rates. With improvements in computational power and in anticipation of high-resolution instruments like ALMA, gap depth and morphology became a topic of interest in its own right. (Zhu et al., 2011) demonstrated that the gaps carved by multiple planets could merge to form a single wide, deep cavity, analogous to those seen in observed "transition disks." (Zhu et al., 2012) ran simulations with an additional dust fluid dynamically coupled to the gas (Section 1.3.4); these runs showed that the pressure maximum at the outer edge of a Jupiter-mass planet's gap would trap millimeter/submillimeter grains observable in ALMA dust continuum, while allowing smaller grains to filter through. Fung and Chiang (2016) made detailed comparisons between 2D and 3D gap-opening simulations, highlighting the differences in the flow patterns created by each. In Bi, Lin, and Dong (2021), it was shown that high-mass planets would be expected to vertically "puff-up" the dust rings outside them, leading to a distinct observational appearance from rings with well-settled dust.

As with spiral arms, thermodynamics—in principle set by the detailed microphysics set out in Chapter 1, in practice often parametrized for computational efficiency—is of key importance in setting the depth and structure of gaps. Zhang, Huang, and Dong (2024) show that gap morphology significantly depends on cooling time, with torque deposition occurring over a smaller radial range for normalized gas cooling times $\beta \approx 1$ than for $\beta \ll 1$ (effectively isothermal) and $\beta \gg 1$ (effectively adiabatic). This results in a somewhat deeper, narrower gap in the regime of intermediate cooling times, agreeing with the fact that spirals show a less extended morphology at such cooling times. Chrenko and Nesvorný (2020) and Ziampras, Nelson, and Rafikov (2023) showed that including radiation hydrodynamics also affects gap structure, leading to heating at the outer gap edge (of disk material that becomes directly exposed to starlight) and favoring the formation of multiple gaps and rings from a single planet. Muley, Melon Fuksman, and Klahr (2024a) found that using an M1 scheme, which includes shadowing, led to the creation of shadow-driven spirals (see next section) at the outer edge of planet-carved gaps, and linked them to the prominent multi-armed spirals found in systems like MWC 758 and SOA 206462.

In the observational context, disk-planet interaction is commonly invoked as an explanation for gap-and-ring structures seen in real protoplanetary disks. The evidence is most convincing in the PDS 70 system, in which the two multi-Jupiter-mass companions, PDS 70b(Keppler et al., 2018; Müller et al., 2018) and c (Haffert et al., 2019), have been confirmed to exist within the wide, deep "transition cavity" of the system[1], which

1 So called because it was historically thought to represent a transition between the Class II and Class III stages of disk evolution.

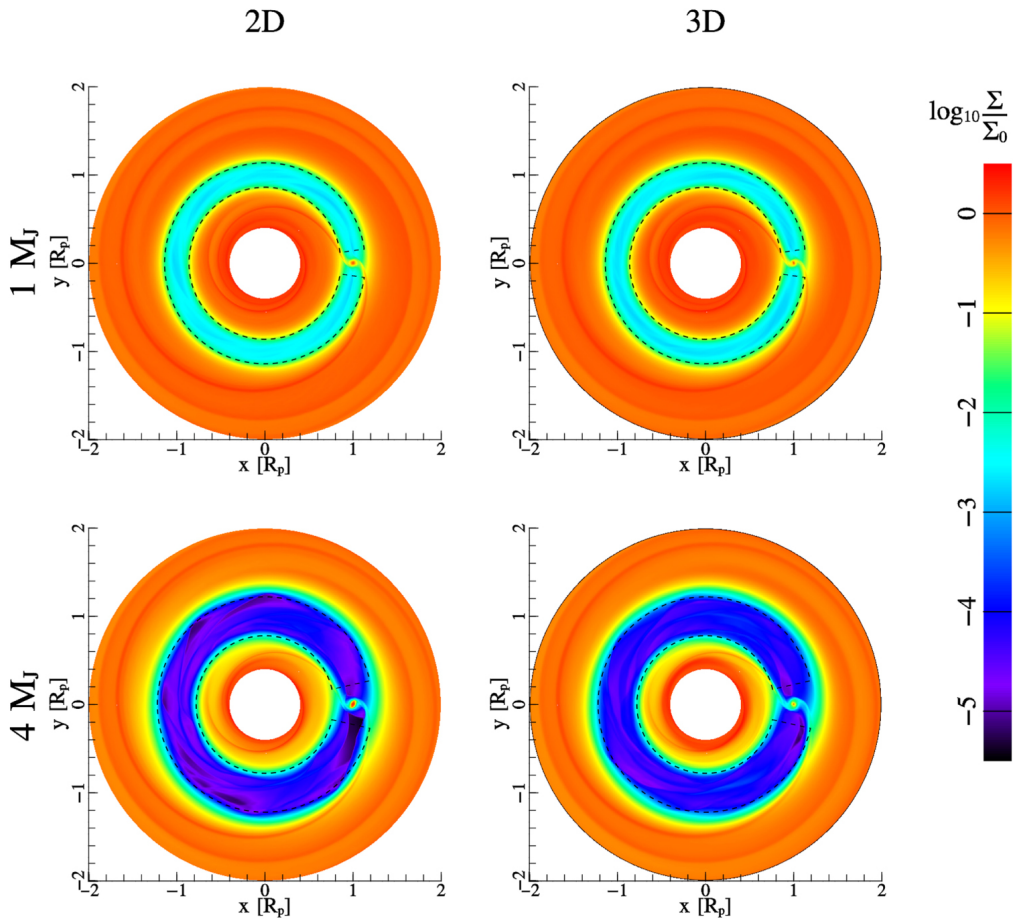

Figure 11: Plots of gap depletion fractions for planet-driven gaps, reproduced from Fung and Chiang (2016). For both of the planet masses tested, there is good agreement between 2D and 3D simulations.

itself has been seen in near-infrared scattered light (tracing small grains), ALMA dust continuum (tracing larger grains), and ^{12}CO (tracing the gas). Numerical simulations (Bae et al., 2019) uphold the validity of the disk-planet interaction hypothesis in this context. In other systems, such as LkCa15 (Kraus and Ireland, 2012), the evidence for planets is less conclusive; and in still others, such as the DSHARP sample (Zhang et al., 2018), the existence of planets below the detection thresholds of instruments such as VLT/SPHERE (Asensio-Torres et al., 2021) and the *James Webb Space Telescope* (JWST) can be inferred only circumstantially, from the existence of narrow gaps and rings in the high-resolution disk observations.

2.2 THERMALLY-DRIVEN SUBSTRUCTURE

Building on the understanding provided by the disk-planet interaction problem, it has also been postulated that azimuthal variations in temperature—and thus, pressure—can also drive substructure within protoplanetary disks. Among the first papers to explore this idea was Montesinos et al. (2016), in which the authors ran 2D simulations of a disk with two low-temperature radial lanes 180 degrees apart, consis-

tent with the bipolar shadow generated by a misaligned inner disk. The resulting azimuthal pressure-gradient forcing, $a_\phi = -(1/r\Sigma)\partial_\phi P$, propagated as a sound wave in a Keplerian-shearing disk, yielding a two-armed spiral structure, similar to those observed in near-infrared scattered light in a number of protoplanetary-disk systems (Shuai et al., 2022). In Montesinos and Cuello (2018), the authors generalized their previous work to include rotating shadows, and found that such shadows would launch spirals at their own Lindblad resonances, much as planets do.

According to the classical theory of disk-planet interaction, two-armed spirals are most consistent with driving by exterior, multi-Jupiter-mass companions (Bae and Zhu, 2018b). Such companions ought to lie comfortably above the detection limits of instruments such as JWST's NIRCam, but recent observations in systems such as MWC 758 (Wagner et al., 2024) and SAO 206462 (Cugno et al., 2024) have been unable to find conclusive evidence for them. These findings, in conjunction with near-infrared observations in other systems of shadows themselves (e.g., Benisty, M. et al., 2017; Debes et al., 2023) have brought increasing attention to the shadow-driven substructure hypothesis. Qian and Wu (2024) demonstrated that within a transition disk containing a large inner cavity, a shadow would excite eccentricity and further the development of asymmetries in the disk. Su and Bai (2024) ran a parameter study of disks with shadows, finding that these could give rise to multi-armed spirals, multiple sets of gaps and rings, and even vortices within protoplanetary disks.

Several simulation works have sought to move beyond parametrized shadows to include fully self-consistent radiation hydrodynamics. Nealon, Price, and Pinte (2020) used smoothed-particle hydrodynamics (SPH) simulations with `Phantom` coupled with Monte Carlo radiative transport (MCRT) to study the shadows generated by a misaligned inner disk. (Zhang and Zhu, 2024) used the fixed-grid `Athena++` hydrodynamics code, with multidimensional radiative transport, to run 3D simulations of a similar setup. Muley, Melon Fuksman, and Klahr (2024a) found that shadow-casting misalignments could in some cases develop spontaneously during disk evolution, while (Ziampras et al., 2024) used 2D simulations to study the long-term evolution of shadow-generated features.

Inspired by these numerical works, Zhu, Zhang, and Johnson (2024) presented the first analytical theory for shadow-generated disk features. Their analysis leads to a set of equations very similar to those of the classical Lindblad resonance theory (Equation 53), with an additional term corresponding to the temperature/sound-speed gradient created by a shadow. Analogously to the planetary case, they Fourier-expand this perturbation:

$$\delta c^2_{s,iso,o} = \sum_{m=1}^{\infty} \delta c^2_{s,iso,o,m}(R) e^{i(m\phi - \Omega_s t)} \tag{63}$$

where Ω_s represents the pattern speed of the shadow. But unlike in the planetary case, in which the perturbation is localized, they consider a temperature perturbation which, as a fraction of the original temperature, is independent of radius. This leads to an oscillatory radial profile for angular momentum flux (AMF), $F_J(R) \approx \Sigma\Omega r^2 \nu_r$. Consequently, $\partial_R F_J(R)$ would have multiple zeros R_{zero} toward which material would accumulate (if $\partial^2_R F_J(R) < 0$ at R_{zero}) or from which material would deplete (if $\partial^2_R F_J(R) > 0$ at R_{zero}) over time, providing a natural explanation for the multiple gaps and rings

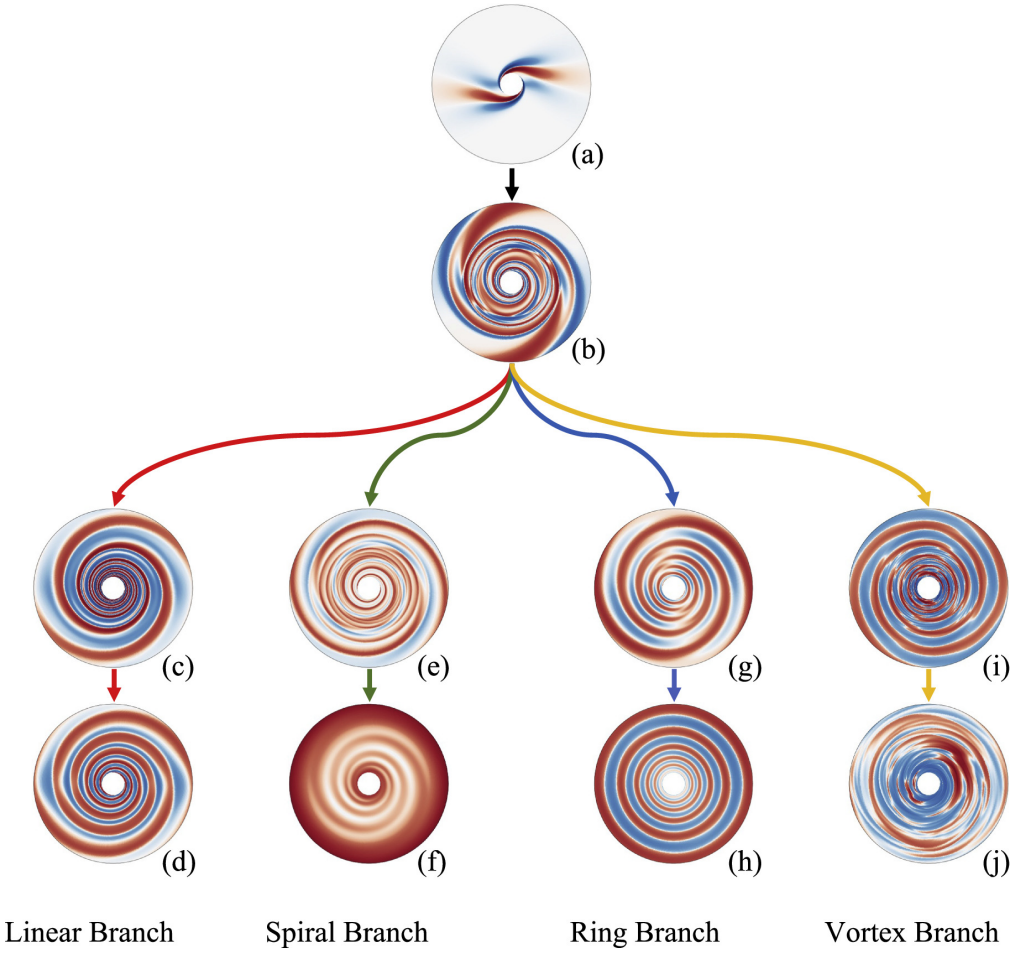

Figure 12: Evolution and taxonomy of disk features presented in (Su and Bai, 2024), showing the transition between the linear spiral-launching phase and nonlinear ring phase as a function of increasing thermal forcing. For a sufficiently strong azimuthal temperature variation and fast thermal relaxation, the velocity of a fluid parcel can change susbtantially as it crosses through a shadow, giving rise to vortices.

seen in shadowed-disk simulations. The field remains an ongoing area of research, both numerical and analytical.

3

NUMERICAL METHODS FOR PROTOPLANETARY DISK STUDIES

Although analytical theory is useful in providing physical intuition and limiting behaviors, most practical problems in protoplanetary disk studies do not admit an analytical solution, and must be approached numerically. Over the years, hydrodynamical codes have been developed and applied in the field, including that of (Kley, 1998, 1999), TRAMP (Klahr, Henning, and Kley, 1999; Klahr and Kley, 2006), FARGO/FARGO3D (Benítez-Llambay and Masset, 2016; Masset, 2000), Pencil (Brandenburg and Dobler, 2002; Pencil Code Collaboration et al., 2021), AREPO (Muñoz et al., 2014; Springel, 2010), and PEnGUIn (Fung, 2015) to name a few. For the studies presented here, we use the PLUTO code (Mignone et al., 2007), which employs a fixed-grid, finite-volume scheme to solve the equations of hydrodynamics. We describe the physical and mathematical underpinnings scheme in what follows, with an emphasis on broad conceptual understanding relevant to comprehending the later chapters, rather than specific detail.

3.1 FINITE-VOLUME SCHEMES

In the equations of hydrodynamics, the evolution of each *conserved quantity* (be it density, momentum, or energy) can be taken to consist of *advection* (spatial transport) and *source terms*. All of these equations have the common form

$$\frac{\partial a}{\partial t} + \nabla \cdot (\vec{F}_a) = S_a \tag{64}$$

where a represents a variable, $\vec{F}_a$ represents the advective flux of that variable, and S_a incorporates additional source terms. In a finite-volume scheme, these quantities are aveaged over a control volume—the volume of a fluid cell—yielding that

$$\frac{\partial}{\partial t}(\bar{a}) + \frac{1}{V}\int_V \nabla \cdot (\vec{F}_a) dV = \bar{S}_a \tag{65}$$

where the overbars denote a volume average. On the second term, we can simplify by applying the divergence theorem (the integral of a divergence of a flux over a volume, equals the integral of the flux over the boundaries of that volume)

$$\frac{1}{V}\int_V \nabla \cdot (a\vec{v}) dV = \frac{1}{V}\int_{\partial V} \vec{F}_a \cdot \ d(\partial V) = \frac{1}{V}\sum_{q=0}^{n_f} \int_{A_q} \vec{F}_a \cdot d\vec{A}_q \tag{66}$$

where after the second equality, we have divided the boundary of the control volume into several discrete faces (points, lines, or surfaces, depending on whether the volume is 1D, 2D, or 3D). Simplifying to the case of one dimension, we obtain for a given cell n

$$\frac{\partial \bar{a}_n}{\partial t} = -\frac{1}{\Delta x_n}\left(F_{a,n+1/2} - F_{a,n-1/2}\right) + \bar{S}_{a,n} \tag{67}$$

where x_i is the cell center, $x_{n-1/2}$ and $x_{n+1/2}$ are its left and right boundaries, and where as before, the overbars denote a cell average. It is clear from this formulation that the net change in the quantity a within the cell is the net of the amount of it flowing in, minus the amount flowing out.

Numerically solving this equation in time requires us to discretize in time. The simplest example is the first-order Euler scheme (for which the error with respect to the true solution scales as $\propto \Delta t^1$. We can write the update from timestep i to $i+1$ as:

$$\frac{1}{\Delta t_i}\left(\bar{a}_i^{i+1} - \bar{a}_n^i\right) = -\frac{1}{\Delta x_n}\left(F^i_{a,n+1/2} - F^i_{a,n-1/2}\right) + \bar{S}^i_{a,n} \tag{68}$$

The above update is completely *explicit*, in that the right-hand side quantities are all known at the start of the timestep. To ensure the stability of the flux term, care must be taken to ensure that the fluid, and the sound waves generated by it, do not cross over multiple cells during one timestep. In other words, the timestep $\Delta t = C\delta x_i/|v_x| + c_s$, where $0 < C < 1$ is the (Courant, Friedrichs, and Lewy, 1928, CFL) factor. The source term $\bar{S}^i_{a,n}$ can also introduce stability if it is very large or sensitive to $\bar{a}$, unless the timestep is sufficiently small. Stability can be restored for larger timesteps by integrating terms *implicitly*, with the right-hand side of the update dependent on terms computed at the end of the step ($F^{i+1}_{a,n\pm1/2}, \bar{S}^{i+1}_{a,n}$) rather than at the beginning ($F^i_{a,n\pm1/2}, \bar{S}^{i+1}_{a,n}$) as in the *explicitly* integrated case. Although the timestep updates can be written analytically in simple cases, implicit integration generally requires the use of an iterative solver.

While it provides an instructive starting point, first-order Euler does not provide sufficient stability or accuracy for physical problems. In the PLUTO simulations we present, we use the second- and third-order explicit Runge-Kutta schemes to carry out time integration. For radiation physics, we opt for implicit-explicit (IMEX; Pareschi and Russo, 2005) schemes in which the transport of radiation is integrated explicitly, while the stiff local source terms—incorporated absorption, emission, scattering, and collision—are handled explicitly.

3.2 RECONSTRUCTION AND RIEMANN SOLVERS

In Equations 65 and 66, we made the assumptions that a and its flux are continuous quantities. In actual practice, however, only the cell-average values of a are known at each timestep, and a procedure (known as *reconstruction*) must be used to estimate these quantities within a cell and at cell boundaries. The simplest such model is *piecewise-constant method* (PCM) reconstruction, where the values at all points within a cell are assumed to be equal to the cell average:

$$\bar{a}(x) = \bar{a}_n \tag{69a}$$

and *piecewise-linear method* (PLM) reconstruction:

$$\bar{a}(x) = \bar{a}_i + D(x - x_n) \tag{69b}$$

where the coordinate is constrained to lie within the cell ($x_{n-1/2} \leqslant x < x_{n+1/2}$), and where D is a function of the cell averages in neighboring cells ($\bar{a}_{n-1}$ and $\bar{a}_{n+1}$). In

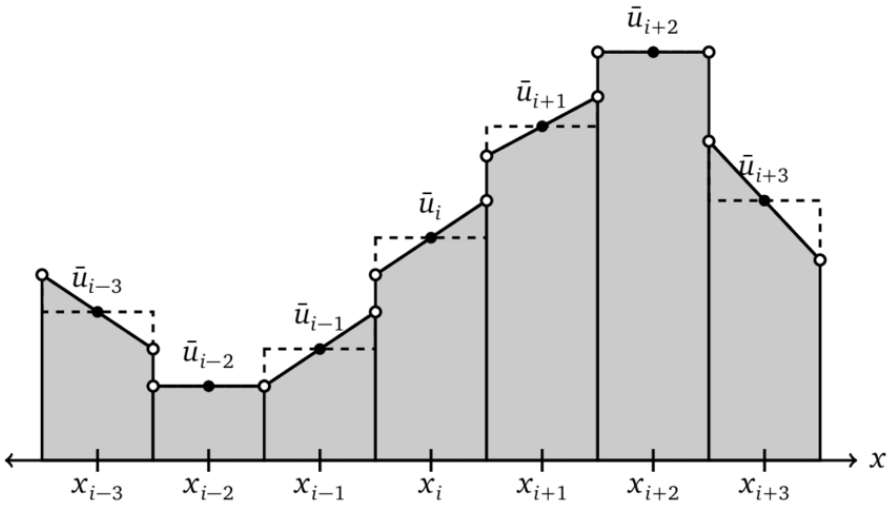

Figure 13: An example of piecewise-linear reconstruction based on the MUSCL scheme (Núñez, 2015).

regions of smooth flow, PCM is accurate to first order in the cell size—that is, the error with respect to the underlying continuous scales as $L_1 \propto \Delta x$, while a properly constructed PLM method is accurate to second order, $L_1 \propto \Delta x^2$. Other reconstruction techniques, such as the piecewise-parabolic method (PPM; Colella and Woodward, 1984) and the weighted essentially non-oscillatory schemes (WENO Liu, Osher, and Chan, 1994), provide estimates that converge with higher order when the flow is smooth, at the cost of increased inaccuracy at discontinuities such as shocks. For the work presented here, we use either PLM or WENO3 reconstruction, depending on the strength of shocks in the problem.

At each cell interface $x_{n+1/2}$, the reconstruction procedure yields two values for each quantity, one computed from i (the *left states*, $a_{n+1/2,L}$) and one from cell $i+1$ (the *right states*, $a_{n+1/2,R}$). This allows one to set up a *Riemann problem* at the interface. In the case of 1D hydrodynamics with an adiabatic equation of state, the relevant conserved quantities are the density, x-momentum, and total energy ($\vec{a} = (\rho, p_x, \mathscr{E}_g)^T$). To understand the Riemann problem arising from this system, it is helpful to recast its evolution (Equation 1, sans source terms aside from pressure) in the form $\partial_t \vec{a} + \mathbf{W}(\vec{a})\partial_x \vec{a} = 0$. In this case, the matrix $\mathbf{W}$ is given by (Toro, 2009):

$$\mathbf{W} = \begin{pmatrix} 0 & 1 & 0 \\ \frac{1}{2}(\gamma-3)v_x^2 & -(\gamma-3)v_x & \gamma-1 \\ -\gamma(\mathscr{E}_g/\rho)v_x + (\gamma-1)v_x^3 & \gamma(\mathscr{E}_g/\rho) - \frac{3}{2}(\gamma-1)v_x^2 & \gamma v_x \end{pmatrix} \tag{70}$$

Substituting $\mathscr{E}_g = \rho c_s^2/\gamma + (1/2)\rho v_x^2$ yields that

$$\mathbf{W} = \begin{pmatrix} 0 & 1 & 0 \\ \frac{1}{2}(\gamma-3)v_x^2 & -(\gamma-3)v_x & \gamma-1 \\ \frac{1}{2}(\gamma-2)v_x^3 - \frac{c_s^2 v_x}{\gamma-1} & \frac{3-2\gamma}{2}v_x^2 + \frac{c_s^2}{\gamma-1} & \gamma v_x \end{pmatrix} \tag{71}$$

It can be shown that $\det\mathbf{W} = v_x(v_x + c_s)(v_x - c_s) = \lambda_-\lambda_0\lambda_+$, and that $\mathrm{Tr}\mathbf{W} = 3v_x = \lambda_- + \lambda_0 + \lambda_+$. We can see that $\boxed{\lambda = \{v_x - c_s, v_x, v_x + c_s\}}$ satisfies both conditions. These

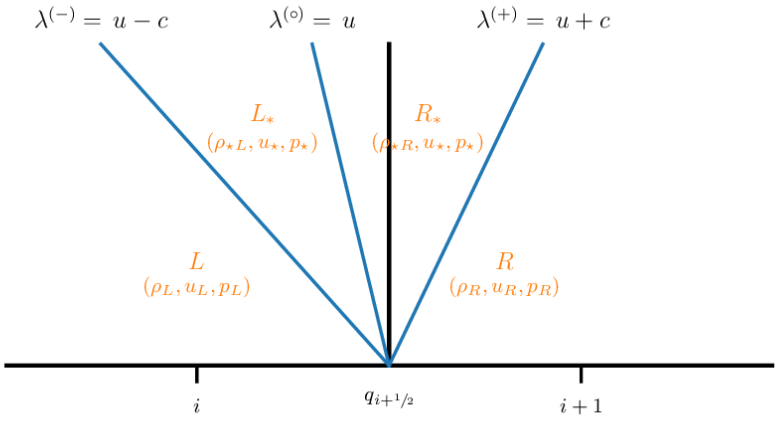

Figure 14: Graphical representation of the Riemann problem, showing the three characteristic lines dividing the left and right states from the intermediate star states (Zingale, 2022). Note that in this case the flux was solved in terms of the primitive, rather than conservative variables.

eigenvalues correspond to the three characteristic wavespeeds associated with system: the bulk motion of the fluid as a whole, plus two sound waves propagating in either direction in the moving frame of the fluid. The corresponding eigenvectors are:

$$\begin{aligned} \vec{\lambda}_0 &= \left(\rho, \rho v_x, \frac{\rho v_x^2}{2}\right)^T \\ \vec{\lambda}_\pm &= (\rho, \rho(v_x \pm c_s), (\mathscr{E}_g + p) \pm \rho c_s v_x)^T \end{aligned} \tag{72}$$

After a time interval δt, the fluid state in regions $(x - x_{n+1/2}) < \lambda_- \delta t$ is given simply by $\vec{a}_L$, while those for which $(x - x_{n+1/2}) > \lambda_+ \delta t$ are given by $\vec{a}_R$. Those in the region $\lambda_- \delta t < (x - x_{n+1/2}) < \lambda_0 \delta t$ are given by some intermediate state $\vec{a}_{L*}$, while those between $\lambda_0 \delta t < (x - x_{n+1/2}) < \lambda_+ \delta t$ are set by another intermediate state, $\vec{a}_{R*}$. These four states correspond to four different cases for the numerical flux at the interface:

$$\vec{F}_{a,\text{Riemann}} = \begin{cases} \vec{F}_{a,L} & \lambda_- > 0 \\ \vec{F}_{a,L*} & \lambda_- < 0 < \lambda_0 \\ \vec{F}_{a,R*} & \lambda_0 < 0 < \lambda_+ \\ \vec{F}_{a,R} & 0 > \lambda_+ \end{cases} \tag{73}$$

Obtaining the intermediate fluxes, and the wavespeeds λ of the characteristics separating them, generally requires solving complicated nonlinear expressions in terms of $\vec{a}_L$ and $\vec{a}_R$. Given that this is intractable in large-scale hydrodynamical simulations, it is more common to simply estimate these quantities. One method commonly used in PLUTO is the Harten-Lax-van Leer-Contact (HLLC; Toro, Spruce, and Speares, 1994) scheme. The older Harten-Lax-van Leer (HLL; Harten, Lax, and Leer, 1983) method is simpler and computationally more efficient, at the cost of ignoring the middle wave λ_0 (setting $F_{a,L*} = F_{a,R*}$) and creating more numerical diffusivity. We refer the reader to Toro (2009) for the full functional forms of the flux expressions.

3.3 IMPLEMENTATION OF RADIATION HYDRODYNAMICS

Although radiation transport plays a key role in astrophysics, incorporating it into hydrodynamical codes is numerically challenging because the timescales involved are typically much shorter than those in fluid dynamics, and because radiation transport is formally a five-dimensional problem (three spatial dimensions, plus two angular directions). Over the years, a number of schemes have been deployed in the protoplanetary disk context, including flux-limited diffusion (FLD; Levermore and Pomraning, 1981), M1 (Levermore, 1984), ray-tracing (e.g., Nealon, Price, and Pinte, 2020), and discrete-ordinate schemes (e.g., Jiang, 2021). In what follows, we describe the radiation-hydrodynamics scheme used in our `PLUTO` simulations, as implemented in Melon Fuksman et al. (2021) and further developed in Part II of this thesis.

3.3.1 *M1 scheme for thermal infrared*

The M1 scheme in `PLUTO` solves a simplified version of simplified radiative transfer equation, integrated over frequency and solid angles. The zeroth and first moments of the equation are:

$$\frac{1}{\hat{c}}\frac{\partial E_r}{\partial t} + \nabla \cdot \vec{F} = -\kappa\rho(E_r - a_r T^4) \tag{74a}$$

$$\frac{1}{\hat{c}}\frac{\partial \vec{F}_r}{\partial t} + \nabla \cdot \mathbf{P}_r = -\chi\rho\vec{F}_r \tag{74b}$$

Where the radiation pressure tensor $\mathbf{P}_r$ is a function of E_r and $\vec{F}_r$, being isotropic and proportional to E_r as $|\vec{F}_r| \to 0$ (diffusion limit), but directed and proportional to $\vec{F}_r$ as $|\vec{F}_r| \to E_r$ (free-streaming limit). The equations, like those of classical hydrodynamics, form a system of conservation laws, and can be solved using the approach laid out in Sections 3.1 and 3.2. They are identical to those in Equation 24 of Section 1.2.3, with the subtle difference that the transport velocity c is replaced with a *reduced speed of light* $\hat{c}$ (RSLA). The RSLA helps speed up integrations by relaxing the restrictive Courant timestep constraint that would be imposed by transporting radiation at its true speed c; nevertheless, it must be faster than typical fluid velocities in a simulation order to ensure the correct physical behavior. Typical values in protoplanetary-disk studies range from $10^{-4} \lesssim \hat{c}/c \lesssim 10^{-2}$, with the exact value being problem-dependent.

In the "two-temperature" (gas, dust) approach of Melon Fuksman et al. (2021), the right-hand side source terms in the radiation energy density and flux evolution equations are augmented by equivalent source terms in the energy and momentum equations respectively:

$$G = c\kappa\rho(E_r - a_r T^4) \tag{75a}$$

$$\vec{G} = c\chi\rho\vec{F}_r \tag{75b}$$

To ensure consistency when the radiation field has reached a steady state, the above source terms are independent of the specific choice of $\hat{c}$. This slightly modifies the conservation of energy and momentum, a topic discussed in Part II of this thesis.

As in Section 3.1, we integrate the left-hand side transport term explicitly, but integrate the right-hand-side source terms implicitly using Newton-Raphson iterations, to ensure numerical stability. These are combined using the IMEX1 and IMEX-SSP(2,2,2) schemes detailed in Pareschi and Russo (2005). As a whole, the radiation block is *operator-split* from the hydrodynamics block. The code advances the radiation fields over a duration $\Delta t_{\mathrm{hydro}}/2$ (divided into n_{rad} radiation substeps of duration Δt_{rad}, set by the $\hat{c}$-based Courant criterion), then takes a full hydrodynamic step, and finally advances the radiation fields another $\Delta t_{\mathrm{hydro}}/2$, thereby completing a full timestep. We use this basic structure as a starting point for the three-temperature scheme.

3.3.2 *Stellar irradiation*

While the grey M1 scheme is useful for simulating the transport of diffuse, thermalized radiation, it is less capable of modeling direct stellar irradiation, which has a very different frequency and angular-direction content. As described in Section 1.2.1 and in (Melon Fuksman et al., 2021), the star is assumed to be a point source, allowing the irradiation flux to be written as:

$$\vec{F}_{\mathrm{irr}}(r,\theta,\phi) = \pi \left(\frac{R_*}{r}\right)^2 \int_{\nu_{\mathrm{min}}}^{\nu_{\mathrm{max}}} d\nu B_\nu(T_*) \exp(-\tau_r(r,\theta,\phi,\nu)) \tag{76}$$

where $\tau_r(r,\theta,\phi) \equiv \tau_{r,0}(\theta,\phi,\nu) + \int_{r_{\mathrm{in}}}^{r} \rho\kappa_\nu dr$, with $\tau_{r,0}$ represents the extinction from an assumed density profile interior to the inner boundary of the simulation. Including this term helps avoid unphysical direct illumination and vertical puffing-up of the disk at the inner boundary of the simulation, which may be located far from the real disk truncation radius ($r \approx 0.1$ au). The (negative) divergence of this flux gives the value of the irradiation source term, S_{irr}:

$$S_{\mathrm{irr}} \equiv -\nabla\cdot\vec{F}_{\mathrm{irr}} = \pi \left(\frac{R_*}{r}\right)^2 \int_{\nu_{\mathrm{min}}}^{\nu_{\mathrm{max}}} d\nu B_\nu(T_*) \rho\kappa_\nu \exp(-\tau_r(r,\theta,\phi,\nu)) \tag{77}$$

which can be discretized both in space and in frequency space as

$$S_{\mathrm{irr}} = \frac{\pi R_*^2}{\Delta V(r_n,\theta_p,\phi_q)} \sum_{n'_\nu=0}^{n_\nu} \left(1-\exp(-(\Delta\tau_r)_{n,p,q,n'_\nu})\right) \exp(-(\tau_r)_{n,p,q,n'_\nu}) B_{n'_\nu}(T_*) \tag{78}$$

where

$$(\tau_r)_{n,p,q,n_\nu} = (\tau_{r,0})_{p,q,n_\nu} + \sum_{n'=0}^{n-1} (\Delta\tau_r)_{n',p,q,n_\nu} \,. \tag{79}$$

Because S_{irr} depends only on the density distribution, we evaluate it only once per hydrodynamical timestep; evaluations in the radiation block, during which density does not evolve, would be superfluous.

Part II

THREE-TEMPERATURE RADIATION HYDRODYNAMICS WITH PLUTO

4

TESTS AND APPLICATIONS TO PROTOPLANETARY DISKS

This chapter is adapted from the publication of Muley, Melon Fuksman, and Klahr (2023).

In circumstellar disks around T Tauri stars, visible and near-infrared stellar irradiation is intercepted by dust at the disk's optical surface and reprocessed into thermal infrared; this subsequently undergoes radiative diffusion through the optically thick bulk of the disk. The gas component—overwhelmingly dominant by mass, but contributing little to the opacity—is heated primarily by gas-grain collisions. In hydrodynamical simulations, however, typical models for this heating process (local isothermality, β-cooling, two-temperature radiation hydrodynamics) incorporate simplifying assumptions that limit their ranges of validity. To build on these methods, we develop a "three-temperature" numerical scheme, which self-consistently models energy exchange between gas, dust, and radiation, as a part of the PLUTO radiation-hydrodynamics code. With a range of test problems in 0D, 1D, 2D, and 3D, we demonstrate the efficacy of our method, and make the case for its applicability to a wide range of problems in disk physics, including hydrodynamic instabilities and disk-planet interaction.

4.1 INTRODUCTION

Protoplanetary disks—the rotationally-supported excess from the star-formation process—consist primarily of hydrogen and helium gas, with trace molecular species. Despite its preponderance by mass, this gas component has a low frequency-integrated opacity, making direct radiative heating and cooling inefficient. The disk's energy exchange with the radiation field is instead mediated by the dust component, typically taken to constitute just 1% of its total mass. Chiang and Goldreich (1997) studied this process semi-analytically, finding that incident stellar radiation—which peaks in the visible and near-infrared for classical T Tauri stars—creates a superheated dust layer at a disk's radial $\tau_r = 1$ surface. This layer reprocesses the radiation into the thermal infrared, half of which dissipates into interstellar space and half of which radiatively diffuses through dust grains in the optically thick disk midplane. The surrounding gas then thermally couples to the dust temperature structure via collisions. In turn, the density structure of the gas, and consequently that of the entrained dust that sets the $\tau_r = 1$ surface, adapt to maintain hydrostatic equilibrium.

By far, the most detailed models of protoplanetary disk thermal structure come from physical-chemical codes (e.g., Bruderer et al., 2012; Bruderer, 2013; Calahan et al., 2021; Woitke, Kamp, and Thi, 2009), followed by standalone, multiwavelength radiative transfer codes (e.g., Dullemond et al., 2012; Whitney et al., 2013). However, the computational expense of these numerical algorithms, along with their implicit assumption that disks are static on timescales relevant to thermal physics, makes them intractable to include in dynamical problems. Hydrodynamical simulations must therefore use various

parametrizations, of which the "locally isothermal" assumption—in which the temperature in each grid cell is fixed to its initial value—has been historically important for its simplicity and ease of interpretation. But more recently, simulations of hydrodynamic instabilities and the anticyclonic vortices they generate (Huang and Yu, 2022; Malygin et al., 2017; Manger, Pfeil, and Klahr, 2021; Pierens and Lin, 2018; Tarczay-Nehéz, Regály, and Vorobyov, 2020), gaps and rings (Miranda and Rafikov, 2019; Ziampras, Kley, and Dullemond, 2020), spiral arms (Miranda and Rafikov, 2020a; Miranda and Rafikov, 2020b), and circumplanetary disks (Fung, Zhu, and Chiang, 2019) have revealed that the choice of disk thermodynamics prescription has a substantial influence on their morphology and behavior. The quality of disk observations continues to improve (e.g., Keppler et al., 2018; Pinte et al., 2022; Ren et al., 2018; Teague et al., 2019), and meaningfully interpreting them requires a more accurate, self-consistent treatment of disk heating and cooling in hydrodynamic models.

To this end, numerical radiation hydrodynamics (RHD) is promising. For computational efficiency, these simulations generally use the "grey approximation", in which radiation energy densities, fluxes, and material opacities are averaged over frequency. One widely-used method in the study of protoplanetary disks (e.g., Binkert, Szulágyi, and Birnstiel, 2023; Bitsch et al., 2013; Flock et al., 2013; Klahr and Kley, 2006; Kley, Bitsch, and Klahr, 2009) is flux-limited diffusion (FLD; Levermore and Pomraning, 1981), in which the radiative flux $\vec{F}_r$ is proportional to the gradient of radiation energy density E_r, subject to a limiter that ensures the system satisfies the speed-of-light limit, $|\vec{F}_r| \leqslant cE_r$. Though FLD works well in optically thick regions, its definition of flux is limited in the thin limit, making it unable to produce anisotropic features in the radiation field such as beams or shadows. The M1 approximation (Levermore, 1984) handles these issues with a separate evolution equation for flux. M1 can accurately reproduce both the optically thick diffusion and optically thin free-streaming limits, but has limitations in situations where free-streaming beams cross one another.

Differentiating between dust and gas temperatures is a comparatively recent development in RHD simulations. The star-formation simulations of Bate and Keto (2015), as well as the thermochemical disk simulations of Wang and Goodman (2017), Wang, Bai, and Goodman (2019) and Hu et al. (2023), use equilibrium prescriptions to compute dust temperature. By contrast, Pavlyuchenkov and Zhilkin (2013), Pavlyuchenkov et al. (2015), and Vorobyov et al. (2020) use iterative Newton-Raphson schemes to self-consistently compute energy exchange between gas, dust, and radiation, while using FLD for radiation transport.

In what follows, we present our own three-temperature scheme, implemented within the PLUTO hydrodynamics code (Mignone et al., 2007). To compute energy exchange, we use Newton-Raphson iterations (albeit with differences from the aforementioned works), while to transport radiation, we use the M1 scheme already developed for PLUTO (Melon Fuksman et al., 2021; Melon Fuksman and Mignone, 2019) to handle both the optically thick and thin regimes in protoplanetary disks. Section 4.2 describes our numerical method. Section 4.3 details our code tests: the first two (0D matter-radiation coupling and 1D Ensman shock tube) have known reference solutions and demonstrate basic function, while the latter two (2D self-shadowing and 3D disk-planet interaction) illustrate applications to realistic disks. Section 4.4 provides a summation of our work and discusses possible future areas of research.

4.2 METHOD

4.2.1 *Basic equations*

We develop a strategy to solve the equations of radiation hydrodynamics, including a secondary dust fluid. In this work, we make the simplifying assumptions that dust grains are kinetically well-coupled to the gas (Stokes number $\mathrm{St} \ll 1$) and that they have negligible inertia (globally constant dust-to-gas ratio $f_d \ll 1$)—in other words, both evolve with the same velocity field, and the dust has no momentum.

$$\frac{\partial \rho}{\partial t} + \nabla \cdot (\rho \vec{v}) = 0 \tag{80a}$$

$$\frac{\partial (\rho \vec{v})}{\partial t} + \nabla \cdot (\rho \vec{v} \vec{v}) = -\nabla p - \rho \nabla \Phi + \vec{S}_m + \vec{G} \tag{80b}$$

$$\frac{\partial E_g}{\partial t} + \nabla \cdot (E_g \vec{v}) = -\nabla \cdot ((p + \rho\Phi)\vec{v}) + S_m + X_{gd} + cG_g + S_g^{\mathrm{irr}} \tag{80c}$$

$$\frac{\partial E_d}{\partial t} + \nabla \cdot (E_d \vec{v}) = -X_{gd} + cG_d + S_d^{\mathrm{irr}} \tag{80d}$$

$$\frac{\partial E_r}{\partial t} + \hat{c} \nabla \cdot \vec{F}_r = -\hat{c}(G_g + G_d) \tag{80e}$$

$$\frac{\partial \vec{F}_r}{\partial t} + \hat{c} \nabla \cdot \mathbf{P}_r = -\hat{c} \vec{G} \tag{80f}$$

where $\rho, \vec{v}, p$ represent the gas density, pressure, and velocity respectively. ρ_d is the dust density, while f_d is the dust-to-gas ratio, Φ is the gravitational potential, and $\{E_g, E_d, E_r\}$ are *total* energy densities for gas, dust, and radiation respectively. c is the speed of light, while the $\hat{c}$ term is a "reduced speed of light" (Gnedin and Abel, 2001) which enables longer timesteps, but must nevertheless exceed all hydrodynamic velocities relevant to the problem (Skinner and Ostriker, 2013).

We assume that the gas follows an ideal equation of state,

$$p = \rho_g k_B T_g / \mu m_H \tag{81}$$

where k_B is the Boltzmann constant, T_g the gas temperature, μ the mean molecular weight, and m_H the mass of a hydrogen atom. The adiabatic index $\gamma \equiv \partial \ln p / \partial \ln \rho$ is a constant, implying an *internal* (thermal) energy density

$$\xi_g = p/(\gamma - 1)\,. \tag{82}$$

Because we do not consider the kinetic energy of dust in this work, the internal energy of dust, ξ_d, is equal to its total energy E_d. For consistency of notation in what follows, we additionally define a symbol $\xi_r \equiv E_r$.

Dust and gas exchange internal energy collisionally via the term

$$X_{gd} \equiv t_c^{-1}(r_{gd}\xi_d - \xi_g) \tag{83}$$

where t_c is the thermal relaxation time and $r_{gd} = k_B/\mu m_H f_d c_d(\gamma - 1)$ is the ratio of heat capacity per unit volume between gas and dust. c_d is the specific heat capacity of dust. We compute the gas cooling time t_c as a function of the dust-gas stopping time t_s, in the Epstein regime (Burke and Hollenbach, 1983b; Speedie, Booth, and Dong, 2022)

$$t_c = \frac{2/3}{\gamma - 1} f_d^{-1} t_s \eta^{-1} \tag{84}$$

where η is an order-unity "accommodation coefficient" which we henceforth ignore. The corresponding dust cooling time is given by

$$t_{c,dust} = r_{gd}^{-1} t_c = \frac{2}{3}\frac{c_d}{k_B/\mu m_H} t_s \,. \tag{85}$$

In a realistic disk, the stopping time is computed by averaging over a grain-size distribution, which we describe as part of Section 4.3.3. The usual two-temperature radiation hydrodynamics represents the limit where $t_c \to 0$.

Net radiative heating/cooling is given for gas by

$$\begin{aligned} G_g \equiv &-\rho\kappa_g(a_r T_g^4 - \xi_r) \\ &-\rho(2\kappa_g - \chi_g)\vec{\beta}\cdot\vec{F}_r - \rho\chi_g\vec{\beta}\cdot(\xi_r\vec{\beta} + \vec{\beta}\cdot\mathbf{P}_r) \end{aligned} \tag{86a}$$

and likewise for dust by

$$\begin{aligned} G_d \equiv &-\rho\kappa_d f_d(a_r T_d^4 - \xi_r) \\ &-\rho f_d(2\kappa_d - \chi_d)\vec{\beta}\cdot\vec{F}_r - \rho f_d\chi_d\vec{\beta}\cdot(\xi_r\vec{\beta} + \vec{\beta}\cdot\mathbf{P}_r) \end{aligned} \tag{86b}$$

Similarly, the attenuation of radiative flux by gas is given by

$$\begin{aligned} \vec{G}_g \equiv &\rho\chi_g\vec{F}_r - \rho\kappa_g(a_r T_g^4 - \xi_r)\vec{\beta} \\ &-2\rho\kappa_g(\vec{\beta}\cdot\vec{F}_r)\vec{\beta} - \rho\chi_g(\xi_r\vec{\beta} + \vec{\beta}\cdot\mathbf{P}_r) \end{aligned} \tag{86c}$$

and for dust by

$$\begin{aligned} \vec{G}_d \equiv &\rho f_d\chi_d\vec{F}_r - \rho f_d\kappa_d(a_r T_d^4 - \xi_r)\vec{\beta} \\ &-2\rho f_d\kappa_d(\vec{\beta}\cdot\vec{F}_r)\vec{\beta} - \rho f_d\chi_d(\xi_r\vec{\beta} + \vec{\beta}\cdot\mathbf{P}_r) \end{aligned} \tag{86d}$$

involving absorption opacities κ, total (absorption plus scattering) opacities χ, temperatures T, the radiation constant $a_r = 4\sigma_{SB}/c$, and the radiation pressure tensor $\mathbf{P}_r$. Typically, κ is computed as a Planck average over frequency, while χ is computed as a Rosseland average. We define $\vec{G} \equiv \vec{G}_g + \vec{G}_d$; because our current implementation assumes dust follows the gas and has negligible inertia, it is this total $\vec{G}$ that gets added to the gas momentum equation and integrated during the hydrodynamic step.

Each of the equations (86) can be divided into a $\vec{\beta}$-independent and $\vec{\beta}$-dependent part, $G = G^w + G'(\vec{\beta})$. The $G'(\vec{\beta})$ parts arise from a Lorentz transformation of the radiation-interaction terms from the fluid's comoving frame to the observer's frame, truncated in the mildly relativistic regime (Melon Fuksman and Mignone, 2019; Skinner and Ostriker, 2013). In protoplanetary disks, $\beta \ll 1$ [1], so these terms are small and can be integrated explicitly.

The radiation pressure tensor $\mathbf{P}_r(E_r, \vec{F}_r)$ is evaluated according to the M1 closure (Levermore, 1984), which accurately reproduces the free-streaming and diffusion limits:

$$\mathbf{P}_r^{ij} = D^{ij} E_r = E_r \left(\frac{1-\Xi}{2} \delta^{ij} + \frac{3\Xi - 1}{2} n^i n^j \right) \tag{87}$$

in which

$$\Xi = \frac{3 + 4w^2}{5 + 2\sqrt{4 - 3w^2}} \tag{88}$$

where $\vec{n} = \vec{F}_r / \|\vec{F}_r\|$, $w = \|\vec{F}_r\| / E_r$, and δ^{ij} is the Kronecker delta.

S_d^{irr} and S_g^{irr} represent radiation emitted directly by the star, which has a higher-frequency spectrum than the dust-emitted radiation represented by E_r; the source terms are computed (e.g., via ray tracing) at every hydrodynamic timestep, rather than being evolved dynamically as E_r and F_r are. S_m and $\vec{S}_m$ represent, respectively, energy and momentum source terms such as thermal conductivity and viscosity that are already implemented into PLUTO and integrated during the hydrodynamic step.

4.2.2 *Conservation laws*

With the reduced speed of light approximation, and ignoring non-ideal source terms other than $\vec{G}_g, \vec{G}_d, G_g, G_d, X_{gd}$, our system conserves the following modified total energy and momentum:

$$E_{tot} = E_r(c/\hat{c}) + E_g + E_d = \xi_r(c/\hat{c}) + \xi_g + \xi_d + \rho\vec{v}^2/2 \tag{89}$$

$$\vec{P}_{tot} = \vec{F}_r/\hat{c} + \vec{p}_g \tag{90}$$

which reduce to the standard definitions when $c = \hat{c}$. As mentioned earlier, Skinner and Ostriker (2013) verified that this modification does not impact the dynamics of the system, provided that $\hat{c}$ is much larger than hydrodynamic velocities characteristic of the system.

4.2.3 *Operator splitting and timestepping*

We solve the dusty radiation-hydrodynamic equations (80) using a Strang split, sandwiching a full step of the hydrodynamic terms Δt between two half-steps $\Delta t/2$ of the radiative terms. In quasi-conservative form:

1 The Keplerian speed of an object orbiting a $1 M_\odot$ at 0.01 au ($1\ R_\odot$ for a T Tauri star)—essentially the maximum attainable in a protoplanetary-disk context—is $\beta \approx 5 \times 10^{-3}$.

$$\frac{\partial \mathcal{U}}{\partial t} + (\nabla \cdot \mathcal{F}_{\rm HD} + \nabla \cdot \mathcal{F}_{\rm rad}) = \left(\mathcal{S}_{\rm HD} + \mathcal{S}^{\rm imp}_{\rm rad} + \mathcal{S}^{\rm exp}_{\rm rad}\right) \tag{91a}$$

where $\mathcal{U}$ is a vector of conserved variables, $\mathcal{S}$ are source terms and $\mathcal{F}$ are advective fluxes:

$$\mathcal{U} = \left(\rho, \rho\vec{v}, E_g, E_d, E_r, \vec{F}_r\right)^\top \tag{91b}$$

$$\mathcal{F}_{\rm HD} = (\rho\vec{v}, \rho\vec{v}\vec{v} + p\mathbf{I}, (E_g + p + \rho\Phi)\vec{v}, E_d\vec{v}, 0, 0)^\top \tag{91c}$$

$$\mathcal{F}_{\rm rad} = (0, 0, 0, 0, \hat{c}E_r, \hat{c}\mathbf{P}_r)^\top \tag{91d}$$

$$\mathcal{S}_{\rm HD} = \left(0, -\rho\nabla\Phi + \vec{S}_m, S_m, 0, 0, 0\right)^\top \tag{91e}$$

$$\begin{aligned}\mathcal{S}^{\rm imp}_{\rm rad} = \Big(&0, \vec{G}^w, X_{gd} + cG^w_g + S^{\rm irr}_g,\\ &-X_{gd} + cG_d + S^{\rm irr}_d, -\hat{c}(G_g + G_d), -\hat{c}\vec{G}\Big)^\top\end{aligned} \tag{91f}$$

$$\mathcal{S}^{\rm exp}_{\rm rad} = \left(0, \vec{G}', cG'_g, cG'_d, -\hat{c}(G'_g + G'_d), -\hat{c}\vec{G}'\right)^\top \tag{91g}$$

The overall timestep duration Δt is set by applying the Courant criterion to the hydrodynamical signal speeds $v_{\rm HD}$. But because $\hat{c} \gg v_{\rm HD}$, the radiation half-steps $\Delta t/2$ must be further divided into substeps of duration $\Delta t_{\rm rad}$ to ensure that the radiation subsystem meets its own Courant criterion. The integration of these substeps can take place through one of two implicit-explicit methods, IMEX1:

$$\begin{aligned}\mathcal{U}^{(1)} &= \mathcal{U}^n + \mathcal{R}^n_{\rm rad}\Delta t_{\rm rad} + \mathcal{S}^{{\rm imp}(1)}_{\rm rad}\Delta t_{\rm rad}\\ \mathcal{U}^{(2)} &= \mathcal{U}^{(1)} + \mathcal{R}^{(1)}_{\rm rad}\Delta t_{\rm rad} + \mathcal{S}^{{\rm imp}(2)}_{\rm rad}\Delta t_{\rm rad}\\ \mathcal{U}^{n+1} &= \frac{1}{2}\left(\mathcal{U}^{(1)} + \mathcal{U}^{(2)}\right)\end{aligned} \tag{92}$$

or IMEX-SSP(2,2,2), both analogous to second-order Runge-Kutta (Pareschi and Russo, 2005):

$$\begin{aligned}\mathcal{U}^{(1)} &= \mathcal{U}^n + \mathcal{S}^{{\rm imp}(1)}_{\rm rad}a\Delta t_{\rm rad}\\ \mathcal{U}^{(2)} &= \mathcal{U}^n + \mathcal{R}^{{\rm imp}(1)}_{\rm rad}\Delta t_{\rm rad}\\ &\quad + \mathcal{S}^{{\rm imp}(1)}_{\rm rad}(1-2a)\Delta t_{\rm rad} + \mathcal{S}^{{\rm imp}(2)}_{\rm rad}a\Delta t_{\rm rad}\\ \mathcal{U}^{n+1} &= \mathcal{U}^n + \frac{\Delta t_{\rm rad}}{2}\left(\mathcal{R}^{(1)}_{\rm rad} + \mathcal{R}^{(2)}_{\rm rad}\right)\\ &\quad + \frac{\Delta t_{\rm rad}}{2}\left(\mathcal{S}^{{\rm imp}(1)}_{\rm rad} + \mathcal{S}^{{\rm imp}(2)}_{\rm rad}\right)\end{aligned} \tag{93}$$

where $\mathcal{R}_{\rm rad}$ is a shorthand for $-\nabla\cdot\mathcal{F}_{\rm rad}+\mathcal{S}^{\rm imp}_{\rm exp}$ and $a=1-1/\sqrt{2}$. $\mathcal{R}_{\rm rad}$ operators are integrated explicitly. However, the $\mathcal{S}^{\rm imp}_{\rm rad}$ operators, incorporating stiff terms such as opacity and gas-grain collision with characteristic timescales potentially much shorter than advective timescales, are integrated implicitly and are in general functions of $t_{\rm rad}$.

In what follows, we concern ourselves with solving the implicit source terms. The explicit, advective radiative terms $\mathcal{F}_{\rm rad}$, encompassing the transport of radiation energy density by radiative flux $\hat{c}\vec{F}_r$, and of radiative flux by the radiation pressure tensor $\hat{c}\mathbf{P}_r$, are updated using a Godunov scheme and Riemann solver as described in Melon Fuksman and Mignone (2019).

4.2.4 *Momentum source terms*

We update the radiative flux using the first-order implicit step

$$\vec{F}_r^{\,i+1}-\vec{F}_r^{\,i}=-\hat{c}\vec{G}^{i+1}\delta t=-\hat{c}\rho\delta t(\chi_d f_d+\chi_g)\vec{F}_r^{\,i+1} \tag{94}$$

where δt equals $\Delta t_{\rm rad}$ times the appropriate order-unity pre-factor for the implicit steps of equations 92 and 93, This can be solved analytically, by rearrangement. The resulting change in fluid momentum

$$(\rho\vec{v})^{i+1}-(\rho\vec{v})^{i}=-\hat{c}^{-1}\left(\vec{F}_r^{\,i+1}-\vec{F}_r^{\,i}\right)\delta t \tag{95}$$

can then be found straightforwardly by conservation.

From the final momenta, we can obtain the change in kinetic energy for gas

$$K_g^{i+1}-K_g^{i}=\left[(\vec{p}_g^{\,i+1})^2-(\vec{p}_g^{\,i})^2\right]/2\rho \tag{96a}$$

in which we make use of the fact that ρ is unchanged during a radiation timestep.

When the total dust and gas opacities χ are constant, the above equations must only be solved once. In general, however, they can be functions of temperature and density, and so must be solved before every iteration of the energy source terms. We describe these in the following section.

4.2.5 *Energy source terms*

The exchange of internal energies ξ between dust, gas, and radiation, is updated as follows:

$$\begin{aligned}\xi_d^{i+1}-\xi_d^{i}=&-(t_c^{-1})^{i+1}\left[r_{gd}\xi_d^{i+1}-\xi_g^{i+1}\right]\delta t\\&-(t_d^{i+1})^{-1}\left[a_r(T_d^{i+1})^4-\xi_r^{i+1}\right]\delta t\end{aligned} \tag{97a}$$

$$\begin{aligned}\xi_g^{i+1}-\xi_g^{i}=&+(t_c^{-1})^{i+1}\left[r_{gd}\xi_d^{i+1}-\xi_g^{i+1}\right]\delta t\\&-(t_g^{i+1})^{-1}\left[a_r(T_g^{i+1})^4-\xi_r^{i+1}\right]\delta t\end{aligned} \tag{97b}$$

with the dust temperature $T_d=\xi_g/(\rho c_d f_d)$ and the gas temperature $T_g=\xi_g/(\rho k_B/\mu)$. To simplify notation, we have introduced the symbols $t_d=(c\rho\kappa_d f_d)$ (the timescale required for light to travel one mean free path through dust) and $t_g=(c\rho\kappa_g)^{-1}$ (the

same, for gas); the relevant absorption opacities κ and cooling times t_c are in general functions of temperature and density. δt indicates the length of an implicit partial step, which is Δt_{rad} in the case of IMEX1, (92) and $a\Delta t_{rad}$ or $(1-2a)\Delta t_{rad}$, depending on the specific partial step, in the case of IMEX-SSP(2,2,2) (93).

The i superscripts indicate quantities at the beginning of the implicit partial step, while those with $i+1$ indicate those at the end. ξ_r^{i+1} is not computed directly in the above system, but is given by conservation of energy, modified to account for the reduced speed of light and the irradiation source terms S_g^{irr} and S_d^{irr}:

$$\begin{aligned}\xi_r^{i+1} - \xi_r^i = &-(\hat{c}/c)\left[(\xi_d^{i+1} - \xi_d^i) + (\xi_g^{i+1} - \xi_g^i)\right] \\ &+ (\hat{c}/c)(S_g^{irr} + S_d^{irr})\delta t\end{aligned} \tag{97c}$$

We insert ξ_r^{i+1} from equation 97c into equations eqs. (97a) and (97b) and solve the system using a multidimensional Newton's method (detailed in Appendix A.1). All equations operate on cell-averaged quantities. We note that the values of the stellar irradiation source term S_d^{irr} are updated, by ray-tracing, only at the start of each overall timestep Δt, even though their contribution to the energy density is added during each radiation substep. For the tests presented here, we set $S_g^{irr} = 0$, but we foresee it being useful in the future to model photoelectric or line heating in the upper disk (Dullemond et al., 2007).

Our implementation has the advantage of conserving total modified energy to machine precision, and converging within a small number of iterations (typically $\lesssim 5-10$ in disk-planet interaction simulations, even with temperature- and density-dependent cooling times). Moreover, it accommodates temperature change that is rapid compared to Δt_{rad}, making it useful in nonequilibrium cases such as accretion shocks, subject to constraints set by the reduced speed of light approximation.

4.3 TESTS

To verify the accuracy of our scheme and demonstrate its applicability to protoplanetary disks, we run test problems in 0D, 1D, 2D, and 3D. For the tests we present, we use third-order Runge-Kutta (RK3) timestepping with third-order weighted essentially non-oscillatory (WENO3) reconstruction (Yamaleev and Carpenter, 2009) and a Harten-Lax-van Leer-Contact (HLLC) Riemann solver for both the gas and radiation. The sole exception is our 2D disk self-shadowing test, in which large contrasts in temperature, density, and velocity emerge in high, close-in regions of the disk. As such, for this problem, we opt for second-order Runge-Kutta (RK2) time integration and piecewise linear method (PLM) spatial reconstruction with a van Leer flux limiter.

4.3.1 *0D test: radiation-matter coupling*

For our first set of tests, we consider a zero-dimensional setup probing only the local evolution of gas, dust, and radiation temperatures. We turn off the hydrodynamic equations and radiation advective terms, and set irradiation source terms and radiative

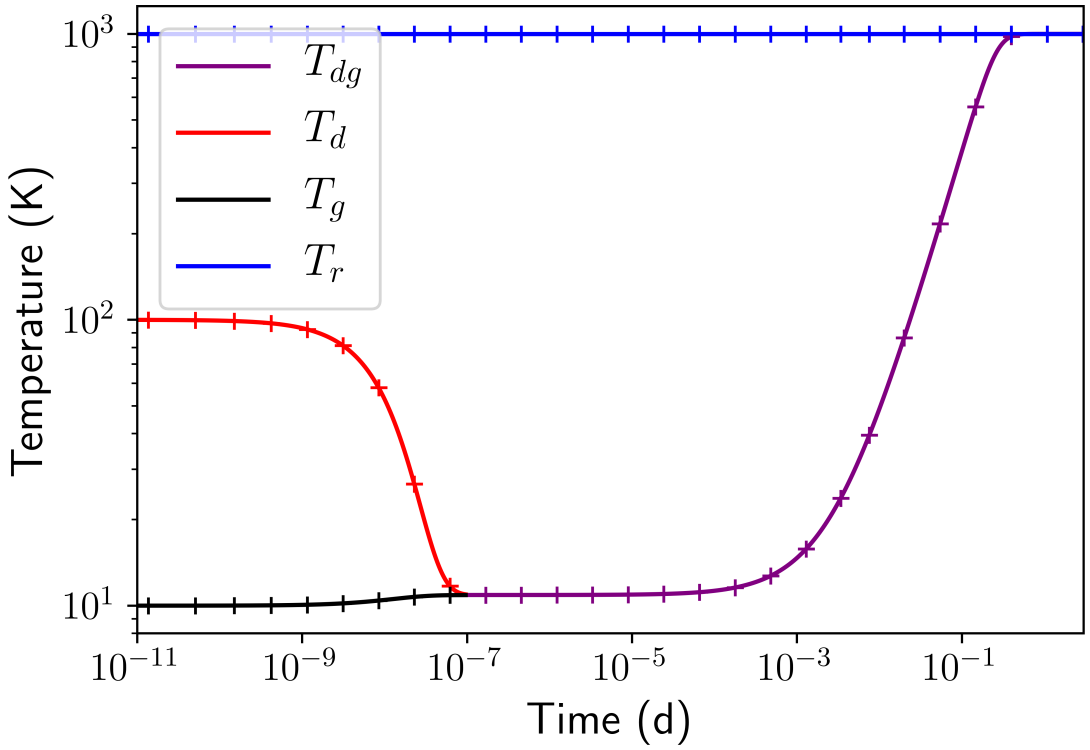

Figure 15: A 0D test of our three-temperature scheme, for which we set the dust-gas stopping time $t_s = 10^{-9} t_0 = 8 \times 10^{-9}$ d and the opacity $\kappa_d = 3.9$ cm^2 g^{-1}. Pluses indicate numerical results, while solid lines indicate analytical solutions taken from equations 100 *(red, black)* and 103 *(purple)*. Because the system is dominated by radiation energy, the radiation temperature *(blue)* is nearly constant throughout the system's evolution.

flux to zero, in order to isolate the effects of radiation-matter coupling. In this case, we can write the evolution of internal energies concisely in terms of $\vec{\xi} = (\xi_d, \xi_g)^\top$:

$$\frac{\partial \vec{\xi}}{\partial t} = \left[\mathbf{C}\vec{\xi}\right] + \left[\vec{A}_{tot} + \mathbf{A}\vec{\xi} + \vec{Q}(\vec{\xi})\right] \tag{98}$$

where $\mathbf{A}$ includes linear absorption terms, $\mathbf{C}$ the collisional terms, $\vec{A}_{tot}$ the constant absorption terms, and $\vec{Q}$ the nonlinear emission terms:

$$\mathbf{C} = \begin{bmatrix} -t_c^{-1} r_{gd} & +t_c^{-1} \\ +t_c^{-1} r_{gd} & -t_c^{-1} \end{bmatrix} \tag{99a}$$

$$\mathbf{A} = \frac{\hat{c}}{c} \begin{bmatrix} -t_d^{-1} & -t_d^{-1} \\ -t_g^{-1} & -t_g^{-1} \end{bmatrix} \tag{99b}$$

$$\vec{A}_{tot} = \xi_{tot} \hat{c}/c \left(t_d^{-1}, t_g^{-1}\right)^\top \tag{99c}$$

$$\vec{Q}(\vec{\xi}) = -a_r \left(t_d^{-1} T_d^4, t_g^{-1} T_g^4\right)^\top \tag{99d}$$

For our setup, we use a gas density of $\rho_g = 7.78 \times 10^{-18} \mathrm{g\,cm^{-3}}$ with a dust-to-gas ratio $f_d = 10^{-2}$ and stopping time $t_s = 10^{-9} t_0$, where $t_0 = 8$ days is the code unit for time. We use a fixed opacity $\kappa_d = 3.9\ \mathrm{cm^2\,g^{-1}}$ and $\hat{c} = c$. At $t = 0$ we set $T_g = 10^1$ K, $T_g = 10^2$ K, and $T_r = 10^3$ K. The specific heat capacity of the gas c_g is defined by its mean molecular weight $\mu = 1$ and adiabatic index $\gamma = 7/5$; we set the dust specific heat capacity c_d equal to that of the gas. By analogy with the determination of Stokes number $\mathrm{St} \equiv t_s \Omega$ of quasi-Keplerian disks, we can compute a characteristic timescale for this system, $t_{cross} = l_{cross}/v_{cross}$, where l_{cross} and v_{cross} are the length and velocity scales of interest. In this case, we choose a $l_{cross} = (\kappa_d f_d \rho_g)^{-1} = 3.38 \times 10^{18}$ cm—the mean free path of the system—and a $v_{cross} = (k_B T_g/\mu m_p)^{1/2} = 287\ \mathrm{m\,s^{-1}}$. This yields a $t_{cross} = 3.6 \times 10^6$ y, or a $t_s/t_{cross} = 5.87 \times 10^{-18}$.

The system should relax to an equilibrium state in which dust, gas, and radiation have equivalent effective temperatures—specifically, $\xi_d = \xi_g/r_{gd} = c_g \rho_g (\xi_r/a_r)^{1/4}$. Furthermore, in several special cases, it has analytical solutions against which our numerical scheme can be tested. For instance, when collisional energy exchange between gas and dust happens much faster than absorption, the system has a solution in terms of matrix exponentials:

$$\vec{\xi}(t) \approx \exp\left[\mathbf{C}t\right] \vec{\xi}_0 \tag{100}$$

Given our simulation parameters, we find that equation 100 is a good description of the temperature evolution at early times. We plot its predictions for T_g and T_d as black and red lines respectively in 15. On timescales $t > t_c/(1 + r_{gd}) \approx t_s$, such a system reaches a quasi-steady state where $\xi_d = \xi_g/r_{gd}$—in other words, the temperatures of dust and gas become equal.

By contrast, when the absorption and emission terms dominate over collisions, and additionally the system is radiation-energy dominated throughout its evolution (i.e., $(c/\hat{c})\xi_r \equiv (\xi_{tot} - \xi_d - \xi_g) \gg \xi_g + \xi_d$), $\hat{c}$ drops out of the equations and we get:

$$\frac{\partial}{\partial t}\begin{bmatrix}\xi_d \\ \xi_g\end{bmatrix} \approx \begin{bmatrix} t_d^{-1}(\xi_{r,0} - a_r(\xi_d/\rho f_d c_d)^4) \\ t_g^{-1}(\xi_{r,0} - a_r(\xi_g/\rho c_g)^4)\end{bmatrix} \tag{101}$$

Each element of 101 is identical to the form found in eq. (69) and Figure 5 of Melon Fuksman and Mignone (2019), and yields an implicit analytic relation that can be inverted by root-finding:

$$\begin{aligned} 2Mt = &\,\mathrm{Re}\,(\arctan(\omega) + \operatorname{arctanh}(\omega)) \\ &- \mathrm{Re}\,(\arctan(\omega_0) + \operatorname{arctanh}(\omega_0)) \end{aligned} \tag{102}$$

where $M_d = (a_r/\xi_{r,0})^{1/4}\xi_{r,0}t_d^{-1}/(\rho f_d c_d)$, $\omega_d = (a_r/\xi_{r,0})^{1/4}(\xi_d/f_d\rho c_d)$, and $\omega_{d,0} = \omega_d(t=0)$; M_g and ω_g are obtained likewise. ξ_r is assumed constant throughout the evolution of the system.

When the collision timescale is much shorter than the absorption-emission timescale, but the dust and gas are already in collisional equilibrium, we can obtain yet another special case by summing the two rows of eq. (101):

$$\frac{\partial \xi_d}{\partial t} = \frac{t_d^{-1} + t_g^{-1}}{1 + r_{gd}}(\xi_{r,0} - a_r(\xi_d/\rho c_d f_d)^4) \tag{103}$$

where we constrain $\xi_d = \xi_g/r_{gd}$. The solution to equation (103) is also in the form of (102), with $M_{dg} = (a_r/\xi_{r,0})^{1/4}\xi_{r,0}(t_d^{-1} + t_g^{-1})((1+r_{gd})\rho f_d c_d)^{-1}$ and $\omega_{dg} = (a_r/\xi_{r,0})^{1/4}(\xi_d/\rho f_d c_d)$.

We plot equation (103) as a purple curve in Figure 15. Our scheme accurately handles the regime where dust and gas temperatures are well-coupled, showing that it is effective at reproducing the "two-temperature" limit of typical radiation-hydrodynamics simulations.

4.3.2 *1D test: Subcritical dusty radiative shock*

Having verified that our scheme accurately reproduces three-temperature static thermal coupling, we seek to study its performance in a a dynamical setting. To this end, we run a modified version of the 1D subcritical radiative shock in Ensman (1994), a standard test for radiation-hydrodynamic codes (see e.g., section 4.1 of Melon Fuksman et al., 2021, and references therein) incorporating sharp transitions in temperature and opacity.

In this setup, our domain spans the interval $[0, 7\times10^{10}\ \mathrm{cm}]$. The initial gas density is $\rho_g = 7.78\times10^{-10}\,\mathrm{g\,cm^{-3}}$, with a dust-to-gas ratio $f_d = 10^{-2}$. Dust, gas, and radiation temperatures are all initialized in equilibrium, $T_r = T_g = T_d = 10$ K; $\gamma = 7/5$, $\mu = 1$, and $c_d = c_g$ are the same as in the 0D case. The dust absorption opacity is set such that the inverse mean free path of radiation through dust, $l_d^{-1} \equiv \kappa_d\rho_d = 3.1\times10^{-10}\mathrm{cm^{-1}}$, with dust scattering opacity $\chi_d - \kappa_d$, and gas total opacity χ_g, both assumed to be zero. To form the shock, given our otherwise equilibrium initial conditions, we set an initial gas velocity $v_x = -6\,\mathrm{km\,s^{-1}}$, and impose a reflective condition on the left boundary. We

fiducially choose a reduced speed of light $\hat{c} = 10^{-3}c$ and a spatial resolution $N_x = 1200$ cells; these figures give results consistent with those of our tests (not shown) at $\hat{c} = c$, and both higher and lower resolutions.

We test stopping times $t_s = \{10^{-7}, 10^{-4}, 10^{-1}\}t_0$, where we again use $t_0 = 8$ d as the code unit for time. For this problem, we define the characteristic timescale using l_d as our length scale and v_x as the velocity scale, yielding a $t_{cross} = 7.78 \times 10^{-2} t_0$ and $t_s/t_{cross} = 1.28 \times \{10^{-5}, 10^{-2}, 10^{1}\}$. The last case is included to demonstrate the properties of our code when dust and gas have weak *thermal* coupling, although the long t_s/t_{cross} would also allow for relative motion between dust and gas, which we do not model.

In Figure 16, we plot temperature snapshots at $t = 0.054 t_0 = 3.75 \times 10^4$ sec for all stopping times, selecting $N_x = 1200$ as our fiducial resolution. For $t_s = 10^{-1}$, the gas temperature is that of a standard hydrodynamic shock. In the pre-shock region dust and gas are essentially in equilibrium; in the post-shock region, by contrast, the dust heats at a rate $\dot{T}_{d,coll} \approx (T_g - T_d) t_{c,dust}^{-1} \approx (T_{g,+} - T_{d,-}) t_{c,dust}^{-1}$, where minuses and pluses denote pre- and post-shock quantities respectively. Deeper in the post-shock region, this trend breaks down, as radiative cooling (which scales as $\dot{T}_{d,rad} \approx -c l_d^{-1} a_r (T_{d,-}^4 - T_{r,-}^4)/c_d \rho_d$) becomes sufficient to counteract the effects of collisional heating.

In the $t_s = 10^{-4} t_0$ case, the cooling time $t_{c,dust}$ is short, and T_d increases rapidly immediately after encountering the shock. Because the collisional heating rate is faster than for $t_s = 10^{-1} t_0$, the radiative cooling rate, and thus the maximum post-shock dust temperature, must be correspondingly higher. In the pre-shock region, this process is inverted: radiation propagating from the shock front heats the dust above its initial preshock value, and via collisions, the gas. For the strongly coupled case, with $t_s = 10^{-7} t_0$, dust and gas are in collisional equilibrium, and we recover the two-temperature results of Melon Fuksman et al. (2021). Because the Courant-limited radiation timestep $\Delta t_{rad} \approx \Delta x/\hat{c}$ is much longer than our dust coupling time, this result demonstrates the efficacy of our IMEX scheme in the stiff regime.

In these 1D simulations, changes in the radiation field are driven by collisional heating of the dust, and ultimately by the rightward motion of the shock front—a process much slower than radiation propagation or absorption/emission. In this regime, we can drop the time derivative terms in Equation 8of and take the nonrelativistic limit

$$\nabla(\Xi E_r) \approx -\rho_d \kappa_d F_x = -l_d^{-1} F_x \tag{104}$$

where the Ξ parameter is defined in Equation 88 as a function of the "reduced flux" w. Adding a sign to this reduced flux $w_x = F_x/E_r = \pm w$ and rearranging terms, we get that

$$\partial_{w_x}(\Xi)\nabla(w_x) \approx -(l_d^{-1} w_x + l_r^{-1}\Xi) \tag{105}$$

where $l_r^{-1} \equiv \nabla(E_r)E_r^{-1}$ is the relative rate of change in the radiation field. In other words, variations in the radiation field on length scales shorter (longer) than some critical scale $l_d \Xi |w_x|^{-1}$ drive (damp) the flux.

This is clearly visible in Figure 16: in the $t_s = 10^{-1} t_0$ case, the relatively moderate gradient in radiation energy means that the transition from the $w_x \approx 0$ diffusion

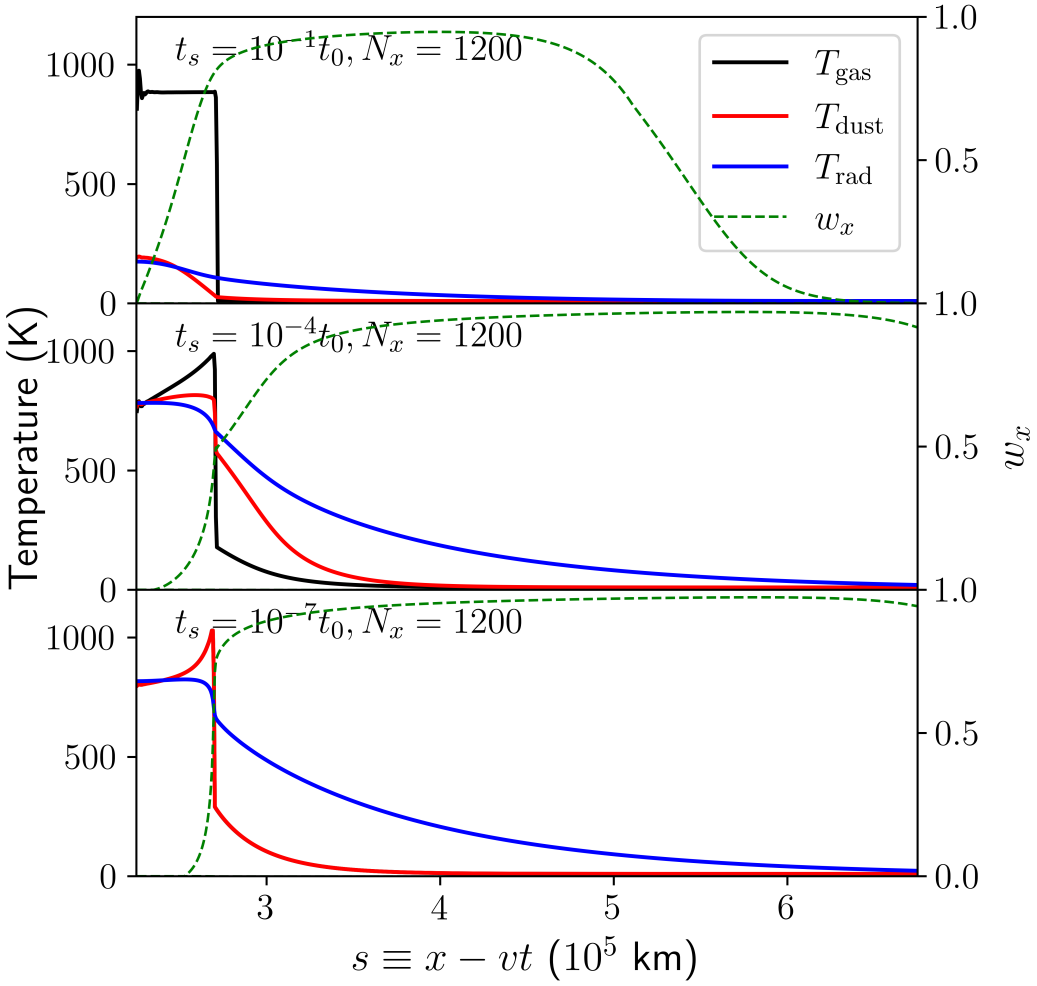

Figure 16: Temperature profiles in the dusty radiative shock test at $t = 0.054 t_0 = 3.75 \times 10^4$ sec, for a variety of stopping times. For $t_s = 10^{-1}$, the gas temperature is that of a standard hydrodynamic shock, with only weak losses to dust and radiation; for $t_s = 10^{-7}$, T_d and T_g have come into equilibrium, and they (along with w_x and T_r) match the results of the two-temperature radiative shock tests in section 4.1 of Melon Fuksman et al., 2021 (note that the signed "reduced flux" $w_x \equiv F_x/E_r$ is denoted as f in their work).

regime to the $w_x \approx 1$ free-streaming regime occurs smoothly over the post-shocked region. For $s \gtrsim 5 \times 10^5$ km, radiation from the shock front is sufficiently extincted that the radiation field is dominated by the flat 10 K background; accordingly, $|l_r| \to \infty$ and w_x damps to zero.

By contrast, the $t_s = 10^{-7} t_0$ case has a flat radiation field for much of the post-shock region, but a sharper one in the immediate vicinity of the shock, creating an abrupt transition between the diffusion and free-streaming regimes. Because the post-shock radiation field is stronger in this case, it propagates to a greater optical depth before decaying into the flat $T_r = 10$ K background, so the w_x damping seen in the $t_s = 10^{-1} t_0$ simulation is not visible in the plotted region. The $t_s = 10^{-4} t_0$ case represents an intermediate case between these two extremes.

4.3.3 *2D test: self-shadowing instability*

The self-shadowing or thermal wave instability (SSI; see e.g., D'Alessio et al., 1999; Dullemond, 2000; Flock et al., 2020; Watanabe and Lin, 2008; Wu and Lithwick, 2021) has been proposed as a planet-free means of generating gaps and rings in circumstellar disks. SSI begins with a disk in initial radiative and (vertical) hydrostatic equilibrium. A small perturbation to the disk's radial $\tau_r = 1$ surface would create slightly raised regions which absorb more stellar irradiation, and lowered, obscured regions which absorb less. To maintain hydrostatic equilibrium, the raised regions would increase in scale height (and thus absorb even more starlight), while the lowered ones would decrease in scale height and absorb even less.

SSI is readily reproduced in 1+1D simulations that parametrize the vertical extent of a disk (e.g., Ueda, Flock, and Birnstiel, 2021). It can also be generated (e.g., Ueda, Flock, and Okuzumi, 2019) by an iterative procedure that first uses radiative transfer to obtain a disk's temperature profile, given its density structure; assuming hydrostatic equilibrium, this profile is then used to recompute the density structure for the next iteration.

However, Melon Fuksman and Klahr (2022) find that this picture breaks down with additional physics: in their two-temperature radiation hydrodynamics simulations, SSI bumps do not grow from noise, and decay rapidly even when artificially introduced via the aforementioned iterative procedure. They explain their results by arguing that the erosion of perturbations at the $\tau_r = 1$ surface—caused by in-plane radiation transport and the hydrostatic adaptation of the gas in the upper disk—occurs on timescales much faster than the classical vertical radiative heating timescale of the disk (Hubeny, 1990; Zhang and Zhu, 2020; Zhu et al., 2015)

$$t_{\mathrm{SSI,rad}} = \frac{3(\tau_v + \tau_v^{-1})(\Sigma_d c_d + \Sigma_g c_g)}{4 c a_r (T_{\mathrm{irr}}^2 + T_{\mathrm{d,mid}}^2)(T_{\mathrm{irr}} + T_{\mathrm{d,mid}})} \tag{106}$$

where $\tau_v = \kappa_d(\Sigma_d/2)$ is the *vertical* optical depth of the disk to the midplane in thermal infrared, Σ_d and Σ_g are the dust and gas surface densities, T_{irr} is the equilibrium temperature of the stellar irradiation field in the optically thin region of the disk, and $T_{\mathrm{d,mid}}$ is the dust midplane temperature. Physically, this means that bumps at the optical surface decay long before they can impact the temperature at the disk surface.

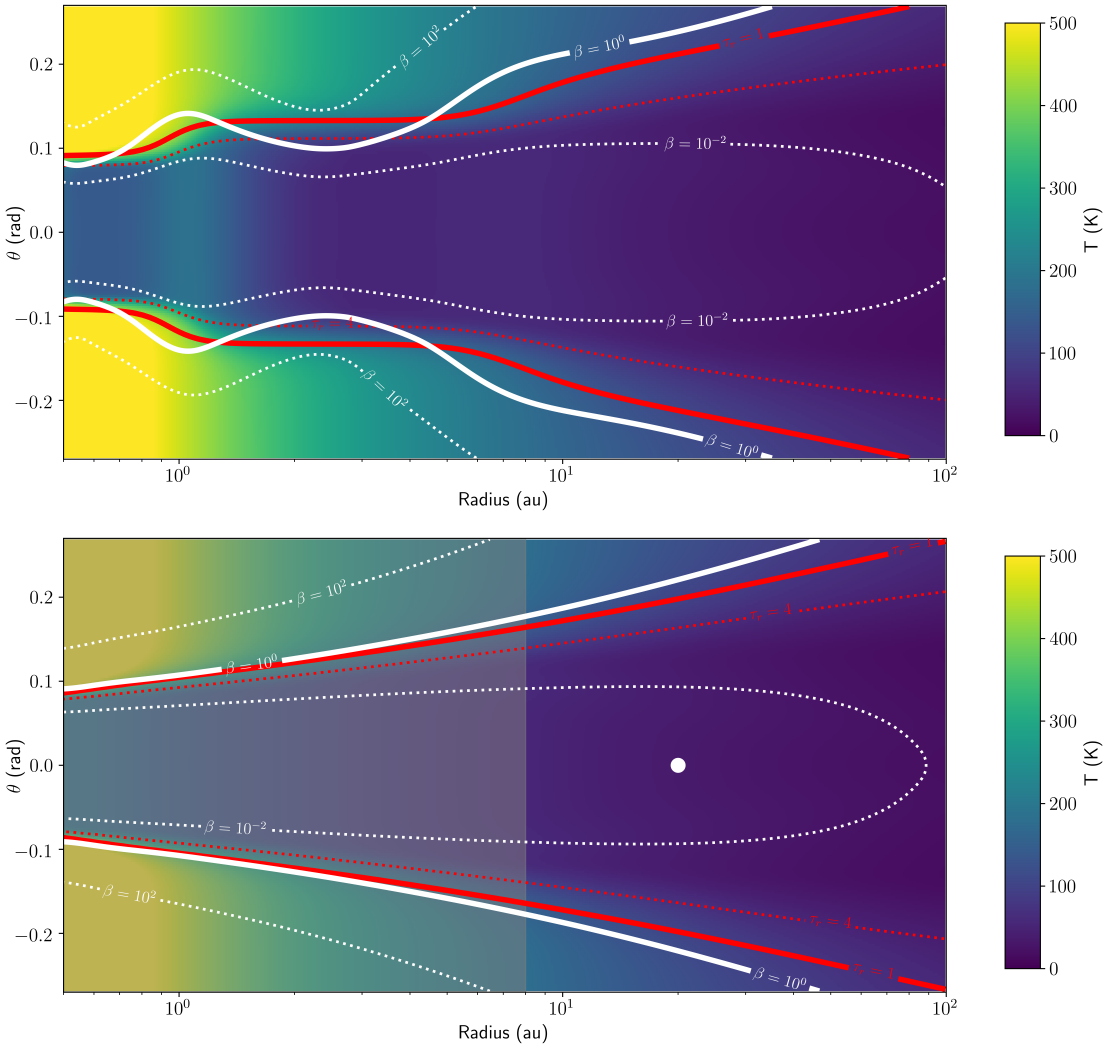

Figure 17: *Above*, initial $T_d = T_g$ for our 2D self-shadowing test (4.3.3), based on `dg3t100` from (Melon Fuksman and Klahr, 2022); *below*, the same for our 3D planet-driven spiral test (4.3.4), based on `dg3t0.1`. We overplot contours for radial optical depth τ_r *(red)* (computed using opacities Planck-averaged over the stellar spectrum) and cooling parameter $\beta \equiv t_c\Omega$. Our calculations of these quantities assume an MRN distribution of small silicon-graphite grains, and a $1M_\oplus$ classical T Tauri star as the source of light and gravity. In the lower plot, a white dot indicates the position of the embedded $1M_J$ planet, while grey shading covers the region outside the $r = [8, 100]$ au boundaries of our 3D simulation.

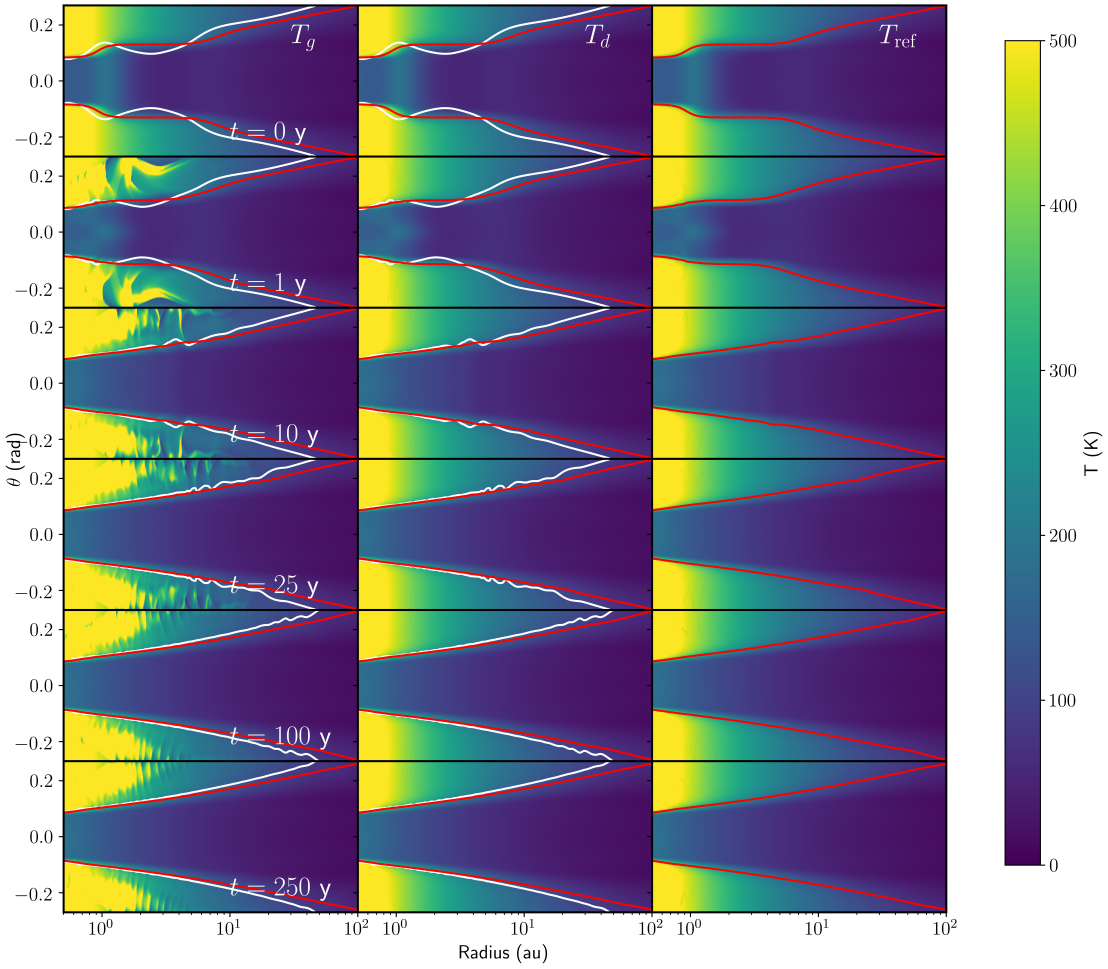

Figure 18: Two-dimensional temperature profiles from our SSI tests. The T_g *(left)* and T_d *(middle)* columns come from our simulations with realistic t_s, whereas T_{ref} *(right)* is from our reference simulations with $t_s = (2\pi)^{-1} \times 10^{-10}$ y. For ease of interpretation, we overplot $\beta = 1$ *(white)* and $\tau = 1$ *(red)* surfaces. The reference disk relaxes rapidly to a smooth hydrostatic configuration; the bulk of the realistic disk does so as well, although differences persist in the slowly-cooling disk atmosphere.

A nonzero coupling time between gas and dust temperatures would allow a temperature perturbation at the $\tau_r = 1$ surface to establish itself in the underlying disk column by propagating only through the dust—a much faster process than that implied by equation (106), in which the gas and dust are heated together. The subsequent adaptation of the gas's vertical structure to this already-established background would conform better to the assumptions of iterative methods which have been successful in reproducing the SSI. Moreover, such a coupling time would delay the response of the perturbed $\tau_r = 1$ gas to in-plane radiation transport, limiting the radial diffusion of SSI bumps. We emphasize that nothing about this prediction accounts for the effects of nonzero coupling times between dust and gas *velocities* on the evolution of the SSI, a topic which we defer to future work.

In the context of protoplanetary disks, a realistic coupling time may be found by computing t_s with the Epstein drag law (see e.g., Melon Fuksman, Flock, and Klahr, 2023; Speedie, Booth, and Dong, 2022)

$$t_s = \frac{\rho_{dg} \left\langle a_{dg}^3 \right\rangle}{\rho_g v_{th} \left\langle a_{dg}^2 \right\rangle} \tag{107}$$

where ρ_{dg} is the bulk density of each dust grain and $v_{th} = \sqrt{8\pi k_B T_g / \mu m_H}$ is the gas thermal velocity. A quantity in angle brackets $\langle g(a_{dg}) \rangle$ represents the integral of that quantity over the (normalized) grain size distribution $n(a)$:

$$\langle g(a_{dg}) \rangle = \int_{a_{min}}^{a_{max}} g(a') n(a') da' \tag{108}$$

For our three-temperature tests of the SSI, we use the setup `dg3t100` from Melon Fuksman and Klahr (2022), generated with the aforementioned iterative procedure, as the basis for our initial conditions. We employ a reduced speed of light $\hat{c} = 10^{-3} c$; our tests at $\hat{c}' = 5\hat{c} = 5 \times 10^{-3} c$ (not shown) yield converged results. The gas follows an ideal equation of state—with an adiabatic index $\gamma = 1.41$ and a mean molecular weight $\mu = 2.3$. We assume a total dust fraction of 1%, of which 10% by mass ($f_d = 10^{-3}$) are taken to be small grains relevant to the gas's thermal evolution. These grains are taken to consist of 62.5% silicate and 37.5% graphite, with a bulk density $\rho_{gr} = 2.5\ \mathrm{g\,cm^{-3}}$ and a specific heat capacity $c_d = 0.7\ \mathrm{J\,g^{-1}\,K^{-1}}$; their sizes follow a classical MRN (Mathis, Rumpl, and Nordsieck, 1977) distribution, $n(a) \propto a^{-3.5}$, with $a_{min} = 5$ nm and $a_{max} = 250$ nm. [2]

From these grain properties, we compute a temperature-dependent, frequency-integrated dust opacity $\kappa_D(T_d)$, based on the tabulated frequency-dependent figures by Krieger and Wolf (2020, 2022) as well as t_s. We additionally bracket the dust stopping time to lie within $[10^{-10}/2\pi, 10^{1}/2\pi]$ years, and take $T_g \to \max(T_g, 10\ \mathrm{K})$ for the purpose of computing v_{th}. We assume a classical T Tauri star with $M_* = 1 M_\odot$, $R_* = 2.0865 R_\odot$, and

2 With the MRN distribution, $\left\langle a_{dg}^3 \right\rangle / \left\langle a_{dg}^2 \right\rangle = \sqrt{a_{min} a_{max}} = 35.4$ nm, and dust fraction $f_d \propto \sqrt{a_{max}/a_{min}} - 1$. With these relations, it can be shown that the gas cooling time t_c (equation 133) converges to a fixed limiting value as long as $a_{max} \gg a_{min}$. Physically, this means that collisional energy exchange is dominated by the smallest grains.

$T_* = 4000$ K, to compute the dust irradiation source term S_d as well as the gravitational potential

$$\Phi_* = -\frac{GM_*}{r_*} \tag{109}$$

where $r_* \equiv ||\vec{x} - \vec{x}_*||$ is the distance between the star and a given point in the domain. We plot the resulting initial condition, as well as relevant contours for radial optical depth τ_r and gas cooling parameter $\beta \equiv t_c\Omega = (2/3)(\gamma-1)^{-1}f_d^{-1}t_s\Omega$, in the upper panel of Figure 17. We emphasize that our β-cooling parameter reflects only gas-grain collisions; because we self-consistently model radiative transfer, we do not incorporate assumptions about time or length scales for radiative diffusion or optically thin cooling, as in some previous work (e.g., Bae, Teague, and Zhu, 2021b).

We run our SSI simulation in 2D axisymmetric polar coordinates, with radial limits at $r = [0.4, 100]$ au and polar limits at $\theta = \pi/2 + [-0.23, 0.23]$. This domain is spanned by $\{N_r, N_\theta\} = \{512, 170\}$ grid cells, logarithmically spaced in the radial direction and uniformly spaced in polar angle. At the boundaries, all fields are set equal to those in `dg3t0.1`, the fiducial smooth hydrostatic setup in Melon Fuksman and Klahr (2022). We also include a damping zone in the region $\{r < r_{\rm damp,in}\} \cup \{p < 0\}$, where $r_{\rm damp,in} = 0.5$ au and $p \equiv -|\theta - \pi/2| + 0.12 + 0.13(r/\text{au})$. In this zone, we enforce $T_d = T_g$, while relaxing ρ and $\vec{v}$ to their smooth hydrostatic values on a timescale

$$t_{\rm damp} = 0.1\Omega(r)^{-1}\cos^2\left[\pi/2(1 + p/p_+)\right] \tag{110a}$$

in the region where $s < 0$, and

$$t_{\rm damp} = 0.1\Omega(r)^{-1}\cos^{-2}\left[\pi/2\left(\frac{r - r_{\rm in}}{r_{\rm damp,in} - r_{\rm in}}\right)\right] \tag{110b}$$

elsewhere in the damping zone; we have tested alternative damping prescriptions and found no substantive change to our results. For comparison with the two-temperature regime, we also run a simulation with a fixed global stopping time $t_s = (2\pi)^{-1} \times 10^{-10}$ y, but otherwise identical.

In Figure 18 we plot T_d and T_g from our realistic three-temperature simulation, as well as the matter temperature $T_{\rm ref}$ in the two-temperature reference simulation, at $t = \{0, 1, 10, 100\}$ y. In the reference simulation, the initial scale-height perturbations at the $\tau_r = 1$ surface dissipate rapidly, and are almost completely absent by $t = 10$ y, reproducing the results of the equivalent two-temperature runs in Melon Fuksman and Klahr (2022). Our three-temperature realistic simulation, in which $\beta \approx 1$ at the $\tau_r = 1$ surface, shows a similar evolution, as T_g still evolves too fast to achieve the smooth, columnar hydrostatic adaptation obtained in 1+1D and iterative approaches that reproduce the SSI. To better understand this temperature evolution, we plot in Figure 19 the time evolution of T_d, T_g, and $T_{\rm ref}$—normalized by the final, relaxed reference temperature $T_{\rm relax}$—in a fiducial disk column at $r = 2$ au.

By $t = 10^2$y, the temperature profile within the $\tau_r = 1$ surface of the realistic simulation has largely reached the same smooth equilibrium as in the reference. The slow-cooling disk atmosphere in the realistic case—heated by waves emitted by the disk's initial relaxation and reflecting off the boundaries—is too low in density and optical depth to substantively alter this picture. It remains an open question to what extent

three-temperature methods can sustain the SSI. In this regard, our numerical experiments with a dust-gas coupling time artificially increased by 100× (described in Appendix A.2) show some promise, allowing SSI waves to survive and propagate inward for roughly $\sim 10^2$ y before decaying.

4.3.4 *3D test: planet-driven spirals*

In recent years, high-resolution observations in NIR (e.g., Benisty et al., 2015; Wagner et al., 2019; Xie et al., 2021) and in various molecular lines (e.g., Teague et al., 2019; Wölfer et al., 2021) have revealed spiral structures in circumstellar disks. It is hypothesized that some fraction of these are driven by embedded, planetary-mass companions (Goldreich and Tremaine, 1978, 1979, 1980; Goodman and Rafikov, 2001).

Early simulations of these spirals (e.g., Kley, 1999) often used two-dimensional, vertically averaged setups, with a locally isothermal equation of state. Subsequent advances in computational power made it feasible to run disk-planet interaction simulations in full 3D (e.g., Dong, Fung, and Chiang, 2016; Fung and Dong, 2015), relax the assumption of local isothermality (Zhu et al., 2015), and implement realistic vertical temperature structures (Juhász and Rosotti, 2018)—which, in turn, enabled meaningful comparisons of simulated spirals to observations in dust (Dong and Fung, 2017) and gas (Muley, Dong, and Fung, 2021). More recently, Bae, Teague, and Zhu (2021b) used a parametrized cooling prescription to include the effects of matter-radiation interaction and gas-grain collisions. In what follows, we build on these previous works by modeling spirals with self-consistent, three-temperature radiation hydrodynamics.

For this test, we use the relaxed hydrostatic setup `dg3t0.1` from Melon Fuksman and Klahr (2022) as a starting point. The dust properties, stellar parameters, and cooling prescription are the same as in section 4.3.3, and we plot our initial condition, as well as the resulting contours for β and τ_r, in the lower panel of Figure 17. For this test, we use a $\hat{c} = 10^{-4}c$. Our simulation is run in 3D spherical coordinates, with radial boundaries at $r = [8, 100]$ au, polar boundaries at $\theta = \pi/2 + [-0.27, 0.27]$, and azimuthal boundaries at $\phi = [0, 2\pi]$; this simulation box is covered by $\{N_r, N_\theta, N_\phi\} = \{234, 54, 583\}$ cells, logarithmic in radius and uniform in azimuthal and polar angle. All fields are fixed to their initial values at the radial and azimuthal boundaries, and periodic at the azimuthal boundary.

In addition to the star and its gravitational potential Φ_*, our simulation includes a $q \equiv M_p/M_* = 10^{-3}$ planet ($M_p \approx 1.05 M_J$), fixed on a circular Keplerian orbit with semimajor axis $a_p = 20$ au; given our temperature profile, this is $q_{th} = 5.5$ times the thermal mass. The planetary potential is given, following Klahr and Kley (2006), by

$$\Phi_p = -\frac{GM_p}{r_p} \begin{cases} 1 & \text{if } r_p \geqslant r_s \\ ([r_p/r_s]^4 - 2[r_p/r_s]^3 + 2[r_p/r_s]) & \text{if } r_p < r_s \end{cases} \tag{111}$$

where $r_p \equiv \|\vec{x} - \vec{x}_p\|$ is the distance between the planet and a point in our domain, and r_s is the smoothing length, implemented to avoid a singularity in the potential. In our simulations, we set $r_s = r_H/2$.

To avoid unphysically shocking the disk at early times, we introduce this companion at $t_i = 1$ y and grow it from zero to its final mass over the following $t_{grow} = 10$ y. We solve our equations in the planet's co-rotating frame, fixing its azimuthal coordinate

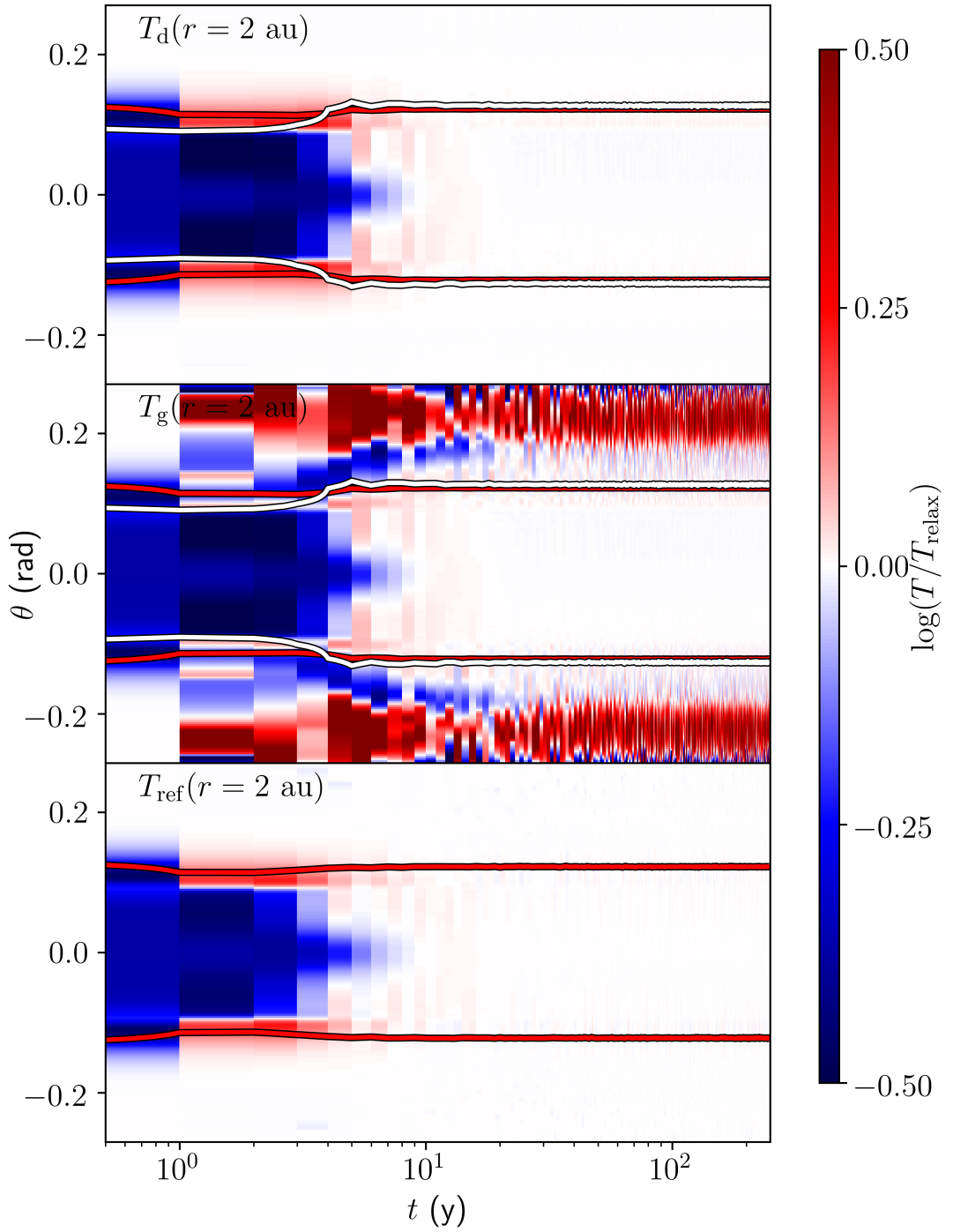

Figure 19: Time evolution of T_d *(top)*, T_g *(center)*, and T_{ref} *(bottom)* in a disk column at the fiducial $r = 2$ au, as compared to the final, relaxed state of T_{ref}. As in Figure 18, we plot the $\tau_r = 1$ optical surface in red and the $\beta = 1$ cooling surface in white. T_{ref}, as well as T_d and T_g, rapidly relax to a smooth equilibrium disk inside the $\beta = 1$ surface. Sound waves in the upper atmosphere—excited by the initial relaxation of the disk—are visible in T_g due to the slow cooling rate at high altitude.

as $\phi_p = \pi/4$. In this frame, the pattern speed of the spiral, and consequently of the non-axisymmetric radiation field, is zero; deviations would be of order $c_s \approx 10^{-6}c \approx 10^{-2}\hat{c}$. Numerical tests at $\hat{c}' = 2 \times 10^{-5} = \hat{c}/5$, not shown here, yield a well-converged spiral amplitude. To prevent the growth of large-scale disk instabilities such as the Rossby wave instability RWI Lovelace and Romanova, 2014, we include a kinematic viscosity $\nu = \alpha c_s^2 \Omega^{-1}$, where $\alpha = 0.001$ is the Shakura and Sunyaev (1973) viscosity parameter. As in section 4.3.3, we run a three-temperature realistic simulation, as well as an otherwise-identical reference simulation with $t_s = (2\pi)^{-1} \times 10^{-10}$ y.

To keep focus on the spirals, we analyze the snapshot at $t_{cut} = 500$ y, before our super-thermal planet has had the chance to carve a gap in the disk. In Figure 20, we present gas densities in our three-temperature realistic (ρ_{gas}) and two-temperature reference (ρ_{ref}) simulations, taken at $r = 30$ au and $\theta = \{0, 0.15, 0.2\}$. At $\theta = 0$, the primary and secondary Lindblad spirals are visible in both ρ_{gas} and ρ_{ref}, and agree to within several percent. This is expected, because the three-temperature midplane $\beta \lesssim 10^{-2}$ and reference simulation global $\beta \lesssim 10^{-11}$ are both much shorter than the spiral-crossing timescale, $\beta_{spiral} \approx (h/r)|1 - \Omega_p/\Omega_{30}|^{-1}$ (Sturm, Rosotti, and Dominik, 2020) where Ω_{30} is the Keplerian frequency at 30 au. In the upper disk, the realistic $\beta \approx 1$ exceeds β_{spiral}, while the reference β remains unchanged. Due to this difference in thermal physics, the density structures become discrepant at the $\sim 20\%$ level, with Lindblad spirals being more sharply defined in ρ_{ref} than in ρ_{gas}.

In Figure 21, we plot temperatures at the same cuts studied in Figure 20. In the midplane of our three-temperature simulation, strong dust-gas coupling ensures that T_d and T_g are equal. At $\theta = 0.15$, dust-gas coupling is somewhat weaker, with a $\beta \approx 10^{-1} \approx \beta_{spiral}$, and differences between T_d and T_g are visible throughout the azimuthal extent of our cut. High in the disk atmosphere, at $\theta = 0.2$, the normalized cooling time is $\beta \approx 1$, much longer than the spiral-crossing timescale for gas. Here, we observe a spiral feature in T_g with an amplitude ~10%—comparable to that found the $\beta = 1$, $M_p = 400 M_\oplus$ spiral simulation in Muley, Dong, and Fung (2021)—which is not visible in T_d or T_{ref}.

At $\theta = 0$, we observe a slight temperature dip centered at $\phi = \phi_p = \pi/4$, while at $\theta = 0.15$ and $\theta = 0.2$, we find a temperature bump at the same azimuthal position. This is ultimately caused by the gravitational influence of the planet, which lowers the $\tau_r = 1$ surface overhead and thus changes the illumination of material in the radial band $\phi \approx \phi_p$, $r \gtrsim r_p$. Such a feature was also observed in the Monte Carlo radiative transfer post-processing of Muley, Dong, and Fung (2021)'s hydrodynamical simulations.

To provide a more visual understanding of these results, we present 2D polar cuts of T_d, T_g, and T_{ref}, at $\theta = 0.0$ and $\theta = 0.2$, in Figure 22. We find, as in our 1D quantitative plots, that the morphology of T_{ref} largely agrees with that of T_d, despite substantial differences in β between and within each simulation, while T_g and T_d only agree with one another when $\beta < \beta_{spiral}$. We interpret this to imply that T_d is set by the very short timescales for *dust* collisional energy exchange $t_{c,dust} = r_{gd}^{-1} t_c$ (following equation 85) and for radiative cooling, either vertically or in-plane (Miranda and Rafikov, 2020a; Ziampras, Kley, and Dullemond, 2020). How T_g, in turn, reacts to the dust depends on the much longer local gas cooling time $t_c = \beta/\Omega$—a result that could affect the observational signatures disk-planet interaction produces in gas and dust. We note, in

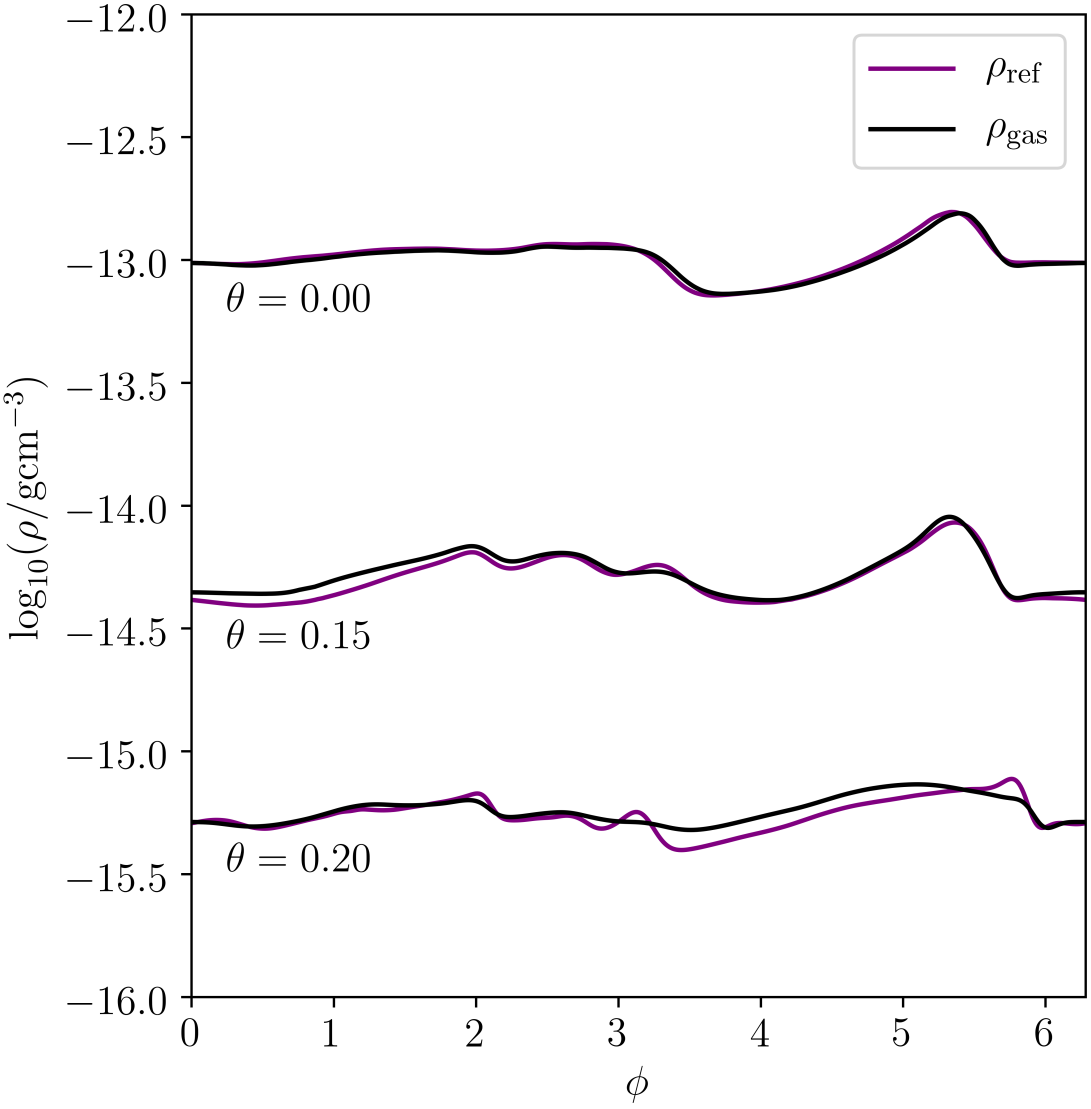

Figure 20: Density values for our three-temperature realistic (ρ_{gas}) and reference (ρ_{ref}) simulations, taken at the indicated θ values at a fixed $r = 30$ au. Densities largely agree to within a few percent between both models, but the discrepancy rises to $\sim 20\%$ at the $\tau_r = 1$ surface, causing a mild impact on the temperature structure below.

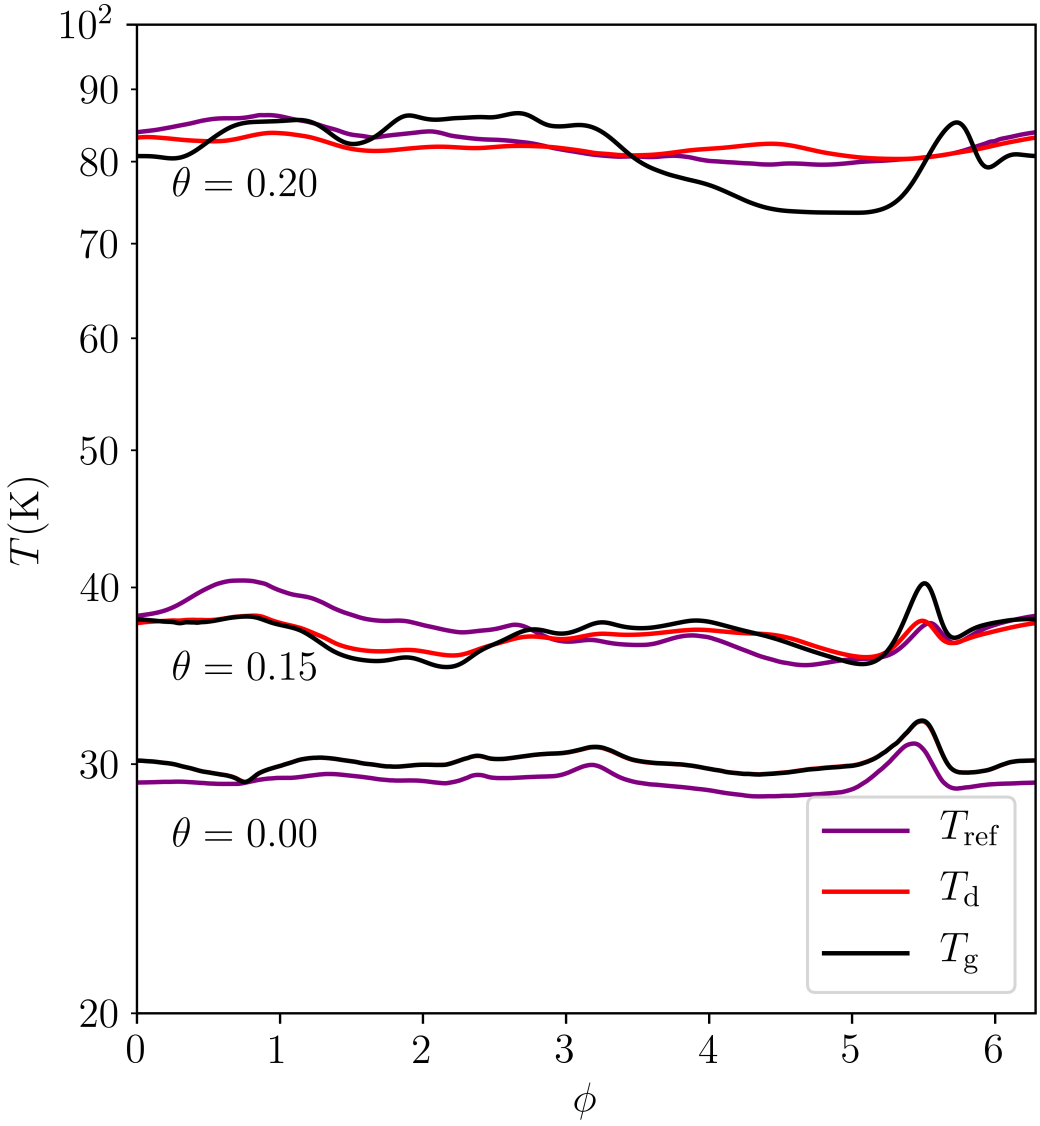

Figure 21: Temperatures in our three-temperature realistic (T_{gas}, T_{dust}) and reference (T_{ref}) simulations, taken at the same cuts as in Figure 20. In the midplane, where coupling times are short, $T_{gas} = T_{dust}$, but in the disk atmosphere, where coupling is weaker, there is a noticeable (~ 10%) discrepancy between the two: T_{dust} reflects the stellar irradiation field, while T_{gas} is driven by the PdV work done by the planetary spiral.

addition, a slight discrepancy between the background T_{dust} and T_{ref}, with the latter being systematically lower throughout the disk; this is because spirals are more vertically extended in the two-temperature limit, and so cast stronger shadows throughout the disk. We intend to investigate these issues further in a future study.

4.4 CONCLUSION

We have developed an implicit-explicit (IMEX) numerical scheme for the PLUTO hydrodynamics code to self-consistently model energy exchange between gas, dust, and radiation. The implicit substep, consisting of nonrelativistic matter-radiation interaction source terms, is solved iteratively with a multidimensional Newton-Raphson method, whereas the explicit substep, consisting of radiation transport and relativistic interaction source terms, is solved using a Godunov scheme, following Melon Fuksman and Mignone (2019). Because this explicit part is Courant-limited, we use the reduced speed of light approximation, as implemented by Melon Fuksman et al. (2021), to improve computational efficiency. This gives physically reasonable results, so long as the reduced speed of light $\hat{c}$ is much larger than all other relevant velocities in the problem.

In our 0D matter-radiation coupling test, we demonstrate the ability of our scheme to reproduce the "two-temperature" regime of traditional radiation hydrodynamics, where dust and gas are well-coupled. For the 1D Ensman (1994) shock tube test, we relax this assumption, and investigate the behavior of gas, dust, and radiation temperatures in different coupling regimes. Our subsequent tests illustrate the applicability of three-temperature radiation hydrodynamics to active problems in circumstellar disk research, including realistic opacities and dust-gas coupling times computed from local temperature and density. Our 2D test shows that the self-shadowing instability—which arises in 1+1D time-dependent models with parametrized disk scale height, as well as 2D iterative techniques that alternate the calculation of radiative and hydrostatic equilibrium—decays rapidly in the two-temperature limit, as well as with realistic three-temperature coupling times, in line with previous expectations (Melon Fuksman and Klahr, 2022). However, an increased cooling time (Appendix A.2) allows dust temperatures in most of the disk column to rapidly adapt to stellar irradiation before the gas can react—which better satisfies the key assumptions of the aforementioned iterative and 1D-hydrostatic methods, and so allows SSI-type scale-height perturbations to survive for somewhat longer before decaying. In our 3D spiral simulations, dust temperatures are remarkably consistent between the two- and three-temperature regimes, but gas temperatures disagree in the upper atmosphere—a result with implications for observations of spirals in gas tracers such as ^{12}CO. Future potential applications of our three-temperature scheme include studies of circumplanetary disk accretion shocks, planetary gap opening, photoevaporation, and hydrodynamic/MHD instabilities such as the vertical shear instability, among many others.

Our scheme makes the simplifications that dust and gas move at the same velocity, and that dust inertia is negligible ($\mathrm{St} \equiv t_s \Omega \ll 1$, $f_d \ll 1$). While these are reasonable assumptions for the sub-μm grains that supply most of a disk's total opacity and set its overall thermal structure, they are invalid for the millimeter grains that concentrate at pressure maxima and produce much of its continuum emission. Including such grains would require accounting for multispecies momentum transfer including back-reaction

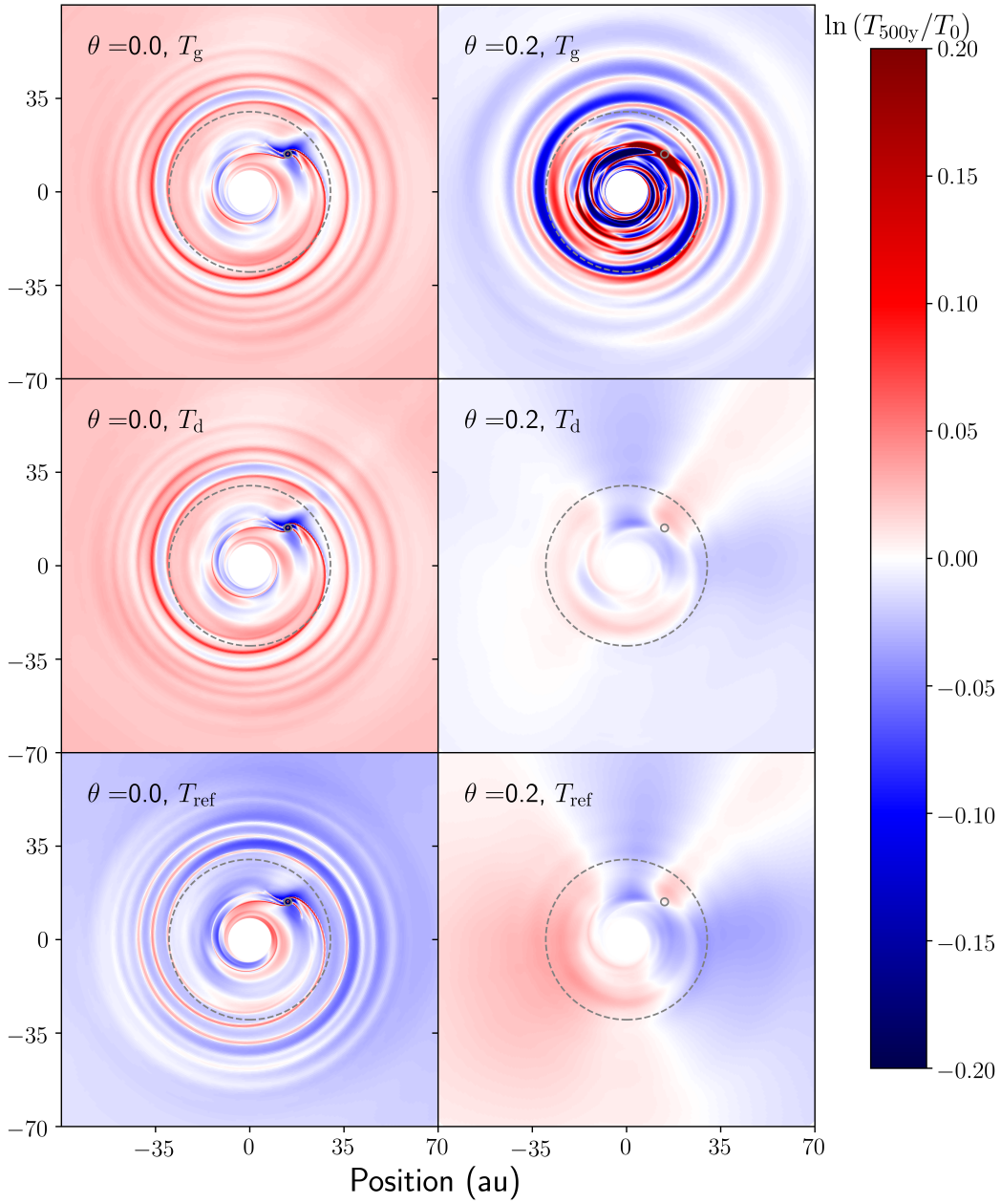

Figure 22: Relative difference between the temperature at t_{cut} = 500 y and the initial profile, in polar cuts at θ = 0.0 and θ = 0.2. The morphology of T_d and T_g agree in the midplane, but diverge at higher altitude, while the morphology of T_d and T_{ref} agree everywhere. In each panel, we indicate the Hill sphere of the planet with a small *solid grey* circle, and our cuts in figures 20 and 21 with a large *dotted grey* circle.

from the gas (using schemes such as those detailed in e.g., Benítez-Llambay, Krapp, and Pessah, 2019; Huang and Bai, 2022) and thermal coupling . While such a method would be immensely helpful in interpreting continuum observations of gaps, rings, and spirals, it would be computationally demanding and require extensive testing beyond the scope of this work.

5

THERMAL AND KINEMATIC SIGNATURES OF ACCRETING PROTOPLANETS

This chapter is adapted from the publication of Muley, Melon Fuksman, and Klahr (2024b).

In circumstellar disks around young stars, the gravitational influence of nascent planets produces telltale patterns in density, temperature, and kinematics. To better understand these signatures, we first performed 3D hydrodynamical simulations of a 0.012 $M_\odot$ disk, with a Saturn-mass planet orbiting circularly in-plane at 40 au. We tested four different disk thermodynamic prescriptions (in increasing order of complexity, local isothermality, β-cooling, two-temperature radiation hydrodynamics, and three-temperature radiation hydrodynamics), finding that β-cooling offers a reasonable approximation for the three-temperature approach when the planet is not massive or luminous enough to substantially alter the background temperature and density structure. Thereafter, using the three-temperature scheme, we relaxed this assumption, simulating a range of different planet masses (Neptune-mass, Saturn-mass, Jupiter-mass) and accretion luminosities (0, $10^{-3} L_\odot$) in the same disk. Our investigation revealed that signatures of disk-planet interaction strengthen with increasing planet mass, with circumplanetary flows becoming prominent in the high-planet-mass regime. Accretion luminosity, which adds pressure support around the planet, was found to weaken the midplane Doppler-flip, potentially visible in optically thin tracers like $C^{18}O$, while strengthening the spiral signature, particularly in upper disk layers sensitive to thicker lines, like those of ^{12}CO.

5.1 INTRODUCTION

The high spectral and spatial resolution of the Atacama Large Millimeter Array (ALMA) have made it possible to accurately probe temperatures and velocities at the $\tau = 1$ surfaces of various molecular lines, such as those associated with ^{12}CO, ^{13}CO, and $C^{18}O$ (Pinte et al., 2023a). Observations in systems such as HD 163296 (Pinte et al., 2018), HD 97048 (Pinte et al., 2019), TW Hya (Teague et al., 2022, 2019), CQ Tau (Wölfer et al., 2021), and Elias 2-24 (Pinte et al., 2023b)—with the background temperature and (sub-)Keplerian velocity profiles subtracted off—have revealed localized velocity kinks, as well as large-scale spiral structures in temperature and velocity. Numerical (e.g., Pérez, Casassus, and Benítez-Llambay, 2018) and analytical (e.g., Bollati et al., 2021) studies indicate that such signatures are consistent with those caused by spiral wakes (Goodman and Rafikov, 2001) launched at Lindblad resonances in the disk, where the Doppler-shifted planetary forcing frequency equals the local epicyclic frequency (e.g., Goldreich and Tremaine, 1978, 1979).

For computational efficiency and ease of interpretation, simulations of disk-planet interaction have historically used a 2D, vertically-integrated approach, with the gas

following a locally isothermal equation of state. But as the quality of observations improve, it has become increasingly necessary to account for more detailed disk structure and thermodynamics in order to offer a meaningful comparison. Zhu et al. (2012) and Lubow and Zhu (2014) simulated 3D adiabatic disks, discovering additional spirals excited at distinct "buoyancy resonances" where the Doppler-shifted planetary forcing frequency equals the Brunt-Väisälä frequency. Lobo Gomes et al. (2015) simulated disk-planet interaction with cooling in 2D, running their simulations to gap-opening timescales with an emphasis on vortex formation at the outer pressure bump formed by the planetary gap. Zhu et al. (2015) performed global 3D simulations of planet-driven spirals with so-called "β-cooling" to a background temperature structure (with β being the ratio of cooling time to local dynamical time, Ω_K^{-1}). Juhász and Rosotti (2018) performed 3D locally isothermal prescriptions, but with a vertically stratified temperature. Miranda and Rafikov (2020a) and Miranda and Rafikov (2020b) performed high-resolution, 2D simulations of spirals with β-cooling, studying the details of angular momentum transport as cooling times varied from short (isothermal) to long (adiabatic), relative to the local dynamical time. The 3D simulations of Muley, Dong, and Fung (2021) incorporated β-cooling along with a vertically stratified temperature structure obtained from radiative-transfer simulations, while those of Bae, Teague, and Zhu (2021b) went a step further and computed β-cooling timescales at each point in the disk, based on radiative diffusion and gas-grain collision times. These studies conclude that Lindblad spirals propagate through the disk for $\beta \ll 1$ (isothermal limit) or $\beta \ll 1$ (adiabatic limit), but damp close to the planet location for $\beta \approx 1$. Temperature stratification also causes the pitch angle and morphology of these spirals to deviate from the 2D, vertically-averaged expectation, particularly at the high altitudes amenable to observations.

In addition to parametrized cooling, radiation-hydrodynamic techniques have also been used in the context of disk-planet interaction. A number of works (e.g., Chrenko and Nesvorný, 2020; Fung et al., 2017; Kley, Bitsch, and Klahr, 2009; Lega et al., 2014; Yun et al., 2022) have concentrated on planetary torques and migration, while others (e.g., Chrenko and Lambrechts, 2019; Klahr and Kley, 2006; Szulágyi, 2017) have focused on flows in the circumplanetary region. These have typically employed a one-temperature (1T; Kley, 1989) scheme—in which gas and radiation are assumed to have the same temperature—or a more involved two-temperature (2T; Bitsch et al., 2013) scheme in which matter and radiation have separate temperatures, coupled by opacity. For the transport of radiation, these simulations have used flux-limited diffusion FLD; Levermore and Pomraning, 1981 approaches to solving the governing equations, including various parametrizations for stellar irradiation. The high-resolution 2D simulations of Ziampras, Nelson, and Rafikov (2023), using the two-temperature FLD scheme outlined in (Ziampras, Kley, and Dullemond, 2020), gave more emphasis to the morphologies of spirals themselves. Their work found that transport of energy across the spiral shock (Commerçon et al., 2011; Ensman, 1994) shifts and broadens the spiral temperature perturbation in ways that an inherently local, β-cooling approximation cannot. Concurrently, Muley, Melon Fuksman, and Klahr (2023) ran 3D simulations with M1 radiation transport (Levermore, 1984; Melon Fuksman and Mignone, 2019) and ray-traced stellar irradiation, as a test of their "three-temperature" (3T) approach, in which gas, grains, and radiation coupled by collisions and opacity. In both two- and

three-temperature simulations, they found weaker pre-shock heating than in Ziampras, Nelson, and Rafikov (2023), potentially attributable to a lower disk mass enabling efficient vertical cooling (Ziampras 2023, private communication).

In this work, we build on these previous disk-planet simulations using our 3T method, with the aim of better connecting kinematic and thermal spiral signatures to the properties of the planets driving them. In Section 2, we describe our methods, including our thermodynamic prescriptions, treatment of planetary accretion luminosity, and disk initial conditions. In Section 3, we discuss the spiral structure, flow patterns, and background temperature created by a non-accreting, Saturn-mass planet orbiting at 40 au in the disk, testing disk-planet interaction under four different thermodynamic prescriptions (local isothermality, physically motivated β-cooling, two-temperature radiation hydrodynamics, and three-temperature radiation hydrodynamics). In Section 4, we run three-temperature simulations only, measuring the effects of changing mass and accretion luminosity. In Section 5, we present polar cuts of temperature and sky-projected velocity high in our simulated disk, and comment on the observational implications. Finally, in Section 6, we summarize and conclude our work.

5.2 METHODS

5.2.1 *Basic equations*

For our study of spiral arms, we use a version of the `PLUTO` hydrodynamical code (Mignone et al., 2007), modified to solve the equations of radiation hydrodynamics (Melon Fuksman et al., 2021; Melon Fuksman and Mignone, 2019) with an additional dust internal energy field (Muley, Melon Fuksman, and Klahr, 2023). This field interacts thermally with the gas and radiation field, but passively traces the same velocity field as the gas without any back-reaction (implying a Stokes number $\mathrm{St} \ll 1$, as well as a globally constant dust-to-gas ratio $f_d \ll 1$):

$$\frac{\partial \rho}{\partial t} + \nabla \cdot (\rho \vec{v}) = 0 \tag{112a}$$

$$\frac{\partial (\rho \vec{v})}{\partial t} + \nabla \cdot (\rho \vec{v} \vec{v}) = -\nabla p - \rho \nabla \Phi + \vec{S}_m + \vec{G} \tag{112b}$$

$$\frac{\partial E_g}{\partial t} + \nabla \cdot (E_g \vec{v}) = -\nabla \cdot ((p + \rho\Phi)\vec{v}) + S_m + X_{gd} + cG_g + S_g^{\mathrm{irr}} \tag{112c}$$

$$\frac{\partial E_d}{\partial t} + \nabla \cdot (E_d \vec{v}) = -X_{gd} + cG_d + S_d^{\mathrm{irr}} \tag{112d}$$

$$\frac{\partial E_r}{\partial t} + \hat{c} \nabla \cdot \vec{F}_r = -\hat{c}(G_g + G_d) \tag{112e}$$

$$\frac{\partial \vec{F}_r}{\partial t} + \hat{c}\nabla \cdot \mathbf{P}_r = -\hat{c}\vec{G} \tag{112f}$$

in which $\rho, \vec{v}, p$ represent the gas density, velocity, and pressure respectively. ρ_d is the dust density, while f_d is the dust-to-gas ratio, Φ is the gravitational potential, and $\{E_g, E_d, E_r\}$ are total energy densities for gas, dust, and radiation respectively. $\vec{S}_m$ represents parabolic source terms such as α-viscosity, X_{gd} represents energy exchange between gas and dust. $\vec{F}_r$ is the radiative flux, while $\vec{P}_r$ is the radiation pressure. G_g, G_d, and $\vec{G}$ terms represent opacity-mediated interaction between the gas, dust and radiation respectively. S_g^{irr} and S_d^{irr} represent, respectively, gas and dust absorption of stellar irradiation. c represents the speed of light, whereas the $\hat{c}$ term is a "reduced speed of light" (Gnedin and Abel, 2001) which enables longer timesteps, but must nevertheless exceed all hydrodynamic velocities relevant to the problem (Skinner and Ostriker, 2013).

The opacity source terms are given by:

$$\begin{aligned} G_g \equiv & -\rho\kappa_g(a_r T_g^4 - E_r) \\ & -\rho(2\kappa_g - \chi_g)\vec{\beta}\cdot\vec{F}_r - \rho\chi_g\vec{\beta}\cdot(E_r\vec{\beta} + \vec{\beta}\cdot\mathbf{P}_r) \end{aligned} \tag{113a}$$

$$\begin{aligned} G_d \equiv & -\rho\kappa_d f_d(a_r T_d^4 - E_r) \\ & -\rho f_d(2\kappa_d - \chi_d)\vec{\beta}\cdot\vec{F}_r - \rho f_d\chi_d\vec{\beta}\cdot(E_r\vec{\beta} + \vec{\beta}\cdot\mathbf{P}_r) \end{aligned} \tag{113b}$$

$$\begin{aligned} \vec{G}_g \equiv & \rho\chi_g\vec{F}_r - \rho\kappa_g(a_r T_g^4 - E_r)\vec{\beta} \\ & -2\rho\kappa_g(\vec{\beta}\cdot\vec{F}_r)\vec{\beta} - \rho\chi_g(E_r\vec{\beta} + \vec{\beta}\cdot\mathbf{P}_r) \end{aligned} \tag{113c}$$

$$\begin{aligned} \vec{G}_d \equiv & \rho f_d\chi_d\vec{F}_r - \rho f_d\kappa_d(a_r T_d^4 - E_r)\vec{\beta} \\ & -2\rho f_d\kappa_d(\vec{\beta}\cdot\vec{F}_r)\vec{\beta} - \rho f_d\chi_d(E_r\vec{\beta} + \vec{\beta}\cdot\mathbf{P}_r) \end{aligned} \tag{113d}$$

where $\vec{G} \equiv \vec{G}_g + \vec{G}_d$ and $\vec{\beta} \equiv \vec{v}/c$ (not to be confused with the β-cooling timescale).

The solution strategy for these equations is described thoroughly in the aforementioned articles (Melon Fuksman et al., 2021; Melon Fuksman and Mignone, 2019; Muley, Melon Fuksman, and Klahr, 2023), and we recapitulate the most relevant details here. Equations (1) are divided into radiation and hydrodynamic subsystems, which are solved using a Strang split (half-step radiation, full-step hydro, half-step radiation). For the radiation subsystem, the Courant-Friedrichs-Levy (CFL) condition imposed by $\hat{c}$ is far more stringent than that imposed on the hydrodynamic subsystem by the sound speed c_s, so the radiation half-step is in turn divided into a number of substeps. Each individual substep is handled using an implicit-explicit (IMEX) strategy (Pareschi and Russo, 2005): radiation transport terms are computed explicitly using the M1 formalism to handle both the optically thick diffusion and optically thin beaming limits (Levermore, 1984), whereas the stiff G_g, G_d, $\vec{G}$, and X_{gd} source terms are solved implicitly with a Newton-Raphson method. The stellar irradiation source term S_d^{irr} is computed explicitly by ray-tracing at the start of each hydrodynamic timestep

(with S_g^{irr} set to zero in the current study); because it depends only on the density distribution, it is sufficient to simply incorporate it into the initial guess of our Newton scheme, without updating it at each iteration.

We assume that the gas follows an ideal equation of state,

$$p = \rho_g k_B T_g / \mu m_H \tag{114}$$

where k_B is the Boltzmann constant, T_g the gas temperature, μ the mean molecular weight, and m_H the mass of a hydrogen atom. The adiabatic index $\gamma \equiv \partial \ln p / \partial \ln \rho$ is a constant, implying an internal energy density

$$\xi_g = p/(\gamma - 1)\,. \tag{115}$$

We note that realistic equations of state—in which γ varies with temperature as rotational, vibrational, and dissociation modes of para- and ortho-hydrogen are activated (Boley, Morris, and Desch, 2013; Boley et al., 2007; Decampli et al., 1978)—would change Equations 114 and 115, as well as the gas-dust energy exchange term in Equation 116, and the gas-dust coupling timescale in Equation 117, in the following section.

5.2.1.1 *Three-temperature simulations*

For our three-temperature simulations, we solve the full set of Equations 112, and define the dust-gas collision term

$$X_{gd} \equiv t_c^{-1}(r_{gd}\xi_d - \xi_g) \tag{116}$$

in which t_c is the dust-gas thermal coupling time, $\xi_d = E_d$ represents the dust internal energy (equivalent in our scheme, but in general different if dust dynamics were to be accounted for), and $r_{gd} = c_g/f_d c_d$ is the ratio of heat capacity per unit volume between gas and dust. c_d is the specific heat capacity of dust, while $c_g \equiv k_B/\mu m_H(\gamma - 1)$ is that of the gas. We compute the gas cooling time t_c as a function of the dust-gas stopping time t_s, calculated in the Epstein regime (Burke and Hollenbach, 1983b; Speedie, Booth, and Dong, 2022)

$$t_c = \frac{2/3}{\gamma - 1} f_d^{-1} t_s \eta^{-1} \tag{117}$$

where we set the "accommodation coefficient" η to unity.

5.2.1.2 *Two-temperature simulations*

In our studies of the "two-temperature" regime of traditional radiation hydrodynamics, in which dust and gas are perfectly well-coupled, we set the stopping time to an artificially low $t_s = 10^{-10}$ yr.

5.2.1.3 *β-cooling simulations*

For beta-cooling simulations, we replace X_{gd} with a term of the form

$$t_{rel}^{-1} \frac{\rho k_B}{\mu m_p (\gamma - 1)} \left(T_g - T_{g,o}(r, \theta)\right) \tag{118}$$

where $T_{g,0}$ is the initial condition for gas temperature (see Section 5.2.3 for more details), $\vec{x}$ is a position in the disk and t_{rel} can in general be a function of any primitive variables. We ignore the G_g and S_g^{irr} terms, while eliminating Equations eqs. (112d) to (112f) entirely. Following Bae, Teague, and Zhu (2021b) and Melon Fuksman, Flock, and Klahr (2023), we set the thermal relaxation/cooling time

$$t_{rel} = t_c + t_{rad} \tag{119}$$

where t_c is defined as in equation 117, and t_{rad} is a radiative cooling timescale incorporating both the optically thick diffusion and optically thin free-streaming limits:

$$t_{rad} \equiv \max(\lambda_{thin}^2, \lambda_{diff}^2)/D \tag{120}$$

where the radiative diffusion coefficient $D \equiv 4ca_r T_g^3/3c_g\kappa_R\rho^2$. The effective optically thin cooling length scale $\lambda_{thin} = (3\kappa_R\kappa_P\rho^2)^{-1/2}$, while the thick diffusion length is assumed to equal the local scale height, $\lambda_{diff} \equiv H = c_{s,iso}\Omega^{-1}$, where Ω is the local Keplerian orbital frequency and $c_{s,,iso} \equiv \sqrt{p/\rho}$ the "isothermal sound speed".

5.2.1.4 *Locally isothermal simulations*

To test the locally isothermal case, we simply run a β-cooling simulation with $t_{rel} = 10^{-10}$ yr everywhere in the disk.

5.2.2 *Implementation of accretion luminosity*

We implement accretion luminosity as part of the irradiation source term, S_d^{irr}. This allows us to use the IMEX strategy discussed in Section 5.2.1 to deposit, exchange, and transport large amounts of energy into each grid cell, avoiding the numerical instabilities that would arise from an explicit approach. In this work, we model only the luminosity, without removing any mass from the grid or adding any to the planet.

We interpolate the luminosity onto the grid using a triangular-shaped cloud (TSC; e.g., Eastwood, 1986) approach, in which the kernel takes the form

$$\begin{aligned}\psi(\vec{x}, \vec{x}_p) = \max\left[\left(1 - \left|\frac{r - r_p}{\Delta r_{i_p}}\right|\right)\left(1 - \left|\frac{\theta - \theta_p}{\Delta\theta_{j_p}}\right|\right)\left(1 - \left|\frac{\phi - \phi_p}{\Delta\phi_{k_p}}\right|\right), 0\right] \\ \times\ (r^2 \sin\theta)^{-1}\end{aligned} \tag{121}$$

where $\{i_p, j_p, k_p\}$ indicate the indices in the $\{r, \theta, \phi\}$ directions of the cell in which the planet is located. The kernel intersects the cells $\{i_p \pm 1, j_p \pm 1, k_p \pm 1\}$, for a total of 27 cells; [1] the fraction of accretion energy deposited in each cell during a timestep is equal to the integral of ψ over the cell volume. TSC avoids creating spurious discontinuities in the deposited radiation field or its gradient, unlike the cloud-in-cell (CIC) or nearest grid point (NGP) methods, where moving across a cell boundary or even within a cell can cause sharp changes in these quantities.

1 This only strictly holds when the cell spacings in all directions are independent of the corresponding coordinate; in the r-direction, where $\Delta r_i \propto r_i$, it is possible for the edge of the kernel to intersect the second cell inward, r_{i_p-2}. The extent of this edge is, at most, $\Delta r_{i_p} - \Delta r_{i_p-1}$, which for our grid is always less than 1% of the kernel half-width; the integral of ψ over this intersecting edge is $< \mathcal{O}(10^{-4})$. We add this small excess to the cells $\{i_p, j_p \pm 1, k_p \pm 1\}$.

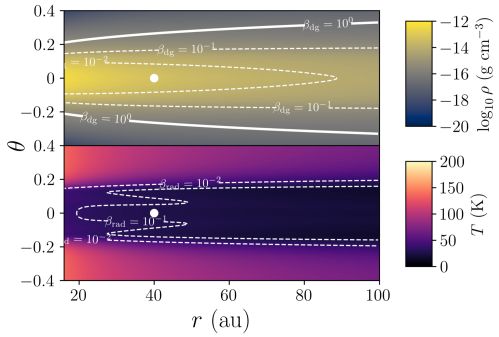

Figure 23: A plot of initial conditions for density (above) and temperature (below), obtained using the iterative procedure described in Section 5.2.3. White lines indicate the corresponding cooling-time contours, computed using Equation 119. Due to our constant dust-to-gas ratio and assumption of small dust grains throughout the disk, we obtain shorter radiative-diffusion and gas-grain coupling times than in Bae, Teague, and Zhu (2021b).

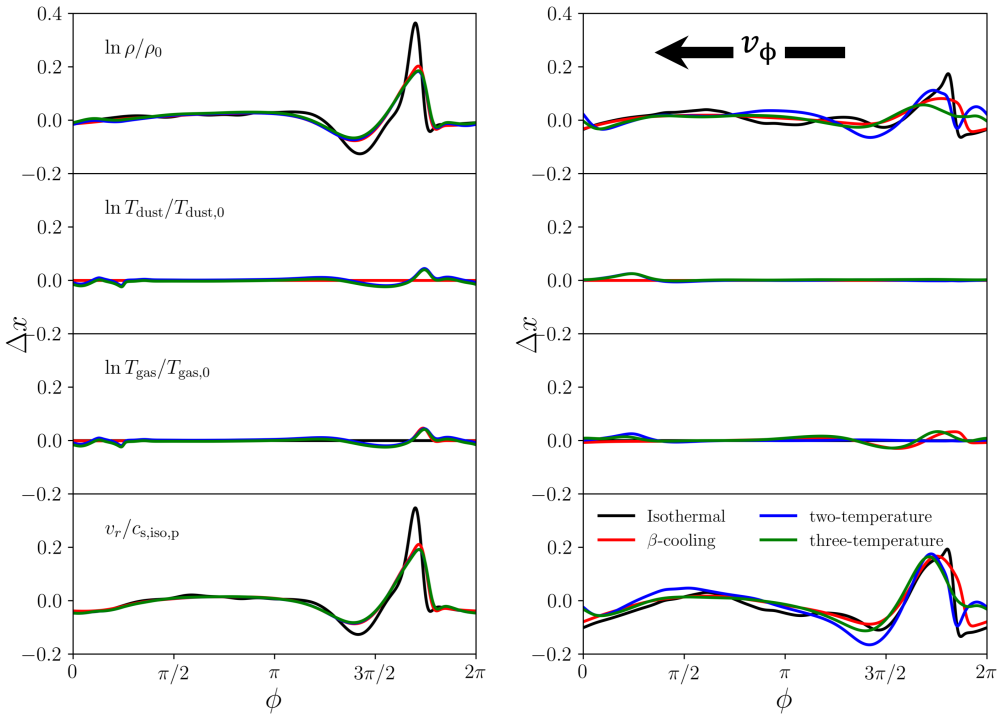

Figure 24: Relative differences in disk density, dust temperature, gas temperature, and radial velocity at $t = 2500\text{yr} \approx 10$ orbits, with respect to initial conditions for different physical prescriptions. We take azimuthal cuts over the whole 2π at fixed $r = 1.5r_p$ and $\theta = 0$ (left) and 0.2 (right) above the midplane. Dust temperatures largely agree between the two- and three-temperature cases, whereas gas temperatures largely agree between the three-temperature and β-cooling cases.

5.2.3 *Setup and initial conditions*

In all simulations presented here, we assume a disk gas surface density profile of

$$\Sigma_g = 200 \mathrm{g\,cm^{-2}} \left(\frac{R}{1\mathrm{au}}\right)^{-1} \tag{122}$$

corresponding to an $M_d = 0.012 M_\odot$ within our domain. As in our previous works (e.g., Melon Fuksman, Flock, and Klahr, 2024a,b; Melon Fuksman and Klahr, 2022), we approximate the behavior of the gas with an ideal equation of state, with adiabatic index $\gamma = 1.41$ and mean molecular weight $\mu = 2.3$ [2] The total dust-to-gas ratio is assumed to be 1%, of which we take 10% by mass (corresponding to $f_d = 10^{-3}$) to be the small grains that we model. These consist of 62.5% silicate and 37.5% graphite, with a material density $\rho_{gr} = 2.5\ \mathrm{g\,cm^{-3}}$ and a specific heat capacity $c_d = 0.7\ \mathrm{J\,g^{-1}\,K^{-1}}$; their sizes follow the MRN (Mathis, Rumpl, and Nordsieck, 1977) distribution, $n(a) \propto a^{-3.5}$, with $a_{min} = 5$ nm and $a_{max} = 250$ nm. Using the frequency-dependent opacities given by Krieger and Wolf (2020, 2022), we create tables of Planck and Rosseland opacity for this grain distribution as a function of temperature.

In order to obtain initial conditions, we employ the same iterative technique used in Melon Fuksman and Klahr (2022), cycling hydrostatic-equilibrium and radiative transfer calculations on a timescale ($t_{iter} = 0.1$ y) much shorter than thermal diffusion times through the disk. We run 1000 iterations in order to obtain a well-converged background profile, and use this profile as the initial condition for all simulations, regardless of the physics prescription implemented.

For our planet, located at $r_p = 40$ au, $\theta_p = \pi/2$, and $\phi_p = \pi/4$, this profile yields a local temperature $T_p = T_{g,0}(r = 40\mathrm{au}, \theta = \pi/2) = 26$ K and a scale-height ratio $(H/r)_p = 0.065$. We plot our initial conditions in Figure 23, along with contours for the gas-grain coupling time (on the upper density plot) and radiative cooling time (on the lower temperature plot), normalized by the local dynamical time to obtain effective β-values; in our β-cooling simulations we simply add $\beta_{dg} + \beta_{rad}$. Compared with the detailed calculations of Bae, Teague, and Zhu (2021b), who self-consistently computed grain settling, opacities, and radiative cooling rates, our assumption of globally constant dust-to-gas ratio and grain size distribution yields shorter cooling times throughout the disk. In the upper atmosphere, this is because our unsettled small grain distribution makes collisional coupling more efficient; in the midplane, the low opacities of these small grains at tens of Kelvin shortens the thermal diffusion timescale.

For all simulations presented here, we use WENO3 reconstruction, along with a van Leer limiter and shock flattening to ensure stability. Our grid resolution is $268(r) \times 116(\theta) \times 919(\phi)$, logarithmically spaced in the radial and evenly spaced in the polar and azimuthal. Our domain extends between $r = \{0.4, 2.5\} \times r_p$, $\theta = \{-0.4, 0.4\} + \pi/2$, and $\phi = \{0, 2\pi\}$. Given these dimensions, our resolution yields ~ 10 cells per scale height at the planet location, the same amount used in historical 2D and 3D simulations of planetary gap-opening (Fung and Chiang, 2016; Fung, Shi, and Chiang, 2014b), and higher than in the 3D spiral simulations of Muley, Dong, and Fung (2021), but

2 We note that within our temperature range of interest ($\approx 20 - 200$ K), γ can vary between 1.3-1.66 as rotational modes of the H_2 molecule are activted, with the exact index depending on the assumed ortho- and para-hydrogen ratio (equilibrium or some fixed fraction; see e.g., Bitsch, Boley, and Kley, 2013).

somewhat lower than in the 2D simulations of Ziampras, Nelson, and Rafikov (2023), which contains a more detailed analysis of angular-momentum fluxes and multi-gap opening induced by spirals. We use a reduced speed of light $\hat{c} = 10^{-4}c$, which Muley, Melon Fuksman, and Klahr (2023) found to work well for analogous simulations of spirals driven by planets tens of au from their host stars.

In the two-temperature case, our test simulations show that disk columns can oscillate around the midplane, with low-order azimuthal modes undergoing linear growth. Because these modes do not manifest in the isothermal and β-cooling simulations, and appear even in the absence of a planet, we tentatively attribute them to some form of irradiation (Fung, Shi, and Chiang, 2014a) or self-shadowing (e.g., Melon Fuksman and Klahr, 2022, and references therein) instability. In the three-temperature case, this effect is naturally suppressed—we surmise due to the decoupling between gas and dust temperatures at the high altitudes where stellar irradiation is intercepted. As such, for the two-temperature simulation only, we impose rapid wave-damping zones in the upper and lower regions of the domain where $|\theta - \pi/2| > 0.3$, and defer further investigation of this phenomenon to future work.

5.3 DISK PHYSICS

5.3.1 *Thermodynamic prescriptions*

In Figure 24, we plot perturbations in density ρ, gas temperature T_g, dust temperature T_d, and perturbations in radial (in center-of-mass coordinates) velocity v_r, for each of our four thermodynamic prescriptions (to recapitulate, local isothermality, β-cooling, two-temperature radiation hydrodynamics, and three-temperature radiation hydrodynamics). We take cuts of these variables at $r = 1.5r_p$ at $\theta = 0$ and $\theta = 0.2$ above the midplane, at $t = 2500$ yr. [3]

In the midplane, we find that perturbations in ρ and v_r are closely aligned with one another in ϕ. In agreement with previous results (e.g., Muley, Dong, and Fung, 2021; Zhu et al., 2015), we find these perturbations strongest in the locally isothermal simulations. Among our non-isothermal runs, perturbations in ρ, v_r, and T_g are similar regardless of whether a β-cooling, 2T, or 3T prescription is used. T_g perturbations capture the work done by compression and expansion (pdV) on a fluid parcel in the disk over one thermal relaxation time. In the midplane of our fiducial disk, this is typically comparable to or shorter than the spiral-crossing time ($\beta \lesssim 1$), so the measured T_g is relatively weak and somewhat offset in ϕ with respect to the ρ perturbation (which traces the integrated compression and expansion over a fluid parcel's orbit).

Owing to the very short dust-gas coupling time t_c in this region, T_d closely follows T_g, and likewise agrees between the two- and three-temperature setups. The β-cooling simulation, which assumes a constant background temperature, is inherently unable to capture changes in T_d. Unlike in the 2D flux-limited diffusion simulations of Ziampras, Nelson, and Rafikov (2023), we do not observe substantial radiative heating of the pre-shock region by emission from hot, post-shock gas (e.g., Ensman, 1994). This may be caused by efficient cooling through the disk surface (Ziampras 2023, private communication) in our relatively low-mass, optically thin disk.

3 Here, and throughout our analysis, θ is implied to be with respect to the midplane angle $\pi/2$.

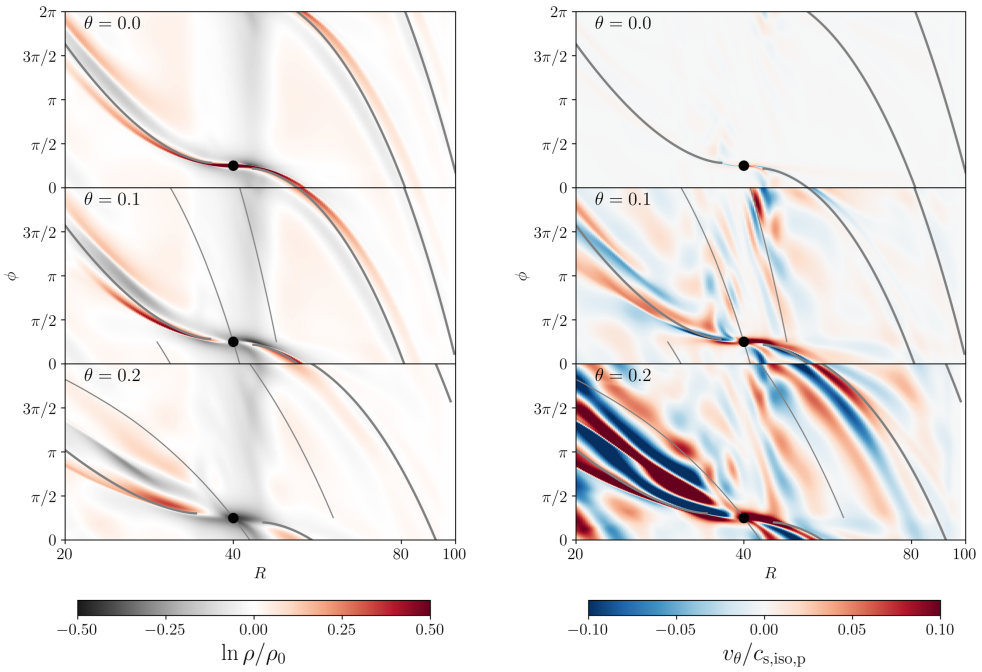

Figure 25: Plots of the density (left), indicating the planetary spirals, and meridional velocity (right), for various altitudes in the disk; phase predictions for the primary Lindblad arm (Equation 124, thick line) and $m = 3$ buoyancy arm (Equation 126, thin line) are overplotted. In all panels, cylindrical radius $R \equiv r \sin\theta$ is plotted on the x-axis and azimuthal angle θ on the y-axis. Due to the relatively rapid thermal relaxation in this simulation, buoyancy spirals are markedly weaker than Lindblad spirals in all cases.

This picture becomes somewhat more complicated at $\theta = 0.2$, where the cooling time lengthens, and becomes dominated by dust-gas decoupling rather than radiative diffusion. The ρ spiral is sharp in the locally isothermal case, but weaker in the other simulations. T_d agrees between the two- and three-temperature simulations, but the gas temperature differs, indicating that observational signatures observable in the upper disk gas (in, e.g., ^{12}CO) may not be reflected in the dust.

5.3.2 *Lindblad and buoyancy resonances*

The observed disk signatures are, in large part, driven by resonant interactions between the disk and the planet's gravitational potential. One such interaction, studied by decades of analytical and numerical work, occurs at the "Lindblad resonances", where the Doppler-shifted planetary forcing frequency times an azimuthal integer wavenumber m equals the epicyclic frequency κ (e.g., Bae and Zhu, 2018a,b; Goldreich and Tremaine, 1978, 1979, 1980; Kley and Nelson, 2012). Assuming that the disk is thin, and that the spirals are tightly wound ($k_r \gg mr^{-1}$) so the Wentzel-Kramers-Brillouin (WKB) approximation holds, we obtain the following dispersion relation:

$$m^2(\Omega - \Omega_p)^2 = \kappa^2 + c_s^2 k_r^2 \tag{123}$$

where Ω_p is the planet's orbital frequency, and k_r is the radial wavenumber of the excitation. Given that in a Keplerian disk $\kappa = \Omega \propto r^{-3/2}$, we can rewrite the above in terms of k_r and m, and integrate to find the phase of the mth spiral mode:

$$\phi_{L,m}(r) = \int_{r_m}^{r} \left[\frac{H(r')}{r'}\right]^{-1} \left[\left(1 - \frac{\Omega_p}{\Omega(r')}\right)^2 - m^{-2}\right]^{1/2} dr' \tag{124}$$

where $r_m = (1 \mp m^{-1})^{2/3} r_p$ is the resonance location. A more detailed analysis, going beyond the WKB approximation (Artymowicz, 1993; Papaloizou et al., 2007) shows that the peak mode strength occurs at approximately $m \gtrsim 2/(H/r)$, above which wave excitation becomes inefficient.

One can also perform a similar analysis on the the "buoyancy resonances", where the m-multiplied, Doppler-shifted forcing frequency equals the (vertical) Brunt-Väisälä frequency $N_z \equiv g\gamma^{-1} [\ln P/\rho^\gamma]^{1/2}$ (Lubow and Zhu, 2014). These are an inherently 3D phenomenon, depending sensitively on the disk's thermal physics prescription. Applying the thin-disk approximation that vertical gravity $g \approx \Omega^2 z$ and assuming a background in hydrostatic equilibrium, one can simplify the above to:

$$m^2(\Omega - \Omega_p)^2 = N_z^2 = \Omega^2 z \left[\frac{1}{T_{g,0}} \frac{dT_{g,0}}{dz} + \frac{\gamma - 1}{\gamma} \frac{\Omega^2 z}{c_{s,iso,0}^2}\right] \tag{125}$$

where $c_{s,iso,0} \equiv \sqrt{p_0/\rho_0}$ is the isothermal sound speed in the initial condition. Following (Bae, Teague, and Zhu, 2021b; Zhu et al., 2015), this can be used to obtain a phase angle for the spiral:

$$\phi_{B,m} = \pm 2\pi m (1 - \Omega_p/\Omega) \left[\frac{z}{T_{g,0}} \frac{dT_{g,0}}{dz} + \frac{\gamma - 1}{\gamma} \frac{\Omega^2 z^2}{c_{s,iso,0}^2}\right]^{-1/2} \tag{126}$$

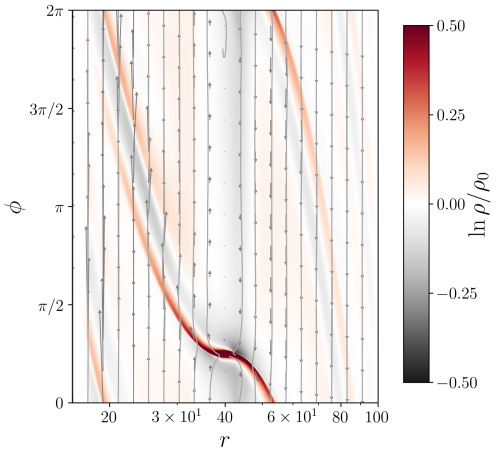

Figure 26: Midplane flow pattern in our disk, in the co-rotating frame of the planet. Streamlines proceed from bottom to top inside the planet radius $r_p = 40$au, and from top to bottom outside the planet radius.

In Figure 25 we plot the phase angles for our three-temperature simulations, density for Lindblad spirals and meridional velocities for buoyancy spirals. Lindblad spirals are clearly visible at all altitudes, but are somewhat less tightly bound than the linear WKB theory of Equation 124 would predict, given the fiducial planet's "thermal mass" $q_{th} \equiv (M_p/M_\odot)h_p^{-3}$ of 1.12. The deviation becomes stronger, and the spiral arm becomes more open, with increasing altitude (an effect also seen in the locally isothermal, temperature-stratified simulations of Juhász and Rosotti, 2018). The vertical velocity component of the Lindblad spirals also becomes more pronounced in the disk upper atmosphere, especially in the inner disk where scale height is lower than at the wave-launching location near the planet.

As expected, buoyancy spirals are only visible in the upper layers of the disk, but likewise deviate somewhat from the linear phase prediction from Equation 126. In comparison to previous works, the fact that the thermal relaxation time $\mathbf{t_{rel} \lesssim N_z^{-1}}$, even at high altitudes, acts to damp the buoyant oscillations. We surmise that they could be strengthened either through substantial dust growth/settling/depletion which would increase the gas-grain coupling time t_c, or alternatively (especially at $\theta \approx 0.1$ from the midplane, and in the inner disk) by a high dust-to-gas ratio or disk mass, which would increase the thermal diffusion time t_{diff}.

5.3.3 *Flow analysis*

We next turn our attention to the flow patterns in the disk. In Figures 26, 27, 28, we plot streamlines of the fluid flow in various disk cuts, along with quivers indicating the instantaneous flow direction (see captions for more details); in the background, we include the density perturbation for reference. Close to the midplane, velocities are essentially restricted to the $r - \phi$ direction as in 2D simulations; however, at the temperature transition, the spiral pattern weakens and bends, with the velocity acquiring a θ-component (see also e.g, Boley and Durisen, 2006, for a more general discussion of vertical spiral velocities).

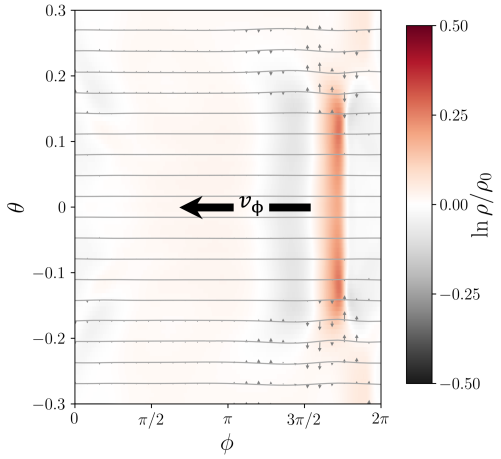

Figure 27: Flow pattern at $r = 1.5r_p = 60$au, in an azimuthal cut of the disk. Streamlines flow right to left; unlike in Figure 26, vector arrows represent velocity differences from the local initial (quasi-)Keplerian value, rather than from the planet's Keplerian speed.

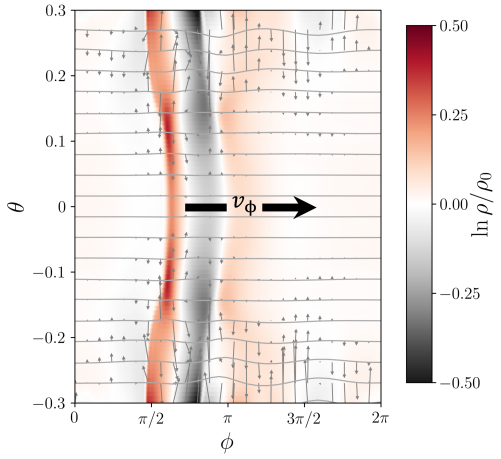

Figure 28: Flow pattern at $r = 0.66r_p = 26.6$au, in an azimuthal cut of the disk. Streamlines flow left to right; as Figure 27, vector arrows represent velocity differences from the local initial (quasi-)Keplerian value.

What gives rise to these flow patterns, and in turn, how do they influence the observed spiral perturbations in density, temperature, and kinematics? Our system begins in a background state $\rho_0, T_{g,0}, \vec{v}_0$, where $\vec{v}_0 = v_{\phi,0}\hat{\vec{\phi}}$ is a divergenceless, axisymmetric, quasi-Keplerian flow set by the stellar potential Φ_* and the initial pressure profile P_0. All quantities $(\rho, T_g, T_d, v_r, v_\theta, v_\phi)$ can be expressed in terms of the initial condition and a perturbation, e.g., $\rho = \rho_0 + \rho'$, both of which are in general dependent on space. Working in the rotating frame of the planet, and given that we do not include gas opacities, we can write the evolution of the perturbations as follows:

$$\frac{\partial \rho'}{\partial t} = -\left[\vec{v}\cdot\nabla\rho' - \vec{v}'\cdot\nabla\rho_0\right] - \left[\rho\nabla\cdot\vec{v}'\right] \tag{127a}$$

$$\frac{\partial T_g'}{\partial t} = -\left[\vec{v}\cdot\nabla T_g' + \vec{v}'\cdot\nabla T_{g,0}\right] - (\gamma-1)\left[T_g\nabla\cdot\vec{v}'\right] - t_c^{-1}\left[T_g' - T_d'\right] \tag{127b}$$

$$\frac{\partial \vec{v}'}{\partial t} = -\left[\vec{v}\cdot\nabla\vec{v}' - \vec{v}'\cdot\nabla\vec{v}_0\right] - \left[\nabla P/\rho - \nabla P_0/\rho_0 + \nabla\Phi_p\right] - 2\vec{\Omega}_p\times\vec{v}' \tag{127c}$$

In the above equations, the partial time-derivative terms represent overall evolution of the quantity at a fixed location; given that the spiral is well-developed at $t = 2500$ yr, and that its pattern speed equals the frame rotation speed, the system is approximately in steady state and these terms net to a small number. The terms in the first set of square brackets, including velocities projected along gradients of various quantities, represent advection of the flow. We consider both the vertical (formally, along the $\hat{\theta}$-direction) and in-plane (formally, along the $\hat{r}$ and $\hat{\theta}$ directions) transport of perturbed density, temperature, and velocity within our stratified disk; we write explicit expressions for these terms in Appendix B.2.

In the second set of square brackets are source terms representing gas compressibility, pdV work, and pressure-gravity balance in Equations 127a, 127b, and 127c respectively. For simplicity, we aggregate the last of these quantities into

$$\left(\frac{\partial \vec{v}'}{\partial t}\right)_{\text{source}} = -\left[\nabla p/\rho - \nabla p_0/\rho_0 + \nabla\Phi_p\right] \tag{128}$$

The final bracketed term in Equation 127b represents the exchange of energy between gas and dust. The term $2\vec{\Omega}_p\times\vec{v}'$ in Equation 127c is the Coriolis acceleration arising from frame rotation. In the second set of square brackets are the source terms, involving divergences of velocities for the scalar quantities, and gradients of pressure/-gravitational potential for the velocity.

We plot all of these terms and vertical-advective terms in a cut at $r = 1.5r_p$ and $\theta = 0.2$ in Figure 29. As fluid in this upper-disk region enters the spiral density wave, its quasi-Keplerian orbit is perturbed down (v_θ pressure-gravity) toward the midplane—against $\nabla\rho_0$, but along $\nabla T_{g,0}$—decreasing the local T_g while increasing ρ (θ-advection). Because this flow pattern (which also includes a perturbation in v_r) has a nonzero divergence, it also increases both ρ and T_g by compression and pdV work, respectively. These terms are balanced by quasi-Keplerian transport of gas through the spiral pattern

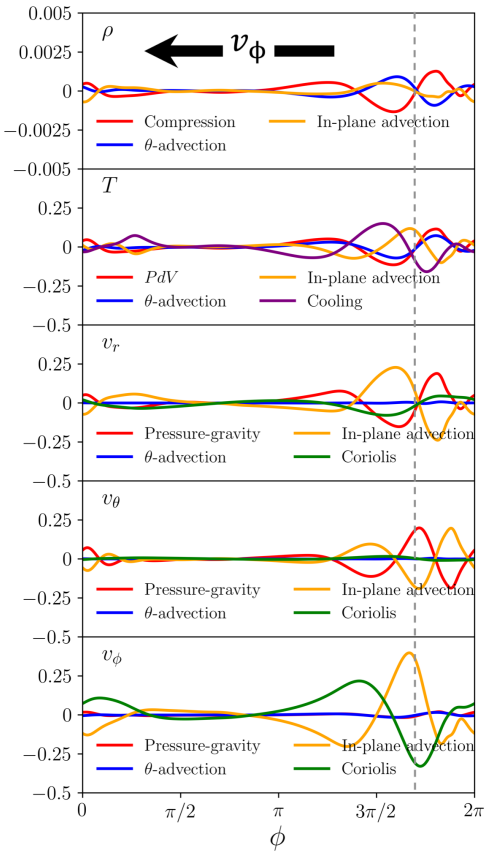

Figure 29: Source (red) and advective (blue) terms at a fixed $r = 1.5r_p$ and $\theta = 0.2$, plotted over azimuthal angle ϕ. From top to bottom, we plot these terms for ρ (in units of $\Omega_p \rho_{0,p}$), T_g ($\Omega_p T_{g,0,p}$), v_r, v_θ, and v_ϕ ($\Omega_p c_{s,iso,p}$), where the p subscript indicates quantities taken at the planet location in the initial condition. A thin, grey, dashed line passes through the azimuthal peak of the density spiral, showing the significant offset between terms driving spiral perturbations in each quantity.

("in-plane" advection), and additionally for T_g, collisional relaxation to the background dust temperature (cooling), which hold the system in an approximately steady state.

For velocity, vertical gradients are much weaker, so θ-velocity does not play a significant role. Instead, perturbations in the v_r and v_θ components are governed primarily by the planet-driven density wave (pressure-gravity) and counterbalanced by in-plane transport across the spiral. Along the ϕ-component, the pressure gradient is weak, and v_ϕ is governed instead by a balance between in-plane advection and Coriolis terms. The fact that v_r and v_{phi} are somewhat out of balance reflects the fact that over the long term, planet-driven spirals open a gap in the disk.

5.3.4 *Equilibrium temperature*

Disk-planet interaction not only heats the disk locally through pdV work, but non-locally by changing the background radiation field. Spiral arms, for instance, push disk material to higher altitudes, intercepting direct stellar irradiation while gently shadowing the regions behind them. Closer to the midplane, the accumulation of ma-

terial in circumplanetary regions leads to more clear, radially-directed shadowing. The gas heating in both regions, whether through spiral compression or gas accretion, also makes them weak [4] sources of radiation. All this impacts the equilibrium temperature T_{eq}, defined by the equation

$$0 = S_d^{irr} + \rho_d \kappa_d (T_{eq})(E_r - a_r T_{eq}^4) \tag{129}$$

which incorporates both stellar irradiation and the thermalized radiation field, and whose solution we find using Newton-Raphson iterations. Because these effects depend on the (inherently non-local) transport of radiation, they cannot be accounted for using a β-cooling approach; conversely, the deviation of $T_{d,eq}$ from the initial condition $T_{d,0}$ provides a good measure of the suitability of a β-cooling prescription for a particular problem.

In Figure 30, we plot deviations of T_{eq}, T_d, and T_g in our 3T, Saturn-mass simulation; we fix $r = 1.5 r_p$ and $\theta = \{0, 0.1, 0.2\}$, and plot the deviations as a function of azimuthal angle. We find that deviations in equilibrium temperature are strongest at $\phi \approx \pi/4$, the angular position of the planet, resulting from midplane shadowing and upper-atmosphere exposure to radiation. This corresponds to the bright "pseudo-arm" observed in Monte Carlo radiative-transfer (MCRT) modeling of near-infrared scattered light from simulated planetary spirals (Muley, Dong, and Fung, 2021). The deviations in T_{eq} located approximately $\pi/4$ rad from the spiral arms are much weaker; given that they are not centered on the gas temperature bump, we attribute them to rearrangement of disk density affecting transport of stellar and reprocessed radiation, rather than emission from the spiral itself found by Ziampras, Nelson, and Rafikov (2023).

As in Muley, Melon Fuksman, and Klahr (2023), we find that dust and gas temperatures largely agree with each other at lower disk layers, whereas in the upper atmosphere, longer dust-gas coupling mean that the gas temperature reflects pdV work from the spirals, while the dust temperature closely tracks the equilibrium temperature. The generally small deviation of T_{eq} explains why the β-cooling approach discussed in Section 5.2.1.3 provides generally accurate results for non-accreting, Saturn-mass planets. However, for other setups—such as those we discuss in the following sections—this need not be the case, and radiation hydrodynamics are essential to obtaining physically consistent results.

5.4 PARAMETER STUDY

In what follows, we test three different planet masses ($M_p = \{5 \times 10^{-5}, 3 \times 10^{-4}, 1 \times 10^{-3} M_\odot$, corresponding to Neptune-, Saturn-, and Jupiter-mass, respectively)[5] with no accretion luminosity, and two planetary accretion luminosities ($L_{acc,p} = \{0, 1 \times 10^{-3}\}$) with a Saturn-mass planet. In order to capture changes to the background radiation field—which become especially pronounced for high-mass or accreting protoplanets—we use the full three-temperature scheme for all of these simulations.

4 The circumplanetary region becomes a much stronger source when accretion luminosity is accounted for; see Section 5.4.2 for more details.

5 Given the scale height ratio $h_p = 0.0646$ at the planet location, these correspond to thermal masses q_{th} of 0.18, 1.12, and 3.74 respectively, spanning the sub-thermal, thermal, and super-thermal mass regimes.

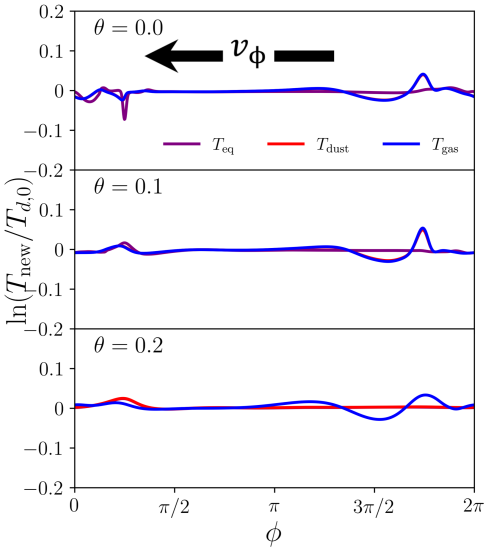

Figure 30: Plots of background equilibrium, gas, and dust temperatures in our 3T, Saturn-mass simulations, at selected altitudes above the midplane for a fixed $r = 1.5r_p$. Background temperatures deviate by only a few percent from the initial condition, most strongly in the region of the planetary shadow ($\phi \approx \pi/4$) and somewhat more weakly near the Lindblad spiral. T_d agrees well with T_g at $\theta = 0.0$ and 0.1 (and is covered by the line for T_g), and with T_{eq} at $\theta = 0.2$ (covering the line for T_{eq}).

5.4.1 *Planet mass*

In Figure 31, we plot the spiral-averaged perturbation amplitude $\langle \Delta x \rangle_{\phi,spiral}$—where x can be any one of various normalized quantities $(\ln \rho/\rho_0, \ln T_g/T_{g,0}, \ln T_d/T_{d,0}, v_r/c_{s,iso,p}, v_\theta/c_{s,iso,p}, v_\phi/c_{s,iso,p})$, and Δx its deviation from the initial condition—as a function of planet mass. As in previous figures, we fix $r = 1.5r_p$ and test $\theta = \{0.0, 0.1, 0.2\}$ above the midplane. We define

$$\langle \Delta x \rangle_{\phi,spiral}(r,\theta) = \frac{1}{4h_p} \int_{\phi_{peak}-2h_p}^{\phi_{peak}+2h_p} \Delta x(r,\theta,\phi)\, d\phi \tag{130}$$

which is analogous to the definition in Muley, Dong, and Fung (2021), with the important distinction that in the present work the amplitude is not vertically averaged. Open circles indicate simulations without accretion luminosity, while filled circles correspond to our simulation with it (Section 5.4.2).

As found in previous works (Dong and Fung, 2017; Fung and Dong, 2015; Muley, Dong, and Fung, 2021), spiral amplitude increases substantially with planet mass, irrespective of the measure used. At $\theta = 0.0$ and $\theta = 0.1$, ρ and $v_r/c_{s,iso,p}$ perturbations follow each other closely; both weaken in the upper atmosphere, but the density perturbation much more so. $v_\theta/c_{s,iso,p}$ is nearly zero in the disk midplane, but rises with increasing altitude (see Section 5.3.3). $v_\phi/c_{s,iso,p}$ is relatively weak in most cases, but is stronger for high-mass cases at $\theta = 0.1, 0.2$ thanks to the distortions introduced by the circumplanetary flow. At every altitude and planet mass, temperature deviations tend to be weaker than those in density and velocity. At $\theta = 0.0, 0.1$ where dust and gas are well-coupled, they reflect both the Lindblad spiral and the radial "pseudo-arm"

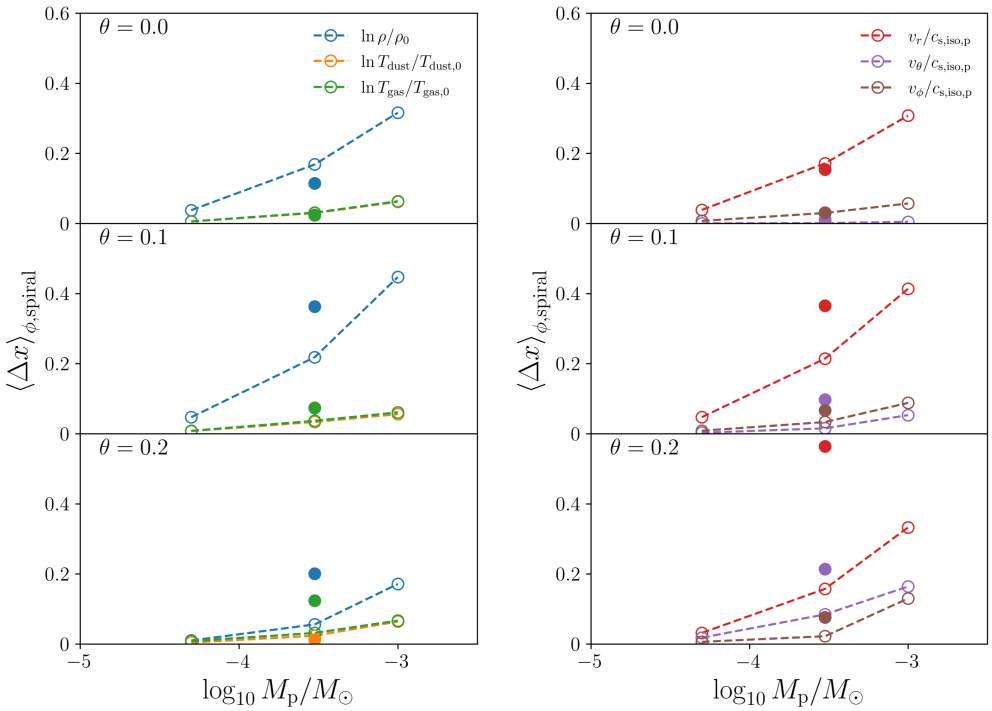

Figure 31: Measurement of the azimuthal perturbation in each normalized quantity x, averaged over an azimuthal range of $\phi_{\rm peak} \pm 2h_{\rm p}$ according to Equation 130. Densities and temperatures are plotted in the left panel while velocities are in the right. Open circles indicate non-accreting planets while closed circles indicate those with accretion luminosity (see Section 5.4.2 for discussion). At $z/r \approx \theta = 0.2$, where dust and gas are not well-coupled, the plotted $T_{\rm dust}$ amplitude reflects the radial "pseudo-arm" (see discussion in Section 5.3.4) rather than the Lindblad spiral.

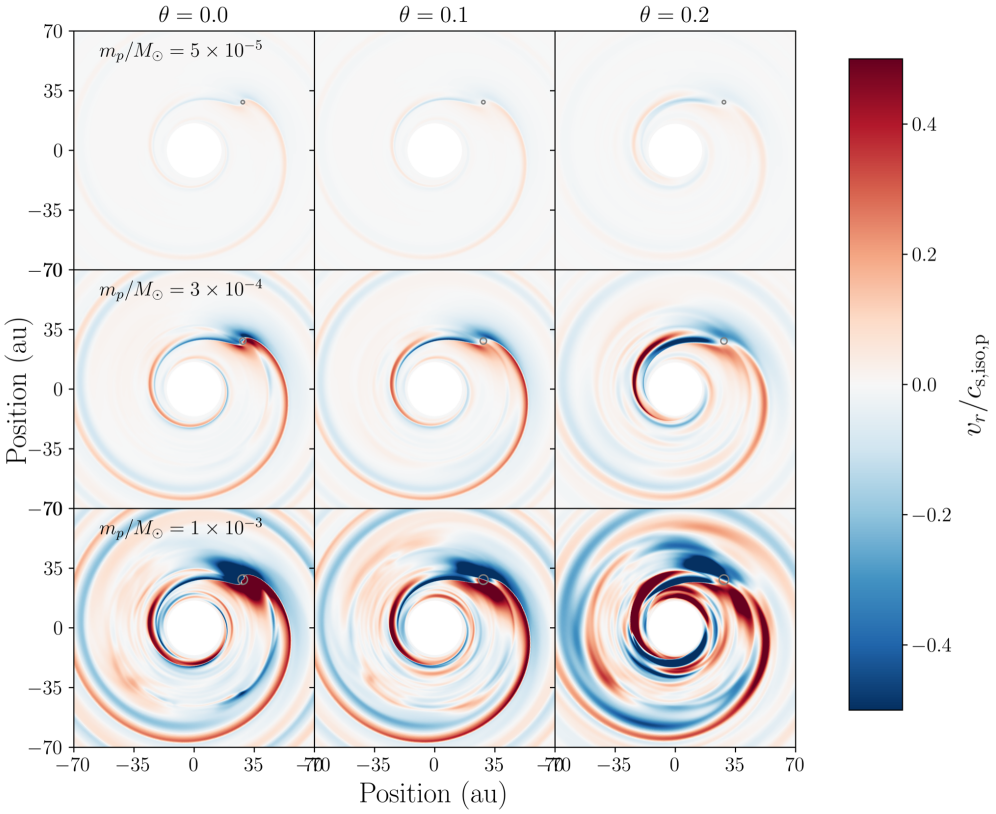

Figure 32: Radial velocities v_r from 3T, zero-accretion-luminosity simulations with Neptune-mass (top row), Saturn-mass (middle row), and Jupiter-mass (bottom row) planets, at various altitudes in the disk (left, middle, right columns). Grey circles indicate the planetary Hill radius. All v_r values are expressed as a function of initial isothermal sound speed at the location of the planet, $c_{iso,p} = \sqrt{p_{p,0}/\rho_{p,0}}$.

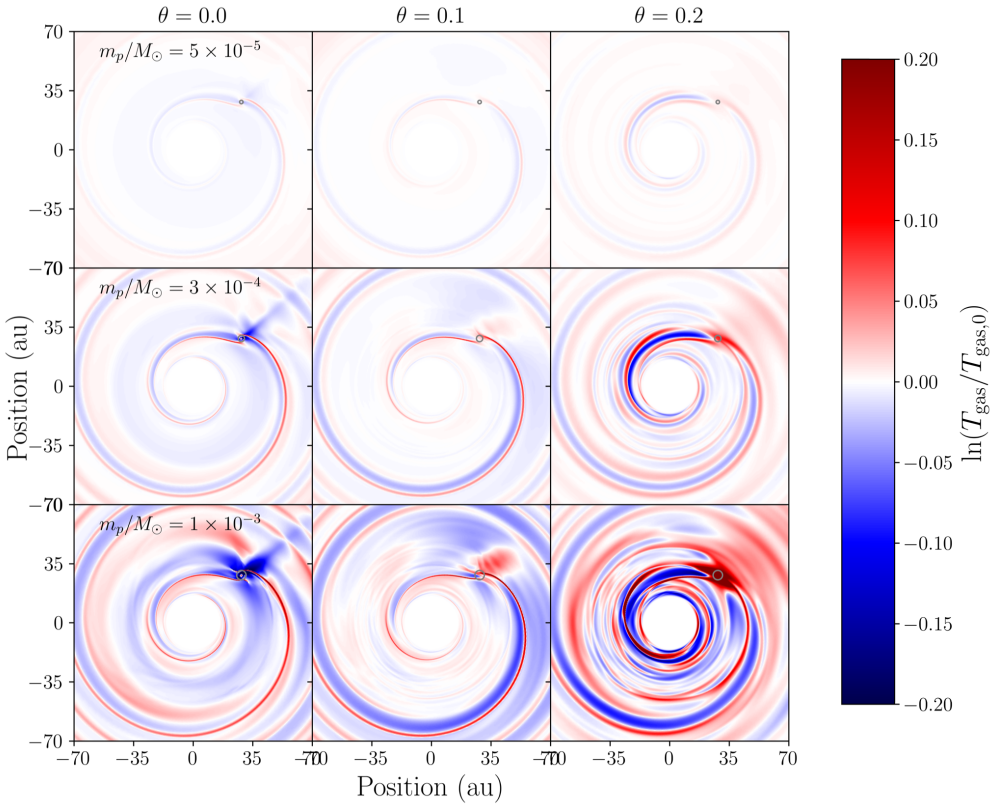

Figure 33: Gas temperature perturbation for Neptune-mass (top row), Saturn-mass (middle row), and Jupiter-mass (bottom row) planets, at various altitudes in the disk (left, middle, right columns). Grey circles indicate the planetary Hill radius. All temperature values are expressed with respect to the initial condition $T_{g,o}$.

instead (Section 5.3.4), but at $\theta = 0.2$, gas temperature primarily reflects the Lindblad spiral while dust temperature reflects the pseudo-arm.

For a more qualitative understanding, we show 2D polar cuts of v_r in Figure 32. Sub-thermal, Neptune-mass planets excite well-behaved kinematic spirals clearly distinct from the laminar background, however, these spirals are rather weak, with typical $|v_r| \lesssim 0.1 c_{s,iso,p}$—corresponding to a physical velocity $\lesssim 30 m\,s^{-1}$ in our disk model. In the Saturn-mass case, velocity spirals have a similar shape, but are significantly stronger—by a factor of ~4 in the outer disk (Figure 31), and even more so in the inner disk. Here, flows at the corotation radius and in the vicinity of the planet, which can be identified with the velocity kinks observed in channel maps (e.g., Pinte et al., 2019), become significantly more prominent.

In the Jupiter-mass case, Lindblad spirals become somewhat stronger, with higher-order spirals (Bae and Zhu, 2018a,b) particularly visible in the inner and upper disks. However, the observed v_r signature is dominated by flows near the planet, which become larger and faster thanks to the greater planet mass and gravitational sphere of influence. In the upper atmosphere, this flow takes on a wing-like shape, and acts to bring material directly above/below the planet, where is funneled toward the planet's Hill radius through the poles (e.g., Fung, Artymowicz, and Wu, 2015; Fung, Zhu, and Chiang, 2019). At all altitudes, the background flow also becomes more turbulent and unsteady.

To complement our understanding from the kinematic signatures, we present perturbations in the gas temperature T_g in Figure 5.3.4, taken at the same 2D polar cuts as in Figure 32. In all simulations, we observe a radial shadow from the circumplanetary region (see Section 5.3.4) whose strength increases with the size of the circumplanetary region and thus, with planet mass. Especially for higher-mass cases, the fact that the integrated one-sided Lindblad torque scales as $\mathcal{T}_{L,+} = C_{L,+}(M_p/M_*)^2 h^{-3} \propto T_g^{-3/2}$ (Tsang, 2011) may contribute to strengthening the outer spiral. In the upper atmosphere, the funneling of gas into a flow toward the midplane along the planetary pole leads to compressional heating, manifesting as a hot spot in T_g above the planet location.

Thermal relaxation, first by gas-grain collision and then by thermal emission from heated dust grains, dissipates pdV work to the radiation field. For the disk setup we choose, the effective relaxation timescale ($\beta = 0.1 - 1$) is approximately equal to or less than the spiral crossing time. As a result, the T_g spiral has a multi-band structure, reflecting the initial compression when the gas strikes the spiral (high-temperature band), expands behind the spiral (low-temperature band), and compresses again to return to the background density (high-temperature band). The first high-temperature band is dominant in the midplane, but both roughly even in the disk upper atmosphere. This stands in contrast to the effectively-adiabatic situation where thermal relaxation is much slower than spiral crossing (Miranda and Rafikov, 2020b; Muley, Dong, and Fung, 2021), where the T_g spiral reflects the accumulated total of compression and expansion rather than individual short phases of it. This picture is clear up to Saturn-mass, but less so at Jupiter-mass, where the T_g Lindblad spiral is distorted by the effects of circumplanetary and turbulent flows.

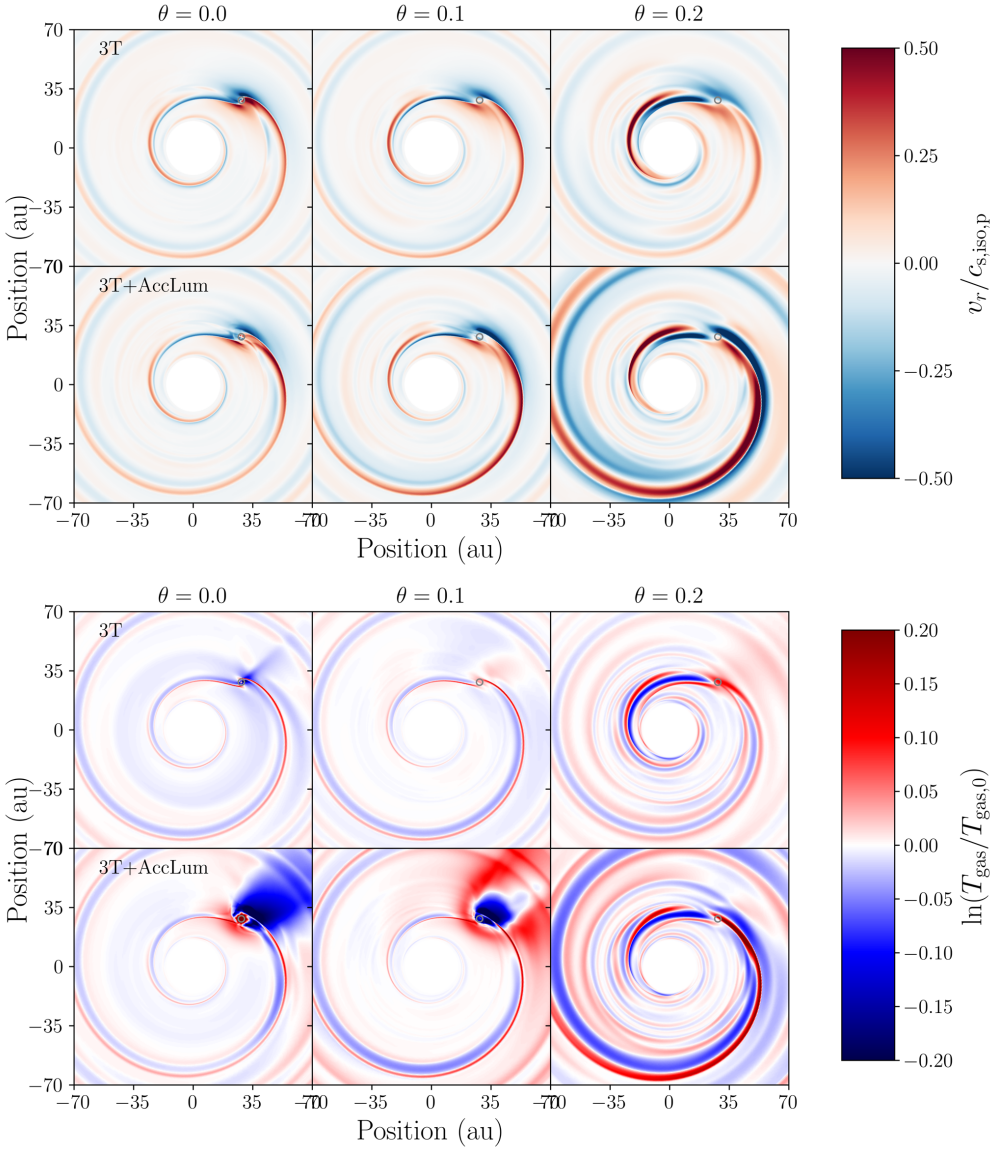

Figure 34: Difference from the initial condition in v_r (above) and T_g (below), for three-temperature simulations of Saturn-mass planets without and with accretion luminosity. The strongly luminous planet alters the vertical and azimuthal structure of the circumplanetary region, causing strong shadows behind the planet and greatly enhancing the kinematic signatures of accretion in the outer disk.

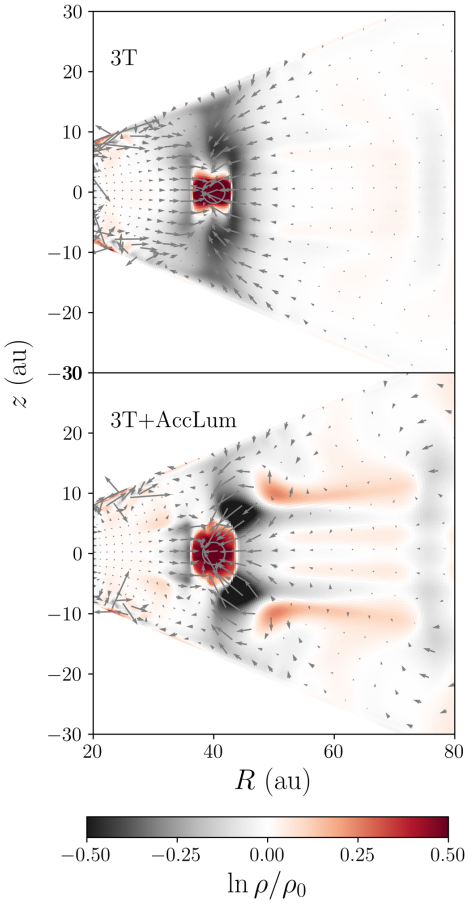

Figure 35: Plot of density perturbation in a cut through $\phi_p = \pi/4$, as a function of cylindrical radius R and vertical position z, for 3T simulations of Saturn-mass planets without (above) and with (below) accretion luminosity. Grey arrows indicate the velocity field, while the grey circle encloses the planetary Hill radius. When accretion luminosity is included, the circumplanetary envelope becomes larger and the flow around it is altered.

5.4.2 *Accretion luminosity*

In recent years, the effect of planetary accretion luminosity has been studied in parametrized 2D global disk simulations (Gárate et al., 2021; Montesinos et al., 2015, 2021), and in local, 3D simulations with full radiative transfer (Szulágyi, 2017) that emphasize the circumplanetary disk. We add to this body of work with our 3D global simulations, including three-temperature radiation transport and a luminous planet. The $L_{acc,p} = 10^{-3} L_\odot$ we use corresponds to a mass accretion rate of of $\dot{M} = 7 M_J/\text{Myr}$, given the fiducial planet mass $M_p = 4 \times 10^{-4} M_\odot$ and assuming a typical radius of $2R_J$ for the forming planet. For this mass, such an accretion rate can only be sustained over brief periods. We thus believe that this scenario, along with the no-accretion base-case, bracket the range of accretion luminosities that the planet might experience during its growth.

We revisit Figure 31, in which spiral amplitudes from our simulations with accretion luminosity are plotted with filled circles. At $r = 1.5 r_p$ and $\theta = 0$, accretion luminosity somewhat weakens the ρ and v_r perturbations, while leaving the others unchanged. At higher altitudes, by contrast, most perturbations are significantly strengthened by accretion luminosity—sometimes by factors of 2 or more—with respect to the non-luminous planet case.

Along the lines of Figures 32 and 33 , we also make qualitative plots of kinematic and temperature perturbations at various disk cuts, and present these in Figure 34. With planetary accretion luminosity, the circumplanetary envelope becomes more pressure-supported, with the hot core overflowing the planetary Hill radius. Close to the midplane, this disrupts the orderly Doppler-flip kinematic signature and enhances the Lindblad spirals in both temperature and velocity, without changing their overall morphology. It also significantly strengthens the outer radial shadow (Montesinos et al., 2021) through its impact on the envelope's vertical and azimuthal structure.

In the upper atmosphere, however, accretion luminosity intensifies the spiral and changes its shape. The radial velocity shows a double-banded structure—as opposed to the single-banded one expected without accretion luminosity—while the temperature shows a cold-hot-cold band structure, rather than hot-cold-hot. With accretion, the spiral also remains strong much farther away from the planet than without.

To understand these results better, we plot the density perturbation in Figure 35, at a vertical cut through the planet's azimuth at $\phi_p = \pi/4$. In this view, it is clear that accretion luminosity puffs the circumplanetary region vertically. This changes the flow pattern significantly, with accretion primarily happening by material diagonally striking the edge of the envelope, rather than being funneled downward into a narrow polar flow perpendicular to the disk midplane, as is classically the picture (e.g., Fung, Artymowicz, and Wu, 2015). This is responsible for many of the observed changes to kinematic and thermal signatures, particularly in the upper atmosphere. Moreover, this means that material flowing into the Hill sphere has higher angular momentum in the accreting than non-accreting case, and as such, preferably gets expelled outward.

5.5 OBSERVATIONAL IMPLICATIONS

Among the cases we test, we find that (non-accreting) Saturn-mass planets, accreting Saturn-mass planets, and Jupiter-mass (non-accreting) planets are best at driving thermal and kinematic signatures that are amenable to observation. In each of these cases, we plot the planet-induced total velocity perturbation—projected along the line of sight ($v'_\perp$)—in Figures 44, 45, and 46, respectively. In Figures 47, 48, and 49, we likewise plot the perturbations in gas temperature T_g. In these figures, we take a cut at $\theta = 0.3$ above the midplane; this corresponds to ~ 4.6 scale heights at r_p, and roughly aligns with the expected ^{12}CO J=$(2-1)$ emission layer (Barraza-Alfaro, Flock, and Henning, 2023). (The $\theta = 0.2$ surface shown prominently in previous figures, at ~ 3.1 scale heights above the midplane, is closer to the ^{1}2CO J=$(3-2)$ layer.) We test disk inclinations $i_d = \{0°, 30°, 60°\}$ and planetary position angles $\phi_p = \{0°, 90°, 180°, 270°\}$.

For an $i_d = 0°$, $v'_\perp$ is dominated by v'_θ. In the non-accreting, Saturn-mass fiducial case, the observed velocity spiral is driven by the local pressure-gradient term, as identified in Section 5.3.3; the redshifted spot above the planet location reflects the polar planetary flow shown in Figure 35. For the Saturn-mass planet with accretion luminosity, the outer Lindblad spiral is noticeably stronger and extends over a greater distance, while the planetary flow—no longer oriented in a polar direction—aligns with it, forming a double-banded velocity profile as discussed in Section 5.2.2. In the Jupiter-mass case, the polar accretion flow is more prominent than in the fiducial case, with the spiral becoming subdominant. In observations, these features could help distinguish between prominent spirals created by high-mass planets and those created by highly luminous ones.

As disk inclination increases from zero, $v'_\perp$ increasingly reflects v'_r (and to a lesser extent v'_ϕ). Because the typical magnitude of v'_r in spirals is typically much larger than v'_θ, this strengthens the observed spiral signature, both in the inner and outer disks. Inclination also interacts with the elevation angle $\theta = 0.3$ of the plotted disk surface to distort the sky-projected areas of surface elements in an azimuthally dependent way, with disk patches on the near side of the star appearing smaller than those on the far side. Depending on the planetary position angle ϕ_p, these properties can emphasize or deemphasize the circumplanetary region, inner, or outer spirals.

In each case, temperature spirals generally follow the same structure as the kinematic spirals; however, the magnitude of the observed temperature perturbation at a given point in the disk is a scalar quantity, and unlike $v'_\perp$ does not change with projection. Furthermore, as discussed in Sections 5.3.1 and 5.4.1, the nonzero, finite cooling time introduces a slight offset between the temperature and velocity perturbations. Conversely, the offset between kinematic and thermal spirals—as well as the prominence of buoyancy spirals—in different tracers probing various disk layers (e.g., as studied in the MAPS program; Calahan et al., 2021) could help put limits on cooling time at various vertical positions in the disk. Planet-induced radial midplane shadows could also be used to measure cooling rates—by measuring their deviation from a straight line going through planet and star—provided that the planet's position angle is well-constrained. However, fully exploring these mechanisms would require a large hydrodynamical parameter study over disk masses and dust size distributions.

Our simulations run for a relatively short period of time, emphasizing the development of spiral density waves. This means that the effects of gap opening—in particular, changes to disk illumination and equilibrium temperature (Jang-Condell and Turner, 2012) and changes to ν'_ϕ due to the pressure gradient at gap edges (Armitage, 2020, Section 2.4)—have not had the time to fully develop. Especially in the Jupiter-mass case, these effects can be substantial. Simulations to gap-opening timescales are currently in progress, and we intend to present them—along with Monte Carlo radiative transfer (MCRT) post-processing and synthetic observations—in a forthcoming work.

5.6 CONCLUSION

We have run 3D, three-temperature radiation hydrodynamical simulations with the aim of better understanding the kinematic signatures that would be generated by forming protoplanets. Our fiducial setup, with a non-accreting Saturn-mass planet located at $r_p = 40$au in a 15 M_J disk, draws inspiration from the TW Hya system, where spiral arms—potentially excited by a forming planet (e.g., Bae, Teague, and Zhu, 2021b; Muley, Dong, and Fung, 2021)—have already been observed in temperature and velocity (e.g., Teague et al., 2019). First, we study the physical properties of the simulated planet-driven spirals, and compare our three-temperature approach to several thermodynamic prescriptions commonly used in the literature. Thereafter, we investigate the effects that changing planetary mass and accretion luminosity have on the strength and morphology of planet-driven disk features.

For our fiducial disk, we find that the results of our three-temperature simulations agree well with those from physically-motivated β-cooling. This naturally follows from the fact that for this setup the background equilibrium temperature, T_{eq}, does not change much from the initial condition. As expected from previous works (e.g., Bae, Teague, and Zhu, 2021b; Juhász and Rosotti, 2018; Muley, Dong, and Fung, 2021), Lindblad spirals become more open with higher altitude in the stratified temperature background; buoyancy spirals are weak in strength, due to the relatively short cooling times we use. In the upper disk—most amenable to observation in ^{12}CO—thermal and kinematic signatures are driven largely by local source terms, rather than transport across vertical gradients within the disk.

Our parameter survey shows that thermal and kinematic Lindblad spirals become stronger at high planet mass. Especially in the super-thermal mass regime, deeper planetary potential wells and larger Hill radii also enhance the signatures of circumplanetary flows. Planetary accretion luminosity adds pressure support to the circumplanetary region, and reorients the classic polar accretion flows (e.g., Fung, Artymowicz, and Wu, 2015; Fung and Chiang, 2016; Fung, Zhu, and Chiang, 2019) slightly outward. The separate effects of increasing planet mass versus accretion luminosity, relative to our fiducial case, are clearly visible in our sky-projected, inclined and rotated plots of the upper disk layers, and thus, potentially, in ALMA line observations.

Future areas of research could include testing different disk masses and dust-to-gas ratios, increasing resolution to allow for the development of hydrodynamical instabilities which may impact the visibility of spiral signatures (e.g., Barraza-Alfaro, Flock, and Henning, 2023), or running simulations to gap-opening timescales (e.g., Fung and

Chiang, 2016; Fung, Shi, and Chiang, 2014b) and post-processing the results to compare to observations; the last work is currently in progress.

More sophisticated numerical approaches would expand the scope of these comparisons. To more closely reproduce spiral pitch angles and morphologies in real disks (Miranda and Rafikov, 2019), particularly for the 20-200 K temperature range spanned by our simulations, it would significantly help to relax the ideal-gas assumption, and compute γ as a function of temperature, as well as hydrogen (para-, ortho-, atomic), helium, and metal fractions (Bitsch, Boley, and Kley, 2013; Boley, Morris, and Desch, 2013; Boley et al., 2007). Incorporating multiple dust species (including momentum exchange and turbulent diffusion) would enable modeling of widened, thickened rings of millimeter grains at planetary gap edges (Bi, Lin, and Dong, 2021, 2023), visible in dust continuum, whereas a short-characteristics approach to radiation transport (e.g., Davis, Stone, and Jiang, 2012), which would allow for beam-crossing between accretion luminosity and reprocessed stellar radiation, could more accurately simulate strengths for radial shadows from luminous planets. Coupling such methods with our three-temperature scheme, however, is a computationally expensive and technically ambitious undertaking that we defer to future work.

6

CAN GAP-EDGE ILLUMINATION EXCITE SPIRALS IN PROTOPLANETARY DISKS?

This chapter is adapted from the publication of Muley, Melon Fuksman, and Klahr (2024a).

The advent of high-resolution, near-infrared (NIR) instruments such as VLT/SPHERE and Gemini/GPI has helped uncover a wealth of substructure in planet-forming disks, including large, prominent spiral arms in MWC 758, SAO 206462, and V1247 Ori. In the classical theory of disk-planet interaction, these arms are consistent with Lindblad-resonance driving by companions of multiple Jupiter masses. Despite improved detection limits, evidence for massive bodies like this in connection with spiral substructure has been inconclusive. In search of an alternative explanation, we used the PLUTO code to run 3D hydrodynamical simulations with two comparatively low planet masses (Saturn mass and Jupiter mass) and two thermodynamic prescriptions (three-temperature radiation hydrodynamics, and the more traditional β-cooling) in a low-mass disk. In the radiative cases, an $m = 2$ mode, potentially attributable to the interaction of stellar radiation with gap-edge asymmetries, creates an azimuthal pressure gradient, which in turn gives rise to prominent spiral arms in the upper layers of the disk. Monte Carlo radiative transfer post-processing with RADMC3D revealed that in NIR scattered light, these gap-edge spirals are significantly more prominent than the traditional Lindblad spirals for planets in the mass range we tested. Our results demonstrate that even intermediate-mass protoplanets, which are less detectable, but more ubiquitous than super-Jupiters, are capable of indirectly inducing large-scale spiral disk features, and underscore the importance of including radiation physics in any efforts to reproduce observations.

6.1 INTRODUCTION

In recent years, high-resolution near-infrared (NIR) imaging with instruments such as VLT/SPHERE, Gemini/GPI, and Subaru/HiCIAO has revealed large-scale spiral structure in a number of systems (e.g., Shuai et al., 2022, and references therein), including MWC 758 (Grady et al., 2013), SAO 206462/HD 135344B (Muto et al., 2012), and V1247 Ori (Ren et al., 2024). Given the ubiquity of planets in our Galaxy, disk-planet interaction has been suggested as a means of creating large-scale, multi-armed spiral structure in disks (among other proposals, including the gravitational instability and stellar flybys). Specifically, hydrodynamical simulations (e.g., Dong, Fung, and Chiang, 2016; Fung and Dong, 2015; Zhu et al., 2015) of planetary wave excitation at the Lindblad resonances (Goldreich and Tremaine, 1978, 1979, 1980) suggest that the observed scattered-light spirals are consistent with launching by exterior, multi-Jupiter-mass planets. Such companions, widely separated from their host stars (van der Marel et al., 2021), should be detectable with angular differential imaging (ADI) in the near-

infrared (Asensio-Torres et al., 2021; Desidera et al., 2021), in the mid-infrared with the *James Webb Space Telescope* (JWST) (e.g., Cugno et al., 2024; Wagner et al., 2019, 2024), and in accretion tracers such as Hα and P$\alpha\beta$ (Biddle et al., 2024; Follette et al., 2023), but evidence thus far is inconclusive. Only in the PDS 70 system are planets confirmed to exist (Haffert et al., 2019; Keppler et al., 2018; Müller et al., 2018) alongside disk substructure of any sort, with additional detections in e.g., AB Aur (Currie et al., 2022) and HD 169142 (Hammond et al., 2023).

What, if not easily-detected, widely-separated super-Jupiters, might generate the observed spirals? Disk illumination and shadowing may have a role to play. Cuello et al. (2019), Montesinos and Cuello (2018), and Montesinos et al. (2016) and (Su and Bai, 2024) ran 2D, vertically-averaged hydrodynamical simulations of disks with parametrized cooling, including radial dark lanes in their temperature structures to model the effect of a misaligned, shadow-casting inner disk. The resulting strong azimuthal pressure gradient excites $m = 2$ spiral arms; MCRT post-processing, assuming a Gaussian vertical profile with a scale height governed by the 2D temperature, revealed that such arms would feature prominently in NIR. Nealon, Price, and Pinte (2020), using SPH simulations with full radiative transfer, and Qian and Wu (2024), using a parametrized cooling prescription in a grid simulation, simulate the dynamical consequences of shadowing from an inner disk. Separately, in their 3D, grid-based simulations with flux-limited diffusion FLD; Levermore and Pomraning, 1981, Chrenko and Nesvorný (2020) find that the outer edge of the gap carved by a $1 M_J$ planet exhibits unstable, non-axisymmetric flow patterns and additional spiral structure, which are absent in their locally-isothermal runs. They attribute this outcome to the fact that the temperature profile in the radiative case—with a cooler, shadowed gap region and warmer, directly illuminated outer gap edge—is more favorable for the excitation of the Rossby wave instability (RWI; Lovelace et al., 1999).

Taken together, these works suggest that even intermediate-mass planets could produce prominent, observable spirals, not through direct driving but by their impact on disk illumination—provided that shadow corotates with some radius within the disk. To investigate this hypothesis, we run 3D hydrodynamical simulations of disk-planet interaction with `PLUTO`, and post-process our results with the `RADMC3D` Monte Carlo radiative transfer code to generate mock near-infrared images of the simulated disk. In Section 2, we describe our methods in more detail, including our implementations of "three-temperature" radiation hydrodynamics (Muley, Melon Fuksman, and Klahr, 2023) and β-cooling to an axisymmetric background. In Section 3, we discuss our results, including the structure of the planet-formed gap, excitation of spirals at the gap edge, and post-processed near-infrared images. In Section 4 we present our conclusions and questions for future work.

6.2 METHODS

6.2.1 *PLUTO radiation hydrodynamics*

For our study of spiral arms, we used a version of the `PLUTO` hydrodynamical code (Mignone et al., 2007), modified to solve the equations of radiation hydrodynamics (Melon Fuksman et al., 2021; Melon Fuksman and Mignone, 2019) with an additional

dust internal energy field (Muley, Melon Fuksman, and Klahr, 2023). This is thermally coupled to the gas- (via collision) and radiation-energy (via opacity) fields, but is a passive tracer of the gas velocity without any inertia or back-reaction (implying a Stokes number $St \ll 1$ and globally constant dust-to-gas ratio $f_d \ll 1$). Radiation transport is computed using the M1 closure, which interpolates between the optically-thick (diffusion) and optically-thin (free-streaming) regimes (Levermore, 1984). We briefly review the most pertinent details below, while referring the reader to the aforementioned works (as well as Muley, Melon Fuksman, and Klahr (2024b)) for a more detailed description of the equations and solution strategy.

6.2.1.1 *Three-temperature simulations*

Our three-temperature module solves the full set of equations described in Muley, Melon Fuksman, and Klahr (2023). The coupling of dust energy with radiation energy (G_d), and of dust momentum with radiation flux ($\vec{G}_d$), are given as follows:

$$G_d \equiv -\rho\kappa_d f_d(a_r T_d^4 - E_r) + r_d(\vec{\beta}) \tag{131a}$$

$$\vec{G}_d \equiv \rho f_d \chi_d \vec{F}_r + \vec{r}_d(\vec{\beta}) \tag{131b}$$

where ρ is the dust density, while $a_r = 4\sigma_{\text{Stefan-Boltzmann}}/c$ is the radiation constant. T_d refers to dust temperature, while E_r refers to the radiation energy density. κ_d is a Planck-averaged (and thus, temperature-dependent) dust absorption opacity, while χ_d is the dust total (absorption plus scattering) opacity. In practice, we equate χ_d to the greater of the Planck- or Rosseland-averaged dust absorption opacities at a given temperature. $r_d(\vec{\beta})$ and $\vec{r}_d(\vec{\beta})$ are relativistic corrections to the above terms, with the vector $\vec{\beta} \equiv \vec{v}/c$ (not to be confused with the β-cooling timescale); these are negligible in the context of protoplanetary disks. In this work, we use the tabulated dust absorption opacities from (Krieger and Wolf, 2020, 2022), while setting gas opacities to zero.

We also include a dust irradiation term, S^d_{irr}, obtained by frequency-dependent ray-tracing from the central star. Here, the effective dust opacity is a Planck average taken at the stellar surface temperature T_*.

The dust-gas collision term X_{gd} is defined as

$$X_{gd} \equiv t_c^{-1}(r_{gd}\xi_d - \xi_g) \tag{132}$$

where t_c is the dust-gas thermal coupling time, ξ_g and ξ_d are the internal energy of dust and gas respectively, and $r_{gd} = c_g/f_d c_d$ is the ratio of heat capacity per unit volume between gas and dust. c_d is the specific heat capacity of dust, while $c_g \equiv k_B/\mu m_H(\gamma-1)$ is that of the gas. The gas thermal coupling time t_c, as a function of the dust-gas stopping time t_s, is calculated in the Epstein regime (Burke and Hollenbach, 1983b; Speedie, Booth, and Dong, 2022).

$$t_c = \frac{2/3}{\gamma-1} f_d^{-1} t_s \eta^{-1} \tag{133}$$

where we set the "accommodation coefficient" η to unity.

6.2.1.2 β-*cooling simulations*

In our β-cooling simulations, we ignore absorption, emission, scattering (G_d, $\vec{G}_d$) and transport ($\vec{F}_r$) of thermalized radiation, as well as dust energy (E_d) and stellar irradiation (S_d^{irr}). To parametrize all of these effects, we replace X_{gd} with a term of the form

$$X_{rel} \equiv t_{rel}^{-1} \frac{\rho k_B}{\mu m_p (\gamma - 1)} \left(T_g - T_{g,0}(r, \theta)\right) \tag{134}$$

where $T_{g,0}$ is the (axisymmetric) initial condition for gas temperature (see Section 6.2.1.3 for more details), r, θ, ϕ are spherical coordinate positions, and t_{rel} can in general be a function of any primitive variables. Following Bae, Teague, and Zhu (2021b) and Melon Fuksman, Flock, and Klahr (2023), we set the thermal relaxation/cooling time

$$t_{rel} = t_c + t_{rad} \tag{135}$$

where t_c is defined as in Equation 133, and t_{rad} is a radiative cooling timescale incorporating both the optically thick diffusion and optically thin free-streaming limits:

$$t_{rad} \equiv \max(\lambda_{thin}^2, \lambda_{diff}^2)/D \tag{136}$$

where the thermal diffusivity $D \equiv 4ca_r T_g^3 / 3c_g \kappa_R \rho^2$. The optically-thin cooling effective lengthscale $\lambda_{thin} = (3\kappa_R \kappa_P \rho^2)^{-1/2}$, while the thick diffusion length is taken to be the local scale height, $\lambda_{diff} \equiv H = c_{s,iso} \Omega^{-1}$, where Ω is the local Keplerian orbital frequency and $c_{s,,iso} \equiv \sqrt{p/\rho}$ the "isothermal sound speed."

Cooling times were computed self-consistently in each cell of the grid at the start of the simulation. For notational convenience, cooling times can be normalized by the local dynamical time Ω^{-1}, with $\beta_{dg} = t_c \Omega$, $\beta_{rad} = t_{rad} \Omega$, and the overall $\beta = \beta_{rad} + \beta_{dg}$.

6.2.1.3 *Setup and initial conditions*

For our simulations, we used the same initial conditions (plotted in Figure 36) as in Muley, Melon Fuksman, and Klahr (2024b), generated with iterative alternation of radiative and hydrostatic computations. As in that work, we use an extended radial grid with an inner edge at 0.4 au, as well as an additional inner padding prescription, to ensure an accurate temperature at the inner edge of our simulated domain. Dust properties remain unchanged between that work and the present one, and dust temperature T_d and gas temperature T_g are assumed to be equal in the initial condition. The specific heat capacity for dust, $c_d = 0.7\ \mathrm{J\,g^{-1}\,K^{-1}}$.

The disk's surface density

$$\Sigma_g = 200\ \mathrm{g\,cm^{-2}} \left(\frac{R}{1\mathrm{au}}\right)^{-1} \tag{137}$$

where $R = r \sin\theta$ is the cylindrical radius. We use a (Shakura and Sunyaev, 1973) $\alpha = 0.001$.

We fix the stellar mass $M_* = 1\ M_\odot$, radius $R_* = 2.08\ R_\odot$, and temperature $T_* = 4000$ K, giving a total luminosity equal to solar. We test two thermodynamic prescriptions

Symbol	Value	Quantity
M_*	$1 M_\odot$	Stellar mass
R_*	$2.08 R_\odot$	Stellar radius
T_*	4000 K	Stellar surface temperature
α	0.001	Shakura-Sunyaev viscosity parameter
μ	2.3	Mean molecular weight of gas
γ	1.41	Adiabatic index of gas
c_d	$0.7 \mathrm{J\,g^{-1}\,K^{-1}}$	Specific heat capacity of dust
c_g	$8.8 \mathrm{J\,g^{-1}\,K^{-1}}$	Specific heat capacity of gas
$\{n_r, n_\theta, n_\phi\}$	$134, 58, 460$	Cells along each dimension (low-resolution, 1000 orbits)
$\{n'_r, n'_\theta, n'_\phi\}$	$268, 116, 919$	Cells along each dimension (high-resolution, 10 orbits)
$\{r_{in}, r_{out}\}$	$\{16 au, 100 au\}$	Inner and outer radial boundaries
$\{\theta_{low}, \theta_{up}\}$	$\{-0.4, 0.4\} + \pi/2$	Lower and upper polar boundaries
r_{inf}	18 au	Outer boundary of inner wave-damping zone
r_{sup}	95 au	Inner boundary of outer wave-damping zone
r_p	40 au	Planet radius
Ω_p^{-1}	40 y	Dynamical time at r_p
	$3 \times 10^{-4} M_\odot$	Mass of Saturn
	$1 \times 10^{-3} M_\odot$	Mass of Jupiter

Table 1: Table of key simulation parameters. More information can be found in Section 6.2.1.3 of this work, and in Section 2 of Muley, Melon Fuksman, and Klahr (2024b).

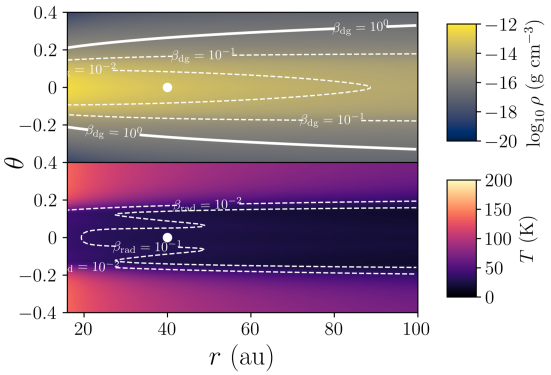

Figure 36: Initial conditions for gas density ρ (above), as well as dust and gas temperatures T_d and T_g (below), which are initially equal. Contours for normalized cooling timescales from gas-grain collision (β_{dg}) are plotted above, and from radiation (β_{rad}) below, with white lines. Figure reproduced exactly from Muley, Melon Fuksman, and Klahr (2024b).

(β-cooling, 3T) and planet masses ($M_p = 3 \times 10^{-4} M_\odot, 1 \times 10^{-3} M_\odot$), with the planet located at $r_p = 40$au, $\theta_p = \pi/2$, and $\phi_p = \pi/4$ in each case. The planets are introduced relatively rapidly into the simulations, with a growth timescale $t_{gr} = 10y$; this has the potential to strengthen gap-edge effects such as the Rossby wave instability (Hammer, Kratter, and Lin, 2017), and thus serves as a caveat of our model. For our hydrodynamic computations, we take a subdomain of the initial disk model generated by our hydrostatic procedure, bounded by $r = \{0.4, 2.5\} \times r_p$, $\theta = \{-0.4, 0.4\} + \pi/2$, and $\phi = \{0, 2\pi\}$. We cover this box with $134(r) \times 58(\theta) \times 460(\phi)$ cells, logarithmic in radius and uniform in polar and azimuthal angle. This yields a resolution of ~4.5 cells per scale height at the planet location, roughly equal to that used in the radiation-hydrodynamic gap-opening simulations of Chrenko and Nesvorný (2020).

We fix the boundary values of all fields to equal that of the initial condition. To ensure numerical stability near these boundaries, we damp ρ, E_r, S_d^{irr}, and the components of $\vec{v}$ to their initial conditions over a timescale $t_{damp} = 2\pi \times 0.1\Omega^{-1}$. We use an HLL Riemann solver for hydrodynamics and HLLC for radiation; to ensure numerical stability in the presence of fast flows and large density contrasts, we make use of a piecewise-linear method (PLM) reconstruction to obtain the states at cell boundaries, rather than the WENO3 method used in Muley, Melon Fuksman, and Klahr (2024b). We run each simulation for 250000yr (approximately 1000 planetary orbits), then interpolate the result onto a higher-resolution $268(r) \times 116(\theta) \times 919(\phi)$ grid; we run this setup for an additional 2500yr to study flow patterns in more detail.

6.2.2 *RADMC3D Monte Carlo radiative transfer*

We used `RADMC3D` (Dullemond et al., 2012) to generate VLT/SPHERE *H*-band ($\lambda_H = 1.62\mu$m) images from our high-resolution simulation outputs, with $N_{phot} = 2.5 \times 10^7$ photon packages launched from the central star. In post-processing of 3T models, dust temperature was taken directly from the simulation output, whereas for β-cooling, it is assumed equal to the gas temperature. To minimize spurious illumination at the inner

edge of our hydrodynamic simulation domain, located at $r_{in} = 16$ au, we pad the disk to $r_{pad} = 0.5$ au using the initial conditions generated in Section 6.2.1.3.
For simplicity and consistency in our radiative-transfer calculations, we used the tabulated dust opacities in (Krieger and Wolf, 2020, 2022), including absorption, scattering, and Henyey and Greenstein (1941) g parameters to accommodate directional scattering; we expect that a more comprehensive calculation including polarization would yield similar results. In generating our H-band images, we assume a fiducial line-of-sight distance $d = 100$pc, and convolve them with a Gaussian kernel (FWHM $\approx 2.35\sigma = 0.06$arcsec) to mimic the effects of instrumental beam size.

6.3 RESULTS

6.3.1 *Temperature structure and thermal spirals*

During our simulations, the Lindblad spirals excited by the planet increased the angular momentum of the disk material exterior to the planet's orbit and decreased that of the material interior; the cumulative effect of this, over many orbits, is to open a gap in the disk. Once the gap became sufficiently deep—at roughly 50 orbits for the Jupiter-mass planet, and 200 for the Saturn-mass planet—the outer gap edge deviates from axisymmetry, potentially due to hydrodynamic instabilities such as the Rossby wave instability (see Section 3.1.6 of Chrenko and Nesvorný, 2020, for a more detailed discussion). With β-cooling, a viscous $\alpha = 1 \times 10^{-3}$ and an axisymmetric background temperature rapidly damp azimuthally-asymmetric structures to restore the classical picture of disk-planet interaction (Zhang and Zhu, 2024). With full radiation hydrodynamics, however, the density asymmetries at the outer gap edge couple with the stellar radiation field to create asymmetries in the temperature structure as well, which in turn alters the density, pressure, velocity, and vorticity (Appendix C.1). Although the vertically-integrated temperature deviation is fairly small—typically no more than 10%—the perturbations in the disk atmosphere became substantial, as disk material adjusted its scale height over the course of an orbit and had work performed on it due to compression and expansion (via the PdV term). In this region—which we define to lie at or above the radial $\tau_r = 1$ surface for stellar irradiation—gas thermal relaxation is dominated by the gas-grain cooling time $t_c \approx 0.1 - 1\Omega^{-1}$, ensuring that this PdV heating was not immediately radiated away.

The temperature asymmetry leads to a pressure asymmetry at the outer gap edge, which drives strong spiral arms Cuello et al., 2019; Montesinos et al., 2016, e.g., in our case, the $m = 2$ mode predominates. Contributing to the observed non-axisymmetry in the upper disk layers is the breakdown of midplane symmetry, with a net $|v'_\theta| \lesssim 0.05 c_{s,iso,p}$ in the midplane, but significantly faster in the upper layers of the disk. In Figure 37, we plot the resulting azimuthal profiles of density, temperature, and velocity components at high altitude near the outer gap edge at $t = 252500$ y (~1000 orbits at low resolution, plus ~10 at the doubled resolution). In the bottom panel, the decoupling between dust and gas temperatures in 3T—mentioned in the previous paragraph—is clearly visible. To better understand this phenomenon, we also conducted a controlled numerical experiment (Appendix C.2) using β-cooling. We initialized the background temperature profile with asymmetries in azimuth and about the midplane. In this test,

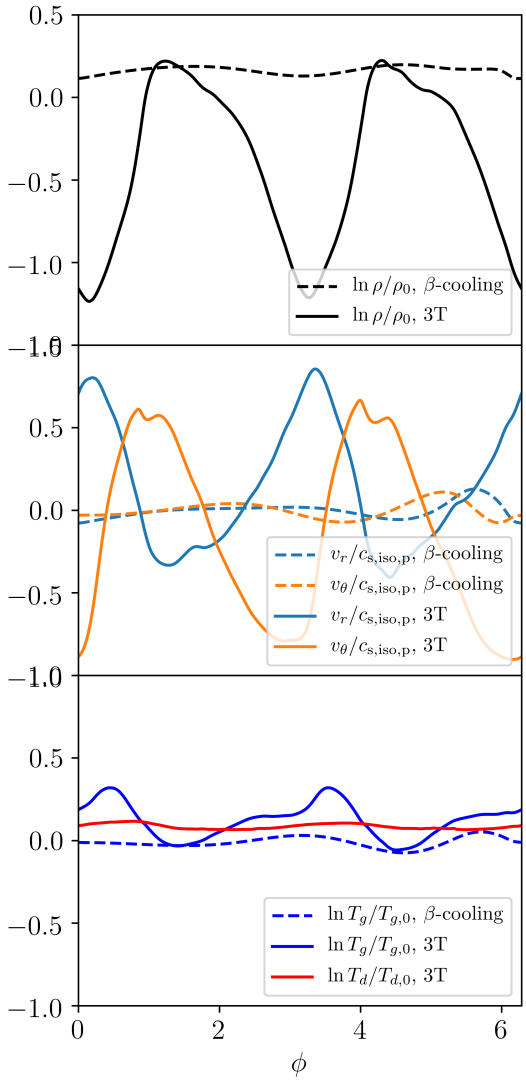

Figure 37: Azimuthal profiles of various quantities at a fiducial radius of $r = 60$ au $= 1.5 r_p$, and at an altitude of $\theta = 0.2$ rad above the midplane in our $M_p = 3 \times 10^{-4} M_\odot$ simulations. In the 3T case, azimuthal asymmetries of even a few percent in disk illumination—potentially induced by the RWI, and visible in the T_d profile—lead to strong non-axisymmetry in ρ, T_g, and the velocity components.

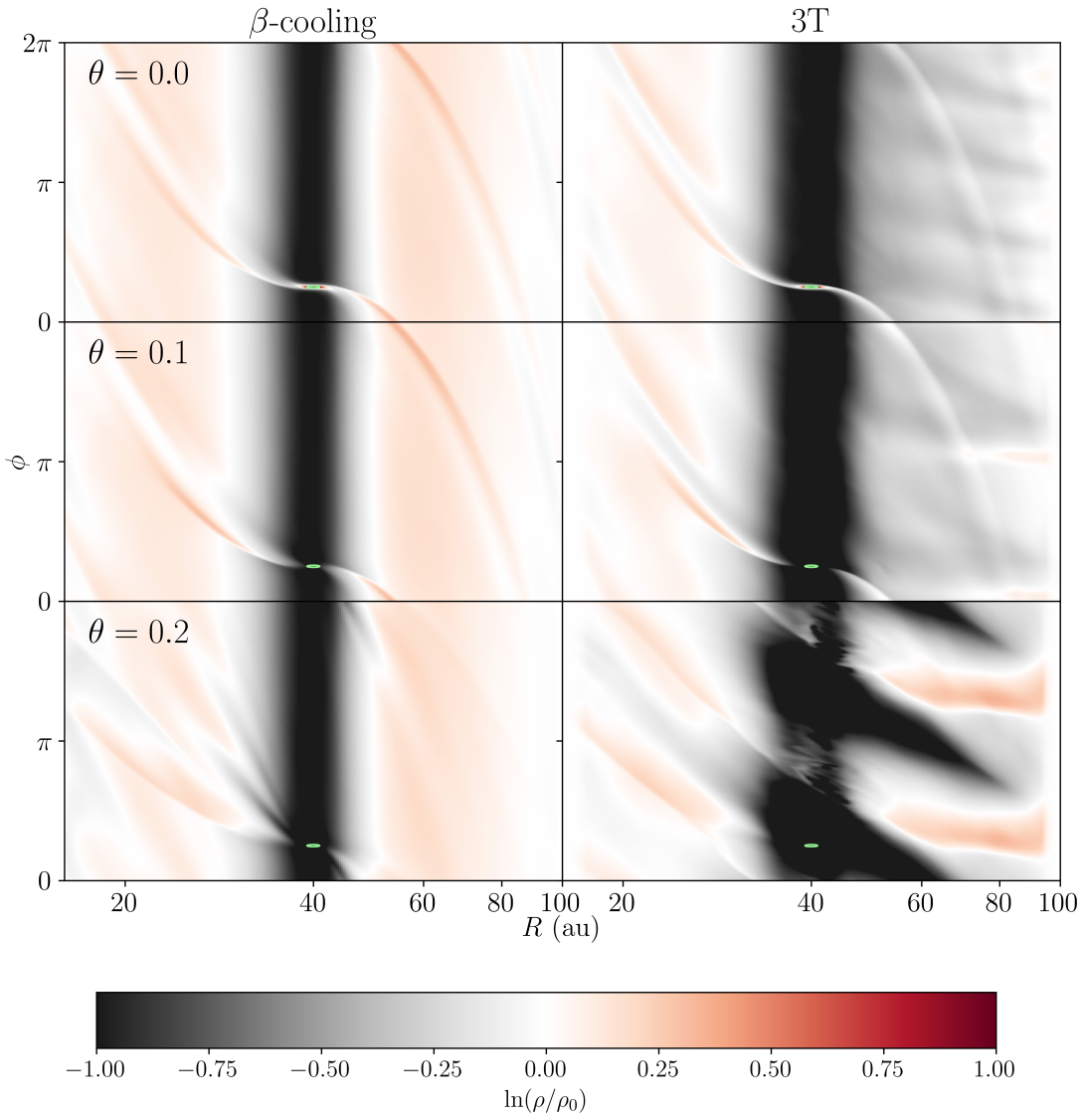

Figure 38: Gas density ρ at t = 1010 orbits (1000 orbits at the fiducial resolution, 10 at the doubled resolution used in Muley, Melon Fuksman, and Klahr (2024b)), with respect to the initial condition ρ_0, for our simulations with a Saturn-mass planet. The green ellipse indicates the planet's Hill radius. With the 3T scheme, the disk atmosphere shows clear development of $m = 2$ spiral arms, which are absent in the β-cooling simulations. White bands at the interior and exterior of the radiative simulation result from wave-damping to the initial condition.

we observed the development of strong spiral structure in the disk atmosphere—as in the 3T fiducial simulation, where the asymmetric temperature structure developed naturally from illumination, rather than being prescribed.

In Figure 38, we plot 2D $r-\phi$ cuts of the density structure at various polar altitudes, comparing the results obtained with the three-temperature and β-cooling approaches. In both cases, the Lindblad spirals generated by planetary forcing are most prominent at $\theta = 0.0$ and $\theta = 0.1$ above the midplane, but weaken at $\theta = 0.2$ in the disk atmosphere. At these high altitudes, spirals excited by the pressure gradient generated by shadowing—with a somewhat larger corotation radius—become more prominent. Both sets of spiral waves propagate through the disk according to the WKBJ dispersion relation for the radial wavenumber k_r and azimuthal wavenumber m (see Bae and Zhu, 2018a, and references therein)

$$m(\Omega - \Omega_c)^2 = \Omega^2 + k_r^2 c_s^2 \tag{138}$$

in which we assume that the epicyclic frequency $\mathcal{K} = \Omega$. From this, the pitch angle $\delta = \arctan(m/k_r r)$ can be derived as

$$\delta = \arctan\left[\frac{c_s}{R\Omega(R)}\left((1-\Omega_c/\Omega(R))^2 - m^{-2}\right)^{-1/2}\right] \tag{139}$$

where Ω_c is the corotation frequency of the perturbation and m is the azimuthal wavenumber. The larger corotation radius for shadow-driven spirals accounts for the difference in pitch angles between the spirals, and mimics the effect of an external planetary driver.

Over hundreds of orbits, the strong vertical flows shown in Figure 37 have the effect of depleting the outer disk; this, in turn, would reduce the strength of the (inward-directed) outer Lindblad torque on the planet, slowing or even reversing inward Type II planetary migration. However, the precise rate of mass depletion from the domain depends on the strength of vertical damping (see also Appendix C.3 for a discussion on how the spiral strength is affected). Moreover, our simulations do not incorporate other sources of mass depletion which become relevant at high altitude, such as photoevaporation and disk winds. As such, we choose to remain agnostic about the true mass-loss rate, and defer such an investigation to future work.

Despite sharing similarities with the models presented in Chrenko and Nesvorný (2020), our simulations do have important differences. In contrast to our 3T, M1 numerical approach, they employ two-temperature (2T) FLD (e.g., Bitsch et al., 2013), which cannot account for free-streaming and shadowing effects below the disk's radial $\tau = 1$ surface, or for the delayed response of gas to changes in illumination due to the nonzero collisional coupling time. They also only simulate the upper half of the grid, locking the disk to midplane symmetry, and impose strong damping of v_θ at the upper polar boundary to more strictly conserve mass within the grid (we find in Appendix C.3 that this somewhat strengthens the observed spiral signature). These differences are a consequence of the separate, but complementary, research goals of each work—their emphasis is on gap structure and planetary torque and migration, while ours is on observational signatures in the upper disk atmosphere.

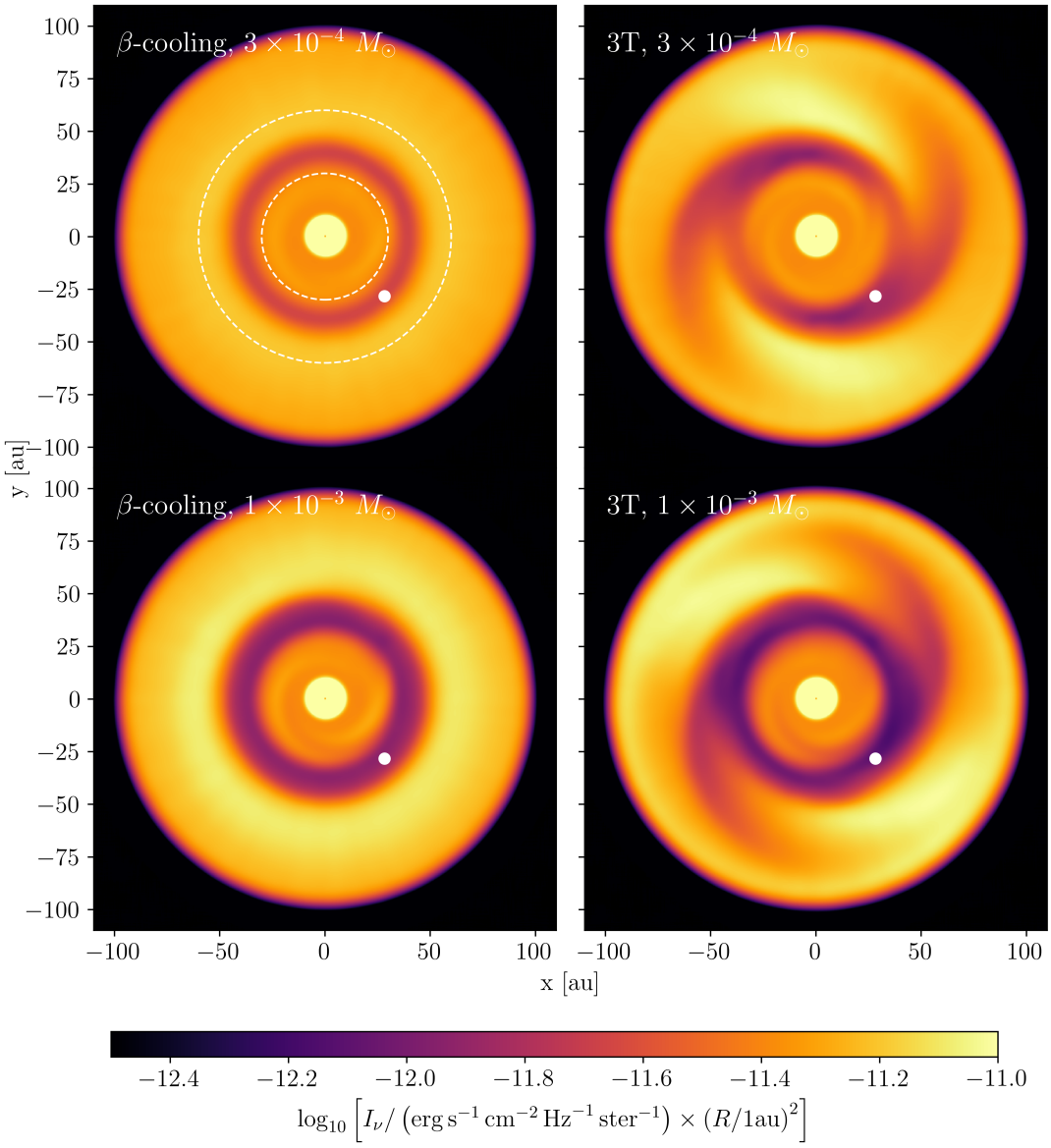

Figure 39: Mock H-band ($\lambda_H = 1.62\mu m$) total intensity for the disks we simulate, including an inverse-square correction factor. We assume the disk is located at a line-of-sight distance $d_r = 100$ pc with a face-on orientation ($i_d = 0°$), and convolve the raw image with a Gaussian of FWHM = 0.06 arcsec to mimic the effects of finite telescope resolution. The differences between the radiative and non-radiative cases are clearly visible.

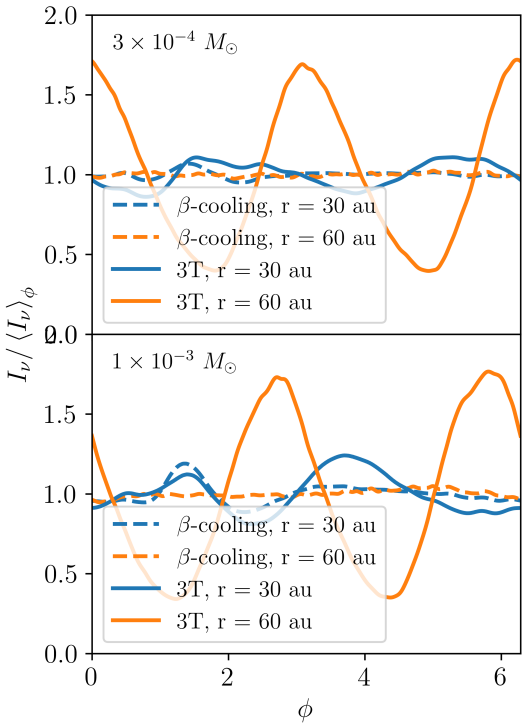

Figure 40: H-band intensity in all of our simulations, taken at fiducial radii $r_{inner,cut} = 30$ au and $r_{outer,cut} = 60$ au, and normalized to the azimuthal average. The 3T simulations show a clear $m = 2$ spiral with a peak-to-trough intensity ratio ~4 in the outer disk and $\sim 1.2 - 1.5$ in the inner disk. By contrast, the β-cooling simulations show negligible asymmetry in the outer disk, alongside asymmetries of $\sim 1.1 - 1.5$ in the inner disk caused by inner Lindblad spirals.

6.3.2 *Radiative transfer post-processing*

In Figure 39, we display face-on simulated NIR images generated with RADMC3D using the procedure described in Section 6.2.2; in order to better show the spiral structure throughout the disk, the intensity is scaled by $(R/1\ \mathrm{au})^2$. For the 3T models, the gap-induced spirals are prominently visible in NIR, far outweighing the planet-driven Lindblad spiral , whose contrast is diluted by beam convolution. By contrast, the β-cooling simulations contain only the Lindblad spiral, which is greatly weakened by the effects of beam convolution.

For a more quantitative view, we plot 1D azimuthal profiles of the brightness contrast at selected radii in Figure 40. In the outer disk (specifically, $r_{\mathrm{outer,cut}} = 60$ au), the peak-to-trough brightness contrast across the spiral reaches a factor of ~ 4 in 3T models, but is negligible for β-cooling models. In the inner disk ($r_{\mathrm{inner,cut}} = 30$ au), the 3T simulations show a contrast of 1.2-1.5, with larger values for higher planet mass. With β-cooling the perturbation amplitude is roughly the same, but results from the Lindblad spiral and not from any azimuthal temperature difference.

6.4 CONCLUSIONS

We conducted three-dimensional hydrodynamical simulations of disk-planet interaction, varying both planet mass (Saturn-mass, Jupiter-mass) and thermodynamic prescription (three-temperature radiation hydrodynamics, β-cooling). In the radiative case, deviations from axi- and midplane symmetry at the outer gap edge of a planet-carved gap are amplified by interaction with the radiation field. The resulting strong azimuthal pressure gradients in the upper disk launch spiral density waves (Montesinos et al., 2016) with an $m = 2$ azimuthal mode structure. Mock H-band images, generated using the RADMC3D Monte Carlo radiative transfer code, showed azimuthal brightness contrasts of a factor of a few, equivalent to those from classical Lindblad spirals generated by multi-Jupiter-mass planets exterior to the spiral (Dong and Fung, 2017). This radiative mechanism neither requires the existence of such a massive exterior companion, nor creates a correspondingly strong spiral structure in the disk midplane which would concentrate millimeter grains. This is consistent with multi-wavelength observations of systems such as V1247 Ori (Ren et al., 2024).

Although our simulations include only Saturn- and Jupiter-mass planets, the spiral-excitation mechanism described here would likewise operate at the outer edge of a gap carved by a super-Jupiter companion. Being interior to the spiral and close to its host star on the sky, such a body would be more easily concealed by the stellar point-spread function than an exterior companion required by the inner-Lindblad-spiral hypothesis. Indeed, high-mass interior companions may provide a natural explanation for observations in systems such as MWC 758 (Boehler et al., 2018; Ren et al., 2018) and SAO 206462 (van der Marel et al., 2016), where deep (Fung, Shi, and Chiang, 2014b), eccentric (Goldreich and Sari, 2003; Kley and Dirksen, 2006) cavities in millimeter continuum and gas tracers exist alongside large-scale NIR spirals.

In principle, the instability we observed could have been obtained using an orthodox, two-temperature approach. However, with 2T, the gas temperature (and consequently, its vertical structure) responds immediately to changes in illumination, which con-

tributes contributes to the development of azimuthal asymmetries at the inner boundary of the disk (also found in Renggli and Szulágyi 2022, private communication). These features, in turn, affect the temperature structure and generate spiral arms even in the absence of a planet. With 3T, however, the nonzero coupling time between gas and grains suppresses these inner-boundary artifacts, leaving only the spirals generated at the outer gap edge.

With the existing 3T implementation in `PLUTO`, one could conduct a parameter study over disk/stellar mass, planet location, and opacity prescription (including molecular opacity) to better understand the properties that give rise to large-scale spirals (van der Marel et al., 2021), and test whether the mechanism we describe can form spiral structures with wavenumbers besides $m = 2$. Line transfer, a feature of `RADMC3D`, could be used to model the kinematic signatures expected from such large-scale spirals, and which would potentially be observable in exoALMA and similar large programs. Incorporating multiple dust species e.g., Krapp et al., 2024a, would allow the dynamics of small and large dust grains to be handled simultaneously, ensuring that post-processed near-infrared and submillimeter images are mutually consistent. Using radiation-transport methods that allow for beam crossing (such as the discrete-ordinates approach of Jiang, 2021) would improve the treatment of shadowing, particularly in the presence of an accreting, luminous planet that radiates in all directions. Pursuing these potential future directions would greatly expand scientific understanding of how radiation impacts disk-planet interaction, and in doing so, help reproduce observations of real systems.

Part III

CONCLUSION AND OUTLOOK

7

MORE REALISTIC SIMULATIONS OF PROTOPLANETARY DISKS

As with any subfield of astronomy, the study of protoplanetary disks must ultimately be driven by observable, measurable reality. In previous decades, disks were often poorly resolved at the length scales relevant to planet formation, so their properties were often parametrically modeled with an interest in reproducing their infrared excess. In this context, the 2D, locally-isothermal classical analytical theories and numerical simulations for disk-planet interaction were more than sufficient. Nowadays, however, protoplanetary-disk observations contain a wealth of spatial and spectral information. Increasingly, simulations seeking to understand these observations require a more comprehensive treatment of disk physics, and we have written our three-temperature scheme with the aim of meeting this need.

In the past several years, several promising tools have come online which promise to deepen our understanding of disk-planet interaction. JWST's Mid-Infrared Instrument (MIRI) is an excellent tool for observing super-Jupiter, planetary-mass companions, enabling direct tests of whether or not large-scale disk substructure is connected with a planetary driver. The telescope's NIRSpec instrument offers unprecedented spectral resolution, with a particular focus on molecules such as H_2O and organics relevant to the origins of life. Mid-infrared interferometers such as VLTI/GRAVITY and VLTI/-MATISSE have achieved sub-au resolution on protoplanetary disks, allowing them to detect planet-driven substructures at orbital separations coinciding with observed populations of extrasolar planets (GRAVITY Collaboration et al., 2021; Gravity Collaboration et al., 2023). In what follows, we recapitulate the investigations carried out on this thesis, and describe how future extensions can help make the most of the increasingly detailed, multiwavelength observations.

7.1 SUMMARY OF THESIS WORK

In this thesis, we describe the development and application of a "three-temperature" (3T) scheme for radiation hydrodynamics. This scheme is built upon the existing implicit-explicit (IMEX) radiation module (Melon Fuksman and Mignone, 2019) in the PLUTO hydrodynamics code (Mignone et al., 2007), which uses an explicit M1 method (Levermore, 1984) with a "reduced-speed-of-light" approximation (see Melon Fuksman et al., 2021, and references therein) to carry out radiation transport, while using an implicit solver to handle energy exchange between matter and radiation. We have updated this module to **self-consistently account for energy exchange between gas, dust, and radiation**, incorporating both absorption/emission (principally by the dust, which supplies most of the opacity) and gas-grain collisions. 3T offers a distinct advantage in the upper layers of a protoplanetary disk, where the low density of gas and dust mean that heating and cooling are limited by the collision rate. In chapter 4, we verified the function of our method in controlled tests, before demonstrating its applicability to

open problems in protoplanetary disk physics, such as the self-shadowing instability and disk-planet interaction.

With the 3T scheme, we have **revisited the classical problem of Lindblad spiral excitation** in protoplanetary disks. In chapter 5, we **compared four prescriptions for disk thermodynamics**: local isothermality, β-cooling, two-temperature (2T; matter, radiation) radiation hydrodynamics, and full 3T. The 2T scheme falls short in the upper atmosphere, where perfect dust-gas coupling means that PdV work done by spiral density waves is immediately radiated away, (in contradiction to observations of temperature spirals in TW Hya; see Teague et al., 2019). β-cooling assumes a constant background temperature, and inherently cannot account for changes in disk illumination during the simulation (such as exposure/shadowing of different disk regions from a changed density distribution, or planetary accretion luminosity). We concluded that 3T is the **best way to obtain thermal and kinematic signatures** of protoplanets, particularly **massive or luminous ones that alter radiation transport within the disk**.

In a follow-up project (chapter 6), we have run these simulations long enough for planetary torques to excavate a gap in the disk. With β-cooling, a picture qualitatively similar to the isothermal simulations of Fung, Shi, and Chiang, 2014b is recovered, with modifications to gap depth with respect to cooling rate (Zhang, Huang, and Dong, 2024). With 3T, radiation couples to asymmetries at the outer edges of sufficiently deep gaps to create temperature asymmetries. These, in turn, excite prominent $m = 2$ spiral arms (Montesinos and Cuello, 2018) in the disk's upper atmosphere—much larger in scale than the Lindblad spirals driven by the Saturn- and Jupiter-mass planets we simulate—while leaving the midplane largely untouched.

In near-infrared mock images generated with the Monte Carlo radiative transfer (MCRT) code RADMC3D, **these spirals resemble those found in VLT/SPHERE observations of MWC 758 and SAO 206462** among others, often held to be the inner Lindblad spirals of multi-Jupiter-mass, exterior planets. In the midplane, these spirals are comparatively weak, aligning with observations of these systems in ALMA continuum (Casassus et al., 2021; Ren et al., 2018), which traces the settled population of large dust grains. Given that recent high-sensitivity JWST observations (e.g., Cugno et al., 2024) have found no conclusive evidence for such companions in these systems, **the revelation of this alternative mechanism is especially timely.** We intend to use RADMC3D and the CASA `simobserve` tool to model the gas kinematic and thermal signatures of these gap-edge spirals, as seen in tracers such as ^{12}CO, ^{13}CO, and C^{18}O at different elevations in the disk, as a guide for what to expect in ALMA line observations of spiral systems.

7.2 FUTURE OUTLOOK

7.2.1 *Multispecies dust dynamics and thermodynamics*

A natural extension to the three-temperature scheme is to incorporate additional dust species, including those dynamically decoupled from the gas. As discussed in section 1.3.3, the rate of collisional energy exchange between dust and gas is proportional to the difference in their temperatures, and to the typical collision timescale (Burke and

Hollenbach, 1983a). For each species i (with $i = g \equiv 0$ implying gas in our notation), collisional exchange of thermal energy is given by

$$X_{gd,i} = \frac{3}{4}\rho_{d,i}\mu^{-1}t_{s,i}^{-1}\eta_{gd,i}(2k_B T_{d,i} - 2k_B T_g) \tag{140}$$

As per eq. (41) in section 1.3.4, the rate of momentum exchange follows an analogous set of equations, and is proportional to the differences in velocities (see also Krapp et al., 2024a):

$$\vec{M}_{gd,i} = -\rho_{d,i}t_{s,i}^{-1}\left(\vec{v}_d - \vec{v}_g\right) \tag{141}$$

These terms could be augmented with the standard terms for the exchange of energy and momentum between the radiation field, and the gas/dust species simulated (Melon Fuksman and Mignone, 2019). As with the existing 3T scheme, these equations could be solved using an iterative, multidimensional Newton's method, using a row-reduction approach (e.g., Krapp et al., 2024a) to reduce the size of the Jacobian matrix at each iteration to improve computational efficiency. Turbulent diffusion, which sets the thickness of the larger, well-settled dust grains, could be implemented using the procedure outlined in Huang and Bai (2022).

7.2.2 *Applications*

To generate mock observations, the density, velocity, and temperature fields for gas and all relevant dust species are passed into Monte Carlo radiative-transfer (MCRT) tools like `RADMC3D` (Dullemond et al., 2012, see also chapter 6 for an example of use), and subsequently to instrument-specific reduction pipelines (in the simplest case a simple beam convolution and distance rescaling, for more detailed investigations a tool such as `CASA` (CASA Team et al., 2022) for ALMA). With the current state of the art, simulations cannot provide all of these fields simultaneously, and one must choose between properly simulating either the background temperature (3T) or the dust dynamics (e.g., Huang and Bai, 2022). The missing values must be estimated: prescriptions for vertical settling and pressure-bump trapping of larger dust grains, an assumption of gas-dust temperature equilibrium, a temperature profile computed as a power law or from the MCRT. Although they can be tuned to fit observations, such equilibrium prescriptions are subject to human bias and may be at odds with the dynamical scenario probed by the simulations.

In contrast to this prevailing approach, the proposed multispecies-radiation method would evaluate densities, velocities, and temperatures for all dust and gas simultaneously, using the same internally consistent set of equations. The resulting mock observations, generated with MCRT tools and reduction pipelines, would likewise be consistent with one another and with the underlying physical setup probed by the simulations. Consequently, they would be usable as **testable predictions, rather than retrospective fits**, to real observations of disk substructure. If a post-processed multispecies-radiation simulation is consistent with observations in one wavelength regions (e.g., the VLT/SPHERE J-band), one could use the mock observations in other wavelength regions (e.g., ALMA continuum bands, ALMA ^{12}CO) to motivate proposals for telescope time. The resulting observations could be used to confirm or refute applicability of the physical scenario studied in the simulations to the real system.

Besides its applicability to studying large-scale disk substructure, the self-consistency of the multispecies-radiation scheme would also be immensely beneficial in the context of planet formation. A nascent, embedded planet draws material from the surrounding protoplanetary disk into its Hill sphere, where it forms a *circumplanetary disk* (CPD). CPD morphology is shaped by the interplay of gas flows, dust dynamics (Krapp et al., 2024b), and planetary accretion luminosity (Muley, Melon Fuksman, and Klahr, 2024b). These factors, in turn, influence the delivery of solids and chemicals to the planet and thus its final mass, density, and atmospheric composition. While simulations of CPDs around high-mass planets would be most directly useful to generate predictions for direct-imaging observations (e.g., with VLT/SPHERE or JWST), the key output of simulations involving lower-mass planets would be the mix of accreted solids. This could be compared to observations, and help link the densities and compositions of the observed exoplanet population (including the so-called "radius valley"; e.g., Burn et al., 2024) to the circumstances of their formation.

Part IV

APPENDIX

A

TESTS AND APPLICATIONS TO PROTOPLANETARY DISKS

A.1 NEWTON-RAPHSON ITERATIONS

We rearrange eqs. (97a) and (97b) as a vector of quantities $\vec{P}(\vec{\xi}_{\rm sub}^{\,i+1}) \equiv (P_d, P_g)^\top$, where $\vec{\xi}_{\rm sub}^{\,i+1} \equiv (\xi_d^{i+1}, \xi_g^{i+1})$.

$$\begin{aligned} P_d = {} & \xi_d^i - \xi_d^{i+1} - t_c^{-1}\left[r_{gd}\xi_d^{i+1} - \xi_g^{i+1}\right]\delta t \\ & - c\rho\kappa_d^{i+1} f_d\left[a_r(T_d^{i+1})^4 - \xi_r^{i+1}\right]\delta t + S_d\delta t \end{aligned} \tag{142}$$

$$\begin{aligned} P_g = {} & \xi_g^i - \xi_g^{i+1} + t_c^{-1}\left[r_{gd}\xi_d^{i+1} - \xi_g^{i+1}\right]\delta t \\ & - c\rho\kappa_g^{i+1}\left[a_r(T_g^{i+1})^4 - \xi_r^{i+1}\right]\delta t + S_g\delta t \end{aligned} \tag{143}$$

where

$$\xi_r^{i+1} = \xi_r^i - \frac{\hat{c}}{c}\left[(\xi_d^{i+1} - \xi_d^i) + (\xi_g^{i+1} - \xi_g^i)\right] \tag{144}$$

Using Newton's method, we attempt to find a vector $\vec{\xi}^{\,i+1,*}$, such that $\vec{P}(\vec{\xi}^{\,i+1,*}) = \vec{0}$ to within some small tolerance $\vec{\alpha}$. The relevant Jacobian matrix $\mathbf{J}(\vec{\xi}^{\,i+1}) \equiv \partial\vec{P}/\partial\vec{\xi}^{\,i+1}$ is:

$$\mathbf{J}(\vec{\xi}_{\rm sub}^{\,i+1}) = \begin{bmatrix} \partial P_d/\partial\xi_d^{i+1} & \partial P_d/\partial\xi_g^{i+1} \\ \partial P_g/\partial\xi_d^{i+1} & \partial P_g/\partial\xi_g^{i+1} \end{bmatrix} \tag{145}$$

where

$$\partial P_d/\partial\xi_d^{i+1} = -(1 + r_{gd}\delta t/t_c) - c\rho\kappa_d^{i+1} f_d\delta t\left[4a_r(T_d^{i+1})^3/\rho f_d c_d + \hat{c}/c\right] \tag{146}$$

$$\partial P_d/\partial\xi_g^{i+1} = +\delta t/t_c - \hat{c}\rho\kappa_d^{i+1} f_d\delta t \tag{147}$$

$$\partial P_g/\partial\xi_d^{i+1} = +r_{gd}\delta t/t_c - \hat{c}\rho\kappa_g^{i+1}\delta t \tag{148}$$

$$\partial P_g/\partial\xi_g^{i+1} = -(1 + \delta t/t_c) - c\rho\kappa_g^{i+1}\delta t\left[4a_r(T_g^{i+1})^3/\rho c_g + \hat{c}/c\right] \tag{149}$$

We omit terms dependent on the derivatives of opacity and cooling time, although (these being, in general, functions of temperature) we update them with each iteration of Newton's method. The update goes as:

$$\mathbf{J}(\vec{\xi}_n^{\,i+1})\left[\vec{\xi}_{n+1}^{\,i+1} - \vec{\xi}_n^{\,i+1}\right] = -\vec{P}_n \tag{150}$$

where n is an iteration index, in contrast to the timestep index i.

A.2 SELF-SHADOWING INSTABILITY WITH LONG COUPLING TIMES

Our investigation in Section 4.3.3 found that, just as in the two-temperature case, our "realistic" three-temperature disk with self-consistently evaluated dust-gas coupling times cannot sustain the self-shadowing instability (SSI). This result, however, leaves open the question of whether there is any circumstance under which three-temperature dynamics could favor the survival of the SSI. To study this possibility, we ran a simulation with dust-gas coupling times $100\times$ larger than those in the realistic run in Section 4.3.3. To facilitate comparison with our previous results, we hold all other simulation parameters—including, crucially, the dust opacity prescription and dust-to-gas ratio—fixed. Formally, solving for t_s in Equation 133, this would imply a Stokes number $\mathrm{St} \approx 0.06$ for grains at the $\tau_r = 1$ surface, which can be expected to experience vertical drift. However, we emphasize that this $100\times$-cooling setup is artificial, and is designed to approximate and long relaxation times that arise in disk upper atmospheres in detailed calculations of grain growth, settling, and depletion (see e.g., Bae, Teague, and Zhu, 2021b, for one such scenario). The dust populations arising from these calculations are, by construction, in steady state, and do not experience net vertical drift.

In Figure 41, we plot the time evolution of T_d, T_g, and T_{ref}—normalized by the final, relaxed reference temperature T_{relax}—in a fiducial disk column at $r = 2$ au. In the two-temperature reference simulation, the initialized self-shadowing perturbations rapidly decay (as already evident from Figure 18), but in the three-temperature $100\times$ realistic simulation, they survive for some time, as evidenced by the vertical bands in T_d and T_g between $t = 10^1 - 10^2$ y.

At the leading edge of a self-shadowing scale-height perturbation, the flaring angle of the $\tau_r = 1$ is high and intercepts more direct stellar irradiation. Although T_d reflects this change immediately, the fact that $\beta \gg 1$ in this disk region means that the response of T_g—and the consequent vertical expansion of the gas column to seek hydrostatic equilibrium—is significantly slower. As the gas column puffs up, it creates a new leading edge immediately to its interior; when this edge puffs up in turn, it blocks stellar irradiation from reaching the original column, causing it to cool and shrink. In this fashion, self-shadowing waves can propagate inward towards the star purely through vertical motions of the fluid elements. This mechanism would not operate when dust and gas are well-coupled; in that regime, both components would have a common temperature, and would respond to surface perturbations via layered radiative diffusion. The long timescale for this diffusion—given very roughly by Equation 106)—means that surface perturbations would decay before having an effect deep in the disk (Melon Fuksman and Klahr, 2022).

For a more quantitative view, we present in Figure 42 the time evolution of T_d, T_g, and T_{ref} at $r = 2$ au and $\theta = \pi/2 + \{0.0, 0.088\}$ (the latter θ corresponding to 3 scale heights above the midplane). At both altitudes, T_{ref} relaxes almost immediately to its hydrostatic equilibrium value, where it remains for the rest of the simulation. The evolution of T_d and T_g is more complex. High in the disk, the dust temperature rises interior to self-shadowing bumps, and drops exterior to them; with some delay due to gas cooling parameters $\beta \approx 1$, T_d relaxes toward T_g and the interior and exterior gas columns adapt to the new hydrostatic equilibrium. The net result, as mentioned earlier and in line with typical expectations for the SSI, is the apparent inward propagation

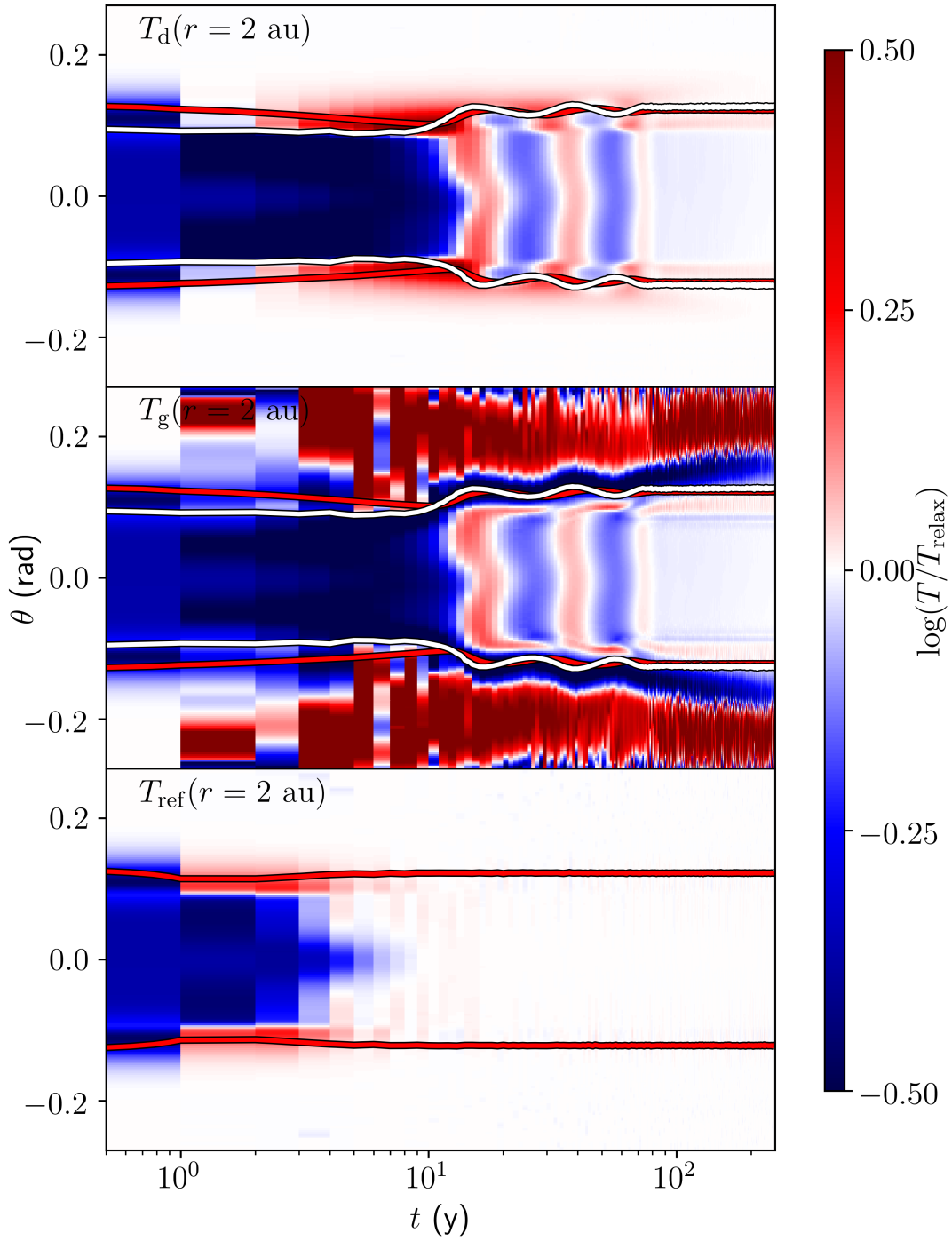

Figure 41: A plot similar to our Figure 19, but with T_d and T_g taken from our simulation with cooling times artificially raised by a factor of 100. There are clear vertical patterns in the dust and gas temperature profiles, corresponding to inward-traveling perturbations at the $\tau_r = 1$ surface characteristic of the SSI.

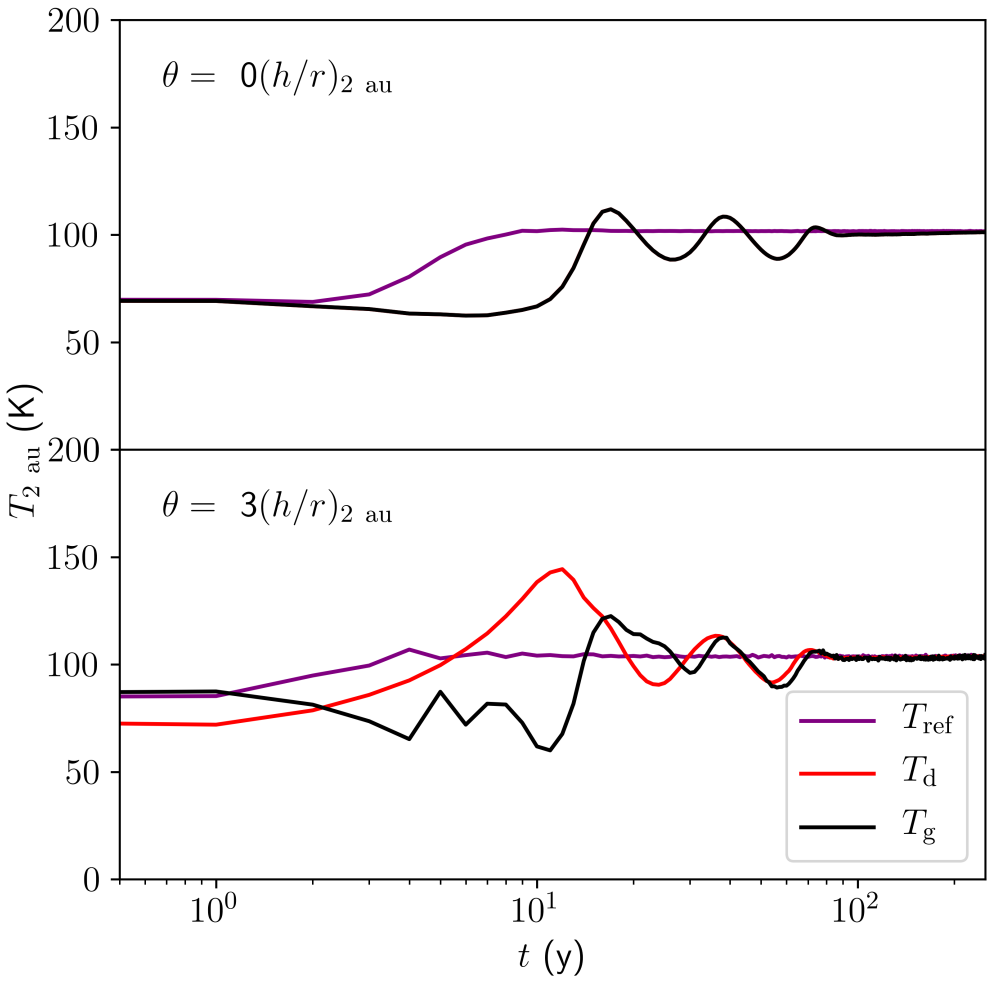

Figure 42: Quantitative time evolution of T_d and T_g from the 100×-realistic simulation, and T_{ref} in the reference simulation, at $r = 2$ au, both in the midplane ($\theta = 0$, *above*) and 3 scale heights above it ($\theta \approx 0.088$, *below*). As qualitatively shown in Figure 41, T_{ref} reaches a smooth equilibrium, whereas T_d and T_g exhibit damped oscillations due to the passage of self-shadowing waves. See text for more details.

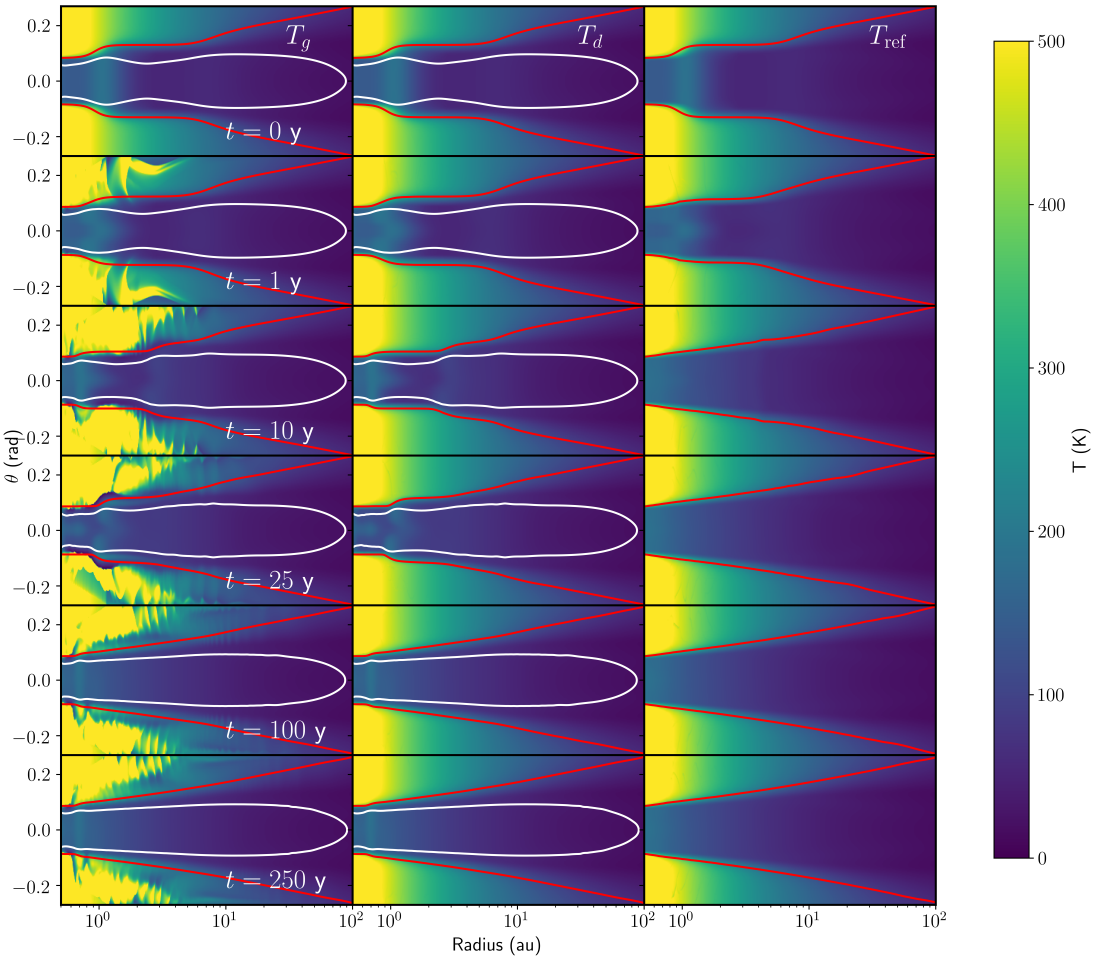

Figure 43: Evolution of the SSI with a dust-gas coupling time 100× longer than in the self-consistent setup presented in 4.3.3. An inward-propagating SSI bump is clearly visible. At t = 250 y, the disk has largely relaxed to the same configuration as in the reference simulation. Differences do persist, however, outside the β = 1 surface and near the inner boundary.

of self-shadowing bumps. The changes these bumps make to the disk's illumination profile impact the midplane temperature, albeit with some delay and attenuation due to radiative diffusion.

In Figure 43, we present snapshots of the full long-coupling disk at selected times. Puffed-up disk columns heated above the background temperature—a hallmark signature of self-shadowing waves—are clearly visible here, and are captured n Figures 41 and 42 as they travel inward through r = 2 au. By t = 250 y, however, the long-cooling disk has largely relaxed to the same smooth equilibrium as the reference disk. Differences persist in the very slowly-cooling disk atmosphere, as well as in the $r \lesssim 1$ au region in the immediate vicinity of our fixed inner radial boundary.

B

THERMAL AND KINEMATIC SIGNATURES OF ACCRETING PROTOPLANETS

B.1 SKY-PROJECTED FIGURES

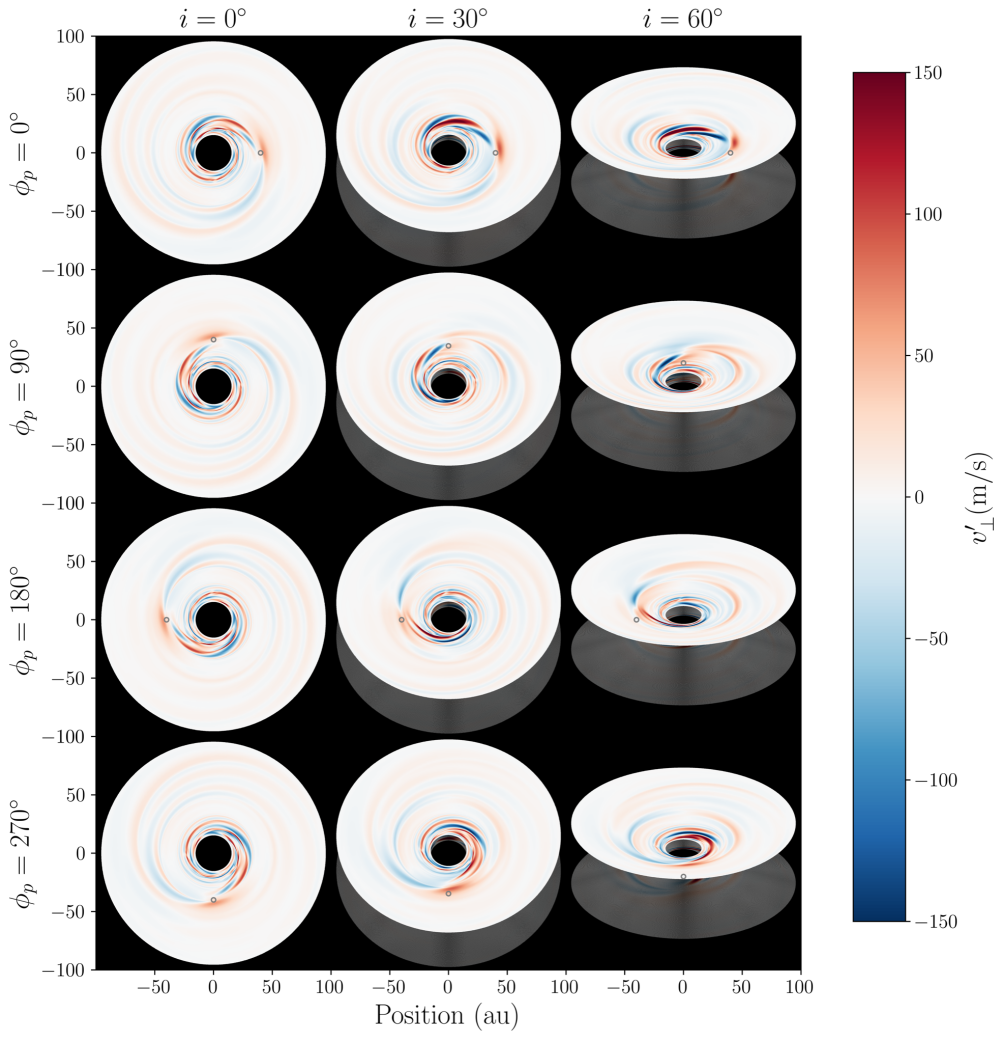

Figure 44: Sky-projected velocity perturbation $v'_\perp$ for our fiducial Saturn-mass planet, in a cut at $\theta = 0.3$ radians above the midplane.

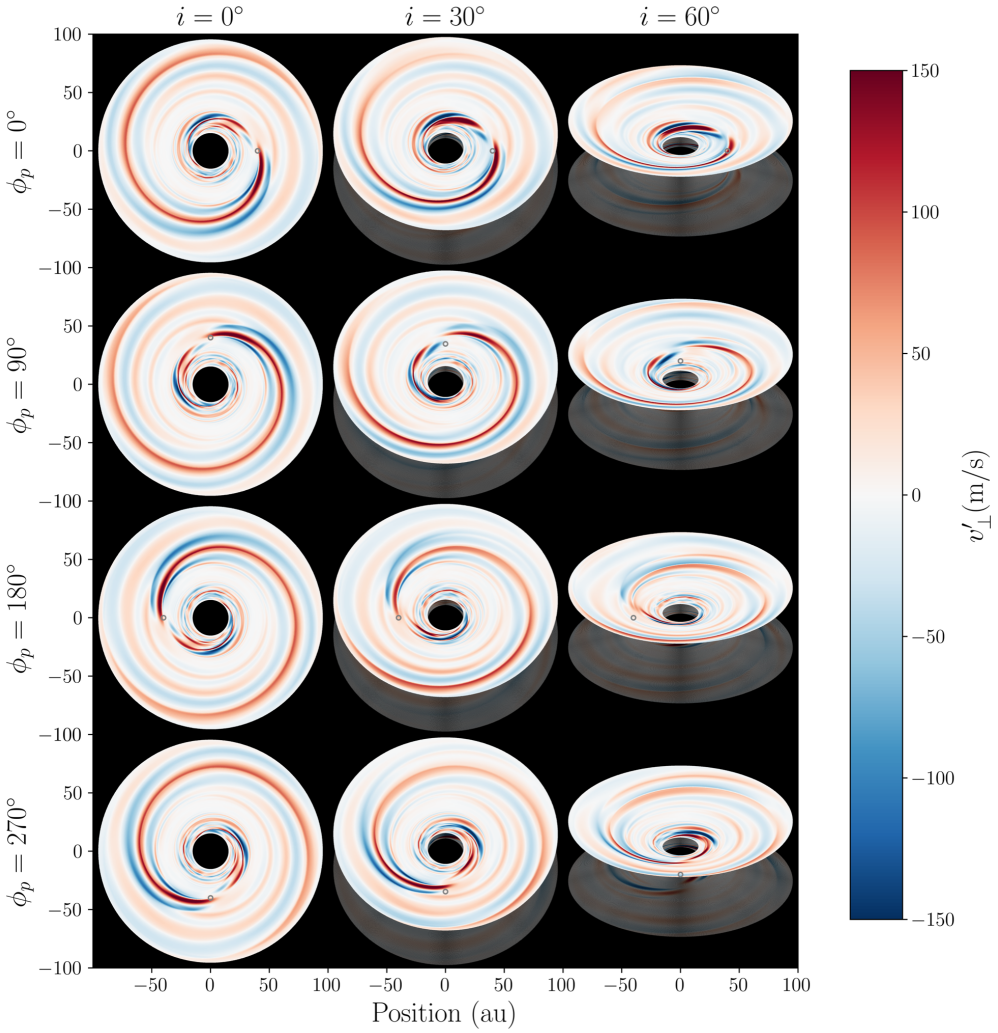

Figure 45: Sky-projected velocity perturbation $v'_\perp$ for a Saturn-mass planet with an accretion luminosity $L_{acc,p} = 10^{-3} L_\odot$. Compared to the fiducial case, the outer spiral becomes significantly stronger and extends through a larger radial range of the disk.

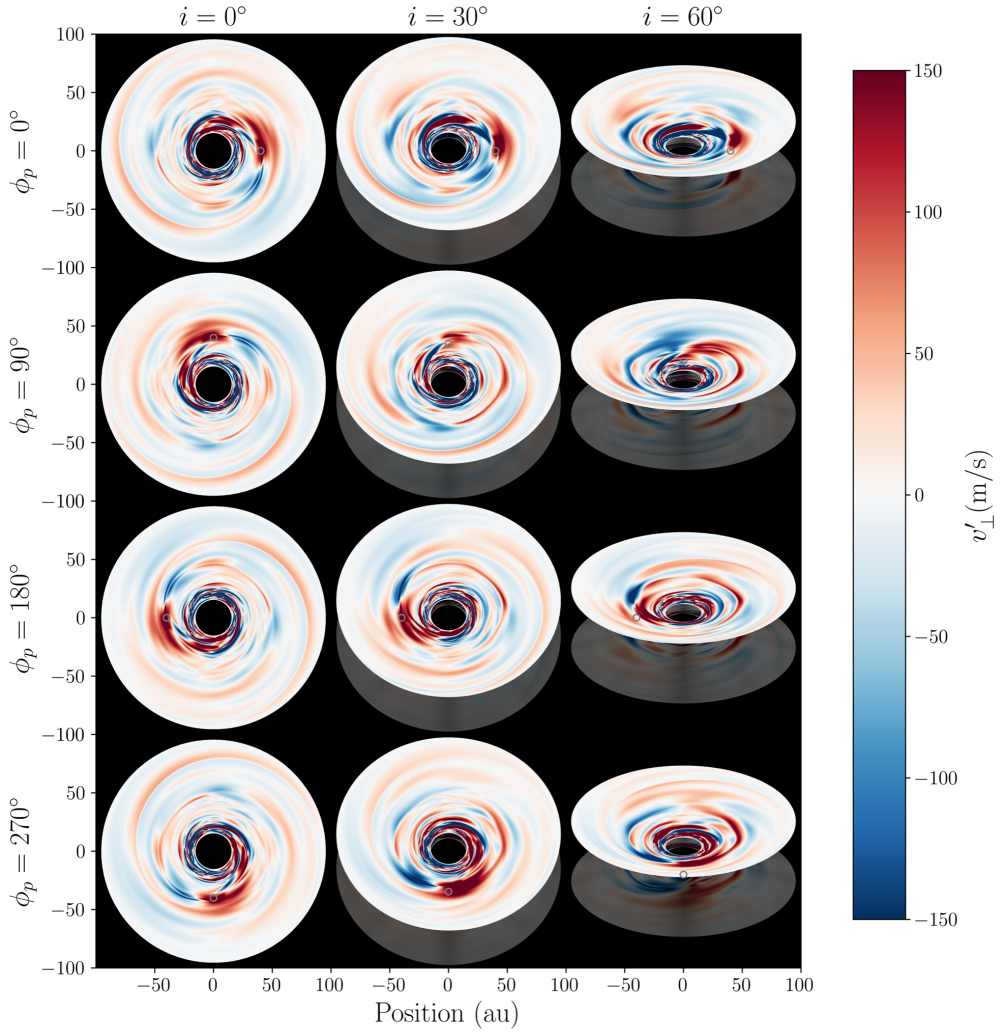

Figure 46: Sky-projected velocity perturbation $v'_\perp$ for a Jupiter-mass planet, with no accretion luminosity. Relative to the fiducial case, circumplanetary and in-gap flow patterns are significantly stronger.

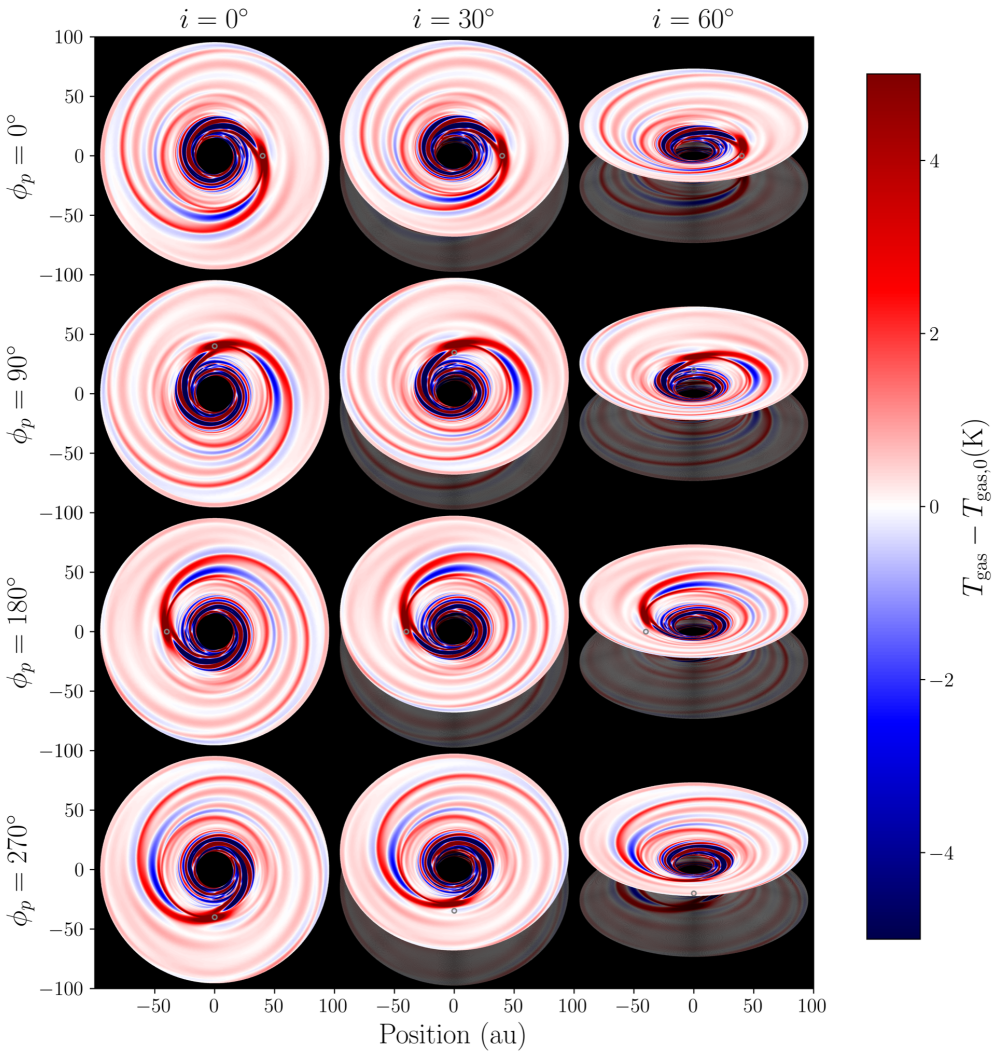

Figure 47: Perturbation in gas temperature $T_g - T_{g,0}$ at $\theta = 0.3$ above the midplane, for our fiducial setup with a Saturn-mass, non-accreting planet. The double-armed structure of the Lindblad spiral in the upper atmosphere is clearly visible here.

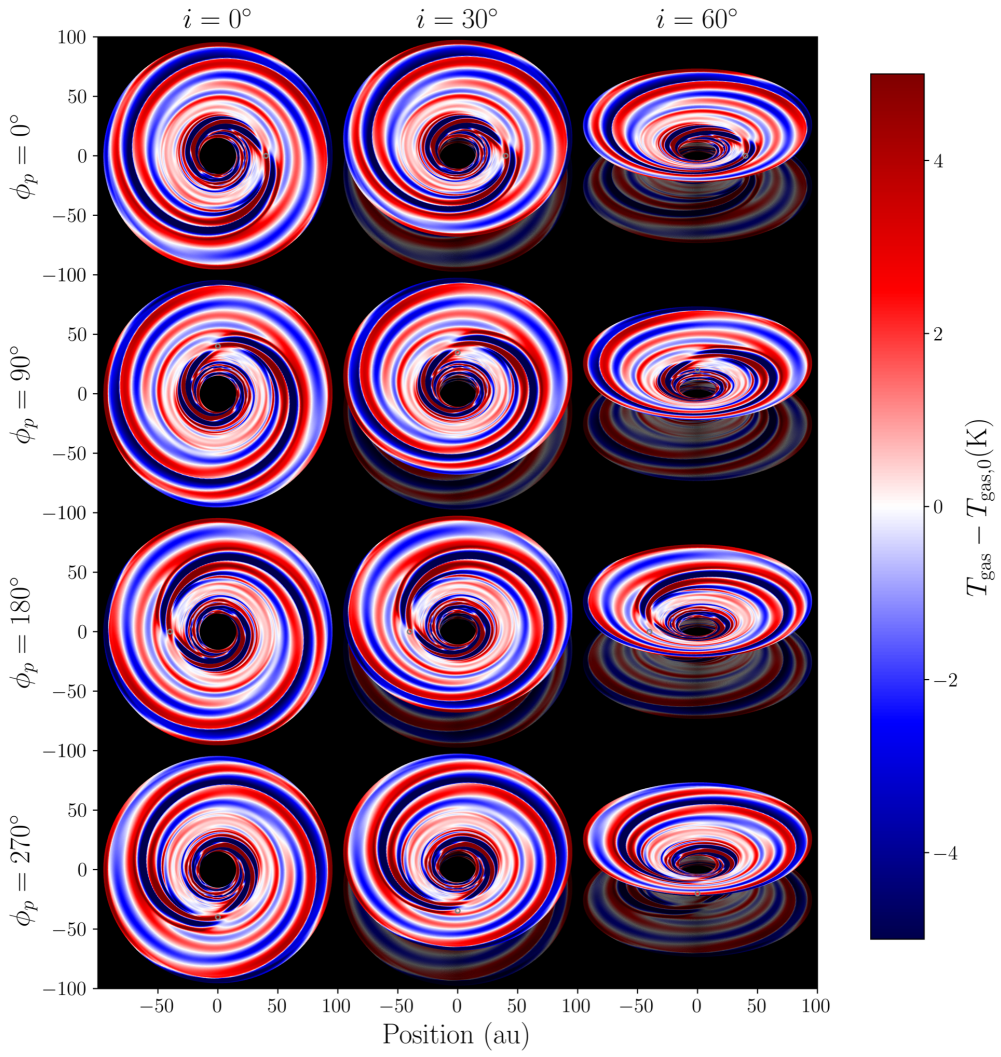

Figure 48: Gas temperature perturbation for an accreting, Saturn-mass planet. As with the kinematic spiral, the thermal spiral extends over a larger radial range and is more prominent than in the non-accreting case.

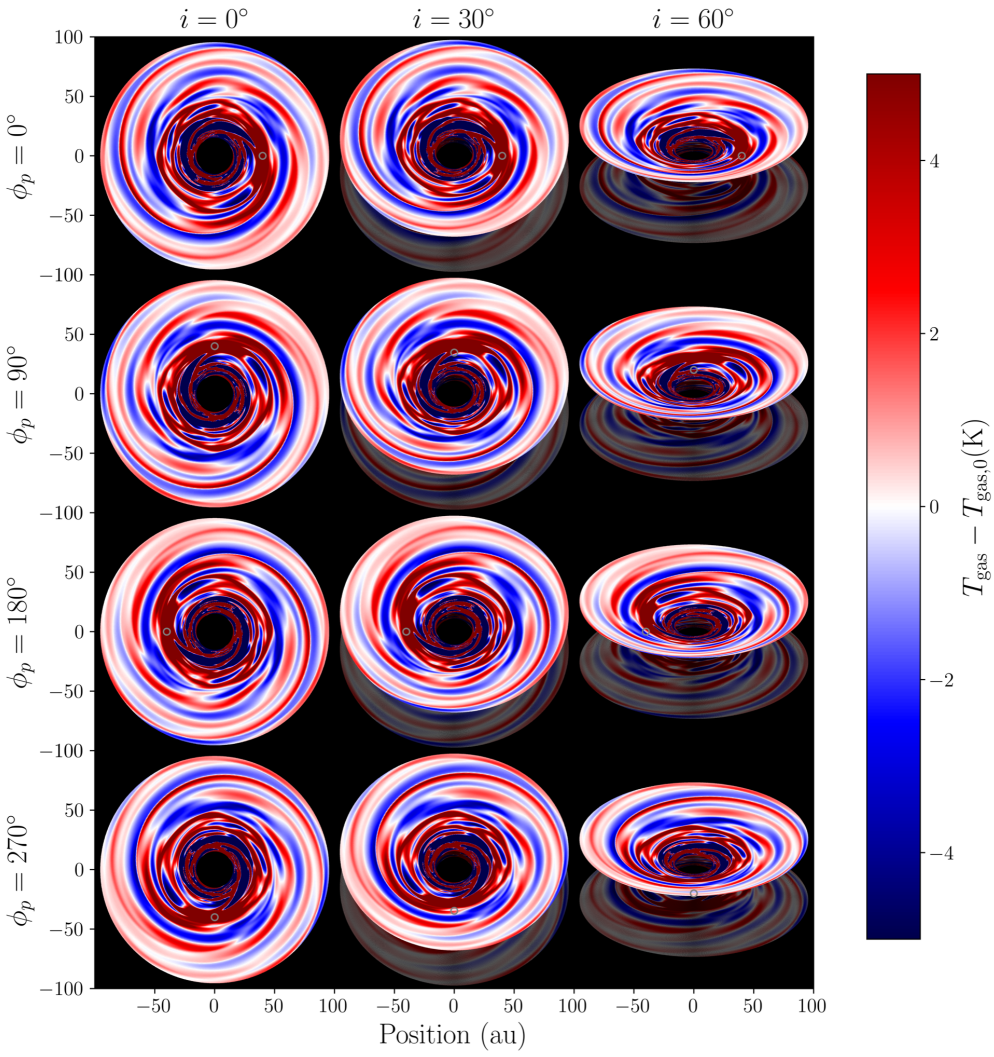

Figure 49: Gas temperature perturbation for a Jupiter-mass planet. As with kinematics, the circumplanetary region and gap make a much larger contribution to the thermal signature than in the fiducial Saturn-mass, non-accreting case.

B.2 ADVECTIVE TERMS IN SPHERICAL COORDINATES

For a scalar quantity such as density or temperature, the rate of change at a specific location due to advection in any given direction is given by the (negative) gradient of the scalar, projected along the velocity in that direction. The advection of perturbations is given by the advective term in the current state, minus advection in the initial condition.

Making use of the fact that our initial condition is axisymmetric in all variables, and that $v_r(t=0) = v_\theta(t=0) \equiv 0$, we can write the evolution of the density perturbation ρ' as:

$$\left.\frac{\partial \rho'}{\partial t}\right|_{\text{advr}} = -v_r' \partial_r \rho \tag{151a}$$

$$\left.\frac{\partial \rho'}{\partial t}\right|_{\text{adv}_{\theta}} = -\frac{v_\theta'}{r} \partial_\theta \rho \tag{151b}$$

$$\left.\frac{\partial \rho'}{\partial t}\right|_{\text{advffi}} = -\frac{v_\phi}{r \sin\theta} \partial_\phi \rho \tag{151c}$$

and that of the gas temperature perturbation T_g' as

$$\left.\frac{\partial T_g'}{\partial t}\right|_{\text{advr}} = -v_r' \partial_r T_g \tag{152a}$$

$$\left.\frac{\partial T_g'}{\partial t}\right|_{\text{adv}_{\theta}} = -\frac{v_\theta'}{r} \partial_\theta T_g \tag{152b}$$

$$\left.\frac{\partial T_g'}{\partial t}\right|_{\text{adv}_{\theta}} = -\frac{v_\phi'}{r \sin\theta} \partial_\phi T_g \tag{152c}$$

For vectors, such as velocity, the advection term includes not only partial derivatives of each component in each coordinate, but also geometric connection terms arising from the change in the basis vectors themselves as a function of coordinate. This yields the following advective terms in each direction:

$$\left.\frac{\partial \vec{v}'}{\partial t}\right|_{\text{advr}} = -v_r' \left[\partial_r v_r' \hat{\vec{r}} + \partial_r v_\theta' \hat{\vec{\theta}} + \partial_r v_\phi \hat{\vec{\phi}}\right] \tag{153a}$$

$$\left.\frac{\partial \vec{v}'}{\partial t}\right|_{\text{adv}_{\theta}} = -\frac{v_\theta'}{r} \left[\left(\partial_\theta v_r' - v_\theta'\right) \hat{\vec{r}} + \left(\partial_\theta v_\theta' + v_r'\right) \hat{\vec{\theta}} + \left(\partial_\theta v_\phi' + \partial_\theta v_{0,\phi}\right) \hat{\vec{\phi}}\right] \tag{153b}$$

$$\begin{aligned}\left.\frac{\partial \vec{v}'}{\partial t}\right|_{\text{advffi}} =& -\frac{v_\phi}{r \sin\theta} \left[\partial_\phi v_r' \hat{\vec{r}} + \partial_\phi v_\theta' \hat{\vec{\theta}} + \left(\partial_\phi v_\phi + v_r \sin\theta + v_\theta \cos\theta\right) \hat{\vec{\phi}}\right] \\ &+ \frac{v_\phi^2 - v_{\phi,0}^2}{r \sin\theta} \left(\sin\theta \hat{\vec{r}} + \cos\theta \hat{\vec{\theta}}\right)\end{aligned} \tag{153c}$$

We emphasize that despite considering only advection in one given coordinate direction, each of the expressions in Equation 153 has three components, arising from the advection of velocity components orthogonal to the advection direction, as well as the aforementioned geometric connection terms. For ease of interpretation, in Figure 29, we define the in-plane advection as the sum $(\partial\vec{v}'/\partial t)_{\mathrm{adv,in-plane}} = (\partial\vec{v}'/\partial t)_{\mathrm{advr}} + (\partial\vec{v}'/\partial t)_{\mathrm{advffi}}$.

C

CAN GAP-EDGE ILLUMINATION EXCITE SPIRALS IN PROTOPLANETARY DISKS?

C.1 VORTICITY OF THE FLOW FIELD

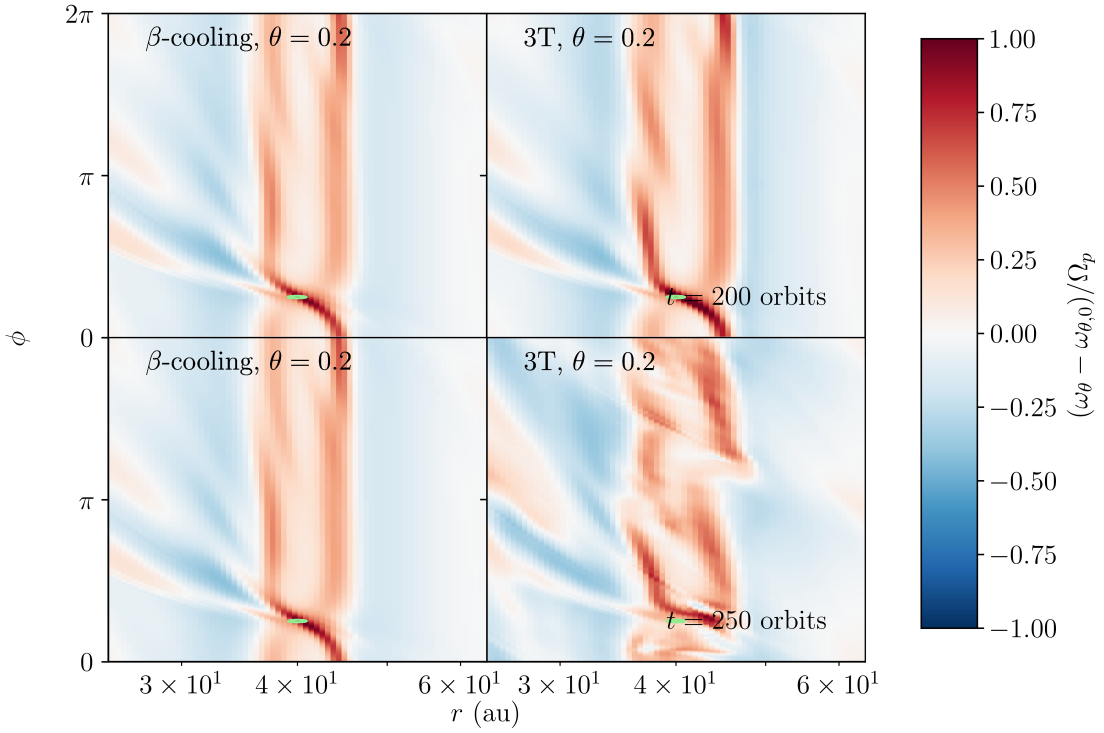

Figure 50: θ-component of vorticity at θ = 0.2, with respect to the initial condition, in units of the planet's orbital frequency Ω_p. Between 200 and 250 orbits, the vorticity profile is largely unchanged in the β-cooling simulations, but deviates strongly in the 3T case as radiation couples to the asymmetries generated by disk-planet interaction.

The vorticity provides a complementary view to that offered by Fig. 38, emphasizing the gap itself rather than the spiral arms. In Fig. 50 we plot the polar component of vorticity, $\omega_\theta = (\nabla \times \vec{v}) \cdot \hat{\theta}$, for our simulations with $M_p = 3 \times 10^{-4} M_\odot$, comparing the β-cooling and 3T prescriptions side-by-side. At t = 200 orbits, right at the onset of the instability described in 6.3.1, the vorticity profile is similar between simulations. At t = 250 orbits, the gap profile with β-cooling remains intact, but that with 3T is substantially disrupted at the outer edge, causing spiral density waves to be launched.

With 3T, the gap profile bears some resemblance to that caused by the irradiation instability of Fung, Shi, and Chiang (2014a). However, the instability that they study is a consequence of radiation pressure directly influencing gas momentum, rather than radiative heating altering the disk's vertical structure. In this latter respect, the simulated

mechanism can be analogized to the self-shadowing instability of Wu and Lithwick (2021).

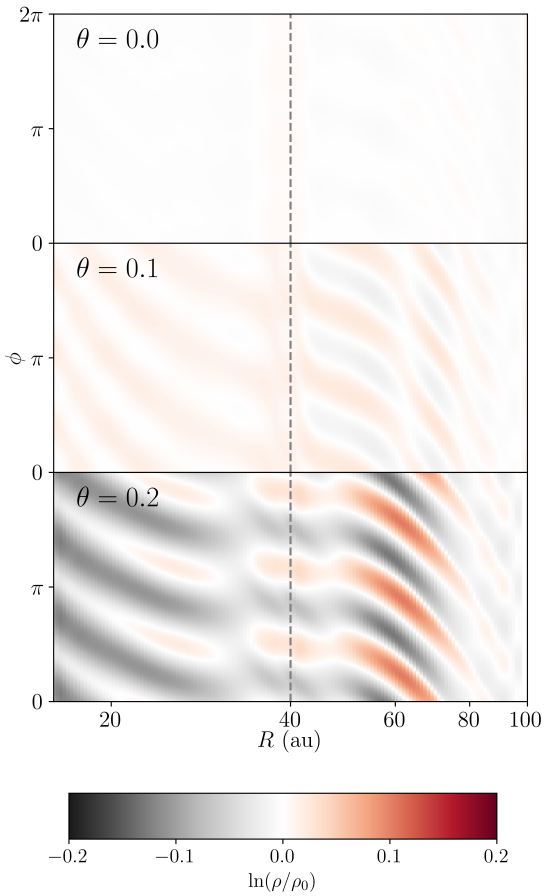

Figure 51: Density perturbation in special β-cooling simulations where the planet is removed, and for which the temperature profile in Fig. 23 is multiplied by the azimuthal perturbation factor $\mathcal{W}_T(\phi, t)$ (Eq. 154). The corotation radius of the temperature profile, equal to the planet radius in the main text, is plotted as a dotted vertical line. Note that the density scale has a much smaller range than in Fig. 38 in the main text.

C.2 β-COOLING TESTS

To validate our hypothesized mechanism for the generation of spirals, we ran β-cooling simulations with no planet. We used the same background temperature profile as in the main text, but multiplied it everywhere by an azimuthally varying factor of

$$\mathcal{W}_T(\phi, t) = 1 + f_t \sin(\theta) \sin(m(\phi - \Omega_p t)) \exp\left(-(r/r_T)^{-4}\right), \tag{154}$$

where $f_t = 0.25$, Ω_p is the Keplerian orbital frequency at $r_p = 40$au, and $r_T = 32$ au. We choose an $m = 3$, as opposed to the $m = 2$ the observed system settles into, to show the full generality of the mechanism. Although the temperature deviation is at most 10% within the domain, the effect it has on the disk's vertical structure means that the spiral signature becomes quite substantial in the upper atmosphere.

In Fig. 51 we plot the resulting density profile at $t = 40$ orbits, by which the system has settled into a quasi-steady state. Because the corotation radius of the temperature pattern ($r_p = 40$au) is closer than the outer gap edge in the 3T simulations, the expected outer set of spirals is also contained within the domain. In our self-consistent

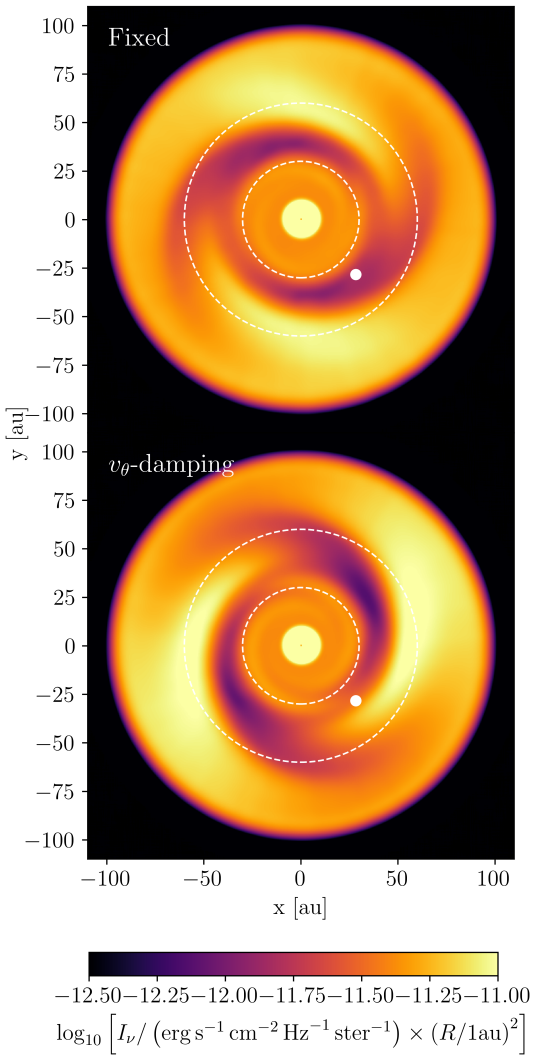

Figure 52: Mock H-band images for different wave-damping prescriptions at the boundary.

radiation-hydrodynamics runs, the RWI mediates spiral formation insofar as it creates an analogous non-axisymmetric temperature structure, rather than through direct launching (as in, e.g., Huang et al., 2019).

C.3 BOUNDARY CONDITIONS

Radiation-induced spirals — absent in our β-cooling simulations with axisymmetric background temperatures — induce strong flows in the vertical direction (formally, v_θ) in the upper layers of the disk. These, together with with our fixed condition at the upper and lower θ-boundaries of the domain, allow mass to escape from the simulation domain over long periods of time. This complicates radiation-hydrodynamic studies of planetary torques, migration, and transition-disk carving, for which an accurate surface density profile is essential.

Mass can be better conserved within the domain by strongly damping v_θ to zero in the uppermost and lowermost regions of the simulation domain (see also Chrenko

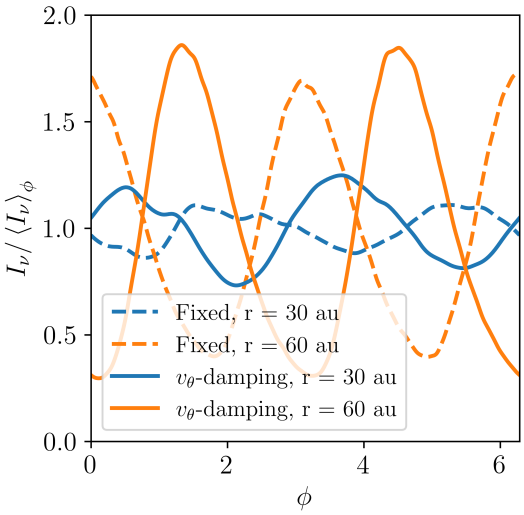

Figure 53: H-band contrast ratios from post-processed simulations with the standard fixed boundary condition, as well as the strong-damping condition.

and Nesvorný, 2020, who damped v_θ to an azimuthal average). However, this would inevitably lead to wave reflection, which could affect the development of radiation-induced spirals. To quantify this effect, we run a test where we take our fiducial low-resolution simulation for a Saturn-mass planet at 1000 orbits, institute an upper wave-damping boundary with an aggressive damping time $t_{damp} = 5 \times 10^{-3}$ orbits, and run it for another 10 orbits—enough to see changes to the spiral arms.

Figures 52 and 53 are analogous to Figs. 39 and 40 but one with the simulation at 1000 orbits with fixed boundaries, and one after 10 more orbits with the wave-damping zone implemented. The spiral is qualitatively similar, but qualitatively somewhat stronger, when reflective boundaries are used. An analogous test with the polar boundaries extended to $\theta = \pm 0.6$ above and below the midplane, as well as another with the fiducial θ-extent, but where reflective polar boundaries are used from the start — neither shown here — show similar results. This demonstrates the robustness of our conclusions with respect to numerical prescription, and clears the way to use reflecting boundary conditions to model upper-disk and midplane dynamics simultaneously.

BIBLIOGRAPHY

Adams, Fred C., Charles J. Lada, and Frank H. Shu (Mar. 1988). "The Disks of T Tauri Stars with Flat Infrared Spectra." In: *ApJ* 326, p. 865. DOI: 10.1086/166144.

Armitage, Philip J. (2020). *Astrophysics of planet formation, Second Edition*.

Armitage, Philip J. and Wilhelm Kley (Jan. 2019). "From Protoplanetary Disks to Planet Formation." In: *From Protoplanetary Disks to Planet Formation: Saas-Fee Advanced Course 45. Swiss Society for Astrophysics and Astronomy*. DOI: 10.1007/978-3-662-58687-7.

Artymowicz, Pawel (Dec. 1993). "On the Wave Excitation and a Generalized Torque Formula for Lindblad Resonances Excited by External Potential." In: *ApJ* 419, p. 155. DOI: 10.1086/173469.

Asensio-Torres, R. et al. (Aug. 2021). "Perturbers: SPHERE detection limits to planetary-mass companions in protoplanetary disks." In: *A&A* 652, A101, A101. ISSN: 1432-0746. DOI: 10.1051/0004-6361/202140325. arXiv: 2103.05377 [astro-ph.EP]. URL: http://dx.doi.org/10.1051/0004-6361/202140325.

Bae, Jaehan, Richard Teague, and Zhaohuan Zhu (May 2021a). "Observational Signature of Tightly Wound Spirals Driven by Buoyancy Resonances in Protoplanetary Disks." In: *ApJ* 912.1, 56, p. 56. DOI: 10.3847/1538-4357/abe45e. arXiv: 2102.03899 [astro-ph.EP].

— (May 2021b). "Observational Signature of Tightly Wound Spirals Driven by Buoyancy Resonances in Protoplanetary Disks." In: *ApJ* 912.1, 56, p. 56. DOI: 10.3847/1538-4357/abe45e. arXiv: 2102.03899 [astro-ph.EP].

Bae, Jaehan and Zhaohuan Zhu (June 2018a). "Planet-driven Spiral Arms in Protoplanetary Disks. I. Formation Mechanism." In: *ApJ* 859.2, 118, p. 118. DOI: 10.3847/1538-4357/aabf8c. arXiv: 1711.08161 [astro-ph.EP].

— (June 2018b). "Planet-driven Spiral Arms in Protoplanetary Disks. II. Implications." In: *ApJ* 859.2, 119, p. 119. DOI: 10.3847/1538-4357/aabf93. arXiv: 1711.08166 [astro-ph.EP].

Bae, Jaehan, Zhaohuan Zhu, Clément Baruteau, Myriam Benisty, Cornelis P. Dullemond, Stefano Facchini, Andrea Isella, Miriam Keppler, Laura M. Pérez, and Richard Teague (Oct. 2019). "An Ideal Testbed for Planet-Disk Interaction: Two Giant Protoplanets in Resonance Shaping the PDS 70 Protoplanetary Disk." In: *ApJ* 884.2, L41, p. L41. DOI: 10.3847/2041-8213/ab46b0. arXiv: 1909.09476 [astro-ph.EP].

Balbus, Steven A. and John F. Hawley (July 1991). "A Powerful Local Shear Instability in Weakly Magnetized Disks. I. Linear Analysis." In: *ApJ* 376, p. 214. DOI: 10.1086/170270.

Barker, A. J. and H. N. Latter (June 2015). "On the vertical-shear instability in astrophysical discs." In: *MNRAS* 450.1, pp. 21–37. DOI: 10.1093/mnras/stv640. arXiv: 1503.06953 [astro-ph.SR].

Barraza-Alfaro, Marcelo, Mario Flock, and Thomas Henning (Oct. 2023). "Kinematic signatures of planet-disk interactions in VSI-turbulent protoplanetary disks." In:

arXiv e-prints, arXiv:2310.18484, arXiv:2310.18484. DOI: 10.48550/arXiv.2310.18484. arXiv: 2310.18484 [astro-ph.EP].

Baruteau, Clément and Frédéric Masset (2013). "Recent Developments in Planet Migration Theory." In: *Tides in Astronomy and Astrophysics*. Ed. by Jean Souchay, Stéphane Mathis, and Tadashi Tokieda. Berlin, Heidelberg: Springer Berlin Heidelberg, pp. 201–253. ISBN: 978-3-642-32961-6. DOI: 10.1007/978-3-642-32961-6_6. URL: https://doi.org/10.1007/978-3-642-32961-6_6.

Bate, Matthew R. and Eric R. Keto (May 2015). "Combining radiative transfer and diffuse interstellar medium physics to model star formation." In: *MNRAS* 449.3, pp. 2643–2667. DOI: 10.1093/mnras/stv451. arXiv: 1503.05369 [astro-ph.SR].

Benisty, M. et al. (2017). "Shadows and spirals in the protoplanetary disk HD 100453." In: *A&A* 597, A42. DOI: 10.1051/0004-6361/201629798. URL: https://doi.org/10.1051/0004-6361/201629798.

Benisty, M. et al. (June 2015). "Asymmetric features in the protoplanetary disk MWC 758." In: *A&A* 578, L6, p. L6. DOI: 10.1051/0004-6361/201526011. arXiv: 1505.05325 [astro-ph.SR].

Benítez-Llambay, Pablo, Leonardo Krapp, and Martin E. Pessah (Apr. 2019). "Asymptotically Stable Numerical Method for Multispecies Momentum Transfer: Gas and Multifluid Dust Test Suite and Implementation in FARGO3D." In: *ApJS* 241.2, 25, p. 25. DOI: 10.3847/1538-4365/ab0a0e. arXiv: 1811.07925 [astro-ph.EP].

Benítez-Llambay, Pablo and Frédéric S. Masset (Mar. 2016). "FARGO3D: A New GPU-oriented MHD Code." In: *ApJS* 223.1, 11, p. 11. DOI: 10.3847/0067-0049/223/1/11. arXiv: 1602.02359 [astro-ph.IM].

Bi, Jiaqing, Min-Kai Lin, and Ruobing Dong (May 2021). "Puffed-up Edges of Planet-opened Gaps in Protoplanetary Disks. I. Hydrodynamic Simulations." In: *ApJ* 912.2, 107, p. 107. DOI: 10.3847/1538-4357/abef6b. arXiv: 2103.09254 [astro-ph.EP].

— (Jan. 2023). "Gap-opening Planets Make Dust Rings Wider." In: *ApJ* 942.2, 80, p. 80. DOI: 10.3847/1538-4357/aca1b1. arXiv: 2210.11488 [astro-ph.EP].

Biddle, Lauren I., Brendan P. Bowler, Yifan Zhou, Kyle Franson, and Zhoujian Zhang (Feb. 2024). "Deep Paβ Imaging of the Candidate Accreting Protoplanet AB Aur b." In: *arXiv e-prints*, arXiv:2402.12601, arXiv:2402.12601. DOI: 10.48550/arXiv.2402.12601. arXiv: 2402.12601 [astro-ph.EP].

Binkert, Fabian, Judit Szulágyi, and Til Birnstiel (May 2023). "Three-dimensional dust stirring by a giant planet embedded in a protoplanetary disk." In: *MNRAS*. DOI: 10.1093/mnras/stad1405.

Birnstiel, Tilman et al. (2018). "The Disk Substructures at High Angular Resolution Project (DSHARP). V. Interpreting ALMA Maps of Protoplanetary Disks in Terms of a Dust Model." In: *The Astrophysical Journal Letters* 869.2, p. L45. DOI: 10.3847/2041-8213/aaf743. URL: https://dx.doi.org/10.3847/2041-8213/aaf743.

Bitsch, B., A. Boley, and W. Kley (Feb. 2013). "Influence of viscosity and the adiabatic index on planetary migration." In: *A&A* 550, A52, A52. DOI: 10.1051/0004-6361/201118490. arXiv: 1301.1516 [astro-ph.EP].

Bitsch, B., A. Crida, A. Morbidelli, W. Kley, and I. Dobbs-Dixon (Jan. 2013). "Stellar irradiated discs and implications on migration of embedded planets. I. Equilibrium discs." In: *A&A* 549, A124, A124. DOI: 10.1051/0004-6361/201220159. arXiv: 1211.6345 [astro-ph.EP].

Boehler, Y., L. Ricci, E. Weaver, A. Isella, M. Benisty, J. Carpenter, C. Grady, Bo-Ting Shen, Ya-Wen Tang, and L. Perez (Feb. 2018). "The Complex Morphology of the Young Disk MWC 758: Spirals and Dust Clumps around a Large Cavity." In: *ApJ* 853.2, 162, p. 162. DOI: 10.3847/1538-4357/aaa19c. arXiv: 1712.08845 [astro-ph.EP].

Bohren, Craig F. and Donald R. Huffman (1983). *Absorption and scattering of light by small particles*.

Boley, A. C. and R. H. Durisen (Apr. 2006). "Hydraulic/Shock Jumps in Protoplanetary Disks." In: *ApJ* 641.1, pp. 534–546. DOI: 10.1086/500396. arXiv: astro-ph/0510305 [astro-ph].

Boley, A. C., M. A. Morris, and S. J. Desch (Oct. 2013). "High-temperature Processing of Solids through Solar Nebular Bow Shocks: 3D Radiation Hydrodynamics Simulations with Particles." In: *ApJ* 776.2, 101, p. 101. DOI: 10.1088/0004-637X/776/2/101. arXiv: 1308.2968 [astro-ph.EP].

Boley, Aaron C., Thomas W. Hartquist, Richard H. Durisen, and Scott Michael (Feb. 2007). "The Internal Energy for Molecular Hydrogen in Gravitationally Unstable Protoplanetary Disks." In: *ApJ* 656.2, pp. L89–L92. DOI: 10.1086/512235. arXiv: astro-ph/0701146 [astro-ph].

Bollati, Francesco, Giuseppe Lodato, Daniel J Price, and Christophe Pinte (Apr. 2021). "The theory of kinks – I. A semi-analytic model of velocity perturbations due to planet–disc interaction." In: *Monthly Notices of the Royal Astronomical Society* 504.4, pp. 5444–5454. ISSN: 0035-8711. DOI: 10.1093/mnras/stab1145. eprint: https://academic.oup.com/mnras/article-pdf/504/4/5444/37975295/stab1145.pdf. URL: https://doi.org/10.1093/mnras/stab1145.

Brandenburg, A. and W. Dobler (Aug. 2002). "Hydromagnetic turbulence in computer simulations." In: *Computer Physics Communications* 147.1-2, pp. 471–475. DOI: 10.1016/S0010-4655(02)00334-X. arXiv: astro-ph/0111569 [astro-ph].

Bruderer, S., E. F. van Dishoeck, S. D. Doty, and G. J. Herczeg (May 2012). "The warm gas atmosphere of the HD 100546 disk seen by Herschel. Evidence of a gas-rich, carbon-poor atmosphere?" In: *A&A* 541, A91, A91. DOI: 10.1051/0004-6361/201118218. arXiv: 1201.4860 [astro-ph.SR].

Bruderer, Simon (Nov. 2013). "Survival of molecular gas in cavities of transition disks. I. CO." In: *A&A* 559, A46, A46. DOI: 10.1051/0004-6361/201321171. arXiv: 1308.2966 [astro-ph.SR].

Burke, J. R. and D. J. Hollenbach (Feb. 1983a). "The gas-grain interaction in the interstellar medium - Thermal accommodation and trapping." In: *ApJ* 265, pp. 223–234. DOI: 10.1086/160667.

— (Feb. 1983b). "The gas-grain interaction in the interstellar medium - Thermal accommodation and trapping." In: *ApJ* 265, pp. 223–234. DOI: 10.1086/160667.

Burn, Remo, Christoph Mordasini, Lokesh Mishra, Jonas Haldemann, Julia Venturini, Alexandre Emsenhuber, and Thomas Henning (Apr. 2024). "A radius valley between migrated steam worlds and evaporated rocky cores." In: *Nature Astronomy* 8, pp. 463–471. DOI: 10.1038/s41550-023-02183-7. arXiv: 2401.04380 [astro-ph.EP].

CASA Team et al. (Nov. 2022). "CASA, the Common Astronomy Software Applications for Radio Astronomy." In: *PASP* 134.1041, 114501, p. 114501. DOI: 10.1088/1538-3873/ac9642. arXiv: 2210.02276 [astro-ph.IM].

Calahan, Jenny K. et al. (Nov. 2021). "Molecules with ALMA at Planet-forming Scales (MAPS). XVII. Determining the 2D Thermal Structure of the HD 163296 Disk." In: *ApJS* 257.1, 17, p. 17. DOI: 10.3847/1538-4365/ac143f. arXiv: 2109.06202 [astro-ph.EP].

Casassus, Simon et al. (Nov. 2021). "A dusty filament and turbulent CO spirals in HD 135344B - SAO 206462." In: *MNRAS* 507.3, pp. 3789–3809. DOI: 10.1093/mnras/stab2359. arXiv: 2104.08379 [astro-ph.EP].

Chambers, J. E. (Nov. 2009). "An Analytic Model for the Evolution of a Viscous, Irradiated Disk." In: *ApJ* 705.2, pp. 1206–1214. DOI: 10.1088/0004-637X/705/2/1206.

Chiang, E. I. and P. Goldreich (Nov. 1997). "Spectral Energy Distributions of T Tauri Stars with Passive Circumstellar Disks." In: *ApJ* 490.1, pp. 368–376. DOI: 10.1086/304869. arXiv: astro-ph/9706042 [astro-ph].

Chrenko, O. and D. Nesvorný (Oct. 2020). "Migration of gap-opening planets in 3D stellar-irradiated accretion disks." In: *A&A* 642, A219, A219. DOI: 10.1051/0004-6361/202038988. arXiv: 2009.14142 [astro-ph.EP].

Chrenko, Ondřej and Michiel Lambrechts (June 2019). "Oscillatory migration of accreting protoplanets driven by a 3D distortion of the gas flow." In: *A&A* 626, A109, A109. DOI: 10.1051/0004-6361/201935334. arXiv: 1904.12497 [astro-ph.EP].

Colella, P. and Paul R. Woodward (Sept. 1984). "The Piecewise Parabolic Method (PPM) for Gas-Dynamical Simulations." In: *Journal of Computational Physics* 54, pp. 174–201. DOI: 10.1016/0021-9991(84)90143-8.

Commerçon, B., E. Audit, G. Chabrier, and J. P. Chièze (June 2011). "Physical and radiative properties of the first-core accretion shock." In: *A&A* 530, A13, A13. DOI: 10.1051/0004-6361/201016213. arXiv: 1102.2921 [astro-ph.SR].

Courant, R., K. Friedrichs, and H. Lewy (1928). "Über die partiellen Differenzengleichungen der mathematischen Physik." In: *Mathematische Annalen* 100.1, pp. 32–74. DOI: 10.1007/BF01448839. URL: https://doi.org/10.1007/BF01448839.

Crida, A. and A. Morbidelli (May 2007). "Cavity opening by a giant planet in a protoplanetary disc and effects on planetary migration." In: *MNRAS* 377.3, pp. 1324–1336. DOI: 10.1111/j.1365-2966.2007.11704.x. arXiv: astro-ph/0703151 [astro-ph].

Cuello, N., M. Montesinos, S. M. Stammler, F. Louvet, and J. Cuadra (Feb. 2019). "Dusty spirals triggered by shadows in transition discs." In: *A&A* 622, A43, A43. DOI: 10.1051/0004-6361/201731732. arXiv: 1811.08441 [astro-ph.EP].

Cugno, Gabriele et al. (Apr. 2024). "JWST/NIRCam Imaging of Young Stellar Objects. II. Deep Constraints on Giant Planets and a Planet Candidate Outside of the Spiral Disk Around SAO 206462." In: *AJ* 167.4, 182, p. 182. DOI: 10.3847/1538-3881/ad1ffc. arXiv: 2401.02834 [astro-ph.EP].

Currie, Thayne et al. (Apr. 2022). "Images of embedded Jovian planet formation at a wide separation around AB Aurigae." In: *Nature Astronomy* 6, pp. 751–759. DOI: 10.1038/s41550-022-01634-x. arXiv: 2204.00633 [astro-ph.EP].

D'Alessio, Paola, Jorge Cantó, Lee Hartmann, Nuria Calvet, and Susana Lizano (Feb. 1999). "On the Thermal Stability of Irradiation-dominated Pre-Main-Sequence Disks." In: *ApJ* 511.2, pp. 896–903. DOI: 10.1086/306704.

D'Angelo, Gennaro, Stephen H. Lubow, and Matthew R. Bate (Dec. 2006). "Evolution of Giant Planets in Eccentric Disks." In: *ApJ* 652.2, pp. 1698–1714. DOI: 10.1086/508451. arXiv: astro-ph/0608355 [astro-ph].

Dartois, E., A. Dutrey, and S. Guilloteau (Feb. 2003). "Structure of the DM Tau Outer Disk: Probing the vertical kinetic temperature gradient." In: *A&A* 399, pp. 773–787. DOI: 10.1051/0004-6361:20021638.

Davis, Shane W., James M. Stone, and Yan-Fei Jiang (Mar. 2012). "A Radiation Transfer Solver for Athena Using Short Characteristics." In: *ApJS* 199.1, 9, p. 9. DOI: 10.1088/0067-0049/199/1/9. arXiv: 1201.2222 [astro-ph.IM].

Debes, John et al. (2023). "The Surprising Evolution of the Shadow on the TW Hya Disk*." In: *The Astrophysical Journal* 948.1, 36, p. 36. DOI: 10.3847/1538-4357/acbdf1. arXiv: 2305.03611 [astro-ph.SR]. URL: https://dx.doi.org/10.3847/1538-4357/acbdf1.

Decampli, W. M., A. G. W. Cameron, P. Bodenheimer, and D. C. Black (Aug. 1978). "Ortho- and para-hydrogen in dense clouds, protoplanets, and planetary atmospheres." In: *ApJ* 223, pp. 854–858. DOI: 10.1086/156318.

Desidera, S. et al. (July 2021). "The SPHERE infrared survey for exoplanets (SHINE). I. Sample definition and target characterization." In: *A&A* 651, A70, A70. DOI: 10.1051/0004-6361/202038806. arXiv: 2103.04366 [astro-ph.EP].

Dong, Ruobing (Sept. 2015). "The Effects of Self-shadowing by a Puffed-up Inner Rim in Scattered Light Images of Protoplanetary Disks." In: *ApJ* 810.1, 6, p. 6. DOI: 10.1088/0004-637X/810/1/6. arXiv: 1507.07925 [astro-ph.SR].

Dong, Ruobing and Jeffrey Fung (Jan. 2017). "How Bright are Planet-induced Spiral Arms in Scattered Light?" In: *ApJ* 835.1, 38, p. 38. DOI: 10.3847/1538-4357/835/1/38. arXiv: 1612.00446 [astro-ph.EP].

Dong, Ruobing, Jeffrey Fung, and Eugene Chiang (July 2016). "How Spirals and Gaps Driven by Companions in Protoplanetary Disks Appear in Scattered Light at Arbitrary Viewing Angles." In: *ApJ* 826.1, 75, p. 75. DOI: 10.3847/0004-637X/826/1/75. arXiv: 1602.04814 [astro-ph.EP].

Dong, Ruobing, Zhaohuan Zhu, Roman R. Rafikov, and James M. Stone (Aug. 2015). "Observational Signatures of Planets in Protoplanetary Disks: Spiral Arms Observed in Scattered Light Imaging Can be Induced by Planets." In: *ApJ* 809.1, L5, p. L5. DOI: 10.1088/2041-8205/809/1/L5. arXiv: 1507.03596 [astro-ph.EP].

Duffell, Paul C. (July 2015). "A Simple Analytical Model for Gaps in Protoplanetary Disks." In: *ApJ* 807.1, L11, p. L11. DOI: 10.1088/2041-8205/807/1/L11. arXiv: 1505.03514 [astro-ph.EP].

Dullemond, C. P. (Sept. 2000). "Are passive protostellar disks stable to self-shadowing?" In: *A&A* 361, pp. L17–L20. DOI: 10.48550/arXiv.astro-ph/0007399. arXiv: astro-ph/0007399 [astro-ph].

Dullemond, C. P., C. Dominik, and A. Natta (Oct. 2001). "Passive Irradiated Circumstellar Disks with an Inner Hole." In: *ApJ* 560.2, pp. 957–969. DOI: 10.1086/323057. arXiv: astro-ph/0106470 [astro-ph].

Dullemond, C. P., D. Hollenbach, I. Kamp, and P. D'Alessio (Jan. 2007). "Models of the Structure and Evolution of Protoplanetary Disks." In: *Protostars and Planets V*. Ed. by Bo Reipurth, David Jewitt, and Klaus Keil, p. 555. DOI: 10.48550/arXiv.astro-ph/0602619. arXiv: astro-ph/0602619 [astro-ph].

Dullemond, C. P., A. Juhasz, A. Pohl, F. Sereshti, R. Shetty, T. Peters, B. Commercon, and M. Flock (Feb. 2012). *RADMC-3D: A multi-purpose radiative transfer tool*. Astrophysics Source Code Library, record ascl:1202.015. ascl: 1202.015.

Eastwood, James W. (1986). "Particle simulation methods in plasma physics." In: *Computer Physics Communications* 43.1, pp. 89–106. ISSN: 0010-4655. DOI: https://doi.org/10.1016/0010-4655(86)90055-X. URL: https://www.sciencedirect.com/science/article/pii/001046558690055X.

Ensman, Lisa (Mar. 1994). "Test Problems for Radiation and Radiation-Hydrodynamics Codes." In: *ApJ* 424, p. 275. DOI: 10.1086/173889.

Flock, M., S. Fromang, M. González, and B. Commerçon (Dec. 2013). "Radiation magnetohydrodynamics in global simulations of protoplanetary discs." In: *A&A* 560, A43, A43. DOI: 10.1051/0004-6361/201322451. arXiv: 1310.5865 [astro-ph.EP].

Flock, Mario, Neal J. Turner, Richard P. Nelson, Wladimir Lyra, Natascha Manger, and Hubert Klahr (July 2020). "Gas and Dust Dynamics in Starlight-heated Protoplanetary Disks." In: *ApJ* 897.2, 155, p. 155. DOI: 10.3847/1538-4357/ab9641. arXiv: 2005.11974 [astro-ph.EP].

Follette, Katherine B. et al. (June 2023). "The Giant Accreting Protoplanet Survey (GAPlanetS)-Results from a 6 yr Campaign to Image Accreting Protoplanets." In: *AJ* 165.6, 225, p. 225. DOI: 10.3847/1538-3881/acc183. arXiv: 2211.02109 [astro-ph.EP].

Fung, Jeffrey (Jan. 2015). "A Study of Protoplanetary Disk Dynamics using Accelerated Hydrodynamics Simulations on Graphics Processing Units." PhD thesis. University of Toronto, Canada.

Fung, Jeffrey, Pawel Artymowicz, and Yanqin Wu (Oct. 2015). "The 3D Flow Field Around an Embedded Planet." In: *ApJ* 811.2, 101, p. 101. DOI: 10.1088/0004-637X/811/2/101. arXiv: 1505.03152 [astro-ph.EP].

Fung, Jeffrey and Eugene Chiang (Dec. 2016). "Gap Opening in 3D: Single-planet Gaps." In: *ApJ* 832.2, 105, p. 105. DOI: 10.3847/0004-637X/832/2/105. arXiv: 1606.02299 [astro-ph.EP].

Fung, Jeffrey and Ruobing Dong (Dec. 2015). "Inferring Planet Mass from Spiral Structures in Protoplanetary Disks." In: *ApJ* 815.2, L21, p. L21. DOI: 10.1088/2041-8205/815/2/L21. arXiv: 1511.01178 [astro-ph.EP].

Fung, Jeffrey, Frédéric Masset, Elena Lega, and David Velasco (Mar. 2017). "Planetary Torque in 3D Isentropic Disks." In: *AJ* 153.3, 124, p. 124. DOI: 10.3847/1538-3881/153/3/124. arXiv: 1610.09375 [astro-ph.EP].

Fung, Jeffrey, Ji-Ming Shi, and Eugene Chiang (Feb. 2014a). "How Empty are Disk Gaps Opened by Giant Planets?" In: *ApJ* 782.2, 88, p. 88. DOI: 10.1088/0004-637X/782/2/88. arXiv: 1310.0156 [astro-ph.EP].

— (Feb. 2014b). "How Empty are Disk Gaps Opened by Giant Planets?" In: *ApJ* 782.2, 88, p. 88. DOI: 10.1088/0004-637X/782/2/88. arXiv: 1310.0156 [astro-ph.EP].

Fung, Jeffrey, Zhaohuan Zhu, and Eugene Chiang (Dec. 2019). "Circumplanetary Disk Dynamics in the Isothermal and Adiabatic Limits." In: *ApJ* 887.2, 152, p. 152. DOI: 10.3847/1538-4357/ab53da. arXiv: 1909.09655 [astro-ph.EP].

GRAVITY Collaboration et al. (Nov. 2021). "The GRAVITY young stellar object survey. VII. The inner dusty disks of T Tauri stars." In: *A&A* 655, A73, A73. DOI: 10.1051/0004-6361/202141624. arXiv: 2109.11826 [astro-ph.SR].

Gárate, M., J. Cuadra, M. Montesinos, and P. Arévalo (Mar. 2021). "Feedback-limited accretion: variable luminosity from growing planets." In: *MNRAS* 501.3, pp. 3113–3121. DOI: 10.1093/mnras/staa3860. arXiv: 1711.01372 [astro-ph.EP].

Ginzburg, Sivan and Re'em Sari (Sept. 2018). "Deep and wide gaps by super Earths in low-viscosity discs." In: *MNRAS* 479.2, pp. 1986–1996. DOI: 10.1093/mnras/sty1466. arXiv: 1803.01868 [astro-ph.EP].

Gnedin, Nickolay Y. and Tom Abel (Oct. 2001). "Multi-dimensional cosmological radiative transfer with a Variable Eddington Tensor formalism." In: *New A* 6.7, pp. 437–455. DOI: 10.1016/S1384-1076(01)00068-9. arXiv: astro-ph/0106278 [astro-ph].

Goldreich, P. and S. Tremaine (June 1978). "The excitation and evolution of density waves." In: *ApJ* 222, pp. 850–858. DOI: 10.1086/156203.

— (Nov. 1979). "The excitation of density waves at the Lindblad and corotation resonances by an external potential." In: *ApJ* 233, pp. 857–871. DOI: 10.1086/157448.

— (Oct. 1980). "Disk-satellite interactions." In: *ApJ* 241, pp. 425–441. DOI: 10.1086/158356.

Goldreich, Peter and Re'em Sari (Mar. 2003). "Eccentricity Evolution for Planets in Gaseous Disks." In: *ApJ* 585.2, pp. 1024–1037. DOI: 10.1086/346202. arXiv: astro-ph/0202462 [astro-ph].

Goodman, J. and R. R. Rafikov (May 2001). "Planetary Torques as the Viscosity of Protoplanetary Disks." In: *ApJ* 552.2, pp. 793–802. DOI: 10.1086/320572. arXiv: astro-ph/0010576 [astro-ph].

Grady, C. A. et al. (Jan. 2013). "Spiral Arms in the Asymmetrically Illuminated Disk of MWC 758 and Constraints on Giant Planets." In: *ApJ* 762.1, 48, p. 48. DOI: 10.1088/0004-637X/762/1/48. arXiv: 1212.1466 [astro-ph.SR].

Gravity Collaboration et al. (June 2023). "The GRAVITY young stellar object survey. X. Probing the inner disk and magnetospheric accretion region of CI Tau." In: *A&A* 674, A203, A203. DOI: 10.1051/0004-6361/202346446. arXiv: 2305.08170 [astro-ph.SR].

Haffert, S. Y., A. J. Bohn, J. de Boer, I. A. G. Snellen, J. Brinchmann, J. H. Girard, C. U. Keller, and R. Bacon (June 2019). "Two accreting protoplanets around the young star PDS 70." In: *Nature Astronomy* 3.8, pp. 749–754. DOI: 10.1038/s41550-019-0780-5. arXiv: 1906.01486 [astro-ph.EP]. URL: https://doi.org/10.1038/s41550-019-0780-5.

Hammer, Michael, Kaitlin M. Kratter, and Min-Kai Lin (Apr. 2017). "Slowly-growing gap-opening planets trigger weaker vortices." In: *MNRAS* 466.3, pp. 3533–3543. DOI: 10.1093/mnras/stw3000. arXiv: 1610.01606 [astro-ph.EP].

Hammond, Iain, Valentin Christiaens, Daniel J. Price, Claudia Toci, Christophe Pinte, Sandrine Juillard, and Himanshi Garg (June 2023). "Confirmation and Keplerian motion of the gap-carving protoplanet HD 169142 b." In: *MNRAS* 522.1, pp. L51–L55. DOI: 10.1093/mnrasl/slad027. arXiv: 2302.11302 [astro-ph.EP].

Harten, Amiram, Peter D. Lax, and Bram Van Leer (1983). "On Upstream Differencing and Godunov-Type Schemes for Hyperbolic Conservation Laws." In: *SIAM Review*

25.1, pp. 35–61. ISSN: 00361445. URL: http://www.jstor.org/stable/2030019 (visited on 02/24/2025).

Henyey, L. G. and J. L. Greenstein (Jan. 1941). "Diffuse radiation in the Galaxy." In: *ApJ* 93, pp. 70–83. DOI: 10.1086/144246.

Hu, Xiao, Zhi-Yun Li, Lile Wang, Zhaohuan Zhu, and Jaehan Bae (Apr. 2023). "Gap Opening in Protoplanetary Disks: Gas Dynamics from Global Non-ideal MHD Simulations with Consistent Thermochemistry." In: *arXiv e-prints* 523.4, arXiv:2304.05972, arXiv:2304.05972. DOI: 10.48550/arXiv.2304.05972. arXiv: 2304.05972 [astro-ph.EP].

Huang, Jane et al. (Dec. 2018). "The Disk Substructures at High Angular Resolution Project (DSHARP). II. Characteristics of Annular Substructures." In: *ApJ* 869.2, L42, p. L42. DOI: 10.3847/2041-8213/aaf740. arXiv: 1812.04041 [astro-ph.EP].

Huang, Pinghui and Xue-Ning Bai (Sept. 2022). "A Multifluid Dust Module in Athena++: Algorithms and Numerical Tests." In: *ApJS* 262.1, 11, p. 11. DOI: 10.3847/1538-4365/ac76cb. arXiv: 2206.01023 [astro-ph.EP].

Huang, Pinghui, Ruobing Dong, Hui Li, Shengtai Li, and Jianghui Ji (Oct. 2019). "The Observability of Vortex-driven Spiral Arms in Protoplanetary Disks: Basic Spiral Properties." In: *ApJ* 883.2, L39, p. L39. DOI: 10.3847/2041-8213/ab40c4. arXiv: 1909.00706 [astro-ph.EP].

Huang, Shunquan and Cong Yu (Aug. 2022). "Rossby wave instabilities of protoplanetary discs with cooling." In: *MNRAS* 514.2, pp. 1733–1740. DOI: 10.1093/mnras/stac1464. arXiv: 2205.11969 [astro-ph.EP].

Hubeny, I. (Mar. 1990). "Vertical Structure of Accretion Disks: A Simplified Analytical Model." In: *ApJ* 351, p. 632. DOI: 10.1086/168501.

Jang-Condell, Hannah and Neal J. Turner (Apr. 2012). "Gaps in Protoplanetary Disks as Signatures of Planets. I. Methodology and Validation." In: *ApJ* 749.2, 153, p. 153. DOI: 10.1088/0004-637X/749/2/153. arXiv: 1202.3465 [astro-ph.EP].

Jiang, Yan-Fei (Apr. 2021). "An Implicit Finite Volume Scheme to Solve the Time-dependent Radiation Transport Equation Based on Discrete Ordinates." In: *ApJS* 253.2, 49, p. 49. DOI: 10.3847/1538-4365/abe303. arXiv: 2102.02212 [astro-ph.IM].

Juhász, Attila and Giovanni P. Rosotti (Feb. 2018). "Spiral arms in thermally stratified protoplanetary discs." In: *MNRAS* 474.1, pp. L32–L36. DOI: 10.1093/mnrasl/slx182. arXiv: 1711.03559 [astro-ph.EP].

Kanagawa, Kazuhiro D., Takayuki Muto, Hidekazu Tanaka, Takayuki Tanigawa, Taku Takeuchi, Takashi Tsukagoshi, and Munetake Momose (June 2016). "Mass constraint for a planet in a protoplanetary disk from the gap width." In: *PASJ* 68.3, 43, p. 43. DOI: 10.1093/pasj/psw037. arXiv: 1603.03853 [astro-ph.EP].

Keppler, M. et al. (Sept. 2018). "Discovery of a planetary-mass companion within the gap of the transition disk around PDS 70." In: *A&A* 617, A44, A44. DOI: 10.1051/0004-6361/201832957. arXiv: 1806.11568 [astro-ph.EP].

Klahr, H. H., Th. Henning, and W. Kley (Mar. 1999). "On the Azimuthal Structure of Thermal Convection in Circumstellar Disks." In: *ApJ* 514.1, pp. 325–343. DOI: 10.1086/306926.

Klahr, H. Hubertus and Thomas Henning (July 1997). "Particle-Trapping Eddies in Protoplanetary Accretion Disks." In: *Icarus* 128.1, pp. 213–229. DOI: 10.1006/icar.1997.5720.

Klahr, H. and W. Kley (Jan. 2006). "3D-radiation hydro simulations of disk-planet interactions. I. Numerical algorithm and test cases." In: *A&A* 445.2, pp. 747–758. DOI: 10.1051/0004-6361:20053238. arXiv: astro-ph/0510391 [astro-ph].

Kley, W. (Jan. 1989). "Radiation hydrodynamics of the boundary layer in accretion disks. I - Numerical methods." In: *A&A* 208.1-2, pp. 98–110.

— (Oct. 1998). "On the treatment of the Coriolis force in computational astrophysics." In: *A&A* 338, pp. L37–L41. DOI: 10.48550/arXiv.astro-ph/9808351. arXiv: astro-ph/9808351 [astro-ph].

— (Mar. 1999). "Mass flow and accretion through gaps in accretion discs." In: *MNRAS* 303.4, pp. 696–710. DOI: 10.1046/j.1365-8711.1999.02198.x. arXiv: astro-ph/9809253 [astro-ph].

Kley, W., B. Bitsch, and H. Klahr (Nov. 2009). "Planet migration in three-dimensional radiative discs." In: *A&A* 506.2, pp. 971–987. DOI: 10.1051/0004-6361/200912072. arXiv: 0908.1863 [astro-ph.EP].

Kley, W. and G. Dirksen (Feb. 2006). "Disk eccentricity and embedded planets." In: *A&A* 447.1, pp. 369–377. DOI: 10.1051/0004-6361:20053914. arXiv: astro-ph/0510393 [astro-ph].

Kley, W. and R. P. Nelson (Sept. 2012). "Planet-Disk Interaction and Orbital Evolution." In: *ARA&A* 50, pp. 211–249. DOI: 10.1146/annurev-astro-081811-125523. arXiv: 1203.1184 [astro-ph.EP].

Krapp, Leonardo, Juan Garrido-Deutelmoser, Pablo Benítez-Llambay, and Kaitlin M. Kratter (Mar. 2024a). "A Fast Second-order Solver for Stiff Multifluid Dust and Gas Hydrodynamics." In: *ApJS* 271.1, 7, p. 7. DOI: 10.3847/1538-4365/ad14f9. arXiv: 2310.04435 [physics.comp-ph].

Krapp, Leonardo, Kaitlin M. Kratter, Andrew N. Youdin, Pablo Benítez-Llambay, Frédéric Masset, and Philip J. Armitage (Feb. 2024b). "A thermodynamic criterion for the formation of Circumplanetary Disks." In: *arXiv e-prints*, arXiv:2402.14638, arXiv:2402.14638. DOI: 10.48550/arXiv.2402.14638. arXiv: 2402.14638 [astro-ph.EP].

Kratter, Kaitlin and Giuseppe Lodato (Sept. 2016). "Gravitational Instabilities in Circumstellar Disks." In: *ARA&A* 54, pp. 271–311. DOI: 10.1146/annurev-astro-081915-023307. arXiv: 1603.01280 [astro-ph.SR].

Kraus, Adam L. and Michael J. Ireland (Jan. 2012). "LkCa 15: A Young Exoplanet Caught at Formation?" In: *ApJ* 745.1, 5, p. 5. DOI: 10.1088/0004-637X/745/1/5. arXiv: 1110.3808 [astro-ph.EP].

Krieger, A. and S. Wolf (Mar. 2020). "Unbiased Monte Carlo continuum radiative transfer in optically thick regions." In: *A&A* 635, A148, A148. DOI: 10.1051/0004-6361/201937355. arXiv: 2003.13334 [astro-ph.IM].

— (June 2022). "Feasibility of detecting and characterizing embedded low-mass giant planets in gaps in the VIS/NIR wavelength range." In: *A&A* 662, A99, A99. DOI: 10.1051/0004-6361/202142652. arXiv: 2203.01891 [astro-ph.EP].

Laibe, G., J. F. Gonzalez, and S. T. Maddison (Jan. 2012). "Revisiting the "radial-drift barrier" of planet formation and its relevance in observed protoplanetary discs." In: *A&A* 537, A61, A61. DOI: 10.1051/0004-6361/201015349. arXiv: 1111.3083 [astro-ph.EP].

Lambrechts, M. and A. Johansen (Aug. 2012). "Rapid growth of gas-giant cores by pebble accretion." In: *A&A* 544, A32, A32. DOI: 10.1051/0004-6361/201219127. arXiv: 1205.3030 [astro-ph.EP].

Law, Charles J. et al. (May 2023). "Mapping Protoplanetary Disk Vertical Structure with CO Isotopologue Line Emission." In: *ApJ* 948.1, 60, p. 60. DOI: 10.3847/1538-4357/acb3c4. arXiv: 2212.08667 [astro-ph.EP].

Lega, E., A. Crida, B. Bitsch, and A. Morbidelli (Mar. 2014). "Migration of Earth-sized planets in 3D radiative discs." In: *Monthly Notices of the Royal Astronomical Society* 440.1, pp. 683–695. ISSN: 0035-8711. DOI: 10.1093/mnras/stu304. eprint: https://academic.oup.com/mnras/article-pdf/440/1/683/9387732/stu304.pdf. URL: https://doi.org/10.1093/mnras/stu304.

Levermore, C. D. (Feb. 1984). "Relating Eddington factors to flux limiters." In: *J. Quant. Spectr. Rad. Tra* 31.2, pp. 149–160. DOI: 10.1016/0022-4073(84)90112-2.

Levermore, C. D. and G. C. Pomraning (Aug. 1981). "A flux-limited diffusion theory." In: *ApJ* 248, pp. 321–334. DOI: 10.1086/159157.

Liu, Xu-Dong, Stanley Osher, and Tony Chan (1994). "Weighted Essentially Non-oscillatory Schemes." In: *Journal of Computational Physics* 115.1, pp. 200–212. ISSN: 0021-9991. DOI: https://doi.org/10.1006/jcph.1994.1187. URL: https://www.sciencedirect.com/science/article/pii/S0021999184711879.

Lobo Gomes, Aiara, Hubert Klahr, Ana Lucia Uribe, Paola Pinilla, and Clément Surville (Sept. 2015). "Vortex Formation and Evolution in Planet Harboring Disks Under Thermal Relaxation." In: *ApJ* 810.2, 94, p. 94. DOI: 10.1088/0004-637X/810/2/94. arXiv: 1508.00903 [astro-ph.EP].

Lovelace, R. V. E., H. Li, S. A. Colgate, and A. F. Nelson (Mar. 1999). "Rossby Wave Instability of Keplerian Accretion Disks." In: *ApJ* 513.2, pp. 805–810. DOI: 10.1086/306900. arXiv: astro-ph/9809321 [astro-ph].

Lovelace, R. V. E. and M. M. Romanova (Aug. 2014). "Rossby wave instability in astrophysical discs." In: *Fluid Dynamics Research* 46.4, 041401, p. 041401. DOI: 10.1088/0169-5983/46/4/041401. arXiv: 1312.4572 [astro-ph.SR].

Lubow, Stephen H. and Zhaohuan Zhu (Apr. 2014). "An Analytic Model for Buoyancy Resonances in Protoplanetary Disks." In: *ApJ* 785.1, 32, p. 32. DOI: 10.1088/0004-637X/785/1/32. arXiv: 1402.4162 [astro-ph.EP].

Malygin, M. G., H. Klahr, D. Semenov, Th. Henning, and C. P. Dullemond (Sept. 2017). "Efficiency of thermal relaxation by radiative processes in protoplanetary discs: constraints on hydrodynamic turbulence." In: *A&A* 605, A30, A30. DOI: 10.1051/0004-6361/201629933. arXiv: 1704.06786 [astro-ph.EP].

Manger, Natascha, Thomas Pfeil, and Hubert Klahr (Dec. 2021). "High-resolution parameter study of the vertical shear instability - II: dependence on temperature gradient and cooling time." In: *MNRAS* 508.4, pp. 5402–5409. DOI: 10.1093/mnras/stab2599. arXiv: 2109.01649 [astro-ph.EP].

Masset, F. (Jan. 2000). "FARGO: A fast eulerian transport algorithm for differentially rotating disks." In: *A&AS* 141, pp. 165–173. DOI: 10.1051/aas:2000116. arXiv: astro-ph/9910390 [astro-ph].

Mathis, J. S., W. Rumpl, and K. H. Nordsieck (Oct. 1977). "The size distribution of interstellar grains." In: *ApJ* 217, pp. 425–433. DOI: 10.1086/155591.

Meheut, H., Z. Meliani, P. Varniere, and W. Benz (Sept. 2012). "Dust-trapping Rossby vortices in protoplanetary disks." In: *A&A* 545, A134, A134. DOI: 10.1051/0004-6361/201219794. arXiv: 1208.4947 [astro-ph.EP].

Melon Fuksman, Julio David, Mario Flock, and Hubert Klahr (Dec. 2023). "Vertical shear instability in two-moment radiation-hydrodynamical simulations of irradiated protoplanetary disks II. Secondary instabilities and stability regions." In: *A&A*, arXiv:2312.06890. submitted, arXiv:2312.06890. arXiv: 2312.06890 [astro-ph.EP].

— (Feb. 2024a). "Vertical shear instability in two-moment radiation-hydrodynamical simulations of irradiated protoplanetary disks. I. Angular momentum transport and turbulent heating." In: *A&A* 682, A139, A139. DOI: 10.1051/0004-6361/202346554. arXiv: 2312.06882 [astro-ph.EP].

— (Feb. 2024b). "Vertical shear instability in two-moment radiation-hydrodynamical simulations of irradiated protoplanetary disks. II. Secondary instabilities and stability regions." In: *A&A* 682, A140, A140. DOI: 10.1051/0004-6361/202346555. arXiv: 2312.06890 [astro-ph.EP].

Melon Fuksman, Julio David and Hubert Klahr (Sept. 2022). "No Self-shadowing Instability in 2D Radiation Hydrodynamical Models of Irradiated Protoplanetary Disks." In: *ApJ* 936.1, 16, p. 16. DOI: 10.3847/1538-4357/ac7fee. arXiv: 2207.05106 [astro-ph.EP].

Melon Fuksman, Julio David, Hubert Klahr, Mario Flock, and Andrea Mignone (Jan. 2021). "A Two-moment Radiation Hydrodynamics Scheme Applicable to Simulations of Planet Formation in Circumstellar Disks." In: *ApJ* 906.2, 78, p. 78. DOI: 10.3847/1538-4357/abc879. arXiv: 2005.01785 [astro-ph.EP].

Melon Fuksman, Julio David and Andrea Mignone (June 2019). "A Radiative Transfer Module for Relativistic Magnetohydrodynamics in the PLUTO Code." In: *ApJS* 242.2, 20, p. 20. DOI: 10.3847/1538-4365/ab18ff. arXiv: 1903.10456 [astro-ph.IM].

Mignone, A., G. Bodo, S. Massaglia, T. Matsakos, O. Tesileanu, C. Zanni, and A. Ferrari (May 2007). "PLUTO: A Numerical Code for Computational Astrophysics." In: *ApJS* 170.1, pp. 228–242. DOI: 10.1086/513316. arXiv: astro-ph/0701854 [astro-ph].

Miranda, Ryan and Roman R. Rafikov (Apr. 2019). "Multiple Spiral Arms in Protoplanetary Disks: Linear Theory." In: *ApJ* 875.1, 37, p. 37. DOI: 10.3847/1538-4357/ab0f9e. arXiv: 1811.09628 [astro-ph.EP].

Miranda, Ryan and Roman R. Rafikov (2019). "On the Planetary Interpretation of Multiple Gaps and Rings in Protoplanetary Disks Seen By ALMA." In: *The Astrophysical Journal Letters* 878.1, p. L9. DOI: 10.3847/2041-8213/ab22a7. URL: https://dx.doi.org/10.3847/2041-8213/ab22a7.

Miranda, Ryan and Roman R. Rafikov (Mar. 2020a). "Planet-Disk Interaction in Disks with Cooling: Basic Theory." In: *ApJ* 892.1, 65, p. 65. DOI: 10.3847/1538-4357/ab791a. arXiv: 1911.01428 [astro-ph.EP].

Miranda, Ryan and Roman R. Rafikov (Mar. 2020b). "Planet-Disk Interaction in Disks with Cooling: Basic Theory." In: *ApJ* 892.1, 65, p. 65. DOI: 10.3847/1538-4357/ab791a. arXiv: 1911.01428 [astro-ph.EP].

Montesinos, Matías, Jorge Cuadra, Sebastian Perez, Clément Baruteau, and Simon Casassus (June 2015). "Protoplanetary Disks Including Radiative Feedback from

Accreting Planets." In: *ApJ* 806.2, 253, p. 253. DOI: 10.1088/0004-637X/806/2/253. arXiv: 1505.03392 [astro-ph.EP].

Montesinos, Matías and Nicolás Cuello (Mar. 2018). "Planetary-like spirals caused by moving shadows in transition discs." In: *MNRAS* 475.1, pp. L35–L39. DOI: 10.1093/mnrasl/sly001. arXiv: 1712.09157 [astro-ph.EP].

Montesinos, Matías, Nicolás Cuello, Johan Olofsson, Jorge Cuadra, Amelia Bayo, Gesa H. M. Bertrang, and Clément Perrot (Mar. 2021). "Radiative Scale Height and Shadows in Protoplanetary Disks." In: *ApJ* 910.1, 31, p. 31. DOI: 10.3847/1538-4357/abe3fc. arXiv: 2102.02874 [astro-ph.EP].

Montesinos, Matías, Sebastian Perez, Simon Casassus, Sebastian Marino, Jorge Cuadra, and Valentin Christiaens (May 2016). "Spiral Waves Triggered by Shadows in Transition Disks." In: *ApJ* 823.1, L8, p. L8. DOI: 10.3847/2041-8205/823/1/L8. arXiv: 1601.07912 [astro-ph.EP].

Mordasini, C., Y. Alibert, W. Benz, and D. Naef (Jan. 2008). "Giant Planet Formation by Core Accretion." In: *Extreme Solar Systems*. Ed. by D. Fischer, F. A. Rasio, S. E. Thorsett, and A. Wolszczan. Vol. 398. Astronomical Society of the Pacific Conference Series, p. 235. DOI: 10.48550/arXiv.0710.5667. arXiv: 0710.5667 [astro-ph].

Muñoz, D. J., K. Kratter, V. Springel, and L. Hernquist (Dec. 2014). "Planet-disc interaction on a freely moving mesh." In: *MNRAS* 445.4, pp. 3475–3495. DOI: 10.1093/mnras/stu1918. arXiv: 1408.6550 [astro-ph.EP].

Muley, Dhruv, Ruobing Dong, and Jeffrey Fung (Oct. 2021). "Observational Signatures of Planets in Protoplanetary Disks: Temperature Structures in Spiral Arms." In: *AJ* 162.4, 129, p. 129. DOI: 10.3847/1538-3881/ac141f. arXiv: 2107.06323 [astro-ph.EP].

Muley, Dhruv, Julio David Melon Fuksman, and Hubert Klahr (Oct. 2023). "Three-temperature radiation hydrodynamics with PLUTO. Tests and applications in the context of protoplanetary disks." In: *A&A* 678, A162, A162. DOI: 10.1051/0004-6361/202347101. arXiv: 2308.03504 [astro-ph.IM].

— (Oct. 2024a). "Spiral excitation in protoplanetary disks through gap-edge illumination: Three-temperature radiation hydrodynamics and NIR image modeling." In: *A&A* 690, A355, A355. DOI: 10.1051/0004-6361/202451554. arXiv: 2408.16461 [astro-ph.EP].

— (July 2024b). "Three-temperature radiation hydrodynamics with PLUTO: Thermal and kinematic signatures of accreting protoplanets." In: *A&A* 687, A213, A213. DOI: 10.1051/0004-6361/202449739. arXiv: 2405.03375 [astro-ph.EP].

Müller, A. et al. (Sept. 2018). "Orbital and atmospheric characterization of the planet within the gap of the PDS 70 transition disk." In: *A&A* 617, L2, p. L2. DOI: 10.1051/0004-6361/201833584. arXiv: 1806.11567 [astro-ph.EP].

Muto, T. et al. (Apr. 2012). "Discovery of Small-scale Spiral Structures in the Disk of SAO 206462 (HD 135344B): Implications for the Physical State of the Disk from Spiral Density Wave Theory." In: *ApJ* 748.2, L22, p. L22. DOI: 10.1088/2041-8205/748/2/L22. arXiv: 1202.6139 [astro-ph.EP].

Nakagawa, Y., M. Sekiya, and C. Hayashi (Sept. 1986). "Settling and growth of dust particles in a laminar phase of a low-mass solar nebula." In: *Icarus* 67.3, pp. 375–390. DOI: 10.1016/0019-1035(86)90121-1.

Nealon, Rebecca, Daniel J. Price, and Christophe Pinte (Mar. 2020). "Rocking shadows in broken circumbinary discs." In: *MNRAS* 493.1, pp. L143–L147. DOI: 10.1093/mnrasl/slaa026. arXiv: 2002.02983 [astro-ph.EP].

Núñez, Jonatan (Oct. 2015). *High-Order Methods for Computational Astrophysics*. ISBN: 9783843922937. DOI: 10.18419/opus-3980.

Ormel, C. W. and H. H. Klahr (Sept. 2010). "The effect of gas drag on the growth of protoplanets. Analytical expressions for the accretion of small bodies in laminar disks." In: *A&A* 520, A43, A43. DOI: 10.1051/0004-6361/201014903. arXiv: 1007.0916 [astro-ph.EP].

Owen, James E., Cathie J. Clarke, and Barbara Ercolano (May 2012). "On the theory of disc photoevaporation." In: *MNRAS* 422.3, pp. 1880–1901. DOI: 10.1111/j.1365-2966.2011.20337.x. arXiv: 1112.1087 [astro-ph.SR].

Papaloizou, J. C. B., R. P. Nelson, W. Kley, F. S. Masset, and P. Artymowicz (Jan. 2007). "Disk-Planet Interactions During Planet Formation." In: *Protostars and Planets V*. Ed. by Bo Reipurth, David Jewitt, and Klaus Keil, p. 655. DOI: 10.48550/arXiv.astro-ph/0603196. arXiv: astro-ph/0603196 [astro-ph].

Pareschi, Lorenzo and Giovanni Russo (2005). "Implicit-explicit runge-kutta schemes and applications to hyperbolic systems with relaxation." In: *Journal of Scientific Computing* 25.1, pp. 129–155. DOI: 10.1007/BF02728986. URL: https://doi.org/10.1007/BF02728986.

Pascucci, I., S. Cabrit, S. Edwards, U. Gorti, O. Gressel, and T. K. Suzuki (July 2023). "The Role of Disk Winds in the Evolution and Dispersal of Protoplanetary Disks." In: *Protostars and Planets VII*. Ed. by S. Inutsuka, Y. Aikawa, T. Muto, K. Tomida, and M. Tamura. Vol. 534. Astronomical Society of the Pacific Conference Series, p. 567. DOI: 10.48550/arXiv.2203.10068. arXiv: 2203.10068 [astro-ph.EP].

Pavlyuchenkov, Ya. N. and A. G. Zhilkin (Sept. 2013). "A multicomponent model for computing the thermal structure of collapsing protostellar clouds." In: *Astronomy Reports* 57.9, pp. 641–656. DOI: 10.1134/S1063772913090035.

Pavlyuchenkov, Ya. N., A. G. Zhilkin, E. I. Vorobyov, and A. M. Fateeva (Feb. 2015). "The thermal structure of a protostellar envelope." In: *Astronomy Reports* 59.2, pp. 133–144. DOI: 10.1134/S1063772915020067. arXiv: 1502.04835 [astro-ph.GA].

Pencil Code Collaboration et al. (Feb. 2021). "The Pencil Code, a modular MPI code for partial differential equations and particles: multipurpose and multiuser-maintained." In: *The Journal of Open Source Software* 6.58, 2807, p. 2807. DOI: 10.21105/joss.02807. arXiv: 2009.08231 [astro-ph.IM].

Pérez, Sebastián, S. Casassus, and P. Benítez-Llambay (Oct. 2018). "Observability of planet-disc interactions in CO kinematics." In: *MNRAS* 480.1, pp. L12–L17. DOI: 10.1093/mnrasl/sly109. arXiv: 1806.05125 [astro-ph.EP].

Persson, Magnus Vilhelm (Aug. 2014). "Current view of protostellar evolution (ENG)." In: DOI: 10.6084/m9.figshare.654555.v7. URL: https://figshare.com/articles/figure/Current_view_of_protostellar_evolution/654555.

Pierens, Arnaud and Min-Kai Lin (Oct. 2018). "On the evolution of vortices in massive protoplanetary discs." In: *MNRAS* 479.4, pp. 4878–4890. DOI: 10.1093/mnras/sty1314. arXiv: 1805.05768 [astro-ph.EP].

Pinte, C., D. J. Price, F. Ménard, G. Duchêne, W. R. F. Dent, T. Hill, I. de Gregorio-Monsalvo, A. Hales, and D. Mentiplay (2018). "Kinematic Evidence for an Embed-

ded Protoplanet in a Circumstellar Disk." In: *The Astrophysical Journal Letters* 860.1, p. L13. DOI: 10.3847/2041-8213/aac6dc. URL: https://dx.doi.org/10.3847/2041-8213/aac6dc.

Pinte, C., R. Teague, K. Flaherty, C. Hall, S. Facchini, and S. Casassus (July 2023a). "Kinematic Structures in Planet-Forming Disks." In: *Protostars and Planets VII*. Ed. by S. Inutsuka, Y. Aikawa, T. Muto, K. Tomida, and M. Tamura. Vol. 534. Astronomical Society of the Pacific Conference Series, p. 645. DOI: 10.48550/arXiv.2203.09528. arXiv: 2203.09528 [astro-ph.EP].

Pinte, C. et al. (Aug. 2019). "Kinematic detection of a planet carving a gap in a protoplanetary disk." In: *Nature Astronomy* 3, pp. 1109–1114. DOI: 10.1038/s41550-019-0852-6. arXiv: 1907.02538 [astro-ph.SR].

Pinte, C. et al. (Nov. 2023b). "Kinematic and thermal signatures of the directly imaged protoplanet candidate around Elias 2-24." In: *MNRAS* 526.1, pp. L41–L46. DOI: 10.1093/mnrasl/slad010. arXiv: 2301.08759 [astro-ph.EP].

Pinte, Christophe, Richard Teague, Kevin Flaherty, Cassandra Hall, Stefano Facchini, and Simon Casassus (Mar. 2022). "Kinematic Structures in Planet-Forming Disks." In: *arXiv e-prints*, arXiv:2203.09528, arXiv:2203.09528. DOI: 10.48550/arXiv.2203.09528. arXiv: 2203.09528 [astro-ph.EP].

Qian, Yansong and Yanqin Wu (Nov. 2024). "Shadows Wreak Havoc in Transition Disks." In: *ApJ* 976.1, 5, p. 5. DOI: 10.3847/1538-4357/ad8233. arXiv: 2407.09613 [astro-ph.EP].

Rafikov, Roman R. (Mar. 2017). "Protoplanetary Disks as (Possibly) Viscous Disks." In: *ApJ* 837.2, 163, p. 163. DOI: 10.3847/1538-4357/aa6249. arXiv: 1701.02352 [astro-ph.EP].

Ren, Bin B. et al. (Jan. 2024). "A companion in V1247 Ori supported by motion in the pattern of the spiral arm." In: *A&A* 681, L2, p. L2. DOI: 10.1051/0004-6361/202348114. arXiv: 2310.15430 [astro-ph.EP].

Ren, Bin et al. (Apr. 2018). "A Decade of MWC 758 Disk Images: Where Are the Spiral-arm-driving Planets?" In: *ApJ* 857.1, L9, p. L9. DOI: 10.3847/2041-8213/aab7f5. arXiv: 1803.06776 [astro-ph.EP].

Sallum, S. et al. (Nov. 2015). "Accreting protoplanets in the LkCa 15 transition disk." In: *Nature* 527.7578, pp. 342–344. DOI: 10.1038/nature15761. arXiv: 1511.07456 [astro-ph.EP].

Schwarz, Kamber R., Joan Najita, Jennifer Bergner, John Carr, Alexander Tielens, Edwin A. Bergin, David Wilner, David Leisawitz, and Christopher K. Walker (Feb. 2023). "Protoplanetary Disk Science with the Orbiting Astronomical Satellite Investigating Stellar Systems (OASIS) Observatory." In: *Space Sci. Rev.* 219.1, 12, p. 12. DOI: 10.1007/s11214-023-00954-2. arXiv: 2302.05223 [astro-ph.EP].

Shakura, N. I. and R. A. Sunyaev (Jan. 1973). "Black holes in binary systems. Observational appearance." In: *A&A* 24, pp. 337–355.

Shuai, Linling, Bin B. Ren, Ruobing Dong, Xingyu Zhou, Laurent Pueyo, Robert J. De Rosa, Taotao Fang, and Dimitri Mawet (Dec. 2022). "Stellar Flyby Analysis for Spiral Arm Hosts with Gaia DR3." In: *ApJS* 263.2, 31, p. 31. DOI: 10.3847/1538-4365/ac98fd. arXiv: 2210.03725 [astro-ph.EP].

Skinner, M. Aaron and Eve C. Ostriker (June 2013). "A Two-moment Radiation Hydrodynamics Module in Athena Using a Time-explicit Godunov Method." In: *ApJS* 206.2, 21, p. 21. DOI: 10.1088/0067-0049/206/2/21. arXiv: 1306.0010 [astro-ph.IM].

Speedie, Jessica, Richard A. Booth, and Ruobing Dong (May 2022). "Observing Planet-driven Dust Spirals with ALMA." In: *ApJ* 930.1, 40, p. 40. DOI: 10.3847/1538-4357/ac5cc0. arXiv: 2203.00692 [astro-ph.EP].

Springel, Volker (Jan. 2010). "E pur si muove: Galilean-invariant cosmological hydrodynamical simulations on a moving mesh." In: *MNRAS* 401.2, pp. 791–851. DOI: 10.1111/j.1365-2966.2009.15715.x. arXiv: 0901.4107 [astro-ph.CO].

Sturm, J. A., G. P. Rosotti, and C. Dominik (Nov. 2020). "Dust dynamics in planet-driven spirals." In: *A&A* 643, A92, A92. DOI: 10.1051/0004-6361/202038919. arXiv: 2009.07575 [astro-ph.EP].

Su, Zehao and Xue-Ning Bai (2024). "Dynamical Consequence of Shadows Cast to the Outer Protoplanetary Disks. I. Two-dimensional Simulations." In: *The Astrophysical Journal* 975.1, arXiv:2407.12659, p. 126. DOI: 10.3847/1538-4357/ad7581. arXiv: Arxiv:2407.12659v1 [astro-ph.EP]. URL: https://dx.doi.org/10.3847/1538-4357/ad7581.

Szulágyi, J. (June 2017). "Effects of the Planetary Temperature on the Circumplanetary Disk and on the Gap." In: *ApJ* 842.2, 103, p. 103. DOI: 10.3847/1538-4357/aa7515. arXiv: 1705.08444 [astro-ph.EP].

Tarczay-Nehéz, D., Zs Regály, and E. Vorobyov (Apr. 2020). "On the vortex evolution in non-isothermal protoplanetary discs." In: *MNRAS* 493.2, pp. 3014–3025. DOI: 10.1093/mnras/staa364. arXiv: 2002.02203 [astro-ph.EP].

Teague, Richard, Jaehan Bae, Sean M. Andrews, Myriam Benisty, Edwin A. Bergin, Stefano Facchini, Jane Huang, Cristiano Longarini, and David Wilner (Sept. 2022). "Mapping the Complex Kinematic Substructure in the TW Hya Disk." In: *ApJ* 936.2, 163, p. 163. DOI: 10.3847/1538-4357/ac88ca. arXiv: 2208.04837 [astro-ph.EP].

Teague, Richard, Jaehan Bae, Jane Huang, and Edwin A. Bergin (Oct. 2019). "Spiral Structure in the Gas Disk of TW Hya." In: *ApJ* 884.2, L56, p. L56. DOI: 10.3847/2041-8213/ab4a83. arXiv: 1910.01532 [astro-ph.EP].

Teague, Richard et al. (Nov. 2021). "Molecules with ALMA at Planet-forming Scales (MAPS). XVIII. Kinematic Substructures in the Disks of HD 163296 and MWC 480." In: *The Astrophysical Journal Supplement Series* 257.1, p. 18. ISSN: 1538-4365. DOI: 10.3847/1538-4365/ac1438. URL: http://dx.doi.org/10.3847/1538-4365/ac1438.

Toro, E. F., M. Spruce, and W. Speares (1994). "Restoration of the contact surface in the HLL-Riemann solver." In: *Shock Waves* 4.1, pp. 25–34. DOI: 10.1007/BF01414629. URL: https://doi.org/10.1007/BF01414629.

Toro, Eleuterio F. (2009). *Riemann Solvers and Numerical Methods for Fluid Dynamics: A Practical Introduction*. Springer Berlin Heidelberg. ISBN: 9783540498346. DOI: 10.1007/b79761. URL: http://dx.doi.org/10.1007/b79761.

Tsang, David (2011). "PROTOPLANETARY DISK RESONANCES AND TYPE I MIGRATION." In: *The Astrophysical Journal* 741.2, p. 109. DOI: 10.1088/0004-637X/741/2/109. URL: https://dx.doi.org/10.1088/0004-637X/741/2/109.

Ueda, Takahiro, Mario Flock, and Tilman Birnstiel (June 2021). "Thermal Wave Instability as an Origin of Gap and Ring Structures in Protoplanetary Disks." In: *ApJ* 914.2, L38, p. L38. DOI: 10.3847/2041-8213/ac0631. arXiv: 2105.13852 [astro-ph.EP].

Ueda, Takahiro, Mario Flock, and Satoshi Okuzumi (Jan. 2019). "Dust Pileup at the Dead-zone Inner Edge and Implications for the Disk Shadow." In: *ApJ* 871.1, 10, p. 10. DOI: 10.3847/1538-4357/aaf3a1. arXiv: 1811.09756 [astro-ph.EP].

Urpin, V. and A. Brandenburg (Mar. 1998). "Magnetic and vertical shear instabilities in accretion discs." In: *MNRAS* 294.3, pp. 399–406. DOI: 10.1046/j.1365-8711.1998.01118.x10.1111/j.1365-8711.1998.01118.x.

Vorobyov, Eduard I., Ryoki Matsukoba, Kazuyuki Omukai, and Manuel Guedel (June 2020). "Thermal evolution of protoplanetary disks: from β-cooling to decoupled gas and dust temperatures." In: *A&A* 638, A102, A102. DOI: 10.1051/0004-6361/202037841. arXiv: 2004.13561 [astro-ph.EP].

Wagner, Kevin, Jordan M. Stone, Eckhart Spalding, Daniel Apai, Ruobing Dong, Steve Ertel, Jarron Leisenring, and Ryan Webster (Sept. 2019). "Thermal Infrared Imaging of MWC 758 with the Large Binocular Telescope: Planetary-driven Spiral Arms?" In: *ApJ* 882.1, 20, p. 20. DOI: 10.3847/1538-4357/ab32ea. arXiv: 1907.06655 [astro-ph.SR].

Wagner, Kevin et al. (Apr. 2024). "JWST/NIRCam Imaging of Young Stellar Objects. I. Constraints on Planets Exterior to the Spiral Disk Around MWC 758." In: *AJ* 167.4, 181, p. 181. DOI: 10.3847/1538-3881/ad11d5. arXiv: 2401.02830 [astro-ph.EP].

Wang, Lile, Xue-Ning Bai, and Jeremy Goodman (Mar. 2019). "Global Simulations of Protoplanetary Disk Outflows with Coupled Non-ideal Magnetohydrodynamics and Consistent Thermochemistry." In: *ApJ* 874.1, 90, p. 90. DOI: 10.3847/1538-4357/ab06fd. arXiv: 1810.12330 [astro-ph.EP].

Wang, Lile and Jeremy Goodman (Sept. 2017). "Hydrodynamic Photoevaporation of Protoplanetary Disks with Consistent Thermochemistry." In: *ApJ* 847.1, 11, p. 11. DOI: 10.3847/1538-4357/aa8726. arXiv: 1706.03155 [astro-ph.EP].

Watanabe, Sei-ichiro and D. N. C. Lin (Jan. 2008). "Thermal Waves in Irradiated Protoplanetary Disks." In: *ApJ* 672.2, pp. 1183–1195. DOI: 10.1086/523347. arXiv: 0709.1760 [astro-ph].

Weidenschilling, S. J. (July 1977). "Aerodynamics of solid bodies in the solar nebula." In: *MNRAS* 180, pp. 57–70. DOI: 10.1093/mnras/180.2.57.

Weidenschilling, Stuart J. (2000). "Formation of Planetesimals and Accretion of the Terrestrial Planets." In: *Space Science Reviews* 92.1, pp. 295–310. DOI: 10.1023/A:1005259615299. URL: https://doi.org/10.1023/A:1005259615299.

Whipple, F. L. (Jan. 1972). "On certain aerodynamic processes for asteroids and comets." In: *From Plasma to Planet*. Ed. by Aina Elvius, p. 211.

Whitney, B. A., T. P. Robitaille, J. E. Bjorkman, R. Dong, M. J. Wolff, K. Wood, and J. Honor (Aug. 2013). "Three-dimensional Radiation Transfer in Young Stellar Objects." In: *ApJS* 207.2, 30, p. 30. DOI: 10.1088/0067-0049/207/2/30. arXiv: 1307.0561 [astro-ph.SR].

Williams, Jonathan P. and Lucas A. Cieza (Sept. 2011). "Protoplanetary Disks and Their Evolution." In: *ARA&A* 49.1, pp. 67–117. DOI: 10.1146/annurev-astro-081710-102548. arXiv: 1103.0556 [astro-ph.GA].

Woitke, P., I. Kamp, and W. F. Thi (July 2009). "Radiation thermo-chemical models of protoplanetary disks. I. Hydrostatic disk structure and inner rim." In: *A&A* 501.1, pp. 383–406. DOI: 10.1051/0004-6361/200911821. arXiv: 0904.0334 [astro-ph.EP].

Wölfer, L. et al. (Apr. 2021). "A highly non-Keplerian protoplanetary disc. Spiral structure in the gas disc of CQ Tau." In: *A&A* 648, A19, A19. DOI: 10.1051/0004-6361/202039469. arXiv: 2012.04680 [astro-ph.EP].

Wu, Yanqin and Yoram Lithwick (Dec. 2021). "The Irradiation Instability of Protoplanetary Disks." In: *ApJ* 923.1, 123, p. 123. DOI: 10.3847/1538-4357/ac2b9c. arXiv: 2105.02680 [astro-ph.EP].

Xie, Chengyan, Bin Ren, Ruobing Dong, Laurent Pueyo, Jean-Baptiste Ruffio, Taotao Fang, Dimitri Mawet, and Tomas Stolker (Jan. 2021). "Spiral Arm Pattern Motion in the SAO 206462 Protoplanetary Disk." In: *ApJ* 906.2, L9, p. L9. DOI: 10.3847/2041-8213/abd241. arXiv: 2012.05242 [astro-ph.EP].

Yamaleev, Nail K. and Mark H. Carpenter (May 2009). "Third-order Energy Stable WENO scheme." In: *Journal of Computational Physics* 228.8, pp. 3025–3047. DOI: 10.1016/j.jcp.2009.01.011.

Youdin, Andrew N. and Jeremy Goodman (2005). "Streaming Instabilities in Protoplanetary Disks." In: *The Astrophysical Journal* 620.1, p. 459. DOI: 10.1086/426895. URL: https://dx.doi.org/10.1086/426895.

Youdin, Andrew N. and Yoram Lithwick (Dec. 2007). "Particle stirring in turbulent gas disks: Including orbital oscillations." In: *Icarus* 192.2, pp. 588–604. DOI: 10.1016/j.icarus.2007.07.012. arXiv: 0707.2975 [astro-ph].

Yun, Han-Gyeol, Woong-Tae Kim, Jaehan Bae, and Cheongho Han (Oct. 2022). "Effects of Radiative Diffusion on Dynamical Corotation Torque in Three-dimensional Protoplanetary Disks." In: *ApJ* 938.2, 102, p. 102. DOI: 10.3847/1538-4357/ac9185. arXiv: 2209.05417 [astro-ph.EP].

Zhang, Minghao, Pinghui Huang, and Ruobing Dong (Jan. 2024). "The Dependence of the Structure of Planet-opened Gaps in Protoplanetary Disks on Radiative Cooling." In: *ApJ* 961.1, 86, p. 86. DOI: 10.3847/1538-4357/ad055c. arXiv: 2310.11757 [astro-ph.EP].

Zhang, Shangjia, Xiao Hu, Zhaohuan Zhu, and Jaehan Bae (Dec. 2021). "Self-consistent Ring Model in Protoplanetary Disks: Temperature Dips and Substructure Formation." In: *ApJ* 923.1, 70, p. 70. DOI: 10.3847/1538-4357/ac2c82. arXiv: 2110.00858 [astro-ph.EP].

Zhang, Shangjia and Zhaohuan Zhu (Apr. 2020). "The effects of disc self-gravity and radiative cooling on the formation of gaps and spirals by young planets." In: *MNRAS* 493.2, pp. 2287–2305. DOI: 10.1093/mnras/staa404. arXiv: 1911.01530 [astro-ph.EP].

— (Oct. 2024). "3D Radiation-hydrodynamical Simulations of Shadows on Transition Disks." In: *ApJ* 974.2, L38, p. L38. DOI: 10.3847/2041-8213/ad815f. arXiv: 2409.08373 [astro-ph.EP].

Zhang, Shangjia et al. (Dec. 2018). "The Disk Substructures at High Angular Resolution Project (DSHARP). VII. The Planet-Disk Interactions Interpretation." In: *ApJ* 869.2, L47, p. L47. DOI: 10.3847/2041-8213/aaf744. arXiv: 1812.04045 [astro-ph.EP].

Zhu, Wei and Subo Dong (2021). "Exoplanet Statistics and Theoretical Implications." In: *Annual Review of Astronomy and Astrophysics* 59.Volume 59, 2021, pp. 291–336.

ISSN: 1545-4282. DOI: https://doi.org/10.1146/annurev-astro-112420-020055. URL: https://www.annualreviews.org/content/journals/10.1146/annurev-astro-112420-020055.

Zhu, Zhaohuan, Ruobing Dong, James M. Stone, and Roman R. Rafikov (Nov. 2015). "The Structure of Spiral Shocks Excited by Planetary-mass Companions." In: *ApJ* 813.2, 88, p. 88. DOI: 10.1088/0004-637X/813/2/88. arXiv: 1507.03599 [astro-ph.SR].

Zhu, Zhaohuan, Richard P. Nelson, Ruobing Dong, Catherine Espaillat, and Lee Hartmann (Aug. 2012). "Dust Filtration by Planet-induced Gap Edges: Implications for Transitional Disks." In: *ApJ* 755.1, 6, p. 6. DOI: 10.1088/0004-637X/755/1/6. arXiv: 1205.5042 [astro-ph.SR].

Zhu, Zhaohuan, Richard P. Nelson, Lee Hartmann, Catherine Espaillat, and Nuria Calvet (Mar. 2011). "Transitional and Pre-transitional Disks: Gap Opening by Multiple Planets?" In: *ApJ* 729.1, 47, p. 47. DOI: 10.1088/0004-637X/729/1/47. arXiv: 1012.4395 [astro-ph.SR].

Zhu, Zhaohuan, Shangjia Zhang, and Ted Johnson (Dec. 2024). "Asymmetric Temperature Variations In Protoplanetary disks: I. Linear Theory, Corotating Spirals, and Ring Formation." In: *arXiv e-prints*, arXiv:2412.09571, arXiv:2412.09571. DOI: 10.48550/arXiv.2412.09571. arXiv: 2412.09571 [astro-ph.EP].

Ziampras, Alexandros, Cornelis P. Dullemond, Tilman Birnstiel, Myriam Benisty, and Richard P. Nelson (Oct. 2024). "Spirals, rings, and vortices shaped by shadows in protoplanetary disks: from radiative hydrodynamical simulations to observable signatures." In: *arXiv e-prints* 528.4, arXiv:2410.13932, arXiv:2410.13932. DOI: 10.48550/arXiv.2410.13932. arXiv: 2410.13932 [astro-ph.EP].

Ziampras, Alexandros, Wilhelm Kley, and Cornelis P. Dullemond (May 2020). "Importance of radiative effects in gap opening by planets in protoplanetary disks." In: *A&A* 637, A50, A50. DOI: 10.1051/0004-6361/201937048. arXiv: 2003.02298 [astro-ph.EP].

Ziampras, Alexandros, Richard P. Nelson, and Roman R. Rafikov (Sept. 2023). "Modelling planet-induced gaps and rings in ALMA discs: the role of in-plane radiative diffusion." In: *MNRAS* 524.3, pp. 3930–3947. DOI: 10.1093/mnras/stad1973. arXiv: 2305.14415 [astro-ph.EP].

Zingale, Michael (2022). "Euler Riemann problem." In: *Tutorial on Computational Astrophysics*. URL: https://zingale.github.io/comp_astro_tutorial/advection_euler/euler/euler-riemann.html.

van der Marel, N., E. F. van Dishoeck, S. Bruderer, S. M. Andrews, K. M. Pontoppidan, G. J. Herczeg, T. van Kempen, and A. Miotello (Jan. 2016). "Resolved gas cavities in transitional disks inferred from CO isotopologs with ALMA." In: *A&A* 585, A58, A58. DOI: 10.1051/0004-6361/201526988. arXiv: 1511.07149 [astro-ph.EP].

van der Marel, Nienke, Til Birnstiel, Antonio Garufi, Enrico Ragusa, Valentin Christiaens, Daniel J. Price, Steph Sallum, Dhruv Muley, Logan Francis, and Ruobing Dong (Jan. 2021). "On the Diversity of Asymmetries in Gapped Protoplanetary Disks." In: *AJ* 161.1, 33, p. 33. DOI: 10.3847/1538-3881/abc3ba. arXiv: 2010.10568 [astro-ph.EP].

COLOPHON

This document was typeset using the typographical look-and-feel `classicthesis` developed by André Miede. The style was inspired by Robert Bringhurst's seminal book on typography "*The Elements of Typographic Style*". `classicthesis` is available for both LaTeX and LyX:

https://bitbucket.org/amiede/classicthesis/

Happy users of `classicthesis` usually send a real postcard to the author, a collection of postcards received so far is featured here:

http://postcards.miede.de/